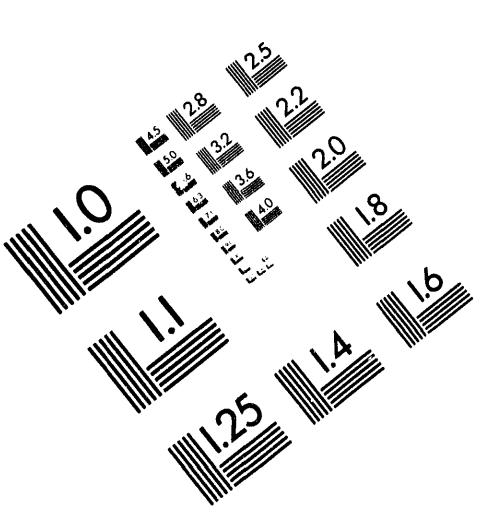

Association for Information and Image Management

1100 Wayne Avenue, Suite 1100
Silver Spring, Maryland 20910

301/587-8202

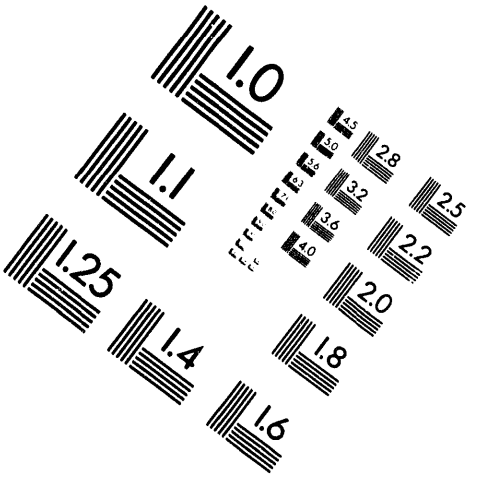

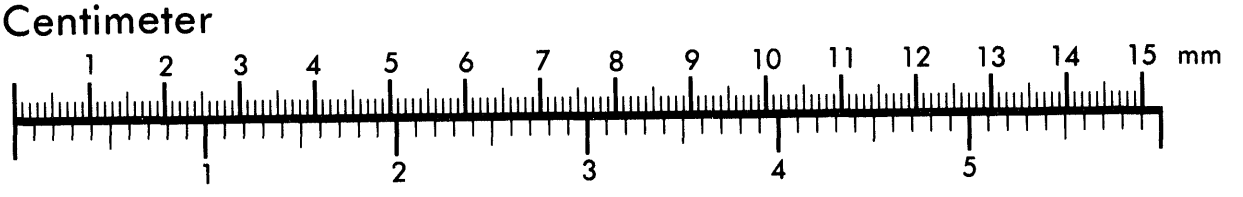

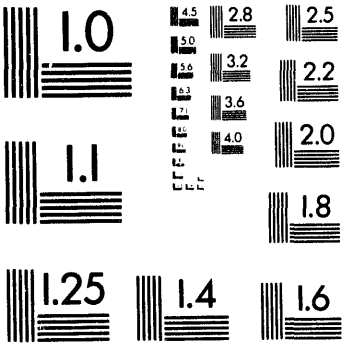

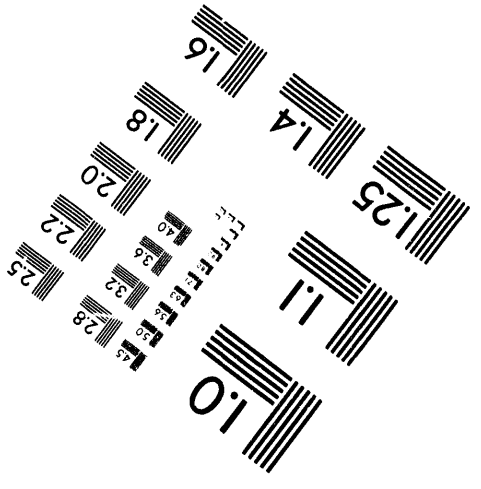

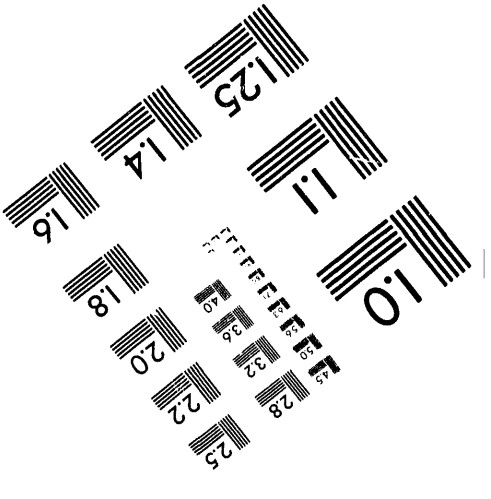

MANUFACTURED TO AIIM STANDARDS
BY APPLIED IMAGE, INC.

1 of 3

Distribution
Category UC-610

SAND94-0938
Unlimited Release
Printed July 1994

MELCOR 1.8.2 Calculations of Selected Sequences for the ABWR

L. N. Kmetyk
Thermal/Hydraulic Analysis Department
Sandia National Laboratories
Albuquerque, NM 87185-0745

Abstract

This report summarizes the results from MELCOR calculations of severe accident sequences in the ABWR and presents comparisons with MAAP calculations for the same sequences. MELCOR was run for two low-pressure and three high-pressure sequences to identify the materials which enter containment and are available for release to the environment (source terms), to study the potential effects of core-concrete interaction, and to obtain event timings during each sequence; the source terms include fission products and other materials such as those generated by core-concrete interactions. Sensitivity studies were done on the impact of assuming limestone rather than basaltic concrete and on the effect of quenching core debris in the cavity compared to having hot, unquenched debris present.

Contents

List of Figures

List of Tables

Acknowledgements

The author would like to acknowledge a number of individuals who contributed significantly to this effort. At Sandia, Richard Griffith was the project manager, and Randy Cole and Sam Thompson of the MELCOR development team helped with code problem diagnosis and correction. At the NRC, John Monninger provided information on the ABWR plant and on the MAAP calculations; John Monninger, Bob Palla and Andre Drozd suggested useful output to be presented, and John Monninger, Andre Drozd and Sudhamay Basu reviewed the manuscript, which resulted in a large number of improvements and clarifications to the text.

This work was funded by the Technical Assistance Management Section, Office of Nuclear Reactor Regulation, U. S. Nuclear Regulatory Commission.

1 Introduction

1.1 Background and Objectives

This report summarizes the results from MELCOR calculations of severe accident sequences in the advanced boiling water reactor (ABWR) plant and presents comparisons with MAAP calculations for the same sequences [1]. The program task was to run the MELCOR code [2] for two low-pressure and three high-pressure sequences to identify the materials which enter containment and are available for release to the environment (source terms), to study the potential effects of core-concrete interaction, and to obtain event timings during each sequence. The source terms include fission products and other materials such as those generated by core-concrete interactions. All calculations, with both MELCOR and MAAP, analyzed loss-of-cooling accidents in the ABWR plant.

The LCLP-PF-R-N and LCLP-FS-R-N sequences are accidents starting with a loss of all core cooling and with vessel failure occurring at low pressure; the LCHP-PF-P-M, LCHP-FS-R-N and LCHP-PS-R-N sequences also are accidents starting with a loss of all core cooling but with vessel failure occurring at high pressure. In all these sequences, the passive flooder automatically floods the lower drywell. The containment is depressurized as planned through a relief rupture disk, except in the LCHP-PF-P-M sequence where containment leakage occurs through movable penetrations. In the LCLP-FS-R-N and LCHP-FS-R-N sequences, the firewater spray provides additional containment cooling; in the LCHP-PS-R-N sequence, the drywell spray provides additional containment cooling. Since all of these accident sequences progressed through core melt, core slumping, reactor vessel failure, and ex-vessel core-concrete interaction, they provided a good test of the ability of MELCOR to simulate integrated accidents that progressed to the point of radionuclide release to the containment or environment.

This report is designed to satisfy the documentation requirements of Task 3.1 in the "Severe Accidents and Containment Performance in Evolutionary and Passive LWRs" Project performed for the U.S. Nuclear Regulatory Commission (NRC) by Sandia National Laboratories (SNL) under FIN L-1632. The purpose of the report is to compare the results of five MAAP analyses of ABWR accident sequences carried out by GE with analyses of the same accident sequences using MELCOR, and to provide sensitivity studies on core-concrete interaction for selected sequences.

Note that this task did not include developing a MELCOR deck for the current ABWR plant design but instead relied on using an ABWR MELCOR input deck developed by Brookhaven National Laboratory and reviewed by Sandia some years ago [3], under FIN A-1392. That plant deck has not been reviewed against the current ABWR plant design; a few design changes have been identified during the course of this work as noted in the text, but it is recognized that other elements of the BNL ABWR MELCOR model also may not reflect the current ABWR plant design exactly.

1.2 MELCOR

MELCOR [2] began development in 1983 as a fully integrated, engineering-level computer code that models the progression of severe accidents in light water reactor nuclear power plants. MELCOR is being developed at Sandia National Laboratories for the U.S. Nuclear Regulatory Commission as a second-generation plant risk assessment tool and the successor to the Source Term Code Package [4]. The entire spectrum of severe accident phenomena, including reactor coolant system and containment thermal-hydraulic response, core heatup, degradation and relocation, and fission product release and transport, is treated in MELCOR in a unified framework for both boiling water reactors and pressurized water reactors. MELCOR has been especially designed to facilitate sensitivity and uncertainty analyses. Its current uses include estimation of severe accident source terms and their sensitivities and uncertainties in a variety of applications.

The newest version of MELCOR, MELCOR 1.8.2 (or 1.8NM), was released in May 1993. The ABWR analyses documented in this report were carried out with a slightly modified, later version (1.8NX).

(This report assumes a reader having some familiarity with MELCOR terminology and capabilities. For those with little or no previous experience with MELCOR, [2] is recommended as a good introduction and source of background information.)

1.3 Organization of Report

Section 2 contains a brief description of the overall ABWR plant design and of some features of particular interest to the sequences being analyzed. The five accident sequences being simulated are summarized briefly in Section 3. Section 4 describes the MELCOR input model for the ABWR plant. Results of the MELCOR calculations, along with comparisons to the MAAP results, are presented in Section 5, for each of the accident sequences. Section 6 gives results from sensitivity studies on core-concrete interaction, while Section 7 contains a brief summary and conclusions.

2 Plant Description

The Advanced Boiling Water Reactor (ABWR) represents the next generation of light water reactors (LWRs) to be introduced into commercial operation in the 1990s. The ABWR is the result of continuing evolution of the BWR, incorporating state-of-the-art technology and improvements, and extensive design and test and development programs.

A general description of the ABWR plant design is provided in the first portion of this section; that overall description is taken mostly from [5] and [6]. The rest of this section gives descriptions of several systems important to the sequences being simulated, taken mostly from [1].

2.1 Overall Plant and Core Design

The reactor thermal output is 3926Mw(th) which provides for a turbine-generator gross output in excess of 1356Mw(e). The reactor core consists of 872 fuel bundles operating at a power density of 50kw/liter. Recent fuel improvements include fuel rods with a zirconium barrier liner, axial variation of enrichment and gadolinia (Gd-absorber), high fuel exposure, minimal control cells, no shallow control rods and no rod pattern exchanges.

The ABWR development focused on an optimized selection of advanced technologies and proven BWR technologies. The new features are intended to provide improvements in construction schedules, reduced maintenance requirements, reduced radiation exposure, and to provide plant operation improvements and increased safety.

The ABWR design is being applied by the Tokyo Electric Power Co., Inc., as Units 6 and 7 at its Kashiwazaki-Kariwa site in Japan. Construction is scheduled for the early 1990s, and commercial operation planned for 1996.

2.2 Reactor Assembly

The reactor assembly (Figure 2.2.1) utilizes a standard BWR reactor pressure vessel configuration. The greatest change in the ABWR vessel from previous BWR designs is the elimination of the external recirculation piping due to the incorporation of internal pumps for reactor coolant recirculation. The reactor pressure vessel (RPV) is $\simeq$7m in diameter and 21m in height. The reactor vessel height and total volume have been minimized, which results in reduced volume requirements for the containment and reactor building. The vessel is of standard BWR vessel design except for two items. The annular space between the RPV shroud and the vessel wall is increased to permit the positioning of the 10 internal pumps used for recirculation flow; also, the standard cylindrical vessel support skirt has been changed to a conical skirt to permit the use of the internal pumps. All large pipe nozzles to the vessel below the top of the active fuel have been eliminated; this improves the safety performance during a postulated loss-of-coolant accident (LOCA) and allows for decreased ECCS capacity.

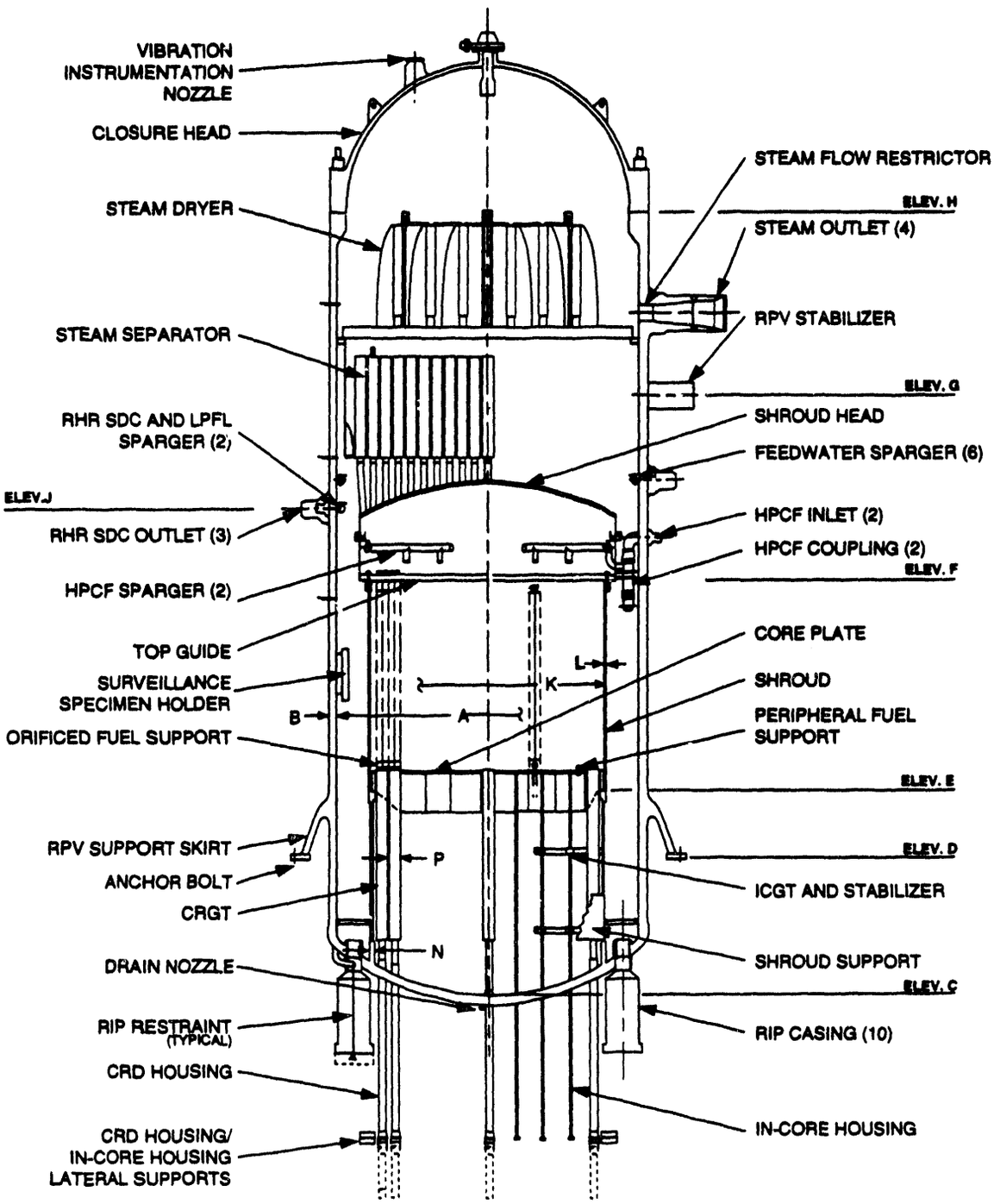

Figure 2.2.1. ABWR Reactor Assembly

2.3 Emergency Core Cooling

The Emergency Core Cooling System (ECCS) and the Residual Heat Removal (RHR) system both incorporate three redundant and independent divisions. The design of the reactor pressure vessel, with the deletion of the external recirculation loops and with no large pipe nozzles in the core region, allows for a reduced-capacity ECCS. The ECCS network has each of the three divisions having one high pressure and one low pressure inventory makeup system. The high pressure configuration consists of two motor driven High Pressure Core Flooders each with its own independent sparger discharging inside the shroud over the core and the Reactor Core Isolation Cooling (RCIC) system which has been upgraded to a safety system. The RCIC has the dual function of providing high pressure ECCS flow following a postulated LOCA, and also providing reactor coolant inventory control for reactor isolation transients. The RCIC, with its steam turbine driven power, also provides a diverse makeup source during loss of all A-C power events. The lower pressure ECCS for the ABWR utilizes the three RHR pumps in the post-LOCA core cooling mode. These pumps provide Low Pressure Flooding and are labelled LPFL. The ECCS pumps provide core makeup over the full pressure range. For small LOCAs that do not depressurize the vessel when high pressure makeup is unavailable, an Automatic Depressurization System (ADS) actuates to vent steam through the safety relief valves to the suppression pool, thus depressurizing the vessel and allowing the LPFL pumps to provide core coolant.

The RHR system has a dual role of providing cooling for normal shutdown and also for providing core and containment cooling during LOCAs. The ABWR RHR systems can achieve core and suppression pool cooling simultaneously since, in the core cooling mode, the flow from the suppression pool passes through the heat exchanger in each of the three divisions of the RHR system.

2.4 Containment and Reactor Building

For the ABWR the containment design is of the pressure suppression type with a covered suppression pool. The cylindrical design is a simple shaped concept that is the same as the Mark III drywell design. Shown in Figure 2.4.1, it is a lined, reinforced concrete structure, and the concrete walls of the cylindrical containment structure have been fully integrated with the reactor building from a structural design standpoint; the annular top slab of the drywell also is integrated with the upper pool girders that run across the building and have direct connections with the building's outer walls. The pressure-retaining concrete wall of the RCCV is lined with leak-tight steel plate.

The upper drywell encloses the reactor, and the process lines and valves of the reactor coolant system. The lower drywell, located under the reactor vessel, is used for installation and maintenance of the internal pump motors and their heat exchangers, and the control rod drives. Piping and cables are arranged inside and lead out of this space. Personnel and equipment access are provided by hatches in the upper drywell and through tunnels in the lower drywell.

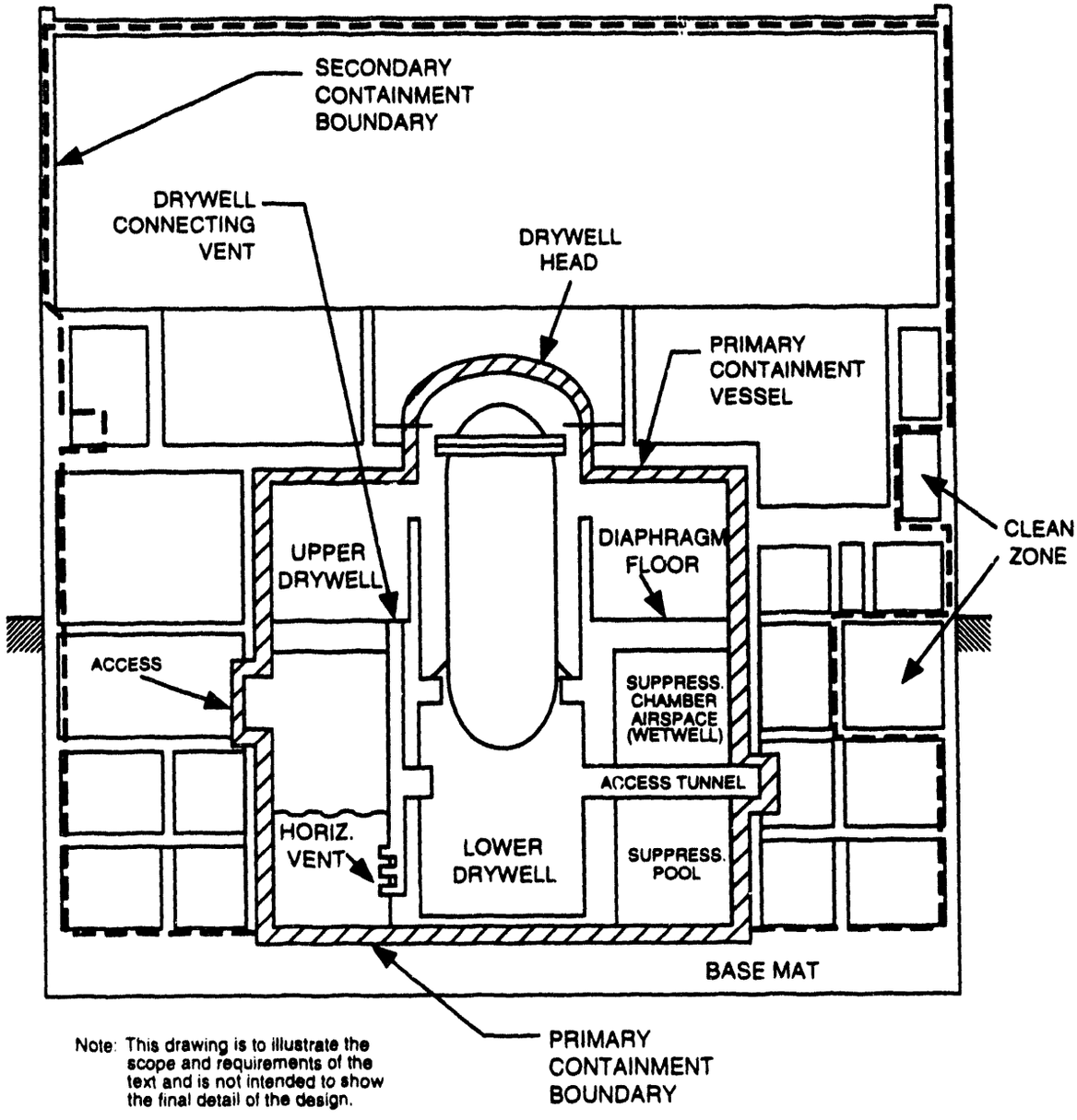

Figure 2.4.1. ABWR Containment and Reactor Building

The wetwell provides a vapor space, initially filled with nitrogen, and a pool to suppress the steam from a postulated LOCA. Multiple horizontal vents, derived from the Mark III containment design, discharge the vessel blowdown steam-water mixture and the nitrogen from the drywell to the wetwell pool. The steam is condensed, and the fission products are scrubbed and retained in the pool.

The ABWR design has a reactor building volume of approximately 167,000m^3.

The structural integration takes advantage of both the containment and the reactor building to carry dynamic and shear loads and thus reduce the overall size and thickness of the supporting walls. The reactor building has been separated into three quadrants to provide separation for the three division of the safety systems (described in Section 2.3). The reactor pedestal has been revised to support the drywell diaphragm floor, connect the access tunnels to the under-vessel area, contain the horizontal vent system and provide connecting vents between the lower and upper drywell.

2.5 Passive Flooder

The passive flooder system automatically opens a connection between the suppression pool and the lower drywell region when the temperature of the lower drywell vapor space reaches 533K. This serves to keep the core debris temperature low, minimizing core-concrete interaction and preventing radiation heat transfer from the debris to the containment structures and atmosphere. The passive flooder system is designed to cause the lower drywell to be flooded when there is no water overlying core debris in the cavity. If there is no overlying water pool, the core debris will heat up and melt the fusible plug material in the valve; if there is water overlying the debris pool, the lower drywell atmosphere will not heat up sufficiently to cause the passive flooder to open. (Because the firewater addition system is expected to operate in most of the accident sequences, the passive flooder is considered a passive backup system not needed in the majority of accidents.)

2.6 Containment Overpressure Protection System (COPS)

The Containment Overpressure Protection System (COPS) is part of the atmospheric control system and consists of two 8in-diameter overpressure relief rupture disks mounted in series on a 14in line which connects the wetwell vapor space to the stack. By engineering the release point in the wetwell vapor space, escaping fission products are forced through the suppression pool; any fission product release to the environment is greatly reduced by the scrubbing provided by the suppression pool.

A rupture disk setpoint of 0.72MPa (90psig) at 366K (200°F) was used. The 8in-diameter rupture disk is sufficient to allow 35kg/s of steam flow at this opening pressure. The rupture disk is not expected to be called upon until about 20hr after scram for most severe accidents.

Table 2.7.1. ABWR Containment Movable Penetration Leakage Areas

Pressure		Leak Area	
(psig)	(MPa)	(in^2)	(cm^2)
0	0	0	0
45	0.41	0	0
52	0.46	0	0
60	0.52	1.23	7.94
70	0.58	2.77	17.87
80	0.65	4.31	28.61
90	0.72	5.85	37.74
100	0.79	7.39	47.68
110	0.86	8.93	57.61
120	0.93	10.47	67.55

In the absence of the COPS, unmitigated over-pressurization of the containment will result in failure of the drywell head for most severe accident scenarios; however, some high-pressure core melt sequences result in fission product leakage through the movable penetrations in the drywell rather than drywell head failure. Failure pressure of the drywell head was assumed to be equal to its media ultimate strength, 1.025MPa (134psig). Most accident sequences show large differences in releases between drywell head failure and COPS cases.

2.7 Containment Movable Penetrations

The ultimate pressure capability of the containment is limited by the drywell upper head, and the postulated failure mechanism being the plastic yield of the torispherical dome. The pressure capability is 1.025MPa at 533K (134psig at 500°F), reduced to 0.93MPa at 644K (120psig at 700°F). At the capability pressure, liner failure which may lead to leakage is not expected to occur. Prior to containment failure there may be some leakage through large operable penetrations. Leakage through fixed mechanical and electrical penetrations is negligible compared to leakage through large operable penetrations such as the drywell head, equipment hatches and personnel airlocks. Assuming no sealing action from degraded seals above 533K (500°F), the estimated total leakage areas before the capability pressure is reached are given in Table 2.7.1.

2.8 Drywell Spray

The drywell sprays are one function of the residual heat removal (RHR) system, described in Section 2.3. The drywell sprays keep the upper drywell cool during severe acci-

dents, preventing degradation of penetration seals to avoid leakage through the movable penetrations and fission product release to the environment below the pressure capacity of the containment. Because the upper drywell drains into the suppression pool, the use of the drywell sprays will not keep the temperature in the lower drywell from increasing; therefore, the passive flooder will open when the lower drywell becomes sufficiently hot.

2.9 Firewater Spray

A firewater addition spray function is available as a backup to the RHR drywell spray (described in more detail in Section 2.8). Used in spray mode the firewater system adds external water to the containment, increasing the thermal mass of the system, and the firewater system provides cooling of the upper drywell region. The spray system is operated if vessel failure has occurred, as determined by the drywell temperature and inability to maintain water level in the vessel. The firewater spray causes the pressure and the temperature of the upper drywell to decrease rapidly. When the water level in the suppression pool reaches the level of the bottom of the vessel, the firewater system is turned off, and turned on again intermittently as needed to keep the temperature from exceeding 533K. (If drywell head failure occurs, the firewater spray system is to be restarted; this causes any fission product aerosols to agglomerate onto the spray droplets, reducing fission product release to the environment.)

3 Accident Sequences

The accident sequences analyzed with MELCOR and documented in this report are described using the nomenclature defined in the ABWR SSAR [1]. A complete accident sequence is designated by an eight character identifier. The first four characters indicate the general conditions of the accident. The next two characters are used to identify any mitigating systems used to prevent or reduce the release of fission products to the environment. The seventh character indicates the mode of containment failure and fission product release, and the eighth character reflects the expected magnitude of that release, as calculated by MAAP. Results for a number of accident sequence analyses done using the MAAP code are presented in the ABWR SSAR. A limited subset of these accident scenarios has been analyzed using the MELCOR code, as described in this report.

3.1 LCLP-PF-R-N Sequence

This accident sequence is a loss of all core cooling ("LC") with vessel failure occurring at low pressure ("LP"), *i.e.*, the ADS system is assumed to work as specified. The passive flooder system ("PF") is the only safety system in this case; it automatically opens a connection between the suppression pool and the lower drywell region when the temperature of the lower drywell vapor space reaches 533K, as described in Section 2.5. The containment overpressure system (COPS) relief rupture disk in the wetwell vapor space is assumed to open as designed ("R"), as described in Section 2.6, providing the mechanism whereby fission products may be released from the containment to the environment after pool scrubbing. The magnitude of release to the environment predicted by MAAP for this severe accident scenario is negligible ("N"), *i.e.*, <100% of the noble gases and <0.1% of the volatile fission products.

3.2 LCLP-FS-R-N Sequence

This accident sequence also is a loss of all core cooling ("LC") with vessel failure occurring at low pressure ("LP"), *i.e.*, the ADS system is assumed to work as specified. The firewater system is used in spray mode ("FS") to add external water to the containment, increasing the thermal mass of the system and providing cooling of the upper drywell region (as described in Section 2.9). This is in addition to the passive flooder opening to pour water from the suppression pool into the lower drywell cavity. The containment overpressure system (COPS) relief rupture disk is assumed to open as intended ("R"), providing the mechanism whereby fission products may be released from the containment to the environment. The magnitude of release predicted by MAAP is negligible ("N"), *i.e.*, <100% of the noble gases and <0.1% of the volatile fission products.

3.3 LCHP-PF-P-M Sequence

This accident sequence again is a loss of all core cooling ("LC") with vessel failure occurring at high pressure ("HP"). In this case, the passive flooder ("PF") is the only mitigating system assumed to operate (as in the corresponding low-pressure sequence, LCLP-PF-R-N). However, in this sequence leakage through movable penetrations in the drywell ("P") is assumed to occur when the atmosphere temperature exceeds 533K and the pressure exceeds 0.515MPa, as described in Section 2.7. Medium ("M") release of fission products is predicted by MAAP for this scenario, *i.e.*, <100% of the noble gases and <10% of the volatile fission products.

3.4 LCHP-FS-R-N Sequence

This accident sequence also is a loss of all core cooling ("LC") with vessel failure occurring at high pressure ("HP"). The firewater addition spray function ("FS") is used as a mitigating system in addition to the passive flooder opening. As in the corresponding low-pressure sequence, LCLP-FS-R-N, the containment overpressure system (COPS) relief rupture disk is assumed to open as intended ("R"), providing the mechanism whereby fission products may be released from the containment to the environment only after scrubbing through the suppression pool. The magnitude of release predicted by MAAP is negligible ("N"), *i.e.*, <100% of the noble gases and <0.1% of the volatile fission products.

3.5 LCHP-PS-R-N Sequence

This accident sequence is a loss of all core cooling ("LC") with vessel failure occurring at high pressure ("HP"), *i.e.*, the ADS system does not depressurize the primary system prior to vessel failure. In this case, the passive flooder and drywell spray ("PS") both operate. The drywell sprays are one function of the residual heat removal (RHR) system, described in Section 2.8. As in the two LCLP sequences, the containment overpressure system (COPS) relief rupture disk is assumed to open as designed ("R"), providing the mechanism whereby fission products may be released from the containment to the environment. The magnitude of release predicted by MAAP is negligible ("N"), *i.e.*, <100% of the noble gases and <0.1% of the volatile fission products.

4 MELCOR Input

The MELCOR ABWR input model consists of 11 control volumes (6 for the primary system, 4 for the containment and 1 for the environment), 21 flow paths, 35 heat structures, and a 52-cell core. The primary and containment system nodalizations are shown in Figures 4.1 and 4.2, respectively.

All control volumes were specified to use nonequilibrium thermodynamics and were specified to be vertical volumes; all heat structures used the steady-state temperature-gradient self-initialization option. Detailed volume-altitude tables and junction flow segments were used to correctly represent subcomponents in and between the major components modelled.

Junctions were defined to be either normal vertical flow paths or normal horizontal flow paths as determined by the system geometry. All area changes were explicitly modelled using flow path segments, and loss coefficients for all elbows, bends, plenum inlets and outlets, *etc.*, derived from the basic facility geometry using standard formulae were input. Flow path opening heights were based on pipe diameters for horizontal junctions, while the opening heights used on vertical flow paths (primarily within the vessel) were generally set to small values (*e.g.*, ~2-3in).

The heat structures were generally specified to use the "internal" set of heat transfer coefficient correlations on the inside of most heat structures, with the heated equivalent diameter input as the characteristic length; on their outside surface, most of the heat structures were specified to use the "external" set of heat transfer coefficient correlations with the heat structure length or height input as the characteristic length. The critical pool fractions for heat transfer to pool and to atmosphere both were set to 0.50, for most of the heat structure surfaces; radiation heat transfer using the gray gas model was enabled with emissivities of 0.7 or 0.9, and mean free paths set to various values.

The primary system (*i.e.*, the reactor pressure vessel) was represented by six control volumes: one each for the downcomer, the lower plenum, the upper plenum and steam separators, the steam dome and the core and bypass channels; the vessel model is depicted in more detail in Figure 4.1, with flow paths and heat structures shown. (The core model is discussed separately later in this section.) The recirculation loop piping was not modelled explicitly for these calculations, because it was assumed that circulation within the recirculation piping would not significantly affect the boiloff results. Flow paths internal to the vessel model are used for the channel and bypass inlets and outlets, for flows from the upper plenum to the steam dome and to the downcomer, to model a liquid return path from the separator to the downcomer and to model the 10 internal recirculation pumps from the downcomer to the lower plenum. Other flow paths connect the primary system model to the containment model, representing the steam line SRV from the steam dome to the suppression pool, the vessel breach from the lower plenum to the lower drywell cavity, and control rod drive (CRD) seal leakage from the lower plenum to the lower drywell cavity.

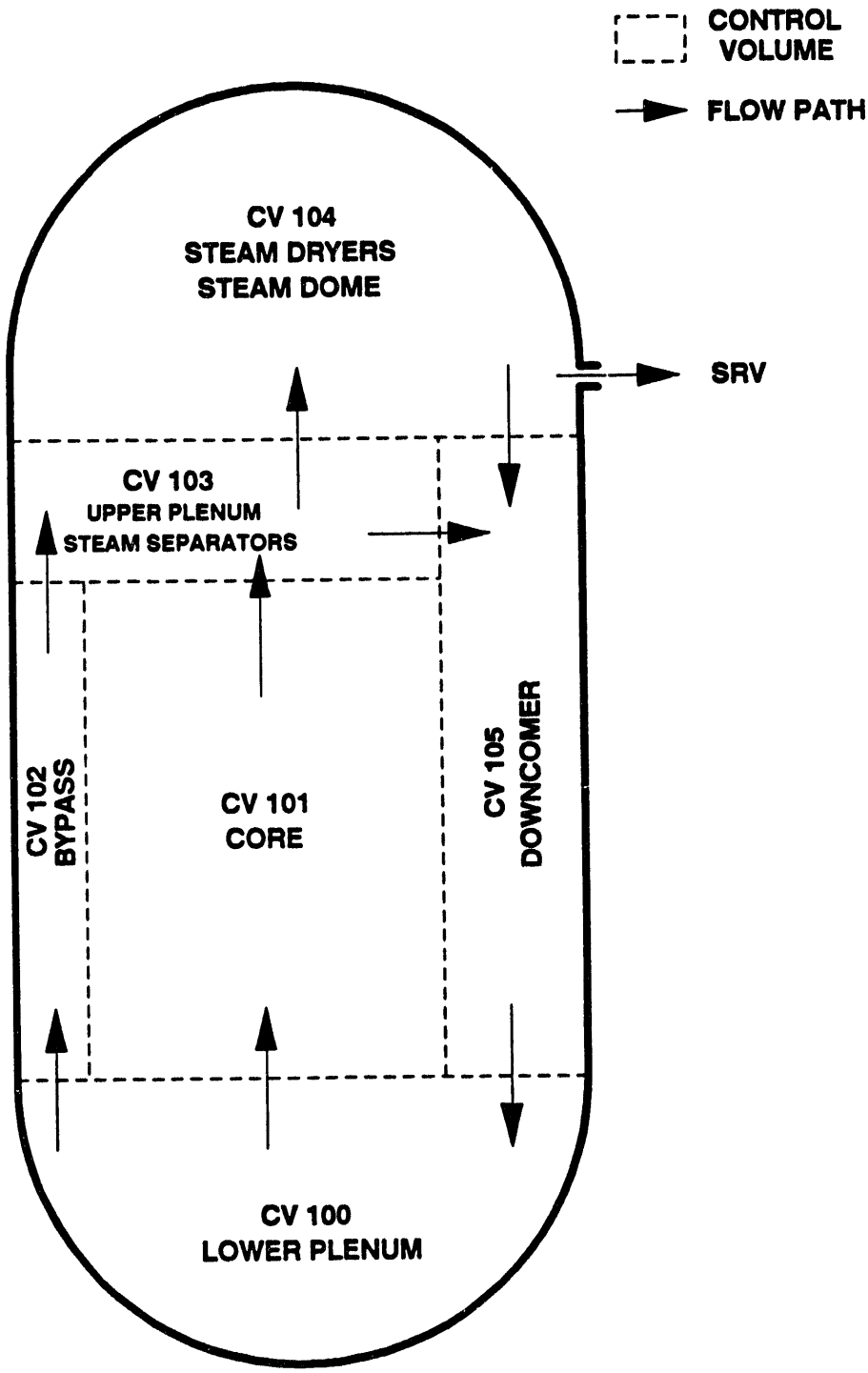

Figure 4.1. MELCOR Nodalization for ABWR Primary System

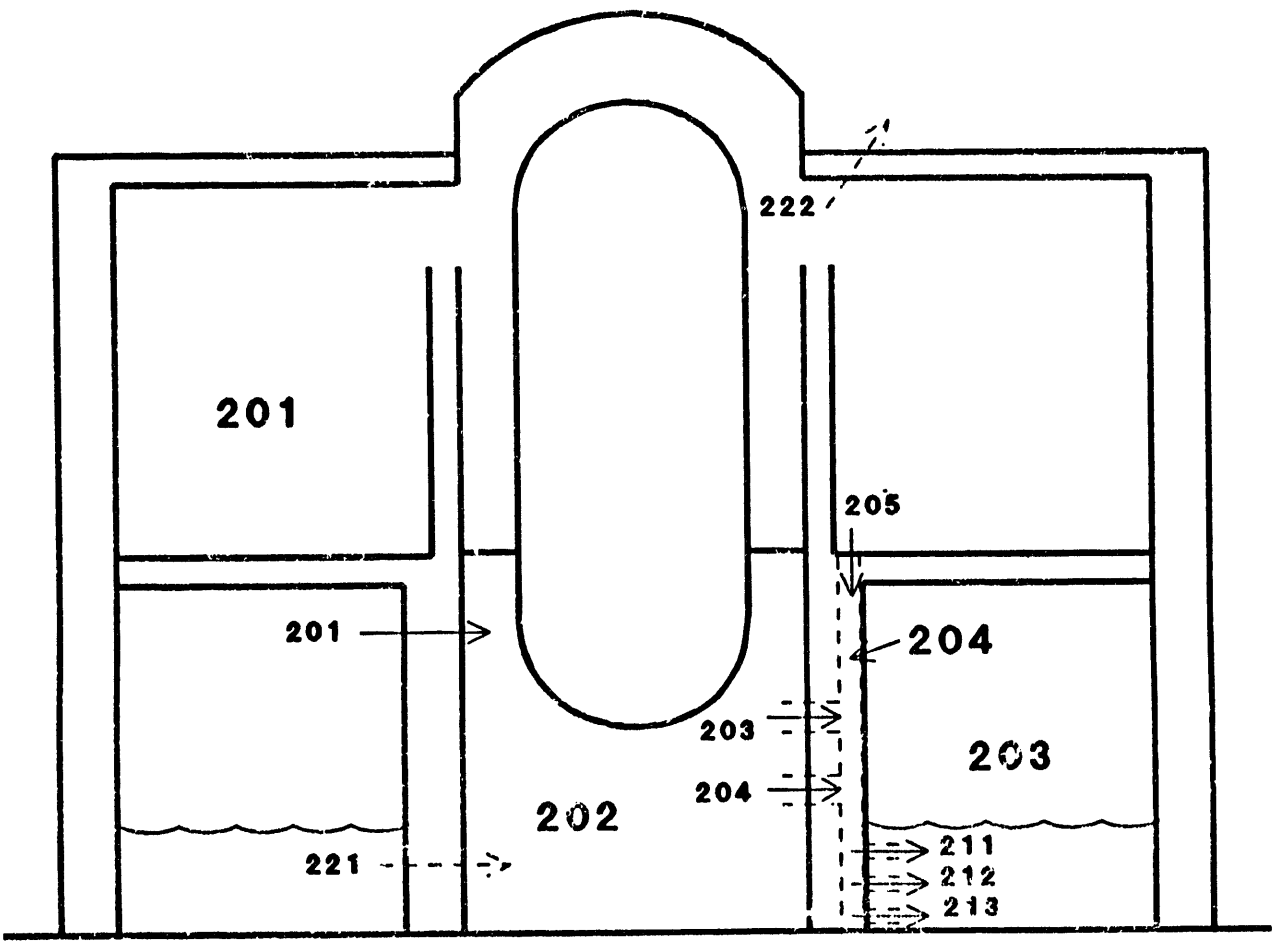

Figure 4.2. MELCOR Nodalization for ABWR Containment

Figure 4.2 highlights the MELCOR input model for the containment. Control volumes initially filled with nitrogen model the upper drywell, the lower drywell (the cavity), the wetwell and suppression pool, and the drywell connecting vent and suppression pool vents. Flow paths internal to the containment include between both the upper and the lower drywell and the connecting vents, the suppression pool return path (*i.e.*, overflow to the pedestal), and the top, middle and bottom suppression pool vents. Valved flow paths internal to the containment include the wetwell/drywell vacuum breakers, and the passive flooder which opens as soon as the lower drywell temperature exceeds 533K; the containment vents to a constant- temperature and -pressure environment, either through the COPS rupture disk in the wetwell at the specified failure pressure of 0.72MPa (90psig) or through leakage from penetration seal failure in the upper drywell (with a defined area vs pressure after reaching temperature).

The ABWR core nodalization, a separate model from the control volumes listed above, consists of 52 core cells divided into 4 radial rings and 13 axial levels. Axial levels 1 through 5 model the lower plenum, including the core support plate in level 5; levels 7 through 12 make up the active core region, while levels 6 and 13 represent non-fueled core regions. Figure 4.3 illustrates the reactor core nodalization used. The four rings contain equal amounts of the active fuel material, with equal areas in the inner three rings and a larger (open to flow) area in the outermost ring. The axial levels containing fuel (levels 7 through 12) are equal in height, with shorter non-fueled bordering levels; the height of axial level containing the core support plate is the thickness of that plate, and the lower plenum noding uses shorter axial levels adjacent to the core plate and adjacent to the lower head, with a larger level in the middle of the lower plenum.

Table 4.1 gives the masses of UO_2, Zircaloy, stainless steel and control rod poison (CRP) material present in the core and lower plenum, available for melt and relocation.

The initial core state is illustrated in Figure 4.4 for the innermost ring in the MELCOR ABWR core model; the materials and their distribution in all four rings are identical at the state of the analysis. For a given ring, in such core material component mass figures, the various materials in the MELCOR "fuel/clad" component are shown in the plot in the upper left, while the materials in the MELCOR "canister" component are shown in the plot in the upper right; materials in the MELCOR "other-structure" component are shown in the lower left, while the materials calculated to be in the "particulate debris" component (none at the start of the transient) are seen on the lower right. (Refer to [2] for an explanation of these MELCOR components, if necessary.) The "elevation" used as the ordinate in these core state figures is the same as the core level elevations shown in Figure 4.3, with the core support plate just above 5m, the lower plenum between 0 and 5m, and the active fuel region from >5m to >9m. The fraction of each core cell occupied by any given material is shown.

Radiation view factors were set to 0.64 for radiation from the canister wall to the fuel rod clad, to 0.94 for radiation from "other structure" (*e.g.*, control blades) to the adjacent canister wall, to 0.14 for radiation radially outward from a core cell boundary to the next adjacent cell, to 0.05 for radiation axially upward from a cell boundary to

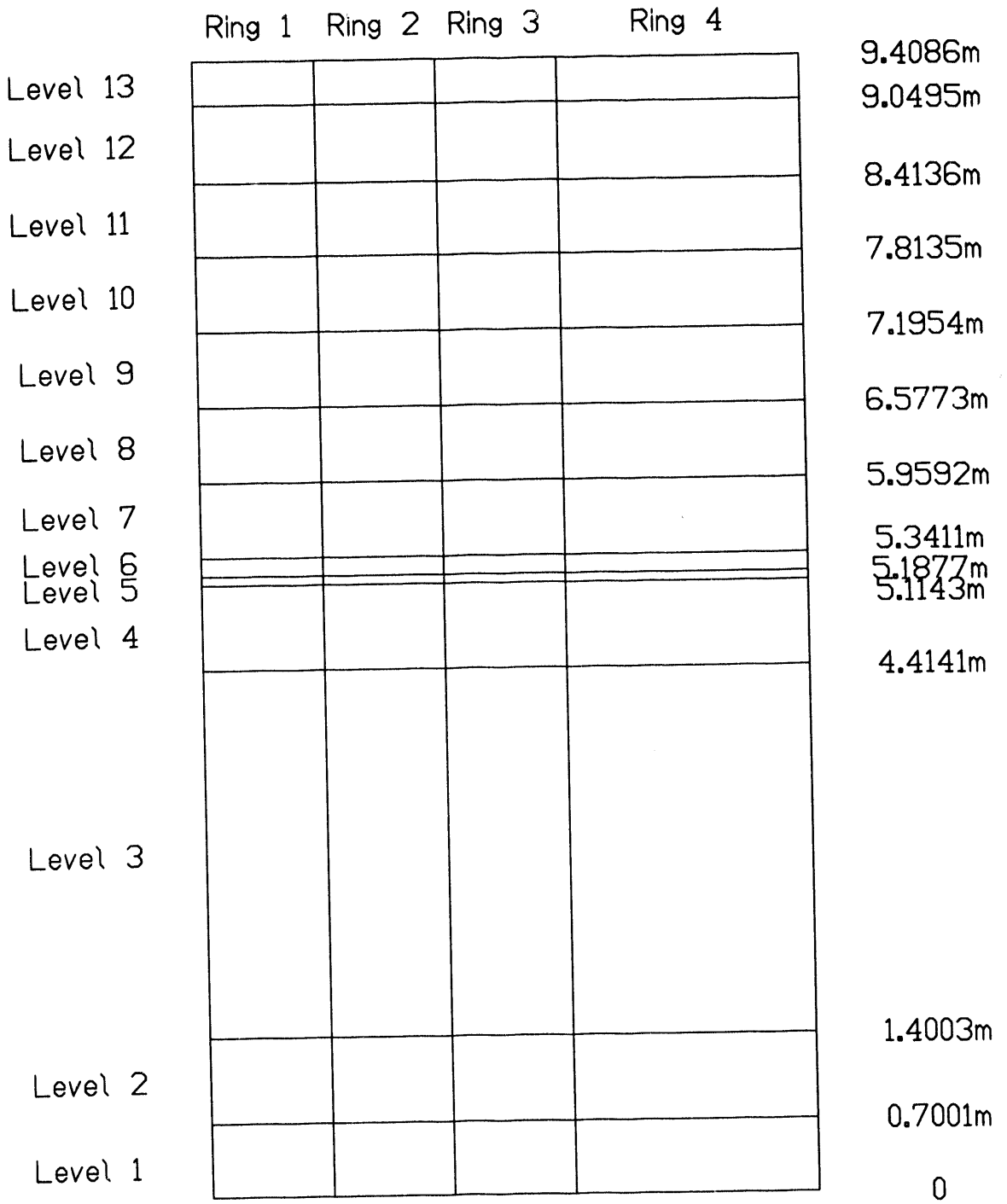

Figure 4.3. MELCOR COR Input Model for ABWR Core and Lower Plenum

Table 4.1. Core Initial Material Masses

Material	Mass (kg)
Active Fuel Region	
UO_2	171,600
Zircaloy (Clad)	42,979
Zircaloy (Canister)	31,800
Steel	33,034
CRP	947.5
Core Support Plate	
Steel	11,586
Lower Plenum	
Steel	47,746
Total	
UO_2	171,600
Zircaloy	74,779
Steel	92,366
CRP	947.5

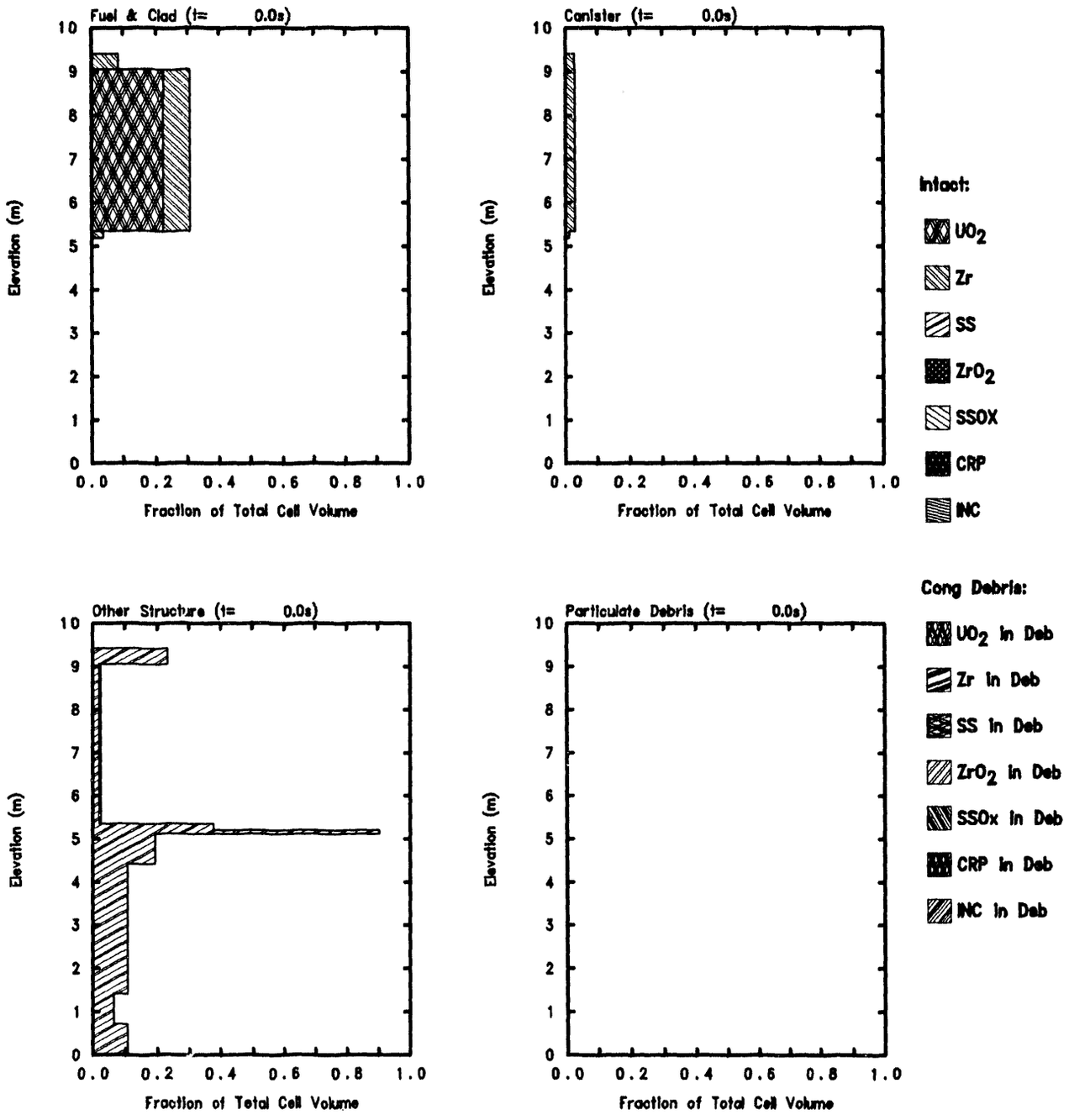

Figure 4.4. Initial Material Masses for ABWR Core and Lower Plenum - Fuel/Clad (upper left), Canister (upper right), Other Structure (lower left) and Particulate Debris (lower right) Component

the next adjacent cell, and to 0.96 for radiation between the liquid pool and the core components.

Candling heat transfer coefficients and secondary material transport, minimum intact oxide shell thicknesses, and core plate and lower head penetration failure temperatures were all kept at default values. The heat transfer coefficients from debris to the lower head and to penetrations in the lower head were reduced from a default value of 1000w/m^2-K to 500w/m^2-K. The new debris radial relocation model is enabled by default in MELCOR 1.8.2 and was therefore used in all these ABWR calculations; the new material eutectic interactions model in MELCOR 1.8.2 is not enabled by default and was not used for these ABWR calculations.

The cavity model used in these MELCOR calculations is presented in Figure 4.5. The cavity was specified to have an internal depth and radius of 3.0m and 5.3m, respectively; the concrete is 1.7m thick on the sides and 2m thick below the cavity. (Note that in the current ABWR plant design, the cavity consists of 1.5m of concrete above a liner with another 3m of concrete below; that was not known or changed before these calculations were done.) The surface of the concrete basemat is initially 11.55m below the bottom of the vessel (which is taken as 0 reference elevation.) The MELCOR default composition for basaltic concrete was used, with an added steel (*i.e.*, Fe) mass fraction of 0.095 representing the rebar in the concrete. Non-standard input was used to disable the treatment of chemical reactions involving concrete oxides, to avoid numerically-induced "layer flipping" problems (as discussed in more detail in Section 6.3).

In the low-pressure LCLP sequence analyses discussed in Sections 5.1 and 5.2, all of the debris lost from the core simply fell directly into the cavity. In the high-pressure LCHP analyses, in contrast, the potential exists for high-pressure melt ejection (HPME) to disperse core debris throughout containment, with direct containment heating (DCH) possible. The MAAP analyses assumed that "the initial discharge of corium and water from the lower plenum is entrained by the steam from the vessel into the upper drywell and wetwell because the vessel fails at high pressure" [1]. MELCOR calculations were done with and without high-pressure debris dispersal assumed, and the results showed that it was necessary to assume some hot core debris entrained into the upper drywell for the upper drywell to heat up sufficiently (to 533K) for penetration leakage to occur (as discussed in more detail in Section 5.3. However, the amount of debris entrained into the upper drywell must be limited so that in the high-pressure sequences with spray injection (discussed in the next two subsections) the sprays can cool the drywell sufficiently that that failure temperature is not reached. Also, the high-pressure melt ejection and associated direct containment heating must be benign enough not to pressurize containment to the rupture disk setpoint immediately upon vessel failure and HPME/DCH interactions.

The debris distribution and interaction times used in these MELCOR ABWR analyses are not necessarily "correct"; they simply satisfy these constraints. The reference case input used for the high-pressure sequence analyses specified 70% of the HPME debris to end up in various containment control volume atmospheres, where it could then result in direct containment heating (35% in the cavity volume, 25% in the upper drywell volume, and 10% in the wetwell volume). The remaining 30% of HPME debris was specified to

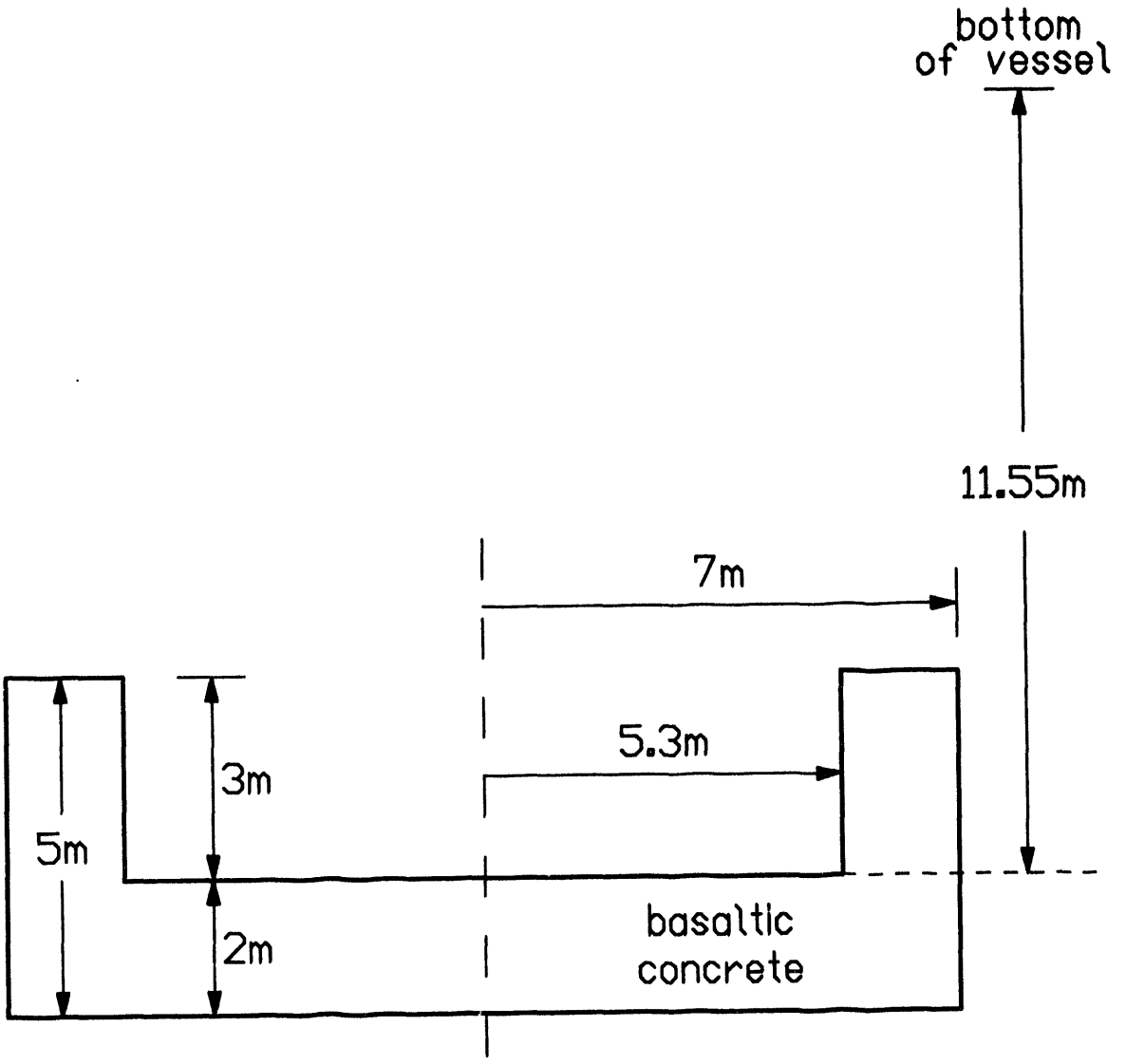

Figure 4.5. MELCOR CAV Input Model for ABWR Lower Drywell Cavity

settle directly into the cavity (with no direct containment heating along the way), and none was specified to adhere directly onto various heat structures in the containment. The characteristic interaction times for airborne-debris oxidation and heat transfer were set to 5s in the lower drywell, 50s in the upper drywell and 25s in the wetwell control volumes, while the characteristic settling time for airborne debris was set to 25s in all three volumes; the characteristic interaction time for oxidation of deposited debris was set to 1800s for all heat structures; these time constants represent a relatively slow and extended DCH transient in the containment atmosphere, and very slow residual oxidation of debris on structures.

The default classes in the MELCOR RN and DCH packages were used, with the addition of CsI as Class 16. Table 4.2 contains a list of the MELCOR fission product material classes, including the total radioactive mass inventory of each class initially present; a small fraction of these were specified to be in the gap rather than in the fuel. (The numbers in parentheses for Classes 2, 4 and 16 are the masses of those radionuclide classes initially present if all available I in the fuel is assumed to bind with Cs to form CsI; in this case, there is no free mass of I2 formed, and the available mass of Cs to form CsOH is slightly reduced.)

All these MELCOR calculations were done using the CORSOR-M fission product release release model [7], without a modifying surface-volume ratio (S/V) term. Most of our ABWR analyses also were done specifying one MAEROS component (the default), with the default number of and diameter bounds for aerosol distribution size bins.

A large number of control functions (435) were used to track the source term release and subsequent distribution, to determine timing and flow of various spray systems, and to adjust valves and breaks as required. In particular, control functions were used to track the total and radioactive masses of each class 1) released from the intact fuel and/or debris in the vessel (either in the core, the bypass or in the lower plenum), 2) released from the debris in the cavity, 3) remaining in the primary system (*i.e.*, the reactor vessel), 4) in the containment, and 5) released to the environment. Those control functions provided time- dependent source term release and distribution data for subsequent postprocessing in a form more convenient for analysis and evaluation.

Spray package input is used for several of the sequences analyzed. The firewater spray used in the LCLP-FS-R-N and LCHP-FS-R-N sequences is represented as a $0.08333 m^3/s$ ($83.33 l/s$ or 1321gpm) flow of 300K (80°F) water into the upper drywell, turned on and off as required by a set of control functions modelling the firewater spray actuation logic summarized in Section 2.9. (The actual rate for the current ABWR design should be $0.04\text{-}0.06 m^3/s$.) The drywell spray used in the LCHP-PS-R-N sequence is modelled as a $0.22854 m^3/s$ ($228.54 l/s$ or 3623gpm) flow of water into the upper drywell, recirculated from the wetwell suppression pool at the suppression pool temperature, starting at 4hr.

The user-input maximum time step in all these MELCOR ABWR calculations was 3s from 0 to 2000s, increased to 5s in the 2000s to 36,000s (10hr) interval, increased again to 10s from 36,000s to 108,000s (50hr), and then set to 25s after 108,000s.

Table 4.2. Radionuclide Classes and Initial Inventories

Class	Class Name	Representative Element	Member Elements	Initial Radionuclide Mass (kg)
1	Noble Gases	Xe	He, Ne, Ar, Kr, Xe, Rn,H, N	508.179
2	Alkali Metals	Cs	Li, Na, K, Rb, Cs, Fr, Cu	294.085 (270.062)
3	Alkaline Earths	Ba	Be, Mg, Ca, Sr, Ba, Ra, Es, Fm	227.426
4	Halogens	I	F, Cl, Br, I, At	22.9386 (0)
5	Chalcogens	Te	O, S, Se, Te, Po	44.7008
6	Platinoids	Ru	Ru, Rh, Pd, Re, Os, Ir, Pt, Au, Ni	336.433
7	Early Transition Elements	Mo	V, Cr, Fe, Co, Mn, Nb, Mo, Tc, Ta, W	384.271
8	Tetravalents	Ce	Ti, Zr, Hf, Ce, Th, Pa, Np, Pu, C	650.908
9	Trivalents	La	Al, Sc, Y, La, Ac, Pr, Nd, Pm, Sm, Eu, Gd, Tb, Dy, Ho, Er, Tm, Yb, Lu, Am, Cm, Bk, Cf	625.813
10	Uranium	U	U	145,082
11	More Volatile Main Group	Cd	Cd, Hg, Zn, As, Sb, Pb, Tl, Bi	1.54139
12	Less Volatile Main Group	Sn	Ga, Ge, In, Sn, Ag	9.41071
13	Boron	B	B, Si, P	0
14	Water	H_2O	H_2O	
15	Concrete			
16	CsI	CsI	CsI	0 (46.96186)

Note that this task did not include developing a MELCOR deck for the current ABWR plant design but instead relied on using an ABWR MELCOR input deck developed by Brookhaven National Laboratories and reviewed by Sandia some years ago [3], under FIN A-1392. That plant deck has not been reviewed against the current ABWR plant design. A few design changes have been identified during the course of this work. The concrete type in the BNL ABWR MELCOR deck was limestone; that has been changed to basaltic. As noted above, the cavity in the BNL ABWR MELCOR model was specified to have 2m of concrete while, in the current ABWR plant design, the cavity consists of 1.5m of concrete above a liner with another 3m of concrete below; that was not known or changed before these calculations were done. Also, the firewater spray injection rate in the BNL ABWR MELCOR deck was somewhat higher than for the current ABWR design; that was not known or changed before these calculations were done. It is possible that other elements of the BNL ABWR MELCOR model also may not reflect the current ABWR plant design exactly.

5 MELCOR Results and Comparisons with MAAP

5.1 LCLP-PF-R-N Sequence

The initiating event for this sequence is a Main Steam Isolation Valve (MSIV) closure, followed by reactor scram. The feedwater is conservatively assumed to trip, with a coastdown of 5s. Four of the reactor internal pumps trip on high vessel pressure. The safety relief valves (SRVs) cycle open and closed to relieve the steam pressure. As the water level falls, the remainder of the reactor internal pumps trip on low level. The ECC injection systems are assumed to fail.

The sequence of events, which includes passive flooder and containment rupture disk opening, predicted by MELCOR for this accident is given in Table 5.1.1, with the timings of the various events as calculated by MAAP (taken from Table 19E.2-5 in [1]) included for comparison.

The swollen and collapsed liquid levels predicted by MELCOR in the vessel control volumes are given in Figure 5.1.1. Within 40min after accident initiation, decay heat has been sufficient to lower the water level in the channel control volume to two-thirds core height, as shown in Figure 5.1.1, and one SRV opens to provide steam cooling; this is calculated to occur slightly later in the MELCOR analysis than in the MAAP analysis (0.4hr$\simeq$24min). The vessel blows down rapidly, as illustrated by the primary system pressure history presented in Figure 5.1.2, while the fuel heats up and begins to melt.

The primary system pressures calculated by MELCOR and by MAAP for this sequence are compared in Figure 5.1.2. (The MAAP result is taken from Figure 19E.2-2A in [1].) The results are qualitatively identical, with the exception of some timing shifts. The early-time pressure drop in the MELCOR analysis is slightly later than in the MAAP calculation, reflecting the difference in core uncovery and consequent SRV opening, but the vessel is predicted to depressurize at the same rapid rate to near the containment pressure in both calculations. The subsequent primary system pressure is controlled by the containment response, discussed in more detail later in this section.

The core plate and lower head are not predicted to fail immediately after core uncovery is completed; core uncovery is complete at about 1hr, while core plate failure and lower head penetration failure are first calculated to occur at 3.3hr. Between those times, the core is maintained in a degraded configuration by steam cooling from boiling off water in the lower plenum.

Figure 5.1.3 shows core clad temperatures in the various axial levels in the active fuel region for each of the four radial rings used in the MELCOR core model (shown schematically in Figure 4.3). Figure 5.1.4 gives core particulate debris temperatures in the same axial levels, in the active fuel region, for each of the four radial rings used in the MELCOR core model. Core particulate debris temperatures in the five axial levels in the lower plenum (with the core support plate in level 5) are presented in Figure 5.1.5, for each of the four radial rings in the MELCOR core nodalization.

Table 5.1.1. Sequence of Events Predicted by MELCOR for LCLP-PF-R-N Sequence, Compared to MAAP

Event	Time	
	MAAP	MELCOR
Accident initiation (MSIV Closure)	0.0	0.0
Reactor scrammed	4.2s	
Core uncovery begins		1,626.1s (0.45hr)
Water level at 2/3 core height; 1 SRV open	0.4hr	2,350.7s (0.65hr)
Clad failure/Gap release		
(Ring 1)		2,980.7s (0.83hr)
(Ring 2)		3,825.1s (1.06hr)
(Ring 3)		4,548.9s (1.26hr)
(Ring 4)		6,731.0s (1.87hr)
Core plate failed		
(Ring 1)		11,818.0s (3.28hr)
(Ring 2)		14,838.4s (4.12hr)
(Ring 3)		15,303.8s (4.25hr)
(Ring 4)		21,586.3s (6.00hr)
Vessel bottom head failed	1.8hr	
Vessel LH penetration failed		
(Ring 1)		11,933.5s (3.31hr)
(Ring 2)		11,938.0s (3.32hr)
(Ring 3)		11,939.5s (3.32hr)
(Ring 4)		11,948.2s (3.32hr)
Commence debris ejection		11,933.5s (3.31hr)
Water in lower drywell boiled off	2.7hr	~22,470s (6.2hr)
Passive flooder opens	5.4hr	22,473.7s (6.24hr)
Rupture disk opens	20.2hr	52,931.5s (14.70hr)
Concrete ablation $\geq$2m		150,967s (41.94hr)
End of calculation	100hr	150,967s (41.94hr)

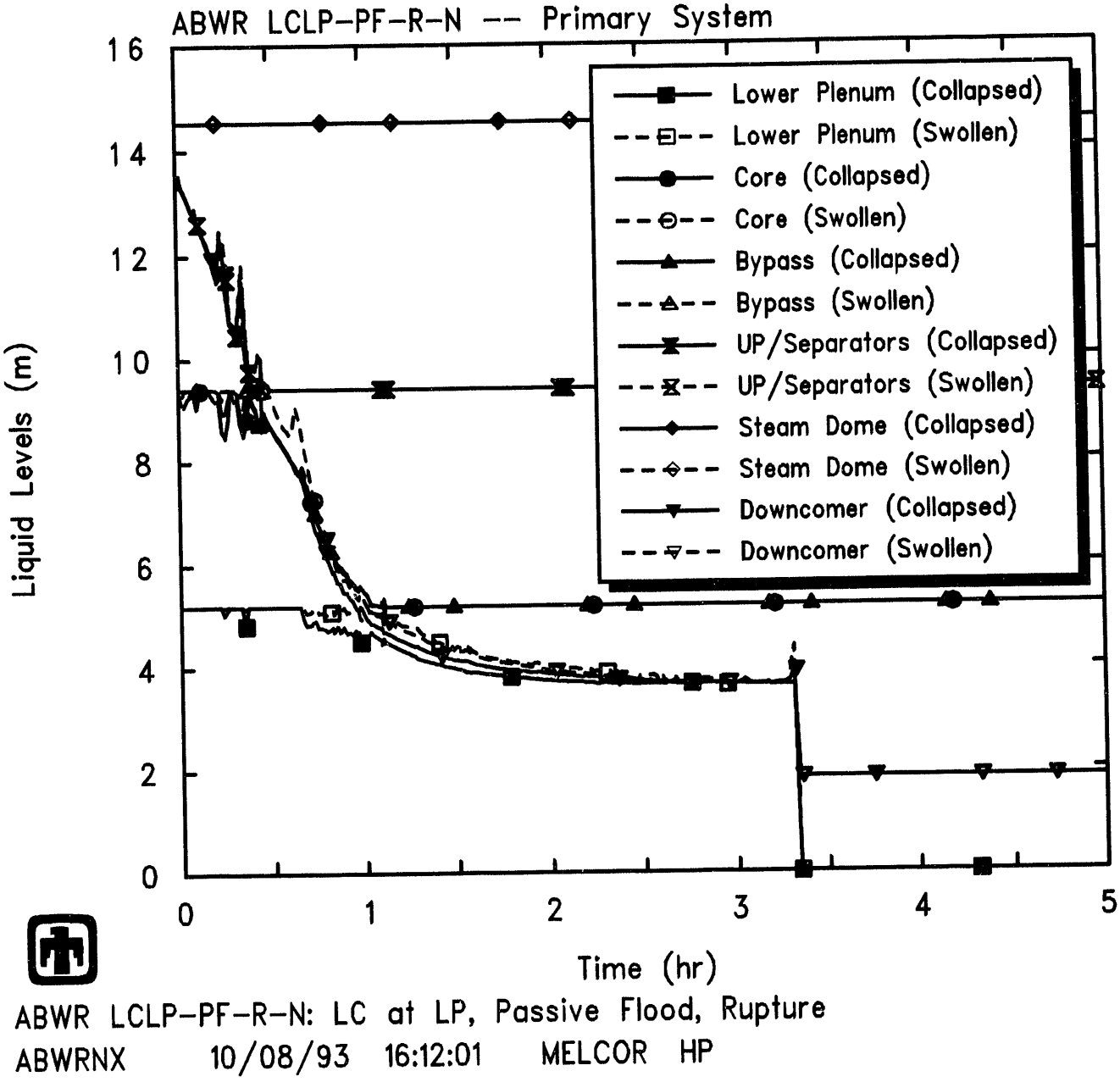

Figure 5.1.1. Vessel Swollen and Collapsed Liquid Levels Predicted by MELCOR for LCLP-PF-R-N Sequence

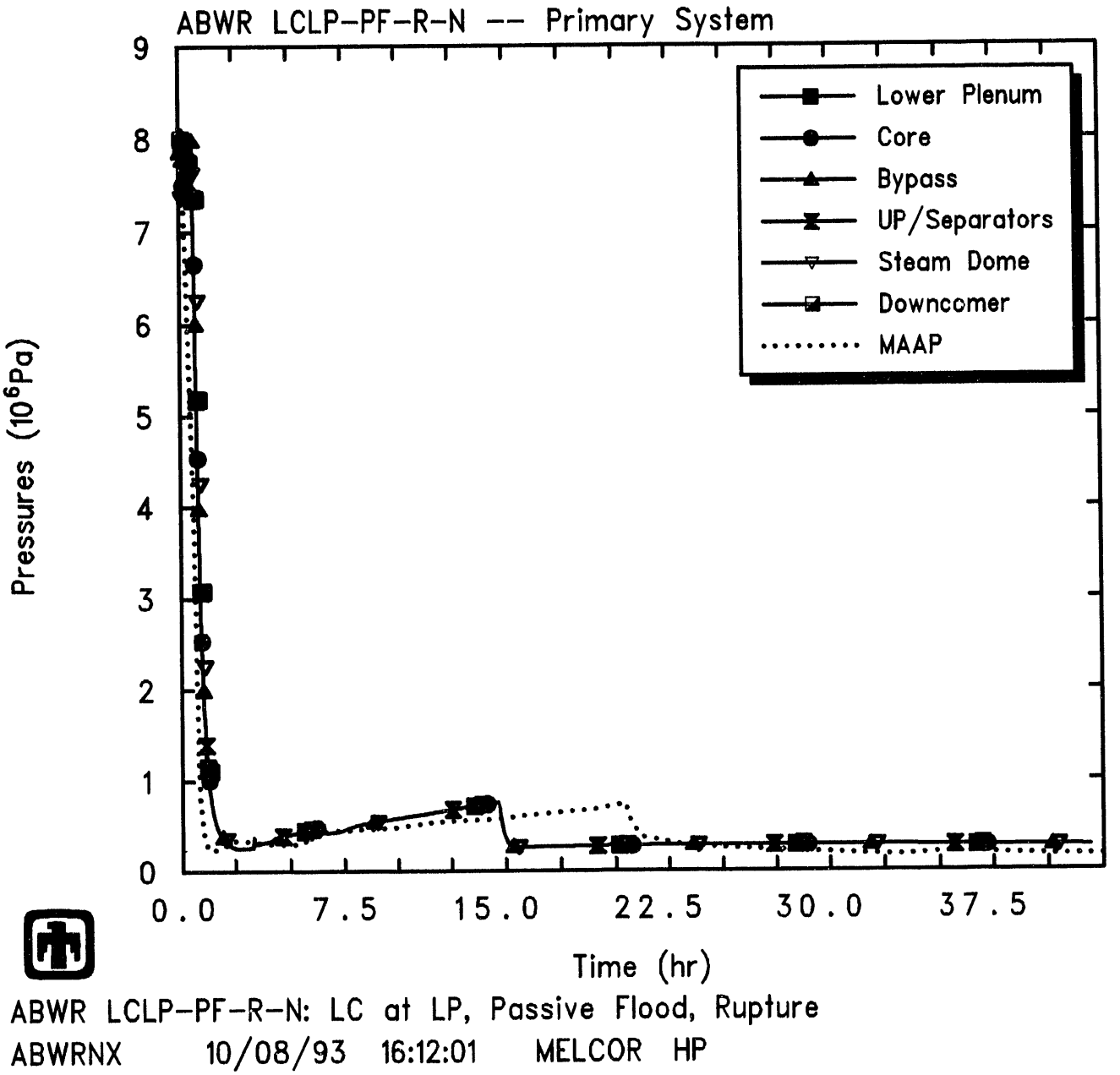

Figure 5.1.2. Primary System Pressures Predicted by MELCOR for LCLP-PF-R-N Sequence, Compared to MAAP

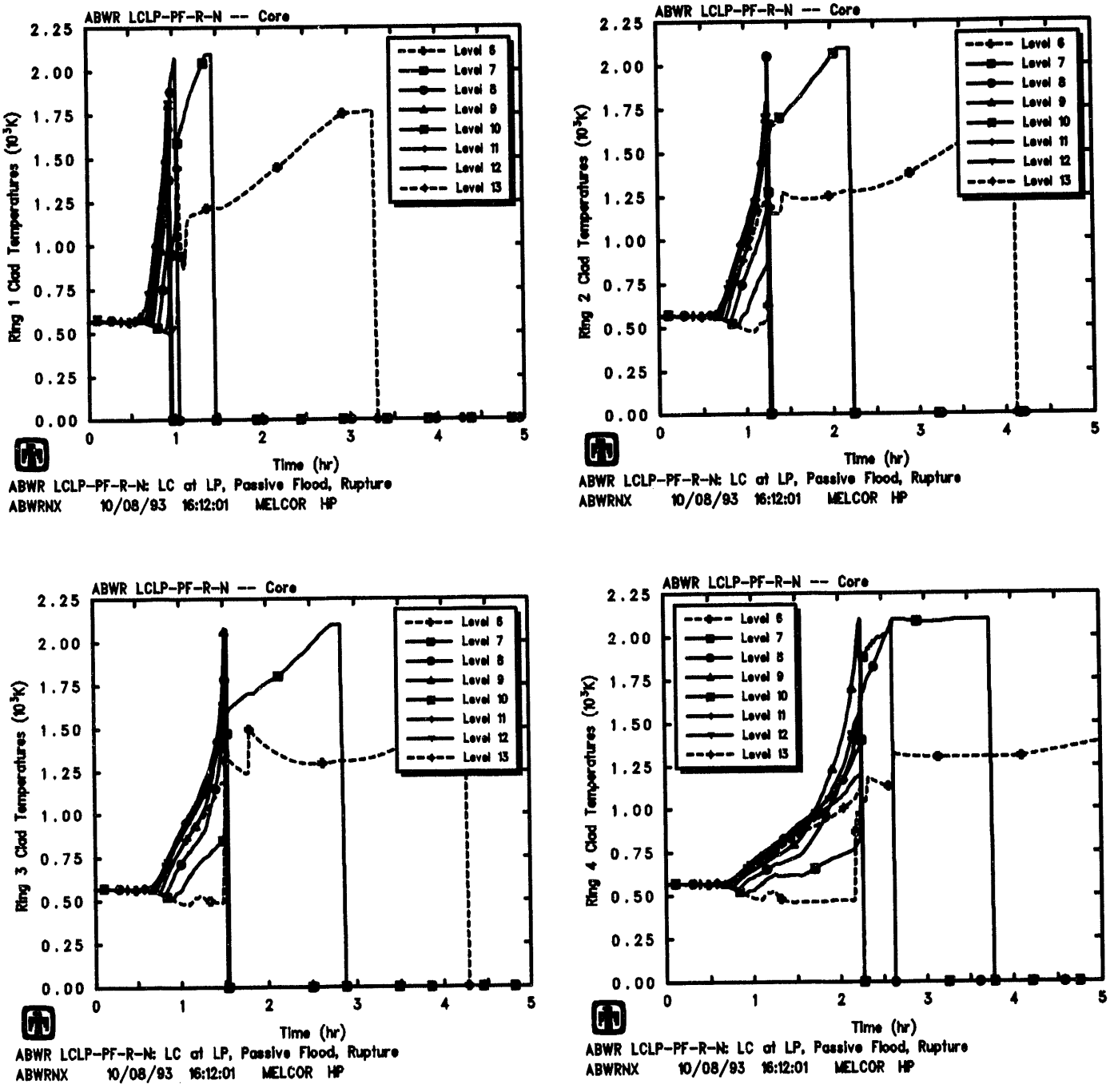

Figure 5.1.3. Core Ring 1 (upper left), Ring 2 (upper right), Ring 3 (lower left) and Ring 4 (lower right) Clad Temperatures Predicted by MELCOR for LCLP-PF-R-N Sequence

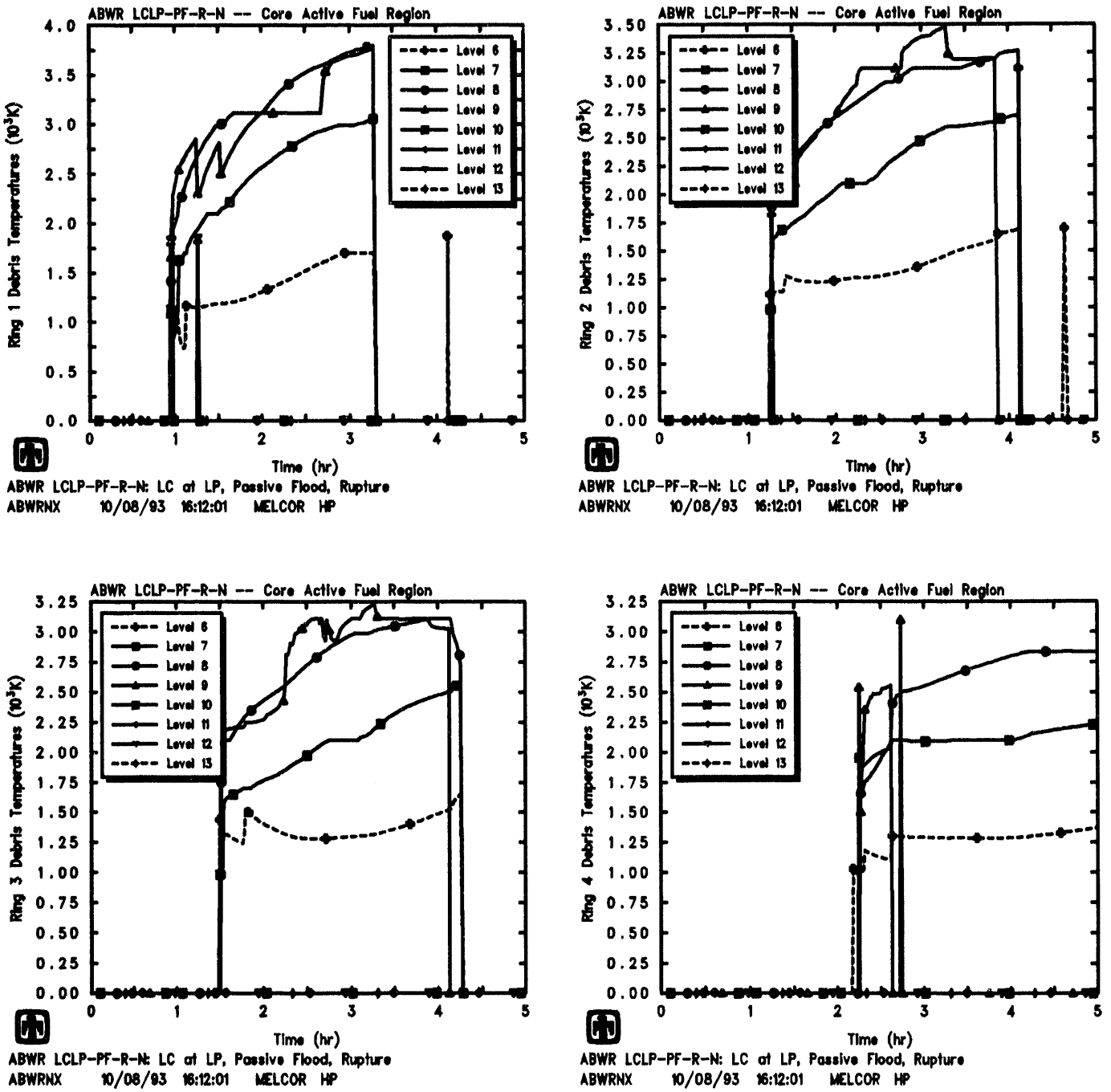

Figure 5.1.4. Core Ring 1 (upper left), Ring 2 (upper right), Ring 3 (lower left) and Ring 4 (lower right) Debris Temperatures in the Active Fuel Region Predicted by MELCOR for LCLP-PF-R-N Sequence

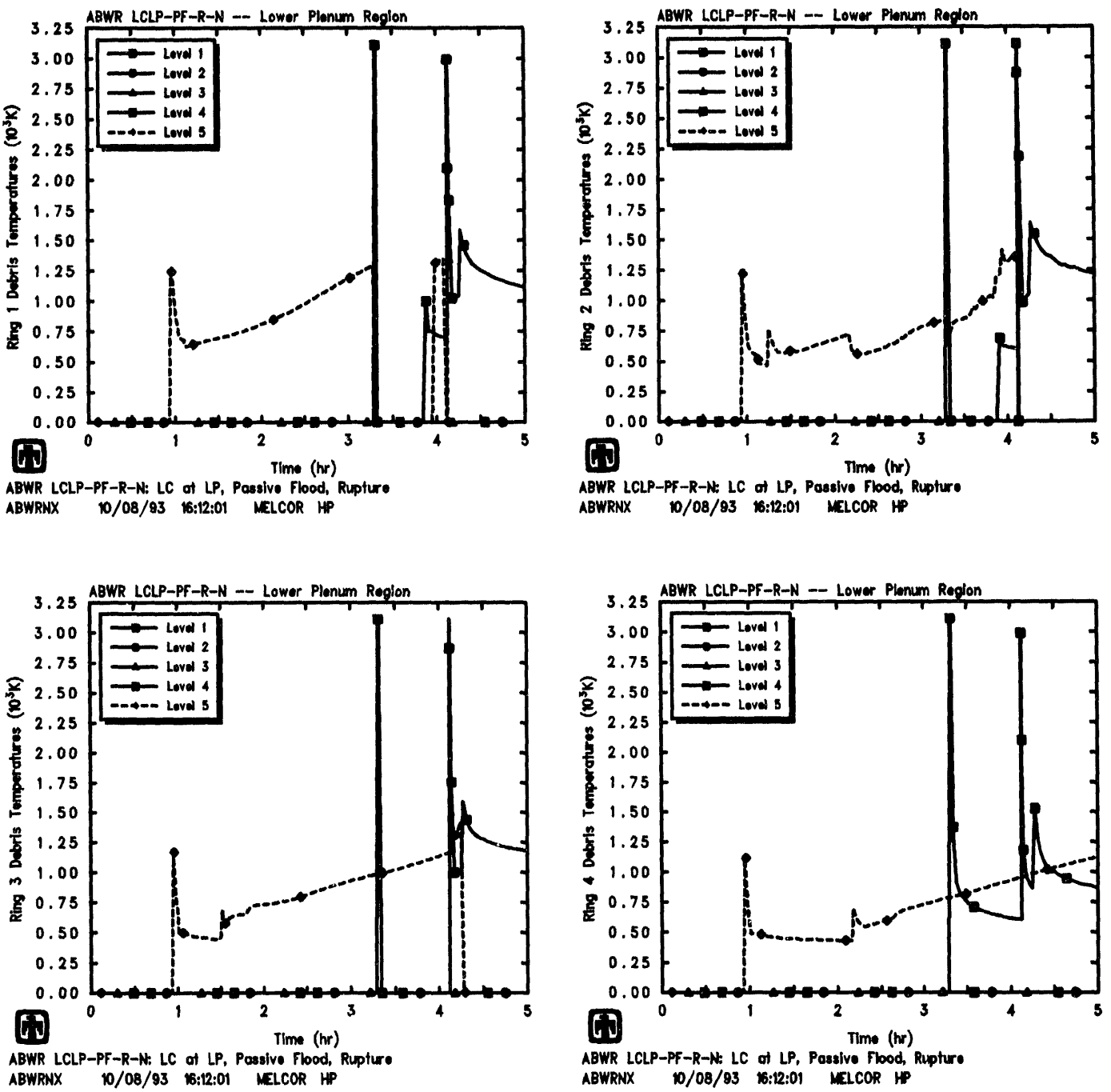

Figure 5.1.5. Core Ring 1 (upper left), Ring 2 (upper right), Ring 3 (lower left) and Ring 4 (lower right) Debris Temperatures in the Lower Plenum Predicted by MELCOR for LCLP-PF-R-N Sequence

The majority of material in the active fuel region (*i.e.*, above the core support plate) heats up without interruption through melt and relocation to debris formation. Most of the fuel and clad in the innermost, highest-powered ring have collapsed into a debris bed by 1hr, and all the fuel and clad in the innermost, highest-powered ring have collapsed into a debris bed by 1.5hr. Most of the fuel and clad in the middle two rings have collapsed into a debris bed by 1.25-1.5hr, and all the fuel and clad in those middle two rings have collapsed into a debris bed by 2.25-2.75hr. Most of the fuel and clad in the outermost, lowest-powered ring have collapsed into a debris bed by 2.25hr, and all the fuel and clad in that outermost, lowest-powered ring have collapsed into a debris bed by 3.75hr. The debris beds formed remain held in the active fuel region for several hours by the core support plate and by support structures in the lowermost, non-fueled level in the active fuel region (*i.e.*, level 6), as illustrated in the debris temperatures in Figure 5.1.4.

The temperatures calculated for the core support plate (*i.e.*, the "other structure" in level 5) are given in Figure 5.1.6. The core support plate begins to heat up as soon as the bottom of the core is uncovered, at 1hr, and then heats up at a generally steady, slow rate due to conduction and/or radiation heat transfer from the hot debris in the active fuel region levels above the core plate. The core support plate first fails at 3.3hr, in the innermost ring where the debris was hottest. When the core support plate fails, some debris falls through the core support plate into the lowest lower plenum level, just above the lower head, as indicated by the debris temperatures given in Figure 5.1.5.

The core support plate in the innermost ring failed by reaching the failure criterion of 1273K at 11,818s (3.28hr), allowing any particulate debris and remaining intact material in the active fuel region and core plate level to fall through into the lower plenum. The lower head surface and penetration temperatures are presented in Figure 5.1.7. The temperature of the lower head penetrations in all four rings quickly rose well above the weld failure temperature of 1273K. The penetrations failed and vessel breach occurred at 11,933.5s (3.31hr) in this MELCOR calculation; this compares to an earlier vessel failure time of about 2hr after transient start in the MAAP analysis. The core support plate in the other three rings failed 1 to 3hr later. This relatively long time delay is largely a result of the new debris radial relocation model allowing debris formed in the outer rings to move laterally to the first, failed ring and fall through the failed core plate and lower head penetration in the first ring, rather than remain stacked in each ring until the core plate fails in that ring.

The calculated core state at vessel failure (*i.e.*, at 11,933.5s or 3.31hr) is illustrated in Figures 5.1.8 through 5.1.11, for the four rings in the MELCOR ABWR core model. For each ring, in each of these figures, the various materials in the MELCOR "fuel/clad" component just prior to vessel failure, both any intact materials remaining in their original position and candled, refrozen conglomerate debris materials, are shown in the plot in the upper left, while the materials in the MELCOR "canister" component, both any intact materials remaining in their original position and candled, refrozen conglomerate debris materials, are shown in the plot in the upper right; materials in the MELCOR "other-structure" component just prior to vessel failure are shown in the lower left, while the materials calculated to be in the "particulate debris" component at the same time are

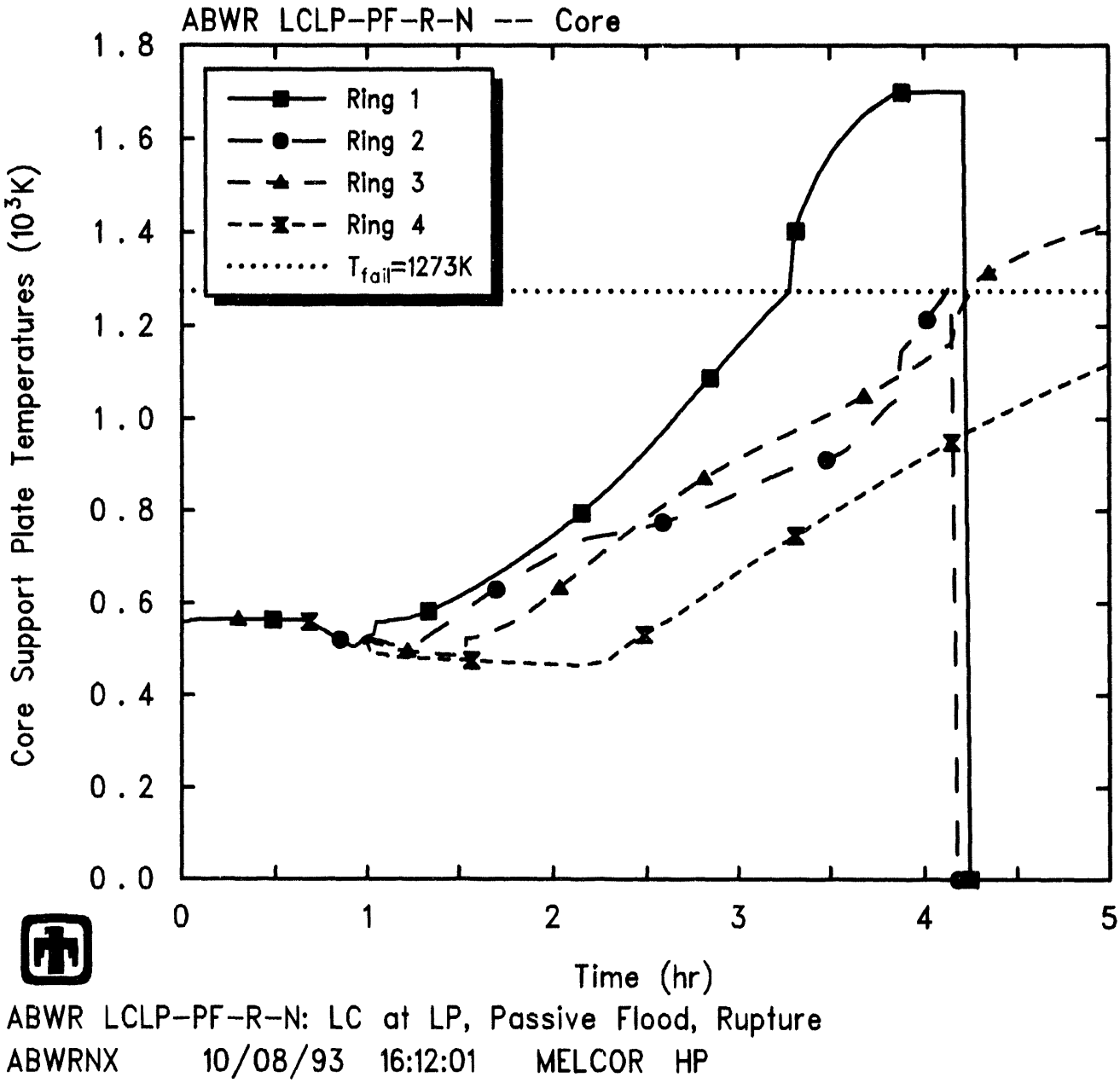

Figure 5.1.6. Core Support Plate Temperatures Predicted by MELCOR for LCLP-PF-R-N Sequence

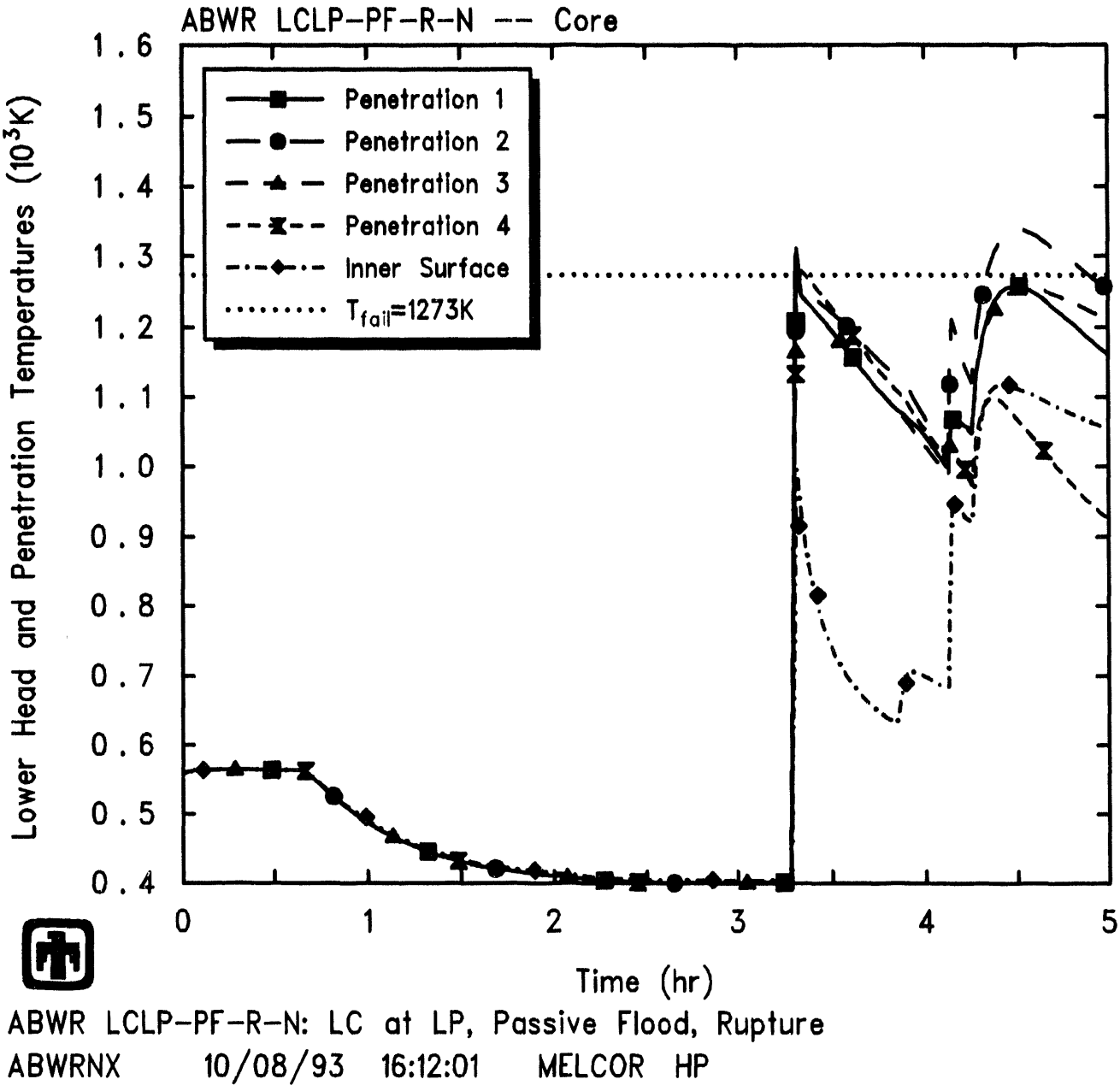

Figure 5.1.7. Lower Head Inner Surface and Penetration Temperatures Predicted by MELCOR for LCLP-PF-R-N Sequence

seen on the lower right. (Refer to [2] for an explanation of these MELCOR components, if necessary.) These core material configurations at the time of vessel failure should be compared to the initial core material configuration given in Figure 4.4, to aid in visualize the amount of material degradation and relocation. The "elevation" used as the ordinate in these core state figures is the same as the core level elevations shown in Figure 4.3, with the core support plate just above 5m, the lower plenum between 0 and 5m, and the active fuel region from >5m to >9m. The fraction of each core cell occupied by any given material is shown.

As visible in Figure 5.1.8, the innermost ring has no intact structure in the active fuel region at all at the time of vessel failure, but there is a substantial debris bed visible in the lowest axial level in the lower plenum. In the second and third rings (Figures 5.1.9 and 5.1.10), a very small intact clad mass is visible, corresponding to the non-fueled core support material in level 6; also in the second and third rings, a small intact canister mass is visible in several levels just above the core support plate. Most of the material in these middle two rings is in the particulate debris bed, held up by the core support plate and the non-fueled core material in level 6. Note that there is a significant debris bed also present in the lower plenum; that debris comes from the failure of the innermost ring, through the debris radial relocation model. The material configuration in the outermost ring at the time of vessel failure, depicted in Figure 5.1.11, is qualitatively similar to the configuration in the middle two rings, but with slightly more intact material and relatively less particulate debris in the active fuel region.

Tables 5.1.2 and5.1.3 summarize the state of the various materials in the core active fuel region, core plate and lower plenum at the time a lower head penetration first fails (*i.e.*, at vessel breach). Masses of intact components and of debris components are given for each region in Table 5.1.2. The fraction of debris molten in each region (included in Table 5.1.3) is estimated from the average debris temperature, which in this case resulted in assuming that Zircaloy, steel, steel oxide and control rod poison in the debris are molten and that UO_2 and ZrO_2 in the debris are solid (*i.e.*, neglecting eutectic mixtures, which are not included in this analysis).

Figure 5.1.12 shows the total masses of core materials (UO_2, Zircaloy and ZrO_2, stainless steel and steel oxide, and control rod poison) remaining in the vessel. As noted in Table 5.1.1, debris ejection began immediately after lower head failure. This figure illustrates that the core material was lost from the vessel to the cavity in step-like stages. Almost all of the UO_2 was transferred to the cavity within about 10.5hr after the start of the transient, as was the unoxidized zircaloy, the associated zirc oxide and the control rod poison. A significant fraction (45%) of the structural steel in the lower plenum, and some associated steel oxide, was predicted to remain unmelted and in place throughout the entire transient period calculated.

Zircaloy oxidation began at about 1hr, as indicated by the production of hydrogen in the core illustrated in Figure 5.1.13. No other gases were calculated to be generated in the core. Figure 5.1.13 includes the hydrogen generation predicted by MAAP (taken from Figure 19E.2-2F in [1]). There is little in-vessel generation of hydrogen gas in the MAAP analysis due to metal water reaction, because the vessel blowdown limits the

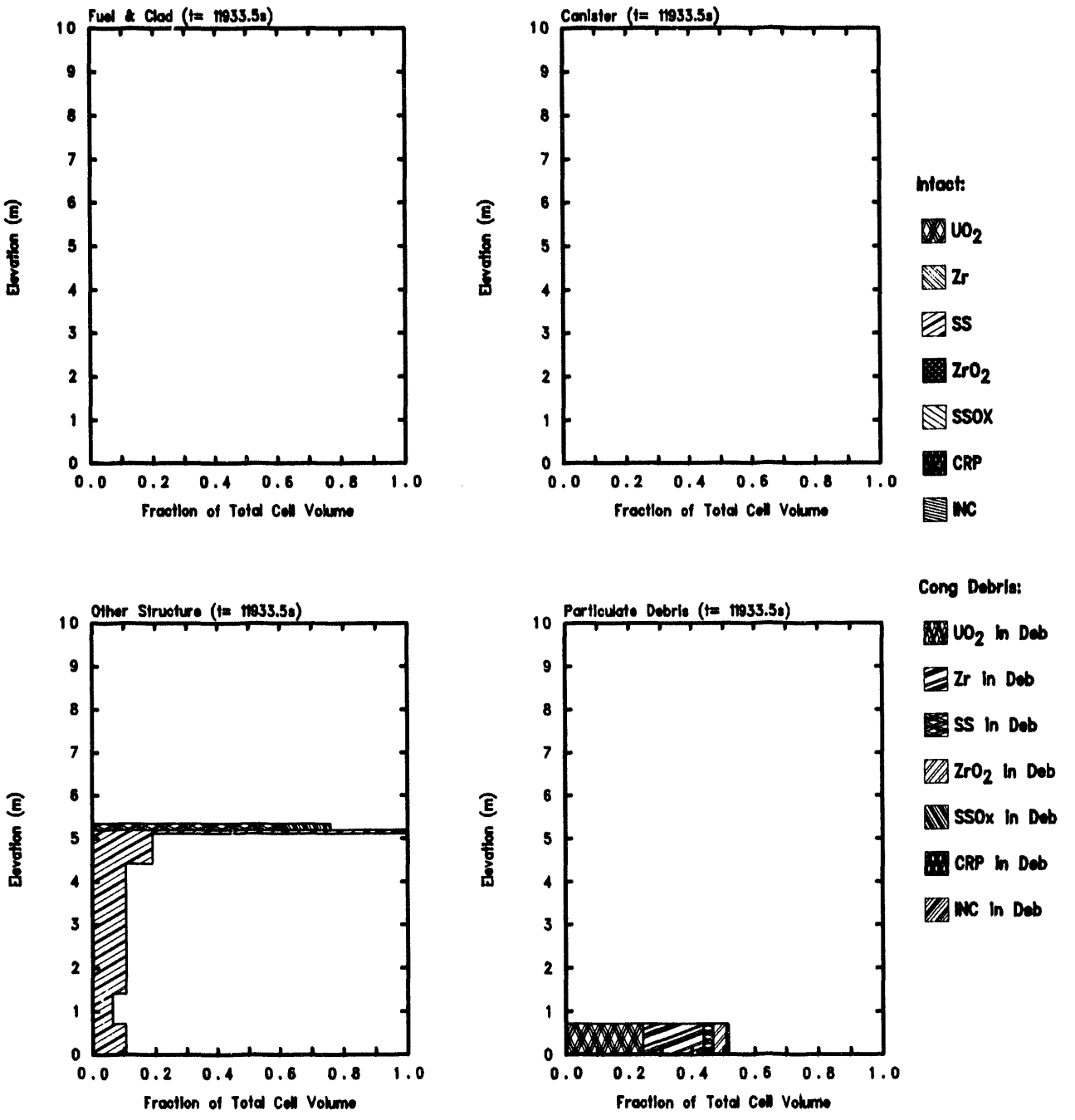

Figure 5.1.8. Core Ring 1 Fuel/Clad (upper left), Canister (upper right), Other Structure (lower left) and Particulate Debris (lower right) Component Material Masses Predicted by MELCOR for LCLP-PF-R-N Sequence

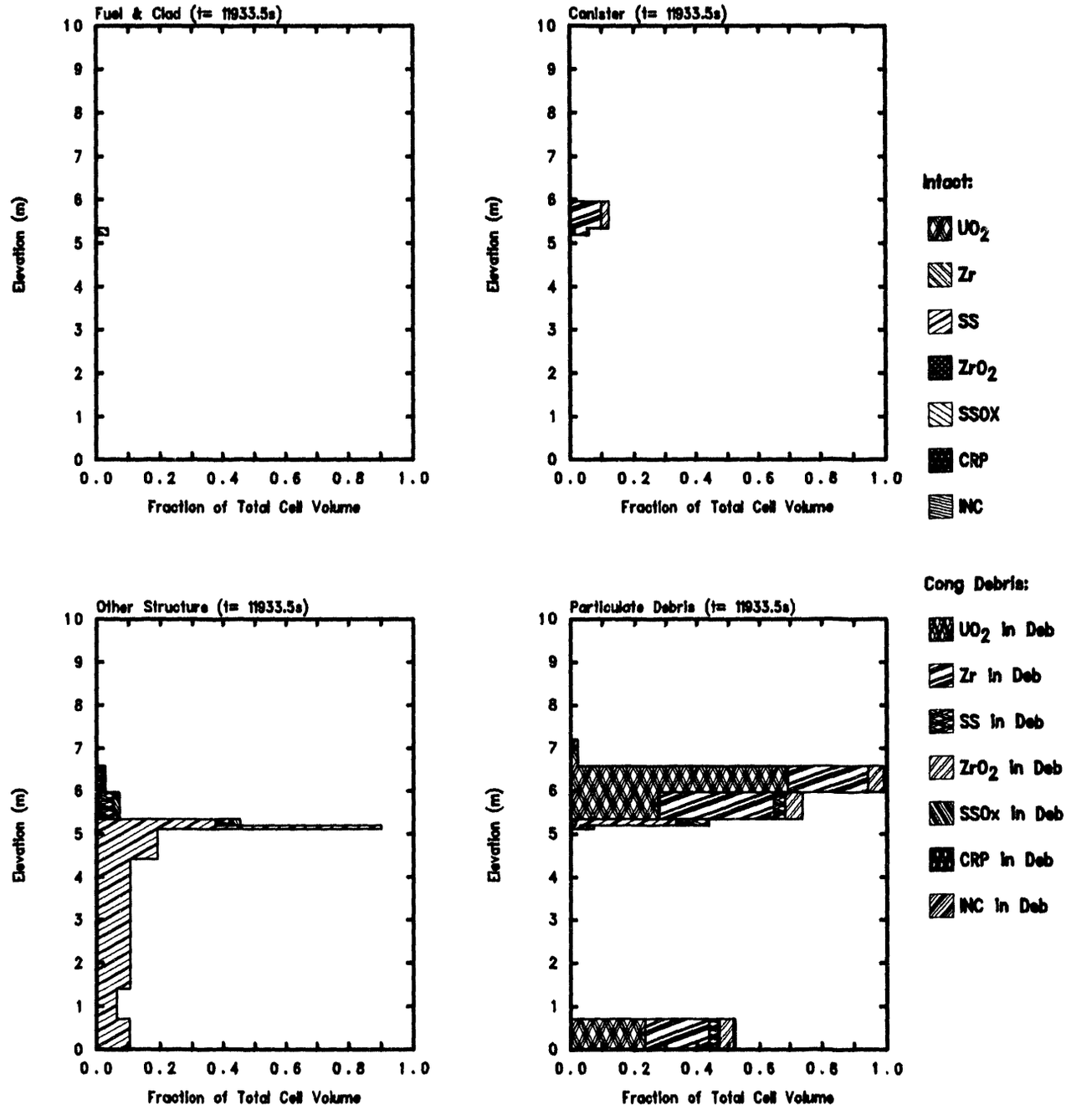

Figure 5.1.9. Core Ring 2 Fuel/Clad (upper left), Canister (upper right), Other Structure (lower left) and Particulate Debris (lower right) Component Material Masses Predicted by MELCOR for LCLP-PF-R-N Sequence

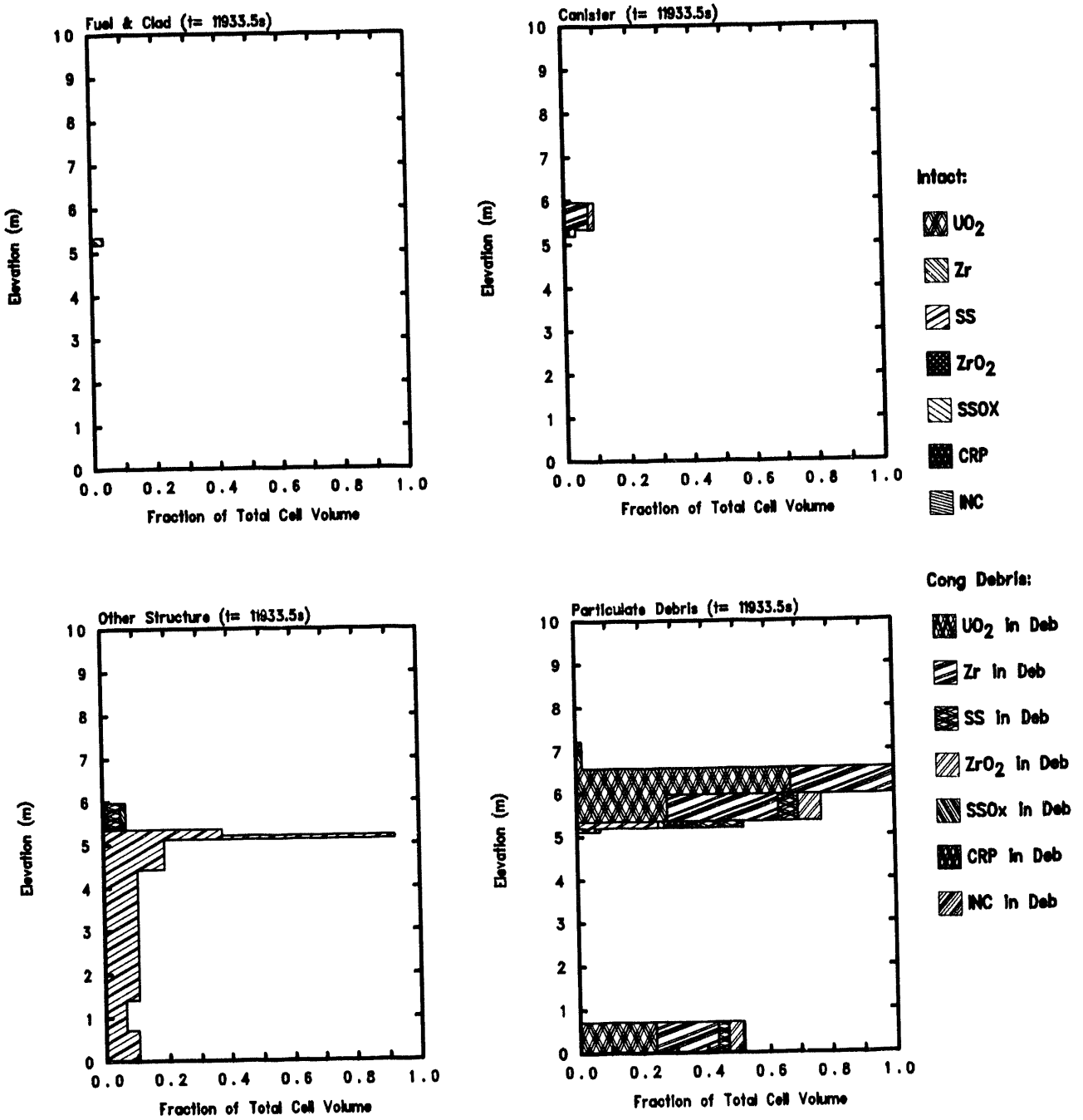

Figure 5.1.10. Core Ring 3 Fuel/Clad (upper left), Canister (upper right), Other Structure (lower left) and Particulate Debris (lower right) Component Material Masses Predicted by MELCOR for LCLP-PF-R-N Sequence

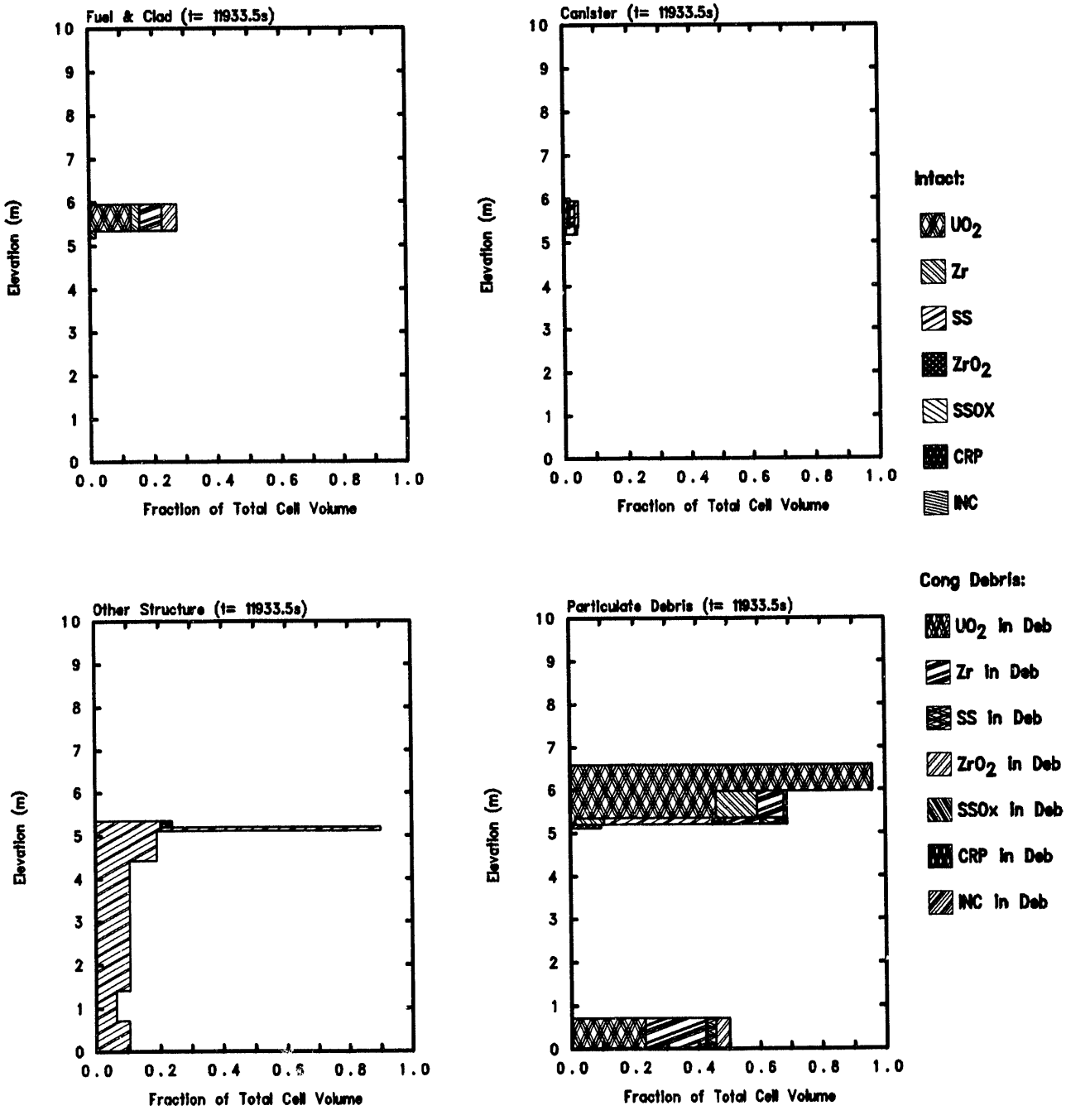

Figure 5.1.11. Core Ring 4 Fuel/Clad (upper left), Canister (upper right), Other Structure (lower left) and Particulate Debris (lower right) Component Material Masses Predicted by MELCOR for LCLP-PF-R-N Sequence

Table 5.1.2. Core Masses at Vessel Failure Predicted during LCLP-PF-R-N Sequence

	Intact	Debris
Active Fuel Region Masses (kg)		
UO_2	7,645	134,692
Zircaloy	14,272	35,212
ZrO_2	4,541	4,473
Steel	15,253	12,835
Steel oxide	1,452	335
Control rod poison	158	513
Total	43,321	188,061
Core Support Plate Masses (kg)		
UO_2	8	13
Zircaloy	239	112
ZrO_2	23	1
Steel	11,642	250
Steel oxide	4	3
Control rod poison	0	121
Total	11,916	500
Lower Plenum Masses (kg)		
UO_2	0	29,241
Zircaloy	0	16,077
ZrO_2	0	3,180
Steel	47,748	2,800
Steel oxide	0	30
Control rod poison	0	156
Total	47,748	51,484

Table 5.1.3. Core State at Vessel Failure Predicted during LCLP-PF-R-N Sequence

Region	Average Debris Temperature (K)	Fraction of Debris Material Molten
Active Fuel	2520	27%
Core Support Plate	841	0%
Lower Plenum	3113	100%

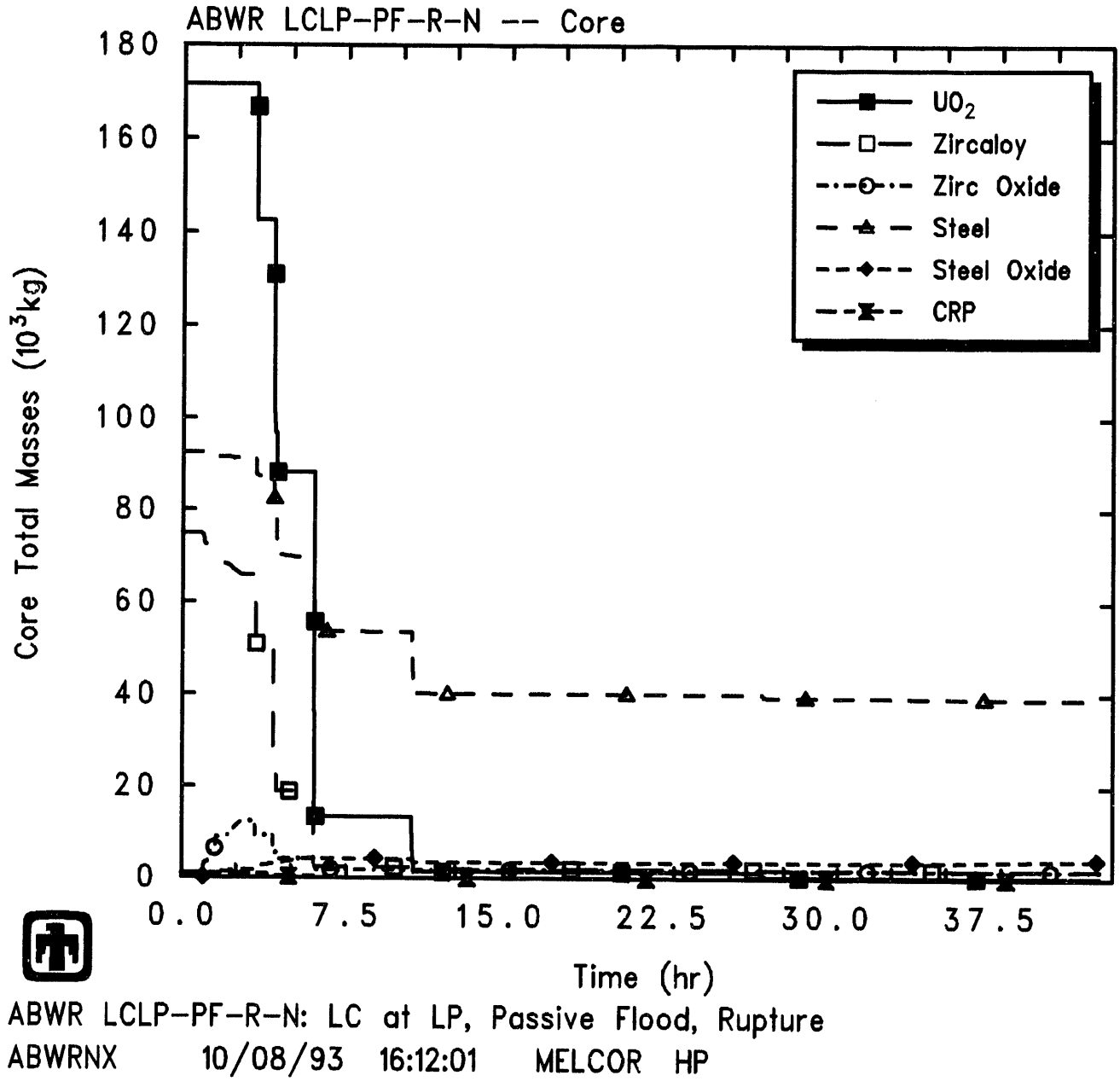

Figure 5.1.12. Core Material Masses Predicted by MELCOR for LCLP-PF-R-N Sequence

available steam and hence limits clad oxidation when the cladding is hot. The in-vessel hydrogen production predicted by MELCOR appears to be in very good agreement with the MAAP result between 1 and 2hr. The in-vessel hydrogen production in the MAAP analysis ends when the vessel fails, at 2hr. The in-vessel hydrogen production in the MELCOR calculation continues until the vessel fails at 3.3hr, and then continues at a somewhat slower rate until just after 6hr, when most of the zircaloy has been ejected from the vessel (as shown in Figure 5.1.12); in-vessel hydrogen production then continues at a very slow rate in the MELCOR calculation as the structural steel remaining in the lower plenum continues to oxidize. The amount of hydrogen produced by the time the vessel fails at 3.3hr in the MELCOR calculation corresponds to oxidation of 16% of all the zircaloy present in the intact core (in the cladding, canisters, *etc.*), 6% of the structural steel initially present in the core and 0.4% of the structural steel present in the lower plenum.

At vessel failure, any remaining water in the lower plenum not flashed by contact with the hot debris flowed through the vessel breach into the cavity, as seen in the liquid levels presented in Figures 5.1.1 and 5.1.14. Figure 5.1.14 shows the collapsed liquid level in the lower drywell (cavity) control volume in the MELCOR calculation; the level is given in terms of a system-wide elevation referenced to 0 at the bottom of the vessel lower plenum, and the bottom of the cavity control volume is indicated in the figure, for reference. The sudden rise in liquid level at 3.3hr corresponds to the remaining lower plenum water pouring out the vessel breach. That water is then steadily boiled away over the next 3hr until the cavity becomes dry, at 6.2hr after accident start. MELCOR predicts the passive flooder to open immediately after the cavity goes dry. MELCOR has no debris quench model, and thus the debris in the cavity remains hot (as will be discussed later in this section). As soon as the cavity goes dry, the lower drywell atmosphere temperature rises rapidly due to heat transfer from the unquenched debris and very quickly reaches the 533K (500°F) setpoint for passive flooder actuation. Water then pours from the wetwell into the drywell to the level of the upper horizontal vent. After an initial transient, the cavity liquid level settles to a constant pool depth of around 2m for the remainder of the transient.

Figure 5.1.15 gives the drywell and wetwell pool masses for the MELCOR analysis, compared to the pool masses calculated by MAAP (taken from Figure 19E.2-2F in [1]). There appears to be a small difference in the suppression pool initial mass (and/or level) in the two calculations, and MELCOR predicts a bigger short-term drop in suppression pool level and corresponding rise in cavity pool level upon opening the passive flooder. However, the results are generally in good qualitative agreement, with both codes showing an initial rise in suppression pool level (due to condensation of steam from the vessel) a drop and then recovery to a slightly lower level after the passive flooder opens, then maintenance of that level until the containment rupture disk opens, followed by a gradual drop in suppression pool level.

The lower drywell and wetwell atmosphere and pool temperatures are presented in Figure 5.1.16. The hot debris in the cavity in the MELCOR calculation keeps the lower drywell pool temperature (400-440K) substantially hotter than the suppression pool tem-

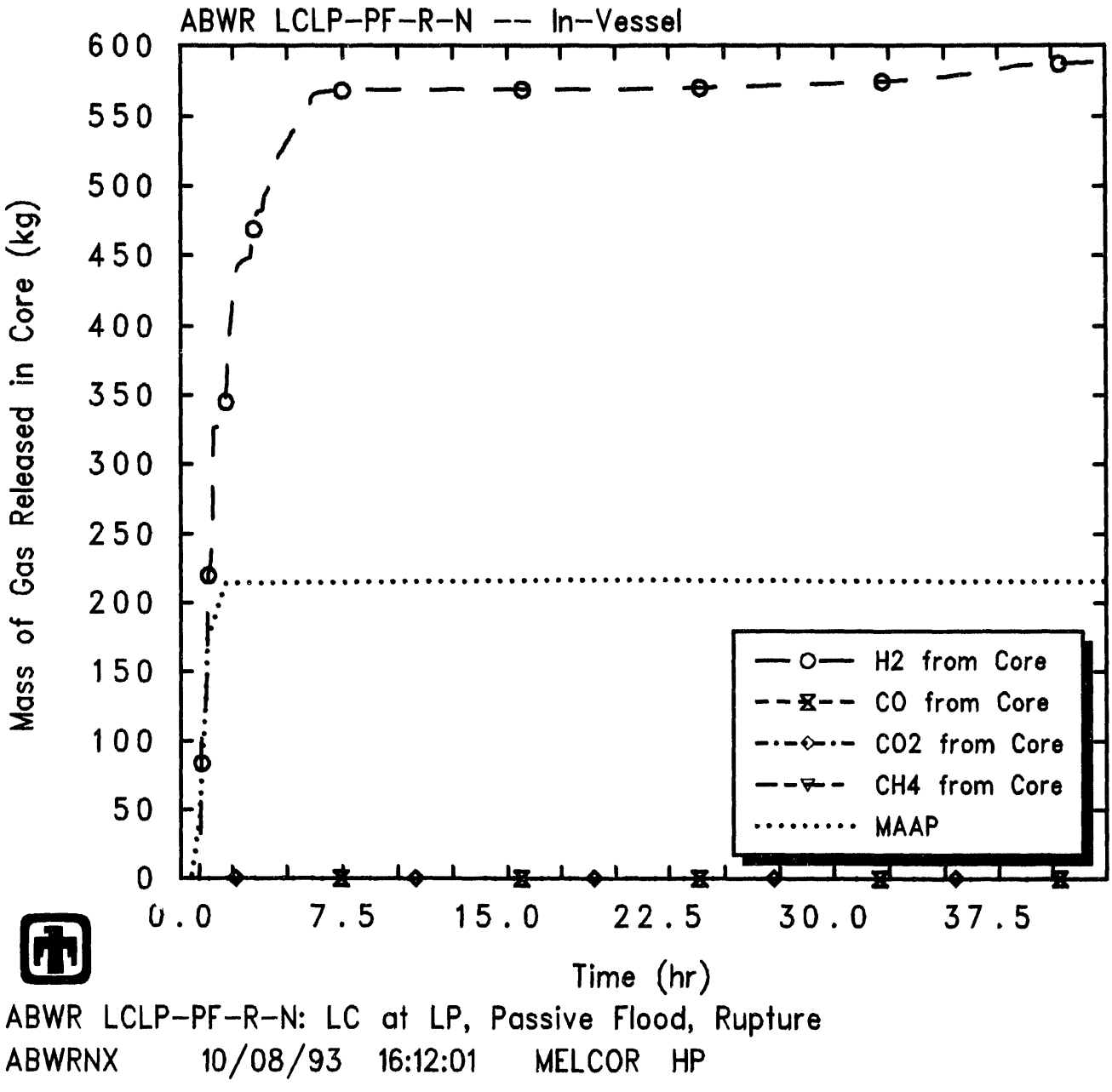

Figure 5.1.13. In-Vessel Hydrogen Production Predicted by MELCOR for LCLP-PF-R-N Sequence, Compared to MAAP

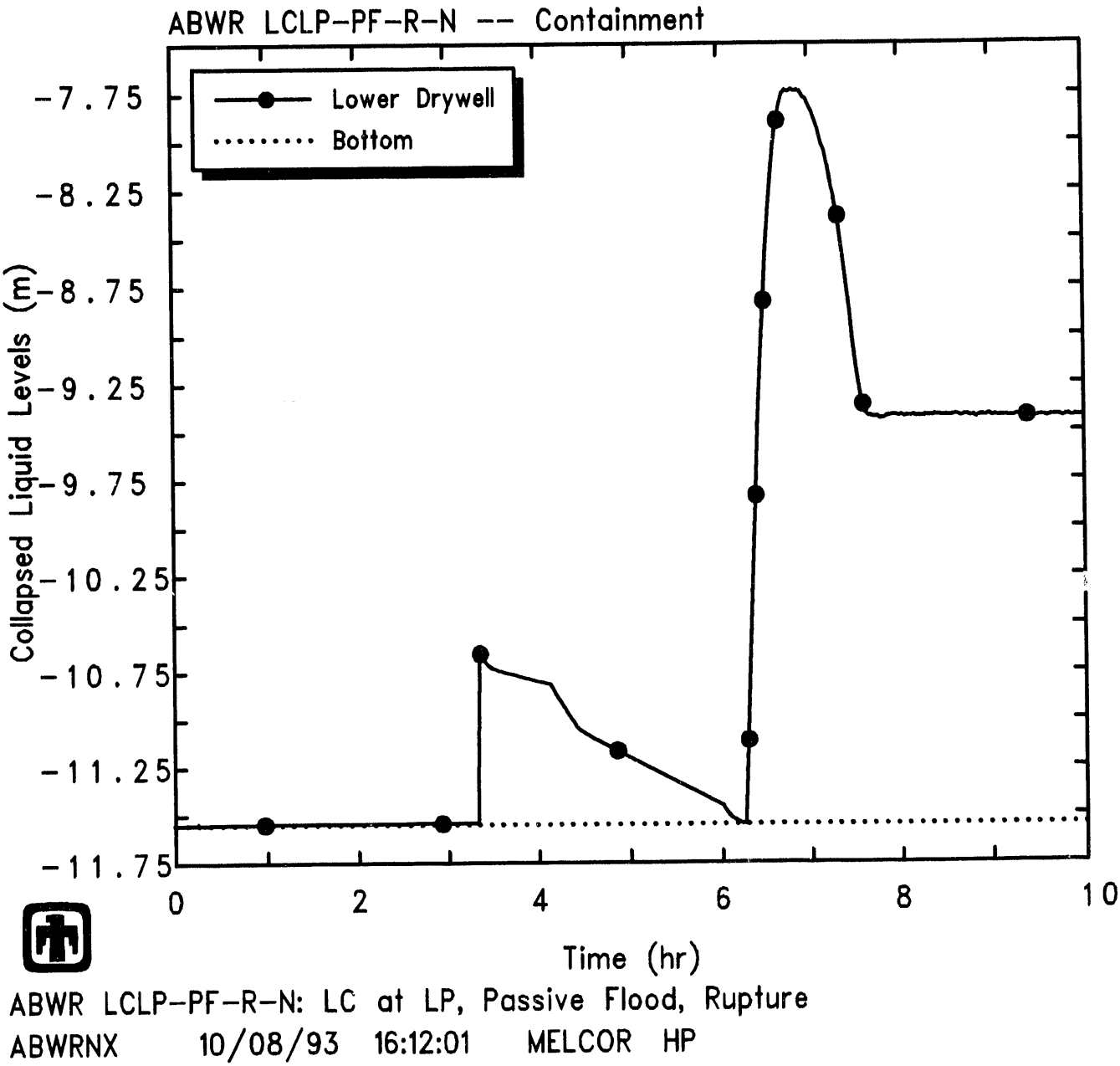

Figure 5.1.14. Lower Drywell Liquid Level Predicted by MELCOR for LCLP-PF-R-N Sequence

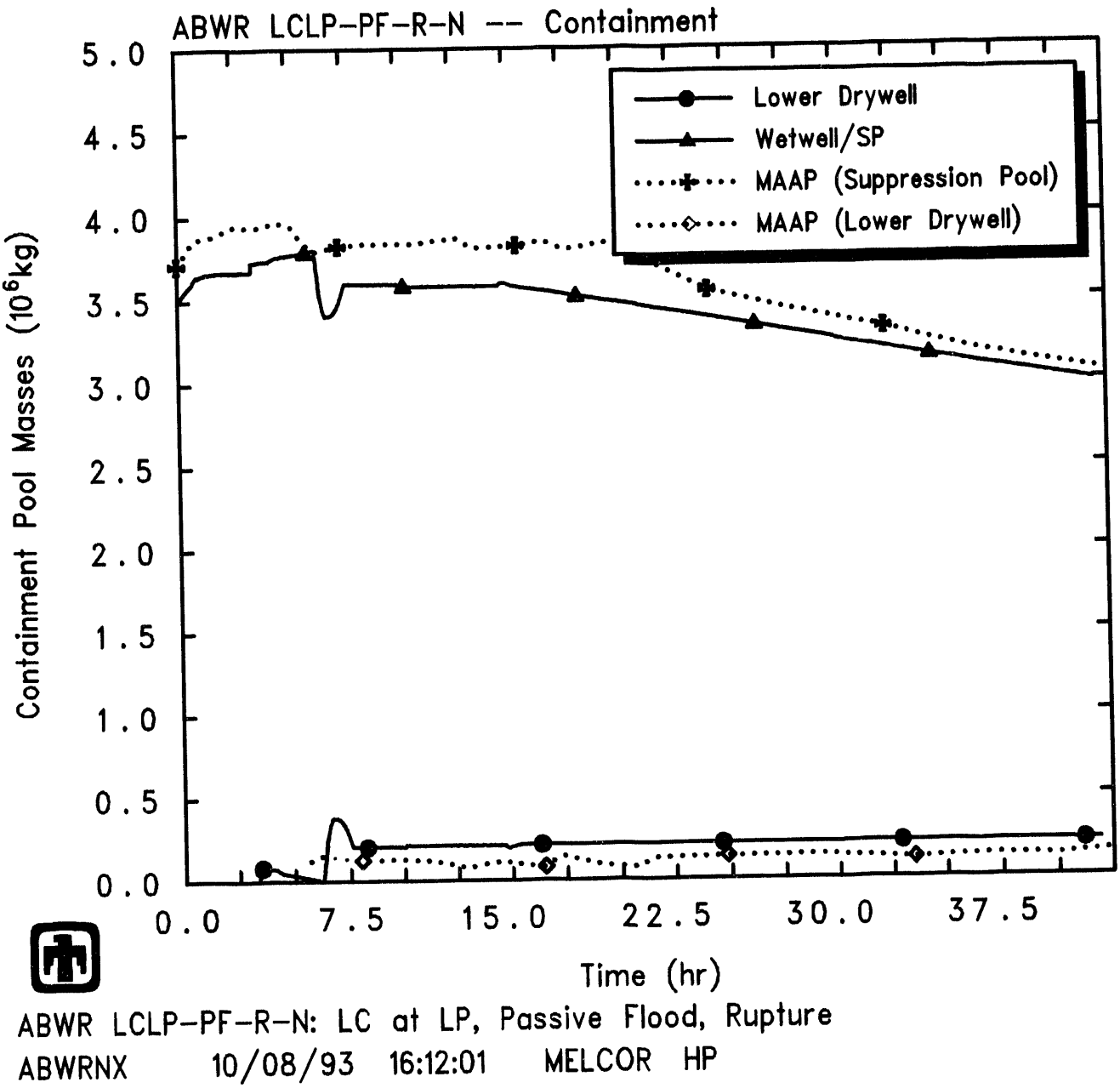

Figure 5.1.15. Lower Drywell and Suppression Pool Masses Predicted by MELCOR for LCLP-PF-R-N Sequence, Compared to MAAP

perature (340-400K), both while the cavity has residual lower plenum water in it and after the passive flooder opens and the cavity is flooded with suppression pool water; the cavity pool temperature drops to near the suppression pool temperature after the containment rupture disk opens and the containment depressurizes. The wetwell atmosphere is ~20K hotter than the suppression pool for the first few hours of this transient (before vessel breach), and the wetwell atmosphere temperature remains nearly constant while the suppression pool continually heats up, until opening of the containment rupture disk after which the wetwell pool and atmosphere (and cavity pool) temperatures remain nearly equal and nearly constant. The cavity atmosphere remains significantly hotter than the cavity pool throughout the transient, even after COPS rupture (and the upper drywell heats up even more, as illustrated in Figure 5.1.18).

The pressures calculated by MELCOR in the various containment control volumes are depicted in Figure 5.1.17, together with the containment pressure from the MAAP analysis (taken from Figure 19E.2-2B in [1]). The results from the two codes are generally similar qualitatively, but with a number of quantitative differences and shifts in timing. Both codes predict a rapid pressure increase in containment immediately after vessel failure, due to steam generation from hot debris and water falling into the cavity from the lower plenum. That initial containment pressurization appears greater in the MAAP analysis than in the MELCOR analysis, probably because the core debris is completely quenched in the MAAP calculation while there is no debris quenching model in MELCOR; the MELCOR calculation therefore predicts some of the debris energy goes into attacking concrete, while the MAAP analysis predicts all of the debris energy to go to steam production. This is probably why the MAAP calculation takes about 1hr to boil away the lower plenum water fallen into the cavity, while the MELCOR analysis requires about 3hr to boil off that residual lower plenum water (although there is no guarantee that the amounts and temperature of core debris and of lower plenum water in the cavity are equal in the two calculations). In the MAAP containment pressure history, after the water in the lower drywell boils off, the drywell pressure decreases because steam is condensed on the containment heat sinks but there is no additional steam generated; in the MELCOR calculation, the containment pressure continues to rise as hot, unquenched core debris continues to boil off the cavity water pool.

There is only 1hr difference in the time that the passive flooder opened in the two calculations. However, MELCOR predicted the passive flooder to open very soon ($\leq$1min) after the cavity dried out, while MAAP predicted a several-hour delay between cavity dryout and passive flooder opening. This is due to the cavity debris being quenched in the MAAP calculation but not in the MELCOR calculation. In both analyses, after the core debris in the cavity is uncovered the debris and the gas above it begin to heat up and, in both cases, when the lower drywell atmosphere reaches 533K (500°F) the passive flooder opens. Figure 5.1.18 gives the upper and lower drywell temperatures calculated by MELCOR, compared to corresponding MAAP results. (The MAAP curves included in this plot were taken from Figure 19E.2-2C in [1].) The lower drywell temperature predicted by MAAP begins increasing when debris first enters the cavity, and increases at a steady rate until the passive flooder opening setpoint of 533K (500°K) is reached;

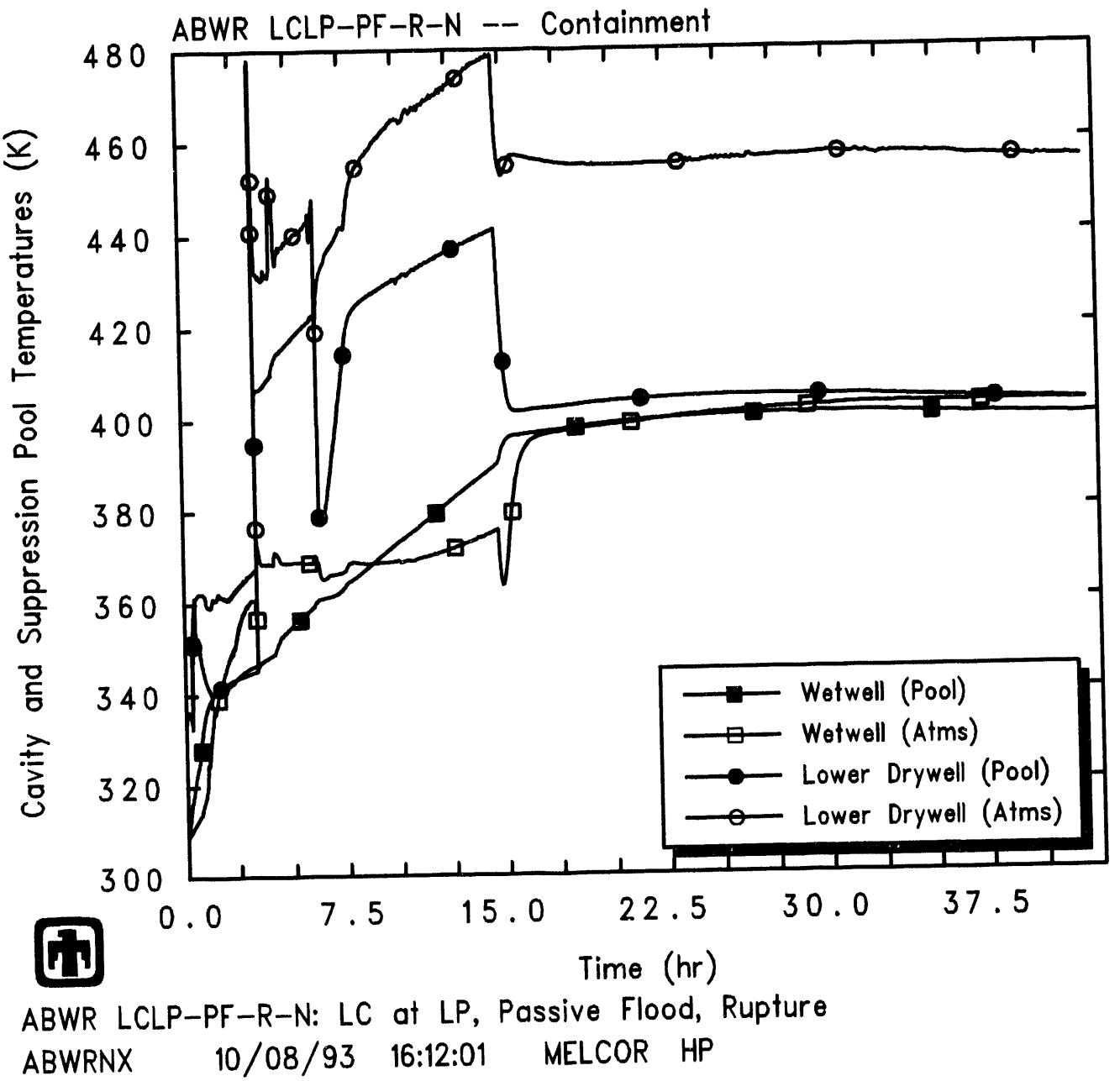

Figure 5.1.16. Lower Drywell and Suppression Pool Temperatures Predicted by MELCOR for LCLP-PF-R-N Sequence

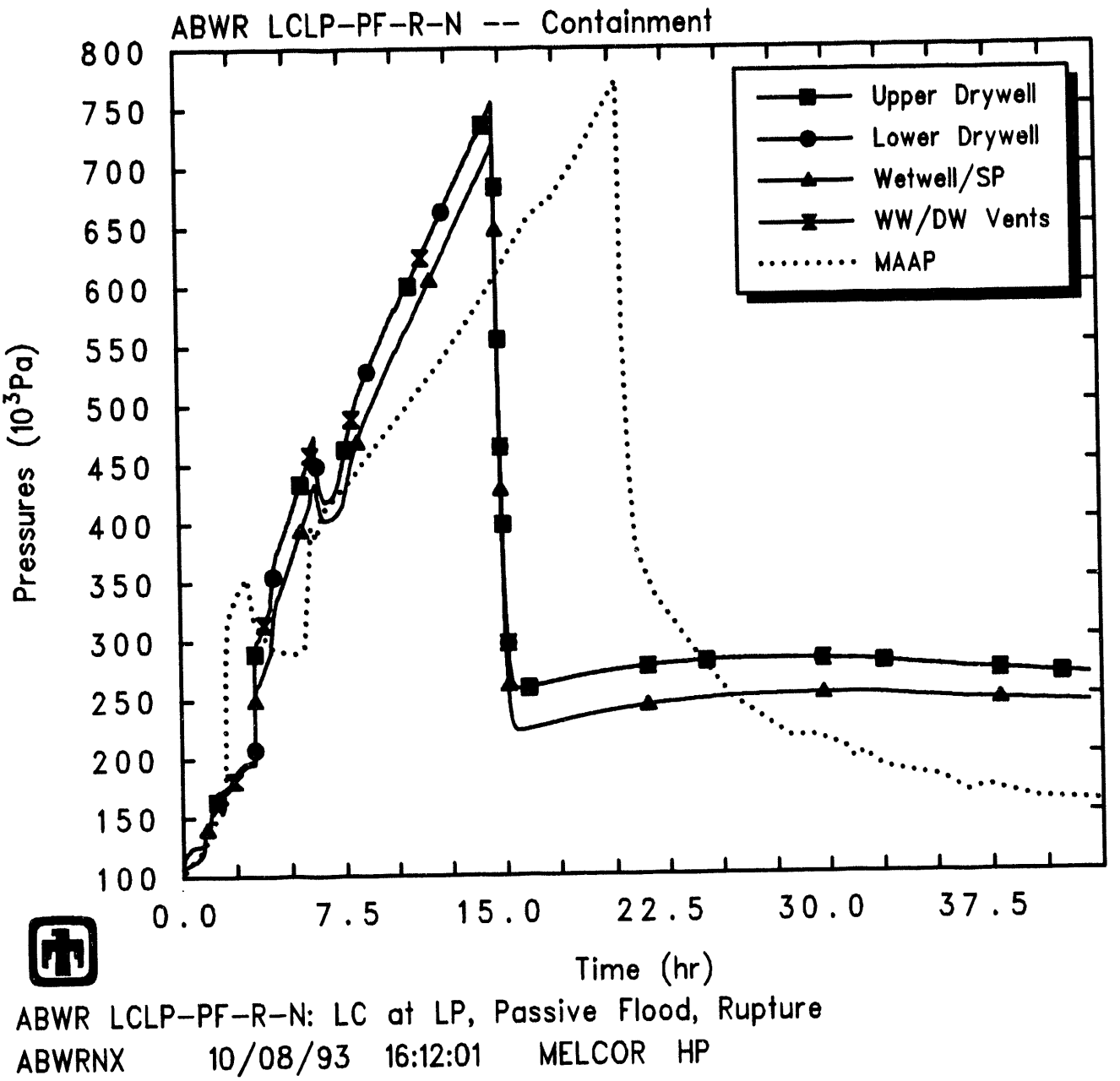

Figure 5.1.17. Containment Pressures Predicted by MELCOR for LCLP-PF-R-N Sequence, Compared to MAAP

the lower drywell temperature then drops precipitously as suppression pool water floods the cavity. In the MELCOR calculation, the lower drywell temperature spikes up when debris first falls into the cavity at 3.3hr but then remains nearly constant during the next 3hr while the water fallen into the cavity is being boiled away; the temperature spike triggering the passive flooder occurs between two plot edits and cannot be seen in this figure, but the subsequent drop in liquid temperature is visible at about 6.2hr.

After the passive flooder opens, the debris in the cavity is covered by an overlying water pool, so the temperature of the lower drywell therefore decreases. The MAAP calculation shows the lower drywell hotter than the upper drywell prior to the opening of the passive flooder, with the upper drywell hotter than the lower drywell for the remainder of the transient calculated (with the temperature difference increasing with time, especially after containment rupture disk actuation). The MELCOR calculation has the lower drywell hotter than the upper drywell for much longer, through passive flooder actuation and for a short time after COPS rupture; the upper drywell atmosphere does get hotter than the lower drywell soon after rupture disk actuation and that temperature difference increases with time, but the difference is much smaller in the MELCOR analysis than seen in the MAAP results given.

The pressurization of the containment continues after the passive flooder is open because the cavity debris is now transferring heat directly to the overlying water pool which produces steaming and, in the MELCOR calculation, because core-concrete interaction is adding noncondensables to the atmosphere. Since the peak cavity debris temperature in the MAAP analysis during this process was 1600K and the average corium temperature in the lower drywell was less than 500K throughout most of the transient (as indicated in Figure 19E.2-2D in [1]), no significant core-concrete attack was predicted to occur during the heatup of the debris; therefore, no additional noncondensable gases were generated. The containment therefore pressurizes more quickly in the MELCOR calculation than in the MAAP analysis.

Figures 5.1.19 and 5.1.20 show the total and partial pressures, and the mole fractions, respectively, in the atmospheres of the four control volumes representing containment (*i.e.*, upper and lower drywell, wetwell and drywell/wetwell vents). The lower drywell and DW/WW vent atmospheres consist of almost all (>90%) steam from vessel failure through calculation end; in the upper drywell, most (60-80%) of the atmosphere consists of steam after vessel failure; in the suppression pool, steam does not predominate until after containment rupture disk opening, while most (50-60%) of the wetwell atmosphere between vessel failure and containment depressurization is hydrogen.

The containment continues to pressurize until the wetwell pressure reaches 0.72MPa (90psig) at 20.2hr in the MAAP analysis and at 14.7hr in the MELCOR calculation, when the rupture disk opens as shown in Figure 5.1.17. The flow out the COPS rupture disk in the MELCOR calculation is presented in Figure 5.1.21. No penetration leakage is predicted by either MAAP or MELCOR, since the temperature in the upper drywell remains below 533K (500°F) until well after the rupture disk opens (as illustrated in Figure 5.1.18).

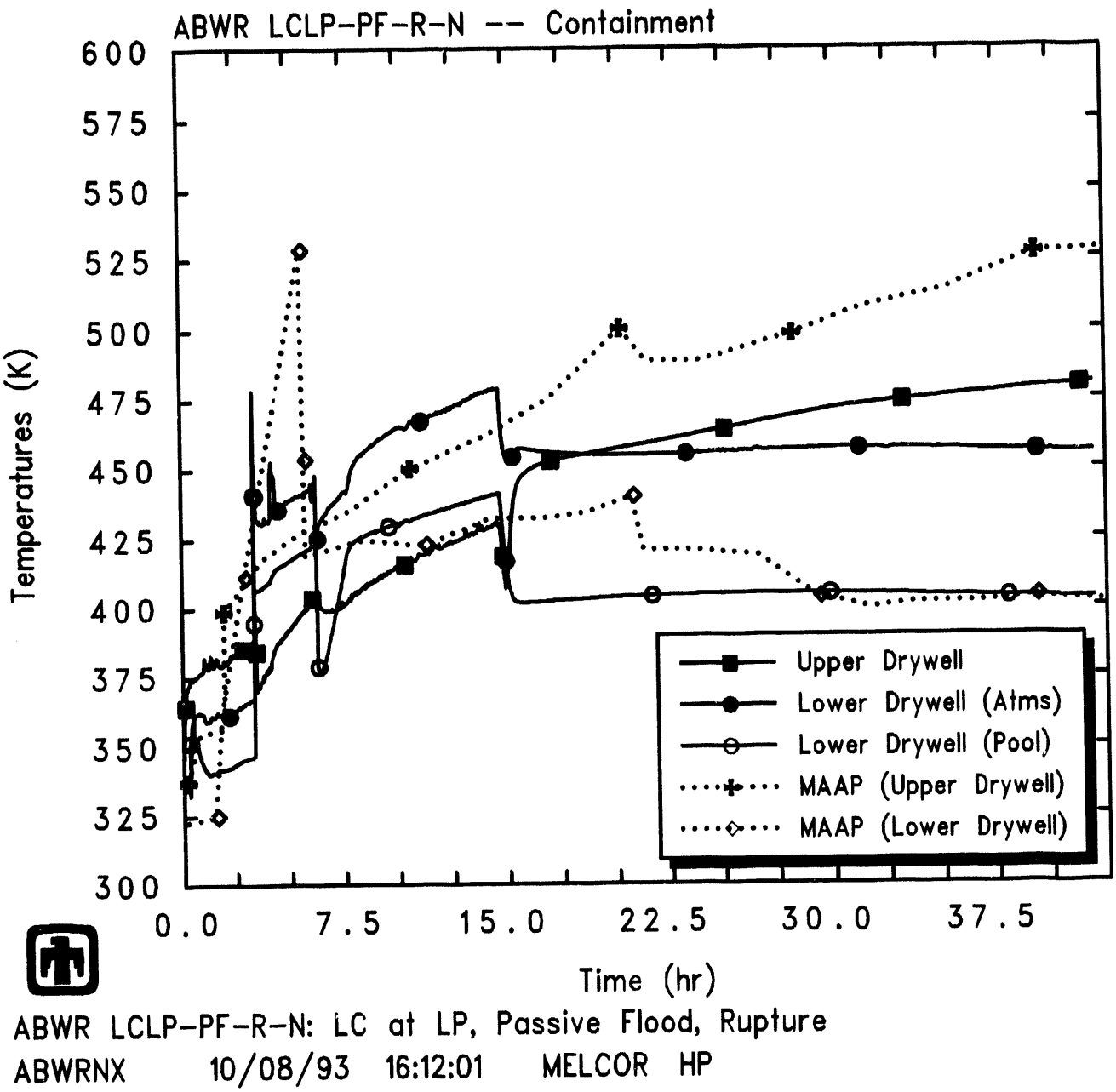

Figure 5.1.18. Containment Temperatures Predicted by MELCOR for LCLP-PF-R-N Sequence, Compared to MAAP

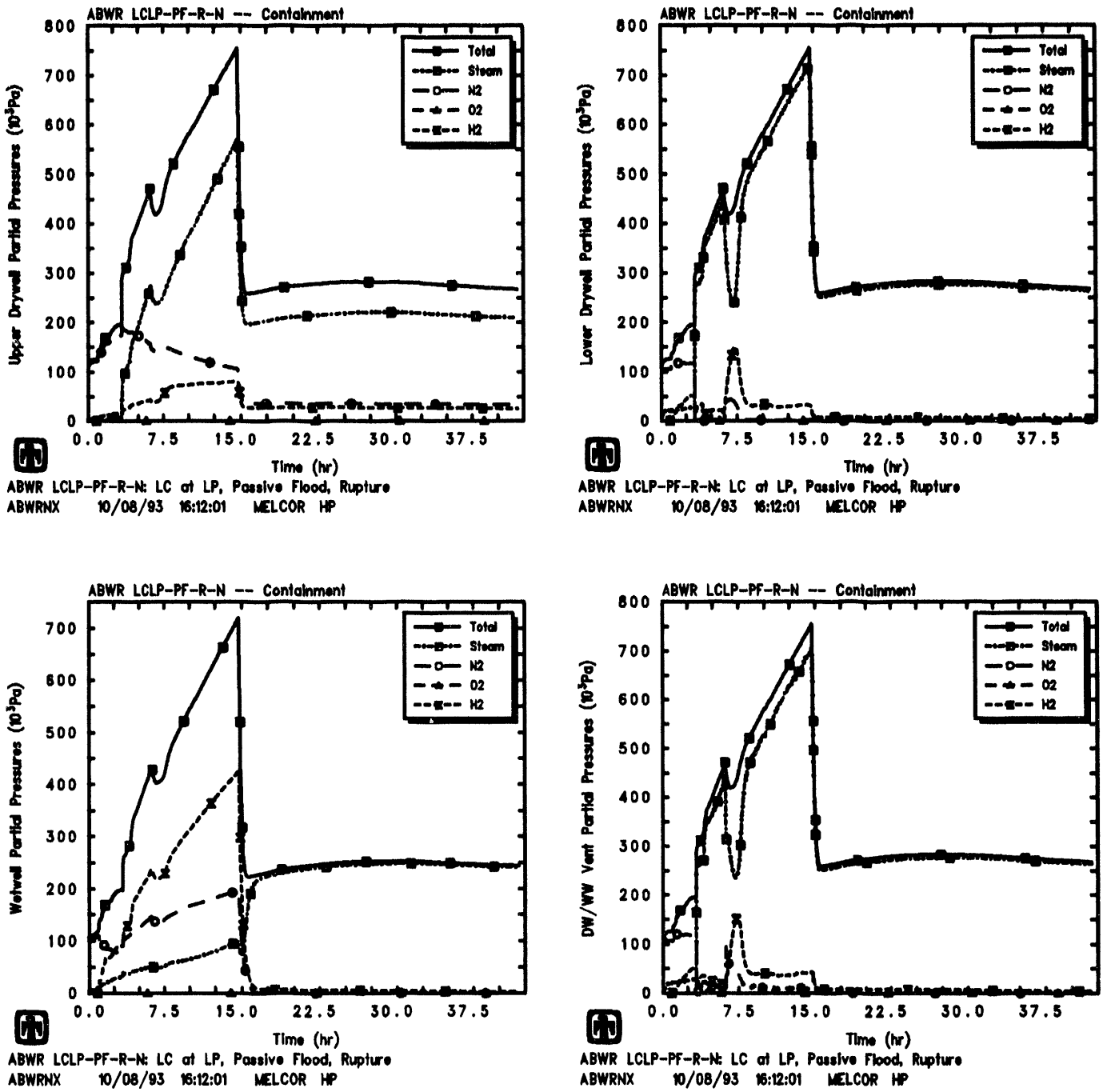

Figure 5.1.19. Containment Upper Drywell (upper left), Lower Drywell (upper right), Wetwell (lower left) and DW/WW Vent (lower right) Partial Pressures Predicted by MELCOR for LCLP-PF-R-N Sequence

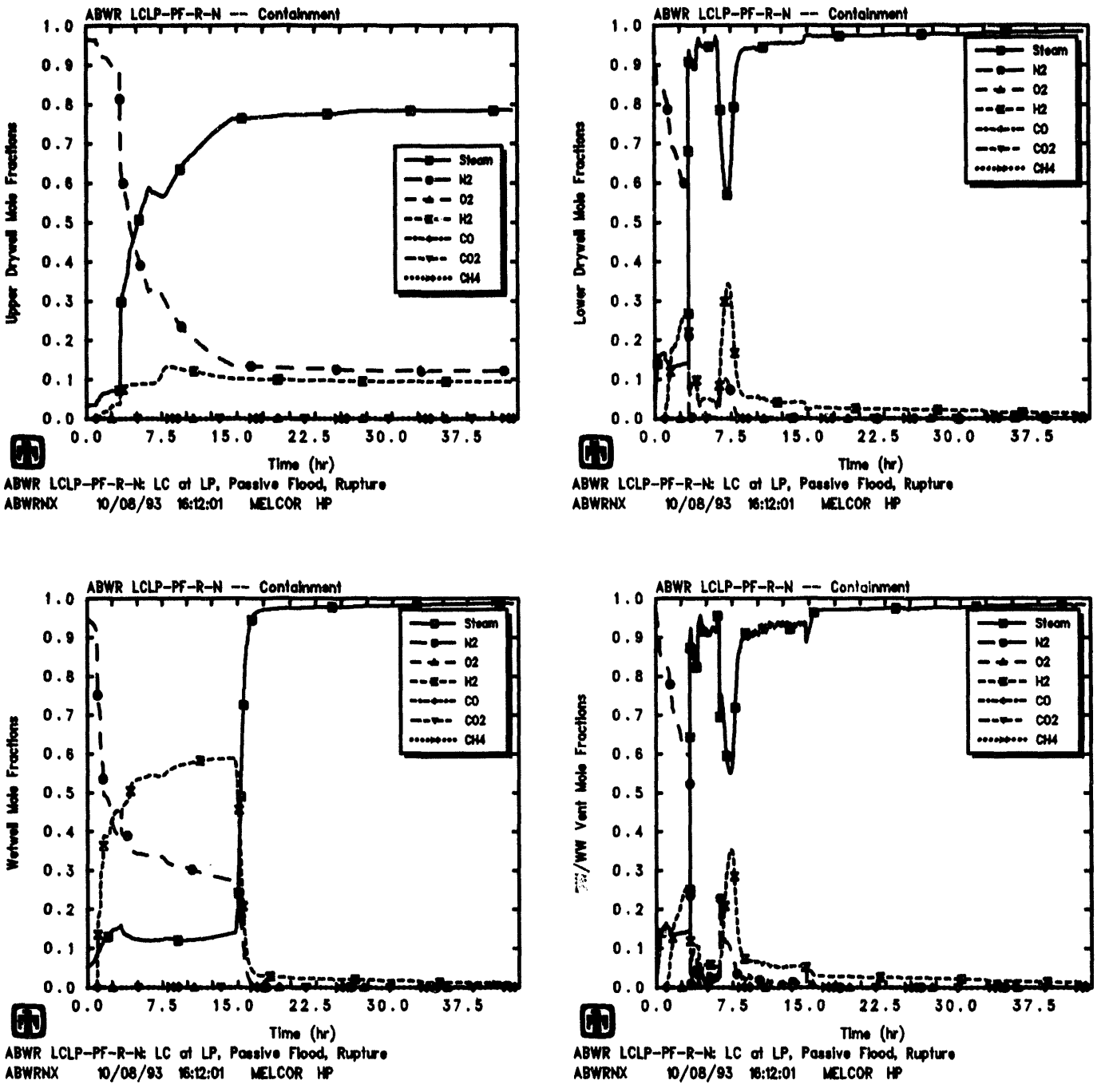

Figure 5.1.20. Containment Upper Drywell (upper left), Lower Drywell (upper right), Wetwell (lower left) and DW/WW Vent (lower right) Mole Fractions Predicted by MELCOR for LCLP-PF-R-N Sequence

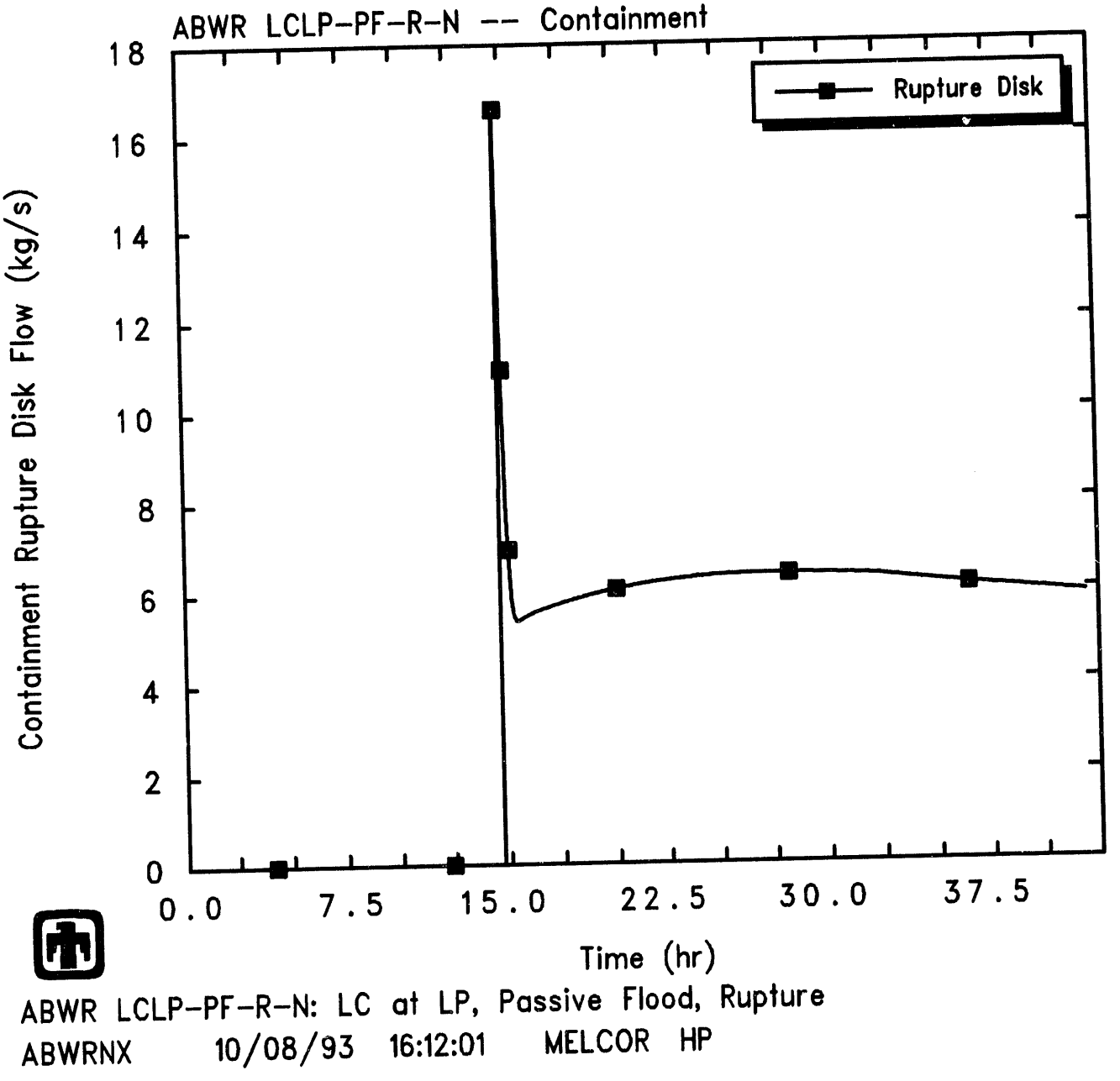

Figure 5.1.21. COPS Rupture Disk Mass Flow Predicted by MELCOR for LCLP-PF-R-N Sequence

The total mass of debris in the cavity, the mass of ejected core debris, the mass of ablated concrete and the mass of gases generated in the cavity calculated by MELCOR are illustrated in Figure 5.1.22. The mass of core debris in the cavity is basically an inversion of the masses retained in-vessel, presented in Figure 5.1.12, and the debris ejection can be seen to occur in discrete steps or stages. In contrast, the mass of concrete ablated increases continuously with time.

MELCOR has no debris quench modelling capability. As soon as the core debris was predicted to enter the cavity, core-concrete interaction began, resulting in the production of carbon dioxide and hydrogen; reduction of these gases by the molten metal also gave rise to carbon monoxide and hydrogen. Figure 5.1.23 presents the production of various noncondensable gases in the cavity due to core-concrete interaction, calculated by MELCOR. Almost all of the cavity gas production is in the form of hydrogen, with a small and growing amount of CO produced after 32-33hr. CO is produced only after all the zironium in the cavity is oxidized to ZrO_2, which happens at about 30hr in this case, because before that time Zr is assumed to reduce any CO_2 generated to pure carbon ("coking"); this reaction can be disabled in MELCOR, but is enabled by default.

Figure 5.1.24 gives the calculated maximum cavity depth and radius. (Note that these represent maximum, not average, ablation distances.) Immediately after core debris is first ejected from the vessel to the cavity upon vessel breach in the MELCOR analysis, there is a brief period of rapid radial ablation lasting 1-2hr, which stops after only 4cm of concrete loss. The bulk of the concrete ablation calculated is axially downward, with the MELCOR calculation stopping at about 42hr when the axial ablation equals and tries to exceed the specified available concrete thickness of 2m.

Figure 5.1.25 shows the predicted masses, thicknesses, temperatures and densities of the light oxide, metallic and heavy oxide debris layers in the cavity. No heavy oxide layer is visible in these plots; MELCOR calculates a stable configuration of a light oxide layer above a metallic debris layer throughout the transient period calculated. The metallic layer remains nearly constant in mass and thickness, with a gradually increasing density; the light oxide layer mass and thickness increase continuously (and the density decreases) as ablating concrete (with its resultant low-density silicate oxides) continues to dilute the high-density zirc oxide and steel oxide debris to an average density value less than the metallic debris density. After some initial oscillations, the temperatures of both layers remain nearly equal, at ~1500K, throughout the transient period calculated.

The heat transfer from the cavity debris pool in the MELCOR analysis, both downward and outward to the concrete surface and upward to the cavity volume atmosphere, is shown in Figure 5.1.26. The energy transfer from the debris in the cavity upward through the debris bed surface to the lower drywell atmosphere and/or overlying water pool is 2-5 times greater than the energy transferred downward (and sideways) to the concrete. In general, that upper surface of the debris bed is covered with a water pool, not exposed to atmosphere.

Tables 5.1.4 and 5.1.5 give the distribution of the released radionuclides at the end of the calculation (*i.e.*, at ~42hr). Table 5.1.4 provides an overview of how much of

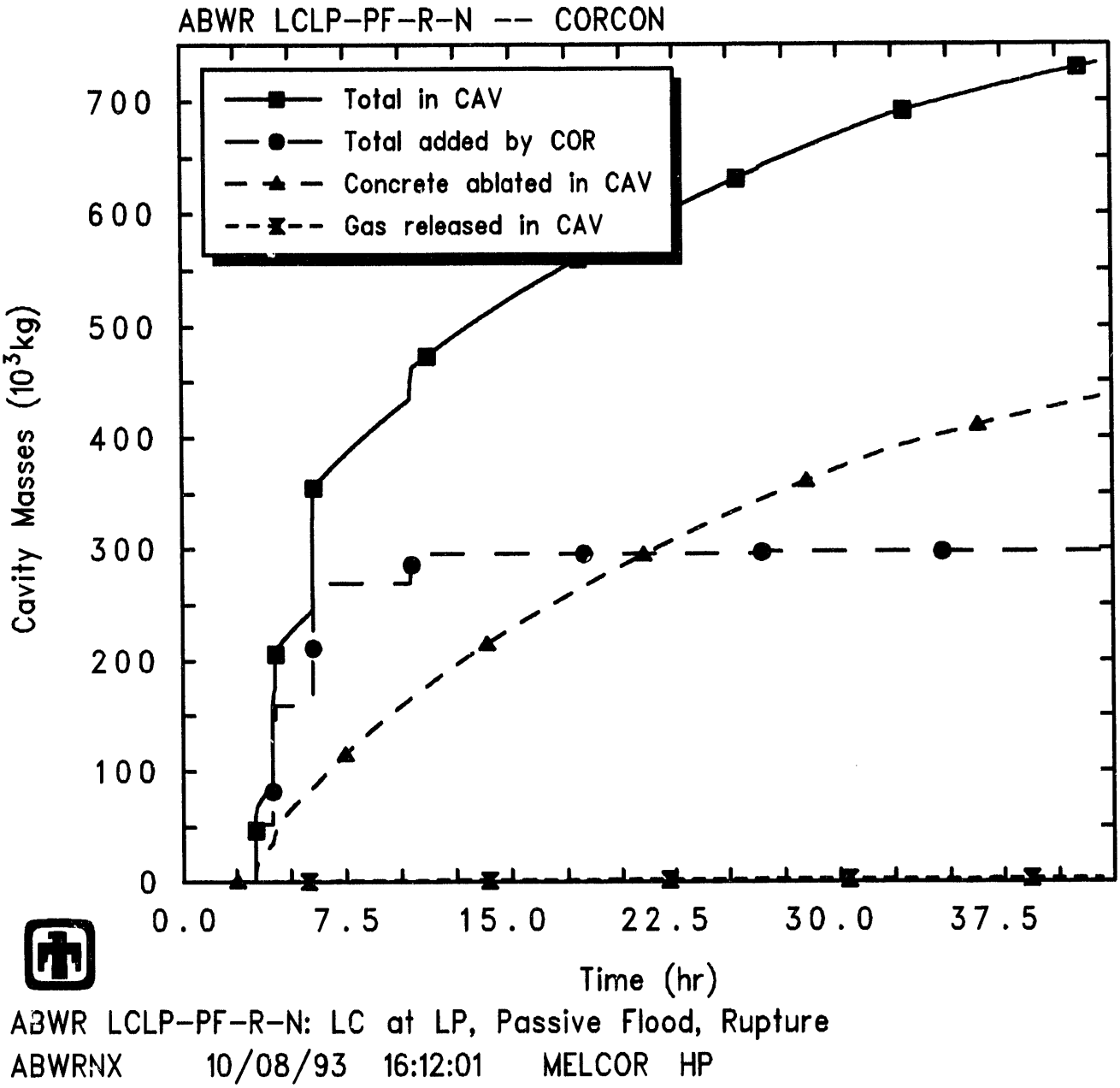

Figure 5.1.22. Cavity Material Masses Predicted by MELCOR for LCLP-PF-R-N Sequence

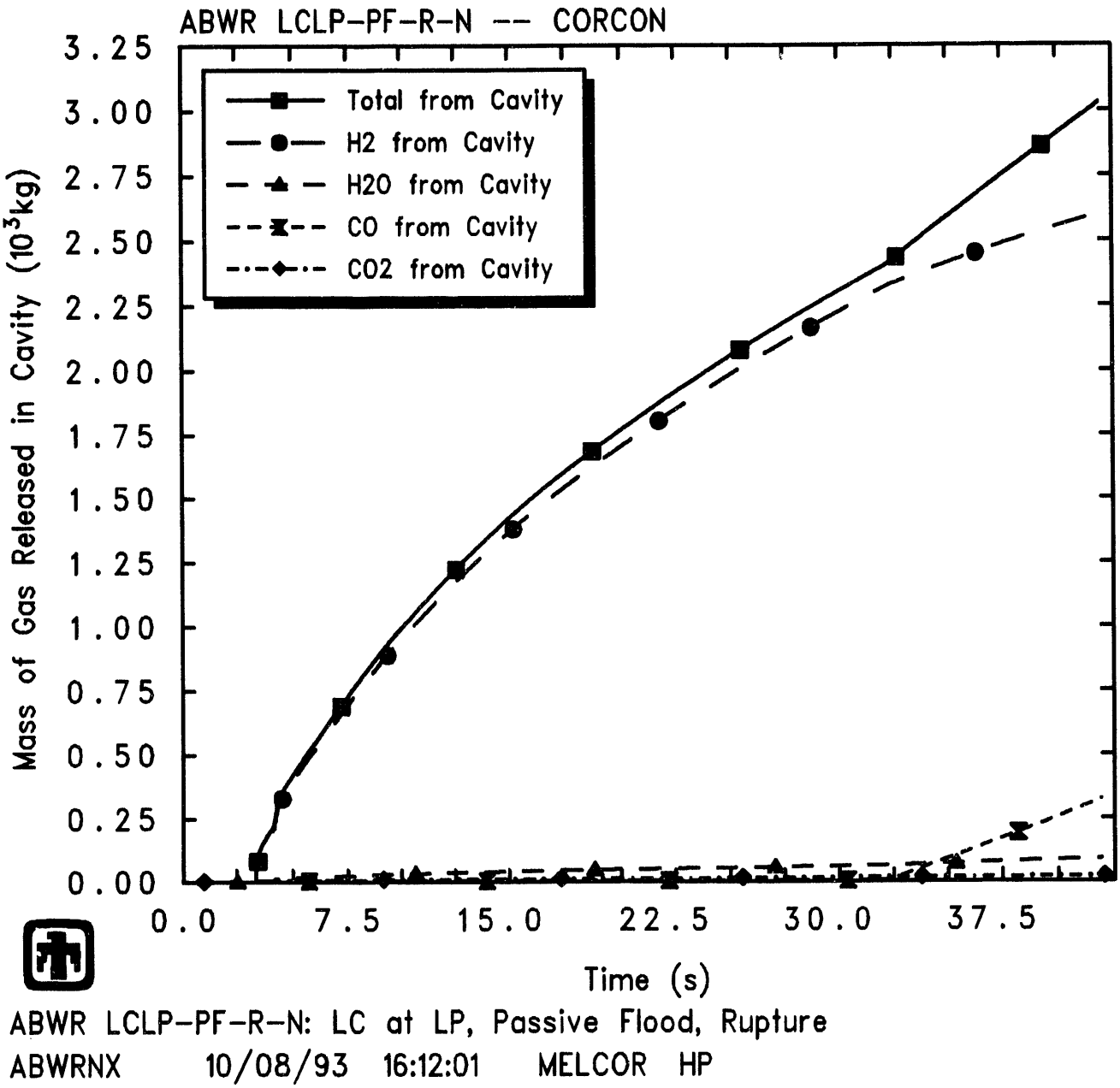

Figure 5.1.23. Cavity Gas Production Predicted by MELCOR for LCLP-PF-R-N Sequence

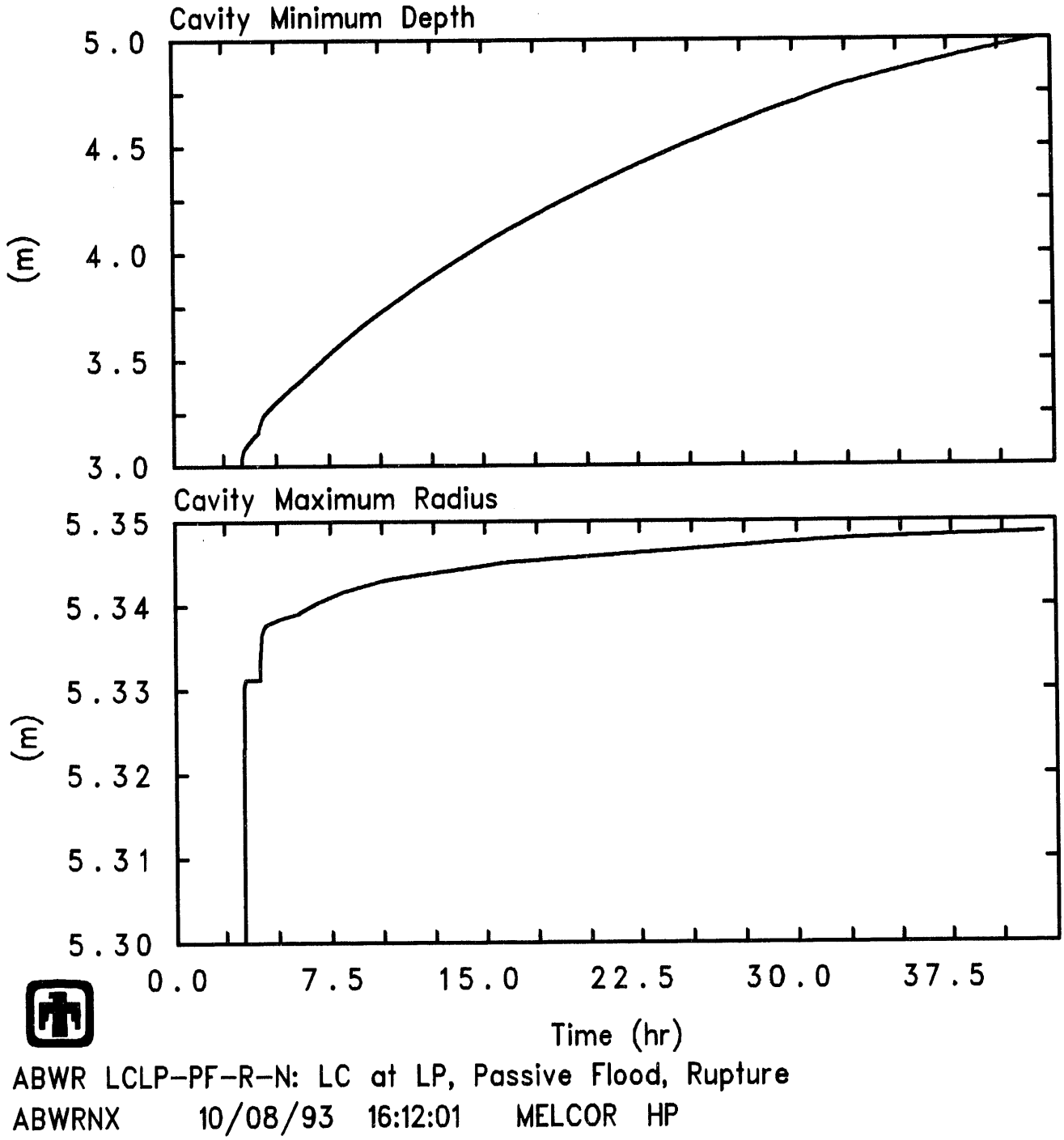

Figure 5.1.24. Cavity Maximum Radius and Depth Predicted by MELCOR for LCLP-PF-R-N Sequence

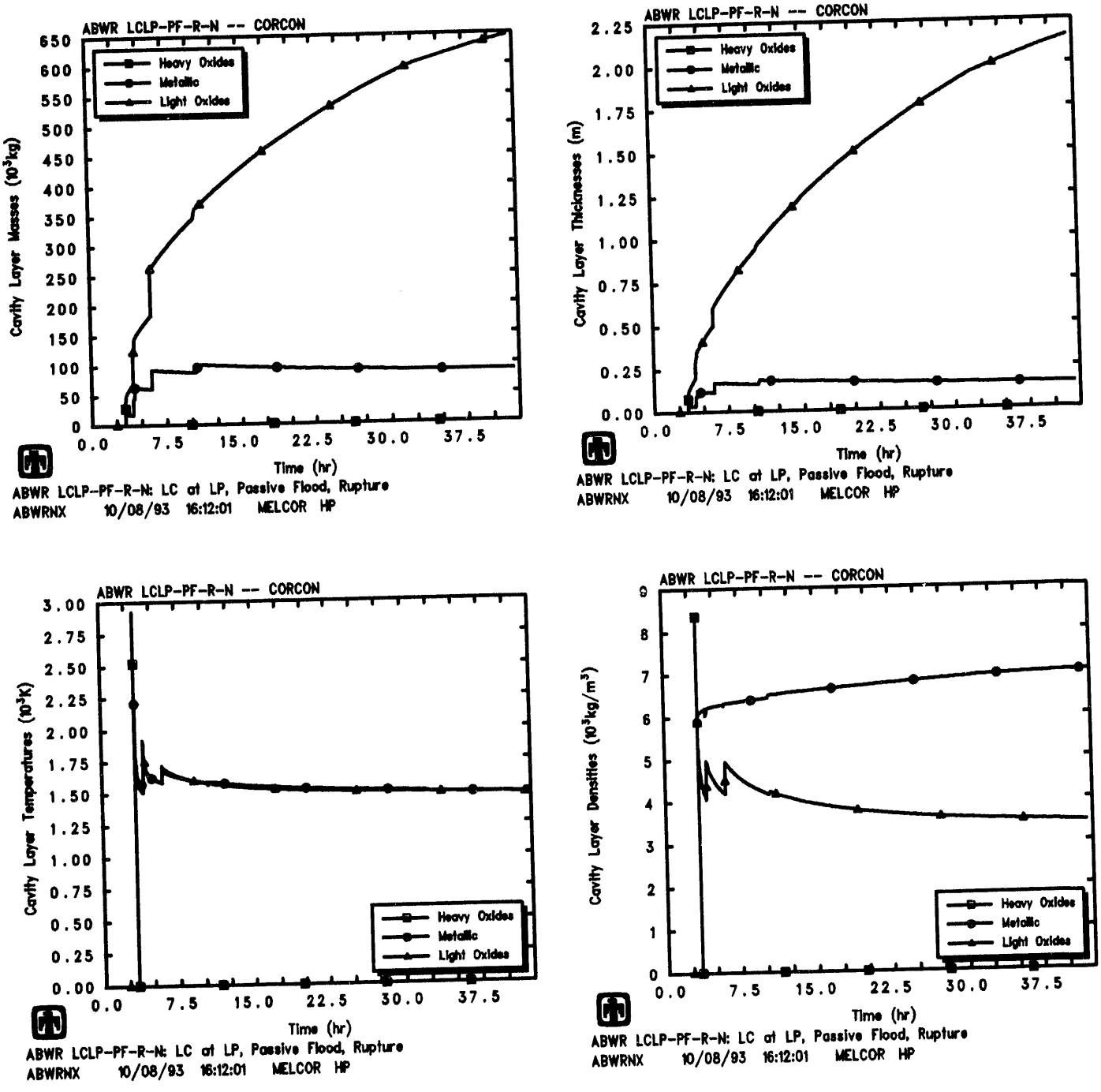

Figure 5.1.25. Cavity Layer Masses (upper left), Thicknesses (upper right), Temperatures (lower left) and Densities (lower right) Predicted by MELCOR for LCLP-PF-R-N Sequence

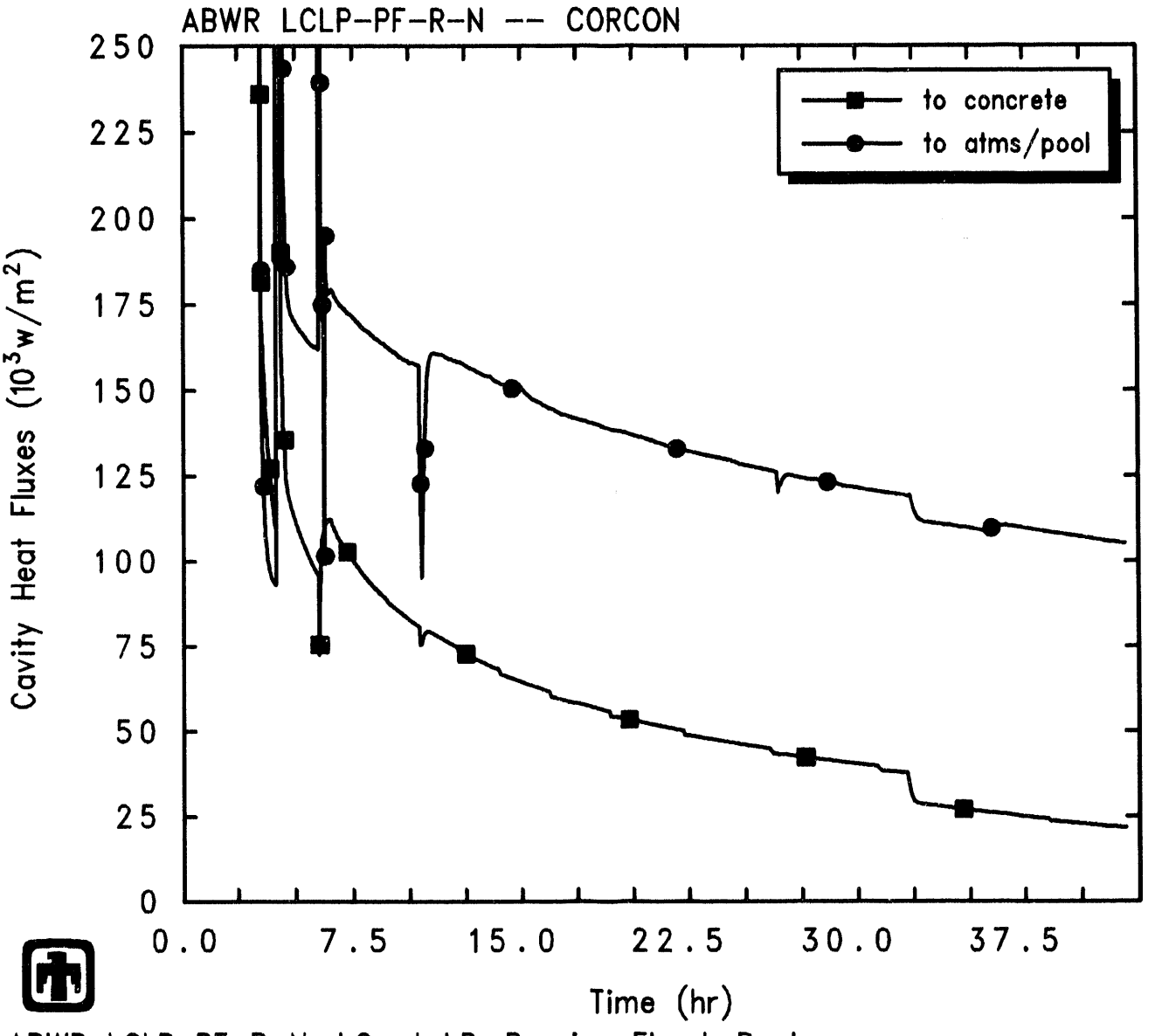

Figure 5.1.26. Cavity Heat Flows Predicted by MELCOR for LCLP-PF-R-N Sequence

the radionuclides remain bound up in fuel in either the core or the cavity, and of how much of the released radionuclides are retained in the primary system *vs* how much of the released radionuclides are released to, or released in, either the drywell or the wetwell in containment and the environment, all normalized to the initial inventories of each class. Table 5.1.5 gives a slightly different breakdown of the released radionuclide final distribution – the fractions of initial inventory released for each class from fuel in-vessel in the core, ex-vessel in the cavity and overall total are given, together with the distribution of the released radionuclides in the primary system, drywell, wetwell and environment normalized by the mass of each class released. (Note that these amounts generally consider only the release of radioactive forms of these classes, and not additional releases of nonradioactive aerosols from structural materials.)

In this sequence, a path to the containment was available and open when the first gap releases occurred in-vessel after 1hr; prior to reactor vessel lower head failure, fission products were transported from the primary system and into the containment via the SRVs. At lower head penetration failure, molten corium was transferred in stages to the cavity, where further fission product release to the containment occurred.

The release behavior predicted by MELCOR can be grouped into several subdivisions. Almost all ($\simeq$100%) of the volatile Class 1 (noble gases), Class 2 (CsOH), Class 5 (Te) and Class 16 (CsI) radionuclide species are released, primarily in-vessel, as are most (80-90%) of the Class 3 (Ba) and Class 12 (Sn) inventories. The next major release fractions (2-4%) are of Ru and Mo, Ce and La. Finally, a total $\leq$0.1% of the initial inventory of uranium and Class 11 (Cd) are predicted to be released. Note that the CORSOR-M fission product release model option used in these analyses has identically zero release in-vessel of Class 7 (Mo), Class 9 (La) and Class 11 (Cd).

These are significantly higher release fractions of Ba, Te, Ru, Ce, La and Sn than seen in MELCOR analyses of severe accidents in current, conventional LWR plants [8, 9, 10], reflecting the high debris temperatures calculated during in-vessel core degradation (shown in Figures 5.1.4 and 5.1.5 and in Table 5.1.3).

Most of the released radionuclides remain in the primary system and/or the containment; only the noble gases show a significant release to the environment. Of the other radionuclides, 0.15-0.25% of the total CsOH and CsI masses are released to the environment, while $\ll$0.1% of the other radionuclides' initial inventory is released to the environment. Of the species with significant (>80%) release from fuel, the wetwell retains most (50-65%) of the released CsOH, Te and CsI volatiles, while the Ba and Sn aerosols are held up both in the primary system (44%) and in the wetwell (25-35%).

Figures 5.1.27 and 5.1.28 give the retention factors for the various radionuclides calculated by MELCOR, for the primary system and for the overall containment, respectively. The retention factors are defined as the fraction of material released in, or transported into, a region which remains in that region. The vessel retention factors fall into three sets:

- essentially no retention for the noble gases and for I_2 (of which there is very little),

Table 5.1.4. Radionuclide Distribution Predicted at 42hr for LCLP-PF-R-N Sequence

Class	Fission Product Distribution (% Initial Inventory)					
	Remaining in Fuel		Released from Fuel			
	Core	Cavity	Primary System	Drywell	Wetwell	Environment
Noble Gases (Xe)	3.99×10^{-3}	0	0.0911	1.91	7.76×10^{-3}	98.0
Alkali Metals (CsOH)	4.26×10^{-3}	$\simeq$0	20.0	17.4	62.4	0.151
Alkaline Earths (Ba)	4.95×10^{-3}	15.8	44.0	14.1	26.1	0.0120
Halogens (I)	$\simeq$0	$\simeq$0	$\simeq$0	$\simeq$0	$\simeq$0	$\simeq$0
Chalcogens (Te)	4.64×10^{-3}	0.0315	31.7	15.0	53.2	0.0285
Platinoids (Ru)	4.94×10^{-3}	97.0	1.61	1.06	0.367	1.07×10^{-4}
Transition Metals (Mo)	4.94×10^{-3}	97.5	7.47×10^{-3}	1.31	1.17	0.0214
Tetravalents (Ce)	4.94×10^{-3}	96.2	1.99	1.43	0.432	1.23×10^{-4}
Trivalents (La)	4.94×10^{-3}	97.5	9.55×10^{-4}	1.41	1.07	4.25×10^{-3}
Uranium (U)	2.01×10^{-3}	99.9	0.0281	0.0220	0.0106	2.79×10^{-5}
More Volatile Main Group Elements (Cd)	4.94×10^{-3}	$\simeq$100	2.06×10^{-5}	0.0271	0.0215	9.72×10^{-5}
Less Volatile Main Group Elements (Sn)	4.94×10^{-3}	8.43	44.0	13.6	34.0	9.11×10^{-3}
CsI	$\simeq$0	0.0219	16.5	17.6	65.6	0.238

Table 5.1.5. Radionuclide Release and Released Distribution Predicted at 42hr for LCLP-PF-R-N Sequence

Class	Released from Fuel (% Initial Inventory)			Distribution (% Released Mass)			
	Core	Cavity	Total	Primary System	Drywell	Wetwell	Environment
Noble Gases (Xe)	99.97	0.03	$\simeq$100	0.0911	1.91	7.76×10^{-3}	97.99
Alkali Metals (CsOH)	99.87	0.03	99.90	20.05	17.36	62.44	0.151
Alkaline Earths (Ba)	81.50	2.61	84.11	52.30	16.72	30.97	0.0143
Halogens (I)	$\simeq$0	$\simeq$0	$\simeq$0	0.039	2.47	9.38×10^{-3}	97.48
Chalcogens (Te)	99.86	1.59×10^{-3}	99.87	31.72	15.02	53.23	0.0285
Platinoids (Ru)	3.04	2.14×10^{-4}	3.04	52.91	35.00	12.08	3.51×10^{-3}
Transition Metals (Mo)	0	2.51	2.51	0.30	52.19	46.66	0.85
Tetravalents (Ce)	3.84	1.550×10^{-3}	3.85	51.59	37.19	11.22	3.10×10^{-3}
Trivalents (La)	0	2.47	2.47	0.0385	56.76	43.03	0.17
Uranium (U)	0.052	0.010	0.062	46.33	36.21	17.41	0.046
More Volatile Main Group Elements (Cd)	0	0.049	0.049	0.042	55.63	44.24	0.20
Less Volatile Main Group Elements (Sn)	91.36	0.035	91.39	48.04	14.82	37.13	0.010
CsI	99.88	8.92×10^{-3}	99.89	16.54	17.59	65.63	0.238

- a retention of 20-30% for the radionuclide species with non-zero vapor pressures (*i.e.*, CsOH, Te, and CsI), and
- over 50% retention of those classes which form aerosols only.

The containment retention factors fall into several distinct categories also:

- essentially no retention for the noble gases and for I_2 after COPS rupture,
- a retention of 70-80% for the radionuclide species with non-zero vapor pressures (*i.e.*, CsOH, Te, and CsI), and
- for those classes which form aerosols only, there is a ~50% retention for those which had some in-vessel release (Ba, Ru, Ce, U and Sn) and an almost-100% retention of those with only ex-vessel release (Mo, La and Cd).

Figures 5.1.29 and 5.1.30 give the decontamination factors (DFs) for the various radionuclides calculated by MELCOR, for the suppression pool and for the overall containment, respectively. The period of interest in these plots is after about 15hr when the rupture disk is predicted to open and the containment is depressurized. After containment rupture disk actuation, the suppression pool and overall containment DFs are simply DF=1.0 for the noble gases and for I_2 (of which there is very little), not shown explicitly in these figures.

As with the retention factors just discussed, the suppression pool DF seems to fall into several subdivisions:

- $DF_{SP} \sim 50$ for classes with no in-vessel release (*i.e.*, Mo, La and Cd),
- $DF_{SP} \leq 100$ for classes with $\ll 1\%$ in-vessel release (U),
- $DF_{SP} \geq 500$ for the majority of classes (CsOH, Ba, Ru, Ce and CsI), and
- $DF_{SP} \geq 1000$ for Class 5 (Te) and Class 12 (Sn).

The latter two classes have very large in-vessel releases, as do some of the classes with $DF_{SP} \sim 500$. The overall containment DF also seems to fall into several, quite different subdivisions:

- $DF_{Cont} \sim 500$ for classes with no in-vessel release (*i.e.*, Mo, La and Cd) and for some of the volatiles (CsOH and CsI),
- $DF_{Cont} \geq 1000$ for classes with $\ll 1\%$ in-vessel release (U),
- DF_{Cont}=2000-5000 for several classes (Ba, Te and Sn), and
- $DF_{Cont} \geq 10{,}000$ for Class 6 (Ru) and Class 8 (Ce).

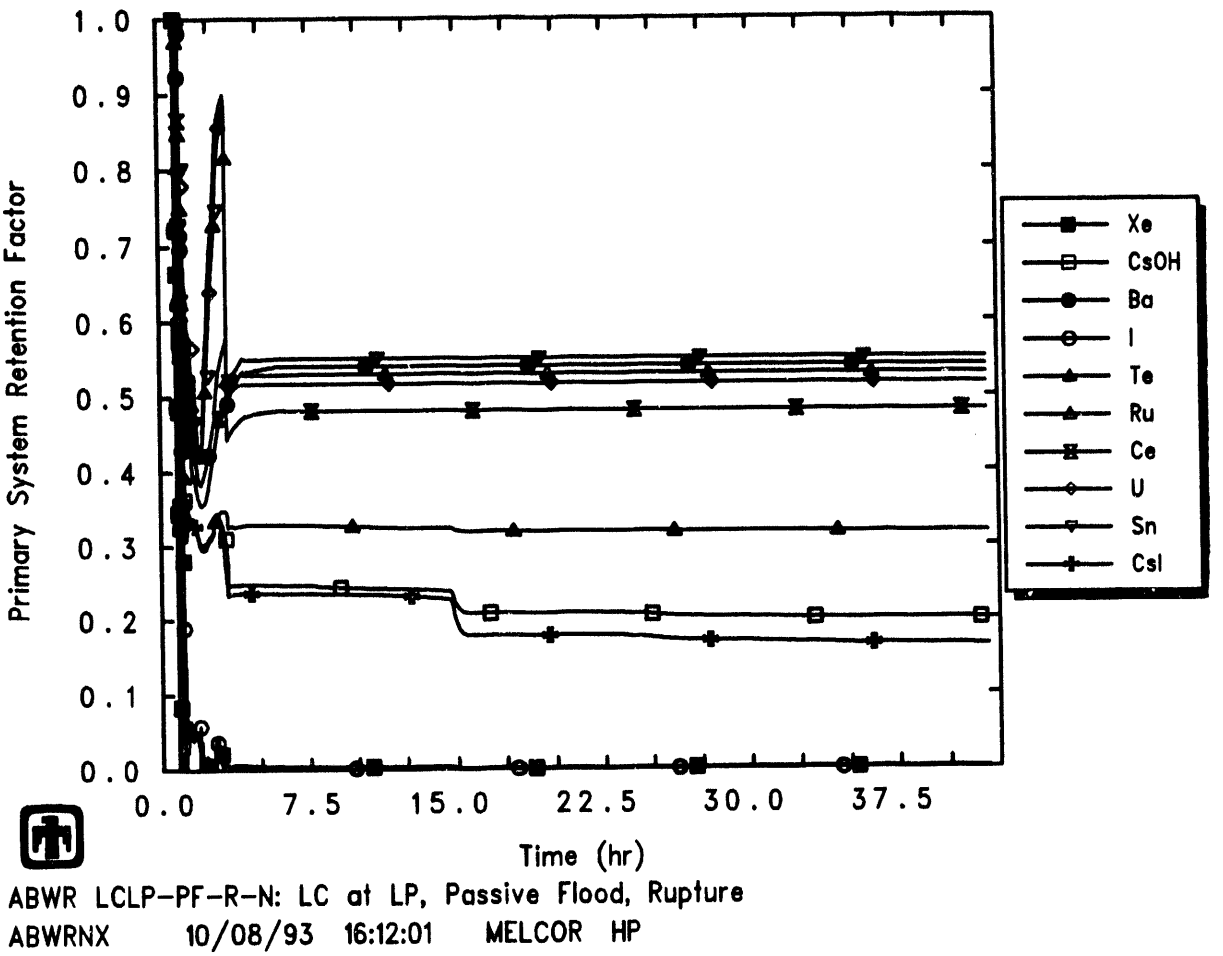

Figure 5.1.27. Primary System Retention Factors Predicted by MELCOR for LCLP-PF-R-N Sequence

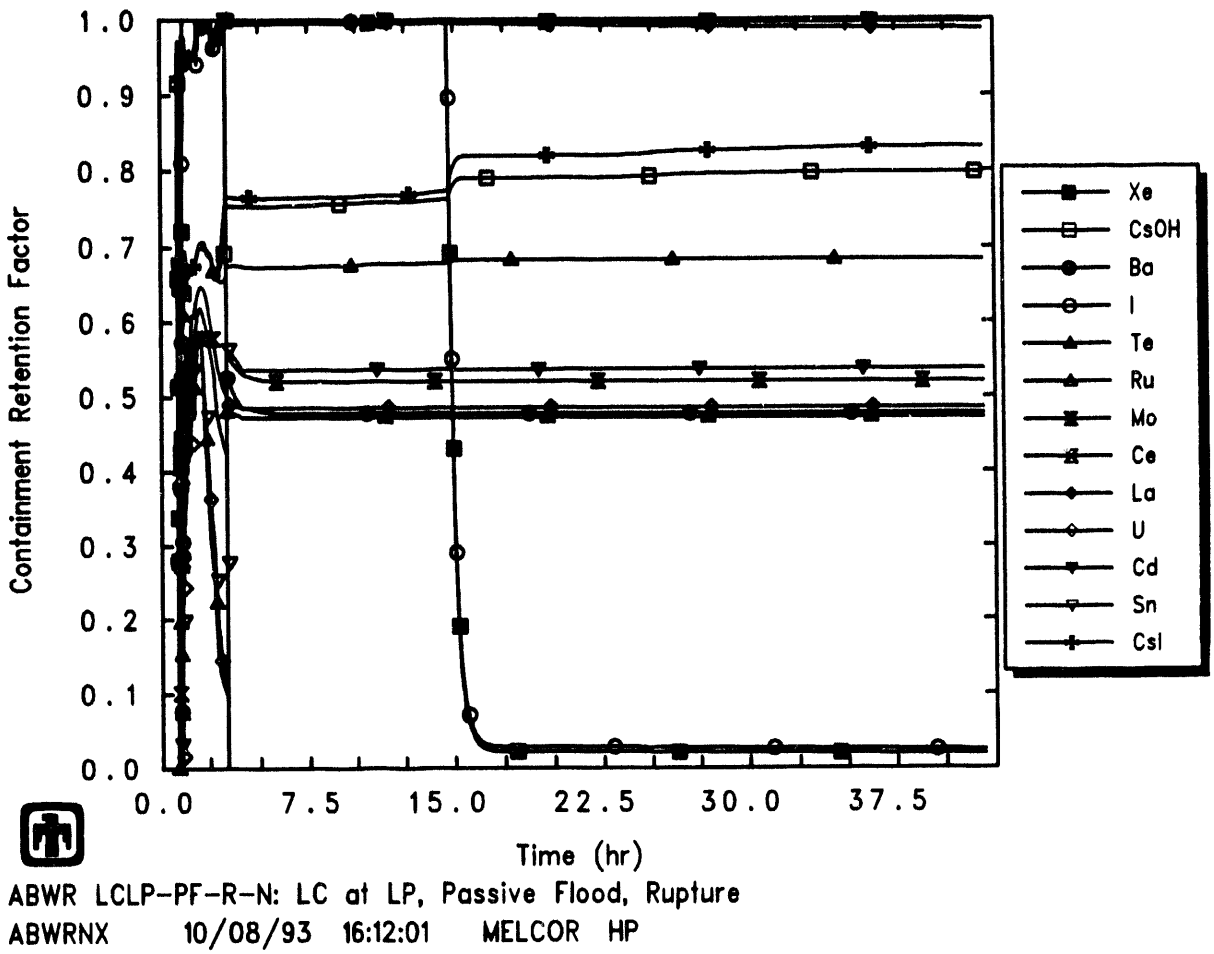

Figure 5.1.28. Containment Retention Factors Predicted by MELCOR for LCLP-PF-R-N Sequence

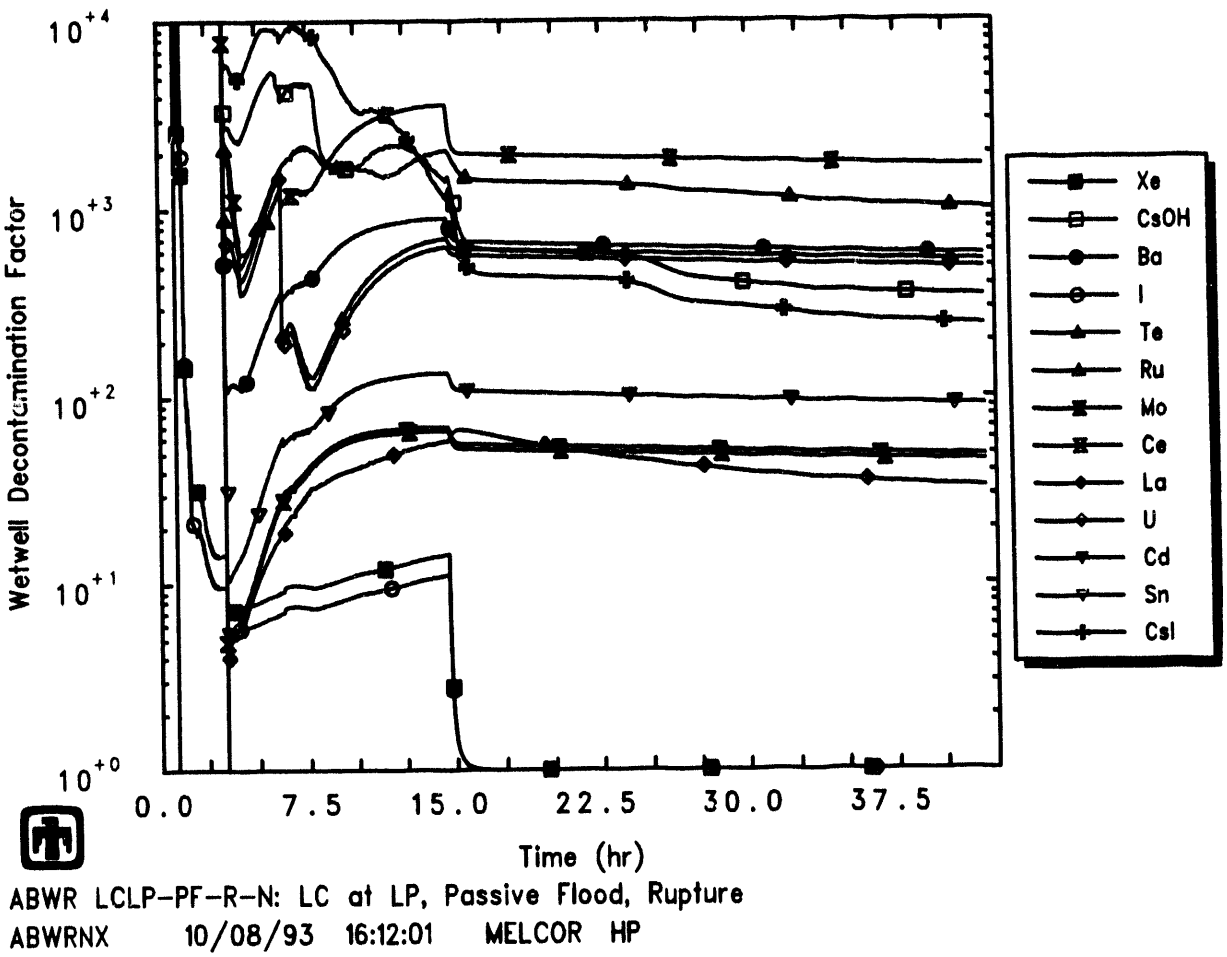

Figure 5.1.29. Suppression Pool Decontamination Factors Predicted by MELCOR for LCLP-PF-R-N Sequence

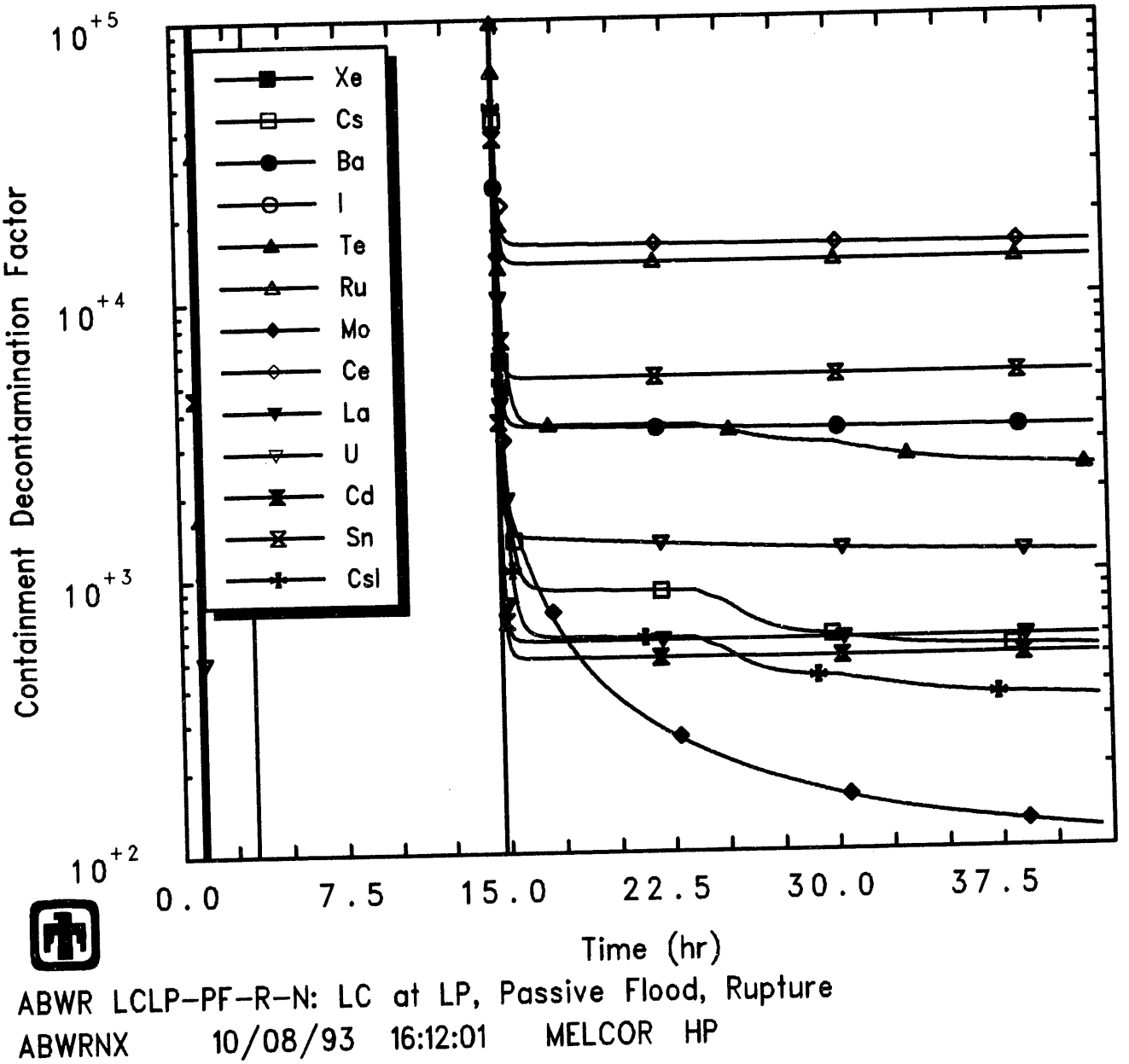

Figure 5.1.30. Overall Containment Decontamination Factors Predicted by MELCOR for LCLP-PF-R-N Sequence

The latter two classes have very small ex-vessel releases, but so do several of the other classes.

Note that both the suppression pool and overall containment decontamination factors remain nearly constant or drop very slowly for most classes after containment rupture disk actuation, but drop steadily for several radionuclide species (*i.e.*, CsOH, Te, Mo and CsI). These are the classes for which a continuing release to the environment is predicted, while for the other classes there is only a single step-like release at COPS rupture, as illustrated in Figure 5.1.31. That continuing release comes from two different causes. The non-zero vapor pressure of CsOH, Te and CsI causes continuous vaporization from the suppression pool and replenishment of these fission product vapors in the wetwell atmosphere as those fission product vapors in the wetwell atmosphere are lost out the COPS rupture. Class 7 (Mo) has no non-zero vapor pressure and therefore remains an aerosol throughout the problem. However, this class is the only one with substantial and continuing radionuclide release in the cavity, and a small fraction of that continuing release (most of which remains in the cavity and/or suppression pools) does survive pool scrubbing and get released to the wetwell atmosphere and then out the containment rupture disk to the environment.

Figure 5.1.31 does not include the release of the noble gases, to allow expansion of the scale for the environmental release of the other radionuclide classes. In the MAAP analysis, the release of noble gases is nearly complete one hour after the rupture disk opens (Figure 19E.2-2G in [1]; the release of the noble gases in the MELCOR calculation also occurs within a brief time after containment rupture disk actuation, and almost all of the noble gases are released. Figure 19.E.2-2H in [1] gives the release fractions of cesium iodide and cesium hydroxide as functions of time from the MAAP analysis. The release of the volatile species, CsI and CsOH, occurs over a much longer period of time than for the noble gases and is nearly complete at 100hr; the release fractions of CsOH and CsI at 72hr are less than 10^{-7}. It is not clear from Figure 19E.2-2H in [1] whether the release fractions of CsOH and CsI were normalized to their initial inventories or to their released inventories. This MELCOR calculation shows environment release fractions for both CsOH and CsI by the end of the calculation (42hr) of about 0.002 of their total available inventory (Table 5.1.4; since almost all of these radionuclides were predicted to be released, the same environment release fractions are obtained normalizing to released inventories (Table 5.1.5). The release fractions calculated by MELCOR are significantly higher than the values predicted by MAAP, primarily due to the continuing steaming of cavity water by non-quenched debris in MELCOR; however, the MELCOR release fractions are still very small fractions of the fission product inventories initially present, released but retained within containment even after containment rupture disk actuation.

5.2 LCLP-FS-R-N Sequence

The first part of this sequence, through core uncovery, heatup and degradation, and vessel lower head failure, is identical to the LCLP-PF-R-N sequence discussed in Section 5.1. The difference is that the firewater system is used in spray mode to add ex-

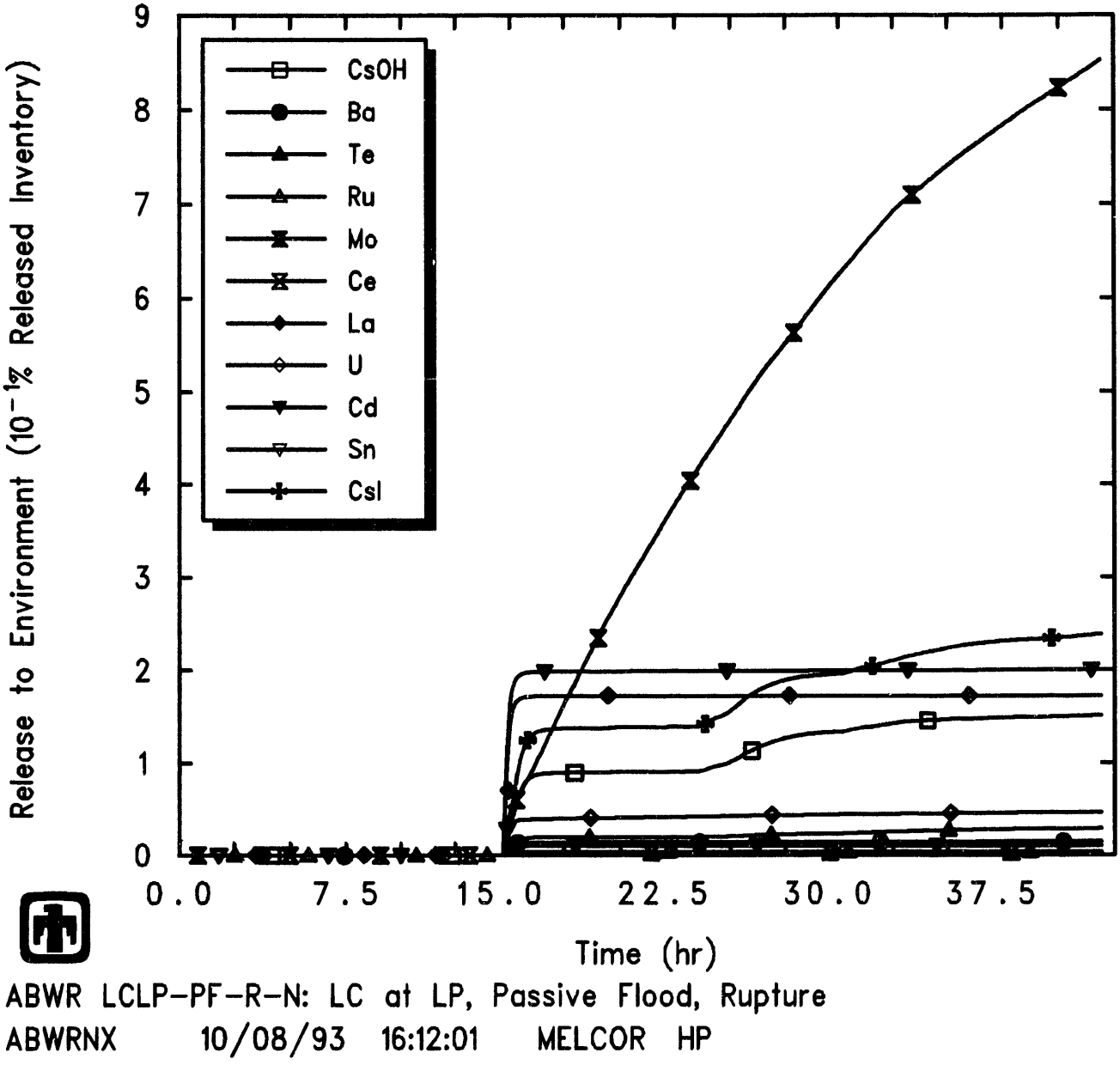

Figure 5.1.31. Radionuclide Environmental Releases Predicted by MELCOR for LCLP-PF-R-N Sequence

ternal water to the containment. The firewater system adds water to the containment through the RHR injection lines. When trying to prevent vessel failure the operator is instructed to inject water to the vessel via the LPFL line. If this is not accomplished in time to prevent vessel failure, the valves are realigned to the drywell spray. The water then pours from the upper drywell into the wetwell via the wetwell/drywell connecting vents, and eventually overflows into the lower drywell. This cools the corium, preventing core-concrete attack and additional metal-water reaction. Since external water is used, the effective heat capacity of the containment is increased. Furthermore, since the decay heat in the corium is delivered by convection to the water, no significant radiation heat transfer takes place, and the lower and upper drywell atmospheres remain cool. Therefore, no degradation of the movable penetration seals is expected, and no leakage through those seals will occur.

The sequence of events predicted by MELCOR for this accident sequence is given in Table 5.2.1, with the timings of the various events as calculated by MAAP (taken from Table 19E.2-6 in [1]) included for comparison.

Before the spray system begins injection, the results of this sequence are identical to those for the LCLP-PF-R-N sequence discussed in Section 5.1. In the MAAP analysis of this sequence, it was assumed that the operator starts the firewater system 4hr after the initiation of the event (as stated in Section 19E.2.2.1(b) and Table 19E.2-6, but with no indication of whether this was a set time or determined by conditions in the plant) and the operator turns off the firewater system when the water level in the suppression pool reaches the elevation of the bottom of the vessel, which occurs in the MAAP calculation at 23.6hr. In the MELCOR calculation, the firewater spray was assumed to turn and/or stay on if:

1. the lower drywell temperature exceeds 500K (first time only), or
2. the upper drywell temperature exceeds 500K, or
3. the spray has been on less than 15min, or
4. the sprays are on and the suppression pool level has never reached the elevation of the bottom of the reactor vessel.

This is the logic in the MELCOR ABWR deck as received from BNL and used for LCHP-PF-D-H sequence analyses in 1990 [3]. The spray thus begins on a high-temperature trip, stays on at least 15min, and then turns off when the suppression pool level reaches the elevation of the bottom of the reactor vessel. This logic caused the spray in the MELCOR calculation to begin injection at 6.1hr (and stop at 18.5hr).

Another difference between the MAAP and MELCOR predictions for this sequence can be seen in Table 5.2.1. In the MELCOR calculation, the lower drywell temperature hits the 500K spray initiation setpoint at 21,942.4s (6.10hr) and the 533K passive-flooder setpoint very soon afterwards, at 21,976.4s (6.10hr); the spray later turns off, followed by containment rupture disk actuation still later. In the MAAP analysis, the sprays begin

Table 5.2.1. Sequence of Events Predicted by MELCOR for LCLP-FS-R-N Sequence, Compared to MAAP

Event	Time	
	MAAP	MELCOR
Accident initiation (MSIV Closure)	0.0	0.0
Reactor scrammed	4.2s	
Core uncovery begins		1,629.1s (0.45hr)
Water level at 2/3 core height; 1 SRV open	0.4hr	2,355.9s (0.65hr)
Clad failure/Gap release		
(Ring 1)		2,985.9s (0.83hr)
(Ring 2)		3,825.9s (1.06hr)
(Ring 3)		4,513.3s (1.25hr)
(Ring 4)		6,688.4s (1.86hr)
Core plate failed		
(Ring 1)		12,257.1s (3.40hr)
(Ring 2)		13,580.5s (3.77hr)
(Ring 3)		16,928.4s (4.70hr)
(Ring 4)		20,436.4s (5.68hr)
Vessel bottom head failed	1.8hr	
Vessel LH penetration failed		
(Ring 1)		12,351.5s (3.43hr)
(Ring 2)		12,351.5s (3.43hr)
(Ring 3)		12,348.5s (3.43hr)
(Ring 4)		12,348.5s (3.43hr)
Commence debris ejection		12,348.5s (3.43hr)
Water in lower drywell boiled off	2.7hr	~22,000s (6.1hr)
Firewater spray started	4.0hr	21,942.4s (6.10hr)
Suppression pool overflows to lower drywell	7.0hr	
Firewater spray stopped	23.6hr	66,584.7s (18.50hr)
Passive flooder opens	61.1hr	21,976.4s (6.10hr)
Rupture disk opens	31.1hr	89,922.6s (24.98hr)
Water in lower drywell boiled off	56.6hr	
Concrete ablation $\geq$2m		156,454s (43.46hr)
End of calculation	100hr	156,454s (43.46hr)

at 4hr but the passive flooder does not open until 61.1hr, after the firewater spray has stopped, the containment rupture disk opened, and the cavity dried out. Thus, not only are the timings of events different, the relative ordering of events is different.

Figure 5.2.1 shows the collapsed liquid level in the lower drywell (cavity) control volume in the MELCOR calculation, for comparison to the LCLP-PF-R-N sequence results given in Figure 5.1.14. The sudden rise in liquid level at 3.3hr corresponds to the remaining lower plenum water pouring out the vessel breach. That water is then steadily boiled away over the next 3hr until the cavity becomes dry, at about 6.1hr after accident start. As soon as the cavity goes dry, the lower drywell atmosphere temperature rises rapidly due to heat transfer from the unquenched debris and very quickly reaches hits the 500K spray initiation setpoint and the 533K passive-flooder setpoint very soon afterwards. Water then pours from the wetwell into the drywell to the level of the upper horizontal vent. The cavity liquid level then oscillates for the remainder of the transient.

Figure 5.2.2 give the drywell and wetwell pool masses for the MELCOR analysis, compared to the pool masses calculated by MAAP (taken from Figure 19E.2-3C in [1]). There appears to be a small difference in the suppression pool initial mass (and/or level) in the two calculations, and MELCOR predicts a bigger short-term drop in suppression pool level and corresponding rise in cavity pool level upon opening the passive flooder. However, the results are generally in good qualitative agreement, with both codes showing a long-term rise in suppression pool level due to firewater spray injection), followed by a gradual drop in suppression pool level. The lower drywell pool masses predicted by both codes are also in good overall qualitative agreement, although driven by different behavior. The lower drywell pool mass in the MAAP analysis initially rises at about 7hr because the suppression pool level has increased enough to overflow to the lower drywell; the lower drywell pool mass in the MELCOR analysis initially rises at about 6hr because the passive flooder opens. The lower drywell pool mass then remains similar in both calculations as water continues to be transferred from the suppression pool to the lower drywell where it is boiled away by the core debris in the cavity. The lower drywell mass predicted by both codes then drops after the spray is stopped, at 18.5hr in the MELCOR analysis and at 23.6hr in the MAAP analysis; the cavity pool mass drops more quickly in the MELCOR analysis than in the MAAP analysis due to more heat transfer from the unquenched cavity debris.

The lower drywell and wetwell atmosphere and pool temperatures are presented in Figure 5.2.3. The hot debris in the cavity in the MELCOR calculation keeps the lower drywell pool temperature (~400K) substantially hotter than the suppression pool temperature (~350K), both while the cavity has residual lower plenum water in it and after the passive flooder opens and the cavity is flooded with suppression pool water; the difference in pool temperature decreases after the containment rupture disk opens and the containment depressurizes as the wetwell pool heats up slightly. The wetwell atmosphere temperature follows the suppression pool temperature closely throughout this sequence. The cavity atmosphere remains significantly hotter than the cavity pool throughout the transient, even after containment rupture disk actuation (and hotter than the upper drywell, as illustrated in Figure 5.2.5).

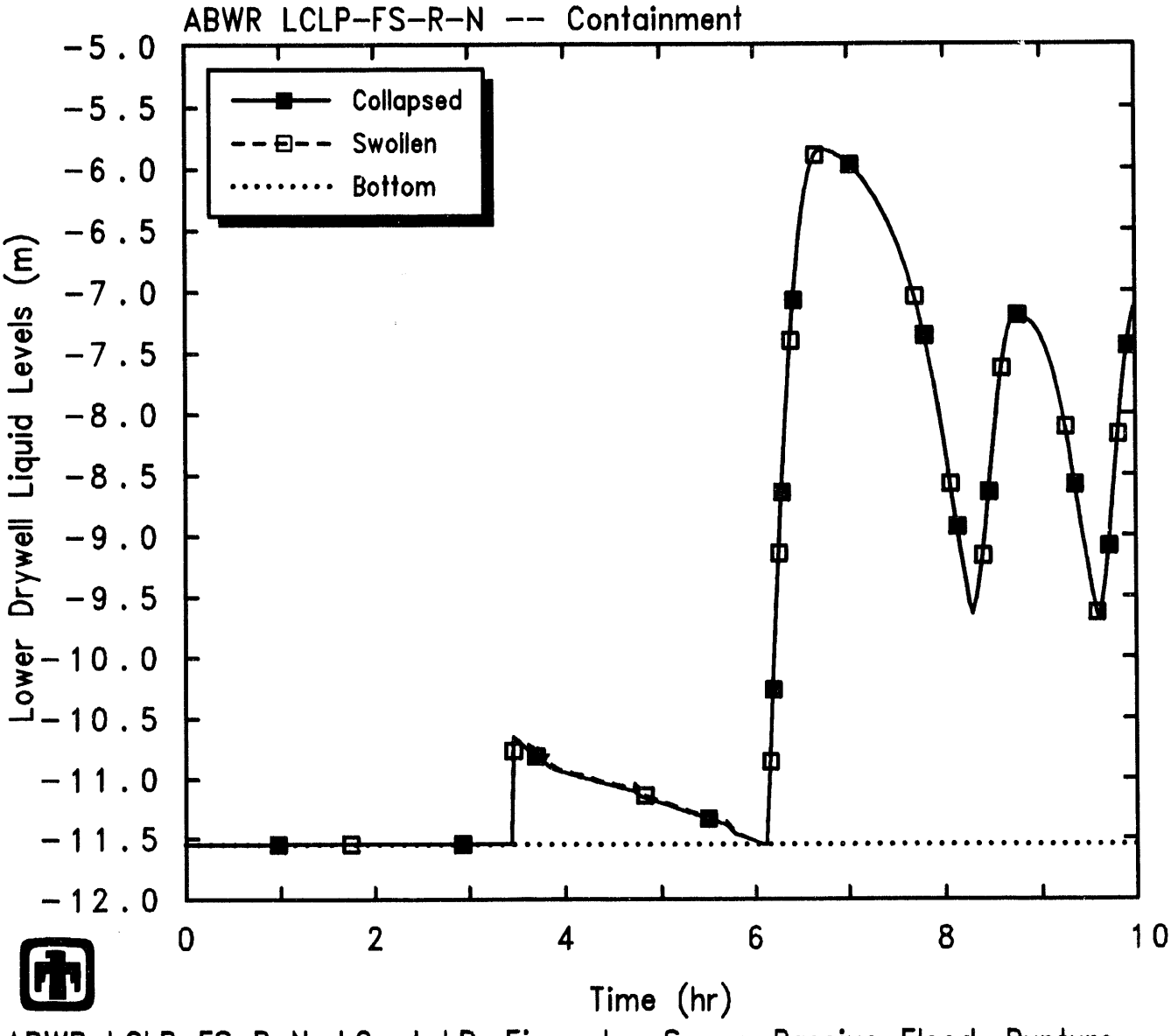

Figure 5.2.1. Lower Drywell Liquid Level Predicted by MELCOR for LCLP-FS-R-N Sequence

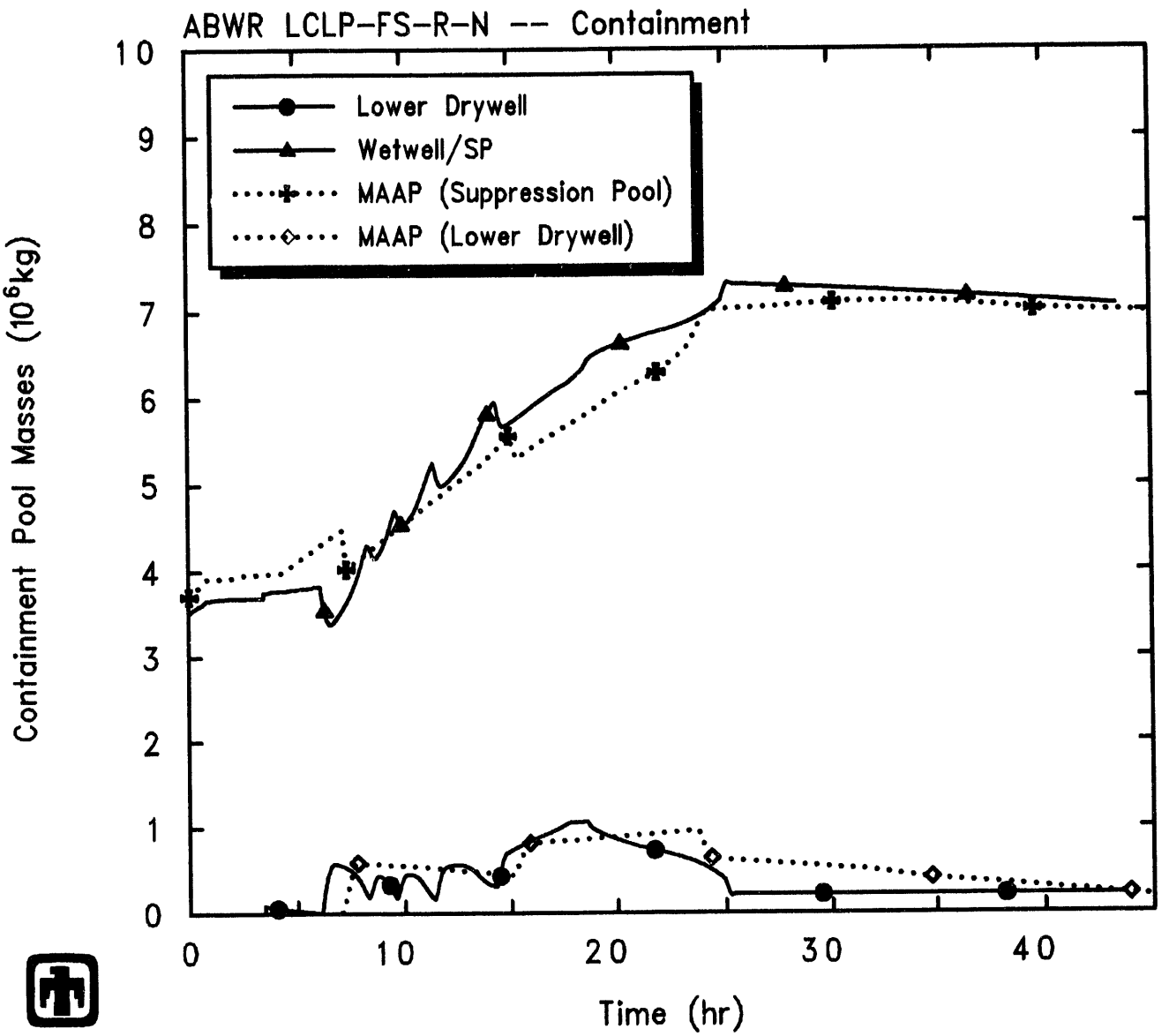

Figure 5.2.2. Lower Drywell and Suppression Pool Masses Predicted by MELCOR for LCLP-FS-R-N Sequence, Compared to MAAP

The pressures calculated by MELCOR in the various containment control volumes are depicted in Figure 5.2.4, together with the containment pressure from the MAAP analysis (taken from Figure 19E.2-3A in [1]). The results from the two codes are generally similar qualitatively, but with a number of quantitative differences and shifts in timing. Both codes predict a rapid pressure increase in containment immediately after vessel failure, due to steam generation from hot debris and water falling into the cavity from the lower plenum. In the MAAP containment pressure history, after the water in the lower drywell boils off, the drywell pressure decreases because steam is condensed on the containment heat sinks but there is no additional steam generated; in the MELCOR calculation, the containment pressure continues to rise as hot, unquenched core debris continues to boil off the cavity water pool.

When the firewater system starts, a pressure spike is observed in the drywell pressure in the MAAP calculation, which is caused by the evaporation of droplets in a superheated atmosphere; after the containment atmosphere is cooled, the pressure drops fairly rapidly to match the droplet temperature. In the MAAP analysis, the suppression pool overflows into the lower drywell at about 7hr, after which the containment repressurizes slowly due to compression of the noncondensable gases above the increasing water pools in both the wetwell and lower drywell; Figure 19E.2-3A indicates that the pressure drop in the MAAP calculation at about 15hr is due to the lower drywell reflooding. The MELCOR calculation shows the containment pressure dropping rapidly immediately after the firewater spray is started (and the passive flooder opens), as the spray condenses steam in the upper drywell, followed by an oscillatory pressurization as the hot core debris in the cavity continues to boil off the lower drywell water pool and as upper drywell draining condenses steam intermittently in the DW/WW vents and the wetwell vapor space.

In both calculations, after the firewater spray is turned off (at 23.6hr in the MAAP analysis and at 18.5hr in the MELCOR calculation), the pressures continue to increase as steam is generated by corium in the lower drywell, until the containment rupture disk opening setpoint is reached (at about 31hr in the MAAP analysis and about 25hr in the MELCOR calculation), after which the containment depressurizes.

Figure 5.2.5 gives the upper and lower drywell temperatures calculated by MELCOR, compared to corresponding MAAP results. (The MAAP curves included in this plot were taken from Figure 19E.2-3B in [1].) In the MELCOR calculation, the lower drywell temperature spikes up when debris first falls into the cavity at 3.3hr but then remains nearly constant during the next 3hr while the water fallen into the cavity is being boiled away; the temperature spike triggering the spray initiation and passive flooder opening can be seen at ~6.1hr, together with the subsequent drop in liquid temperature. The upper drywell temperature in the MELCOR calculation is kept low (305-325K) while spray injection is on, slightly above the 300K temperature specified for the spray injection. After the spray injection is stopped, the upper drywell temperature increases to nearly equal the lower drywell temperature. However, except at the very end of the transient period calculated, the upper drywell temperature predicted by MELCOR remains below the lower drywell temperature. The MAAP calculation also shows the upper drywell

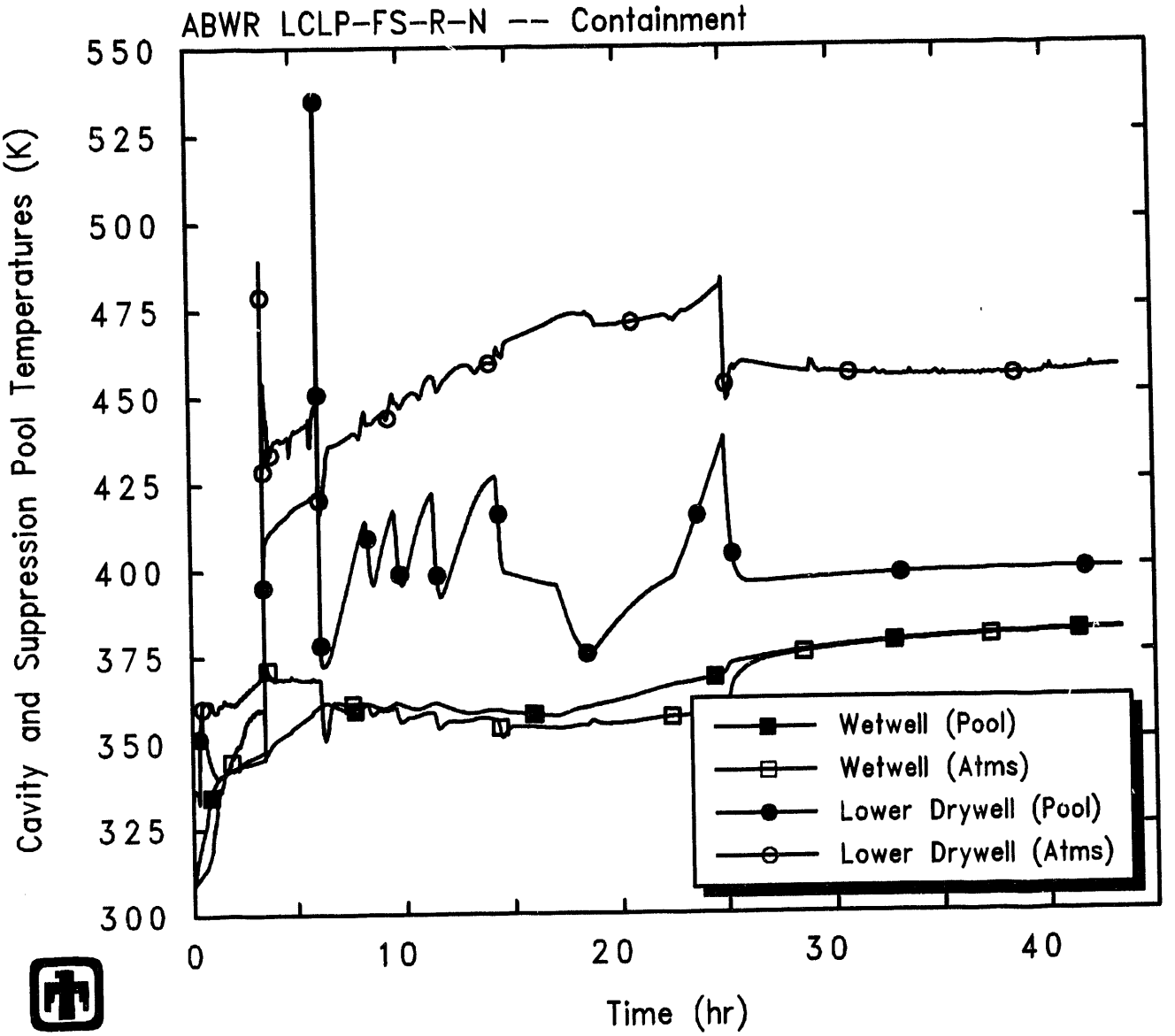

Figure 5.2.3. Lower Drywell and Suppression Pool Temperatures Predicted by MELCOR for LCLP-FS-R-N Sequence

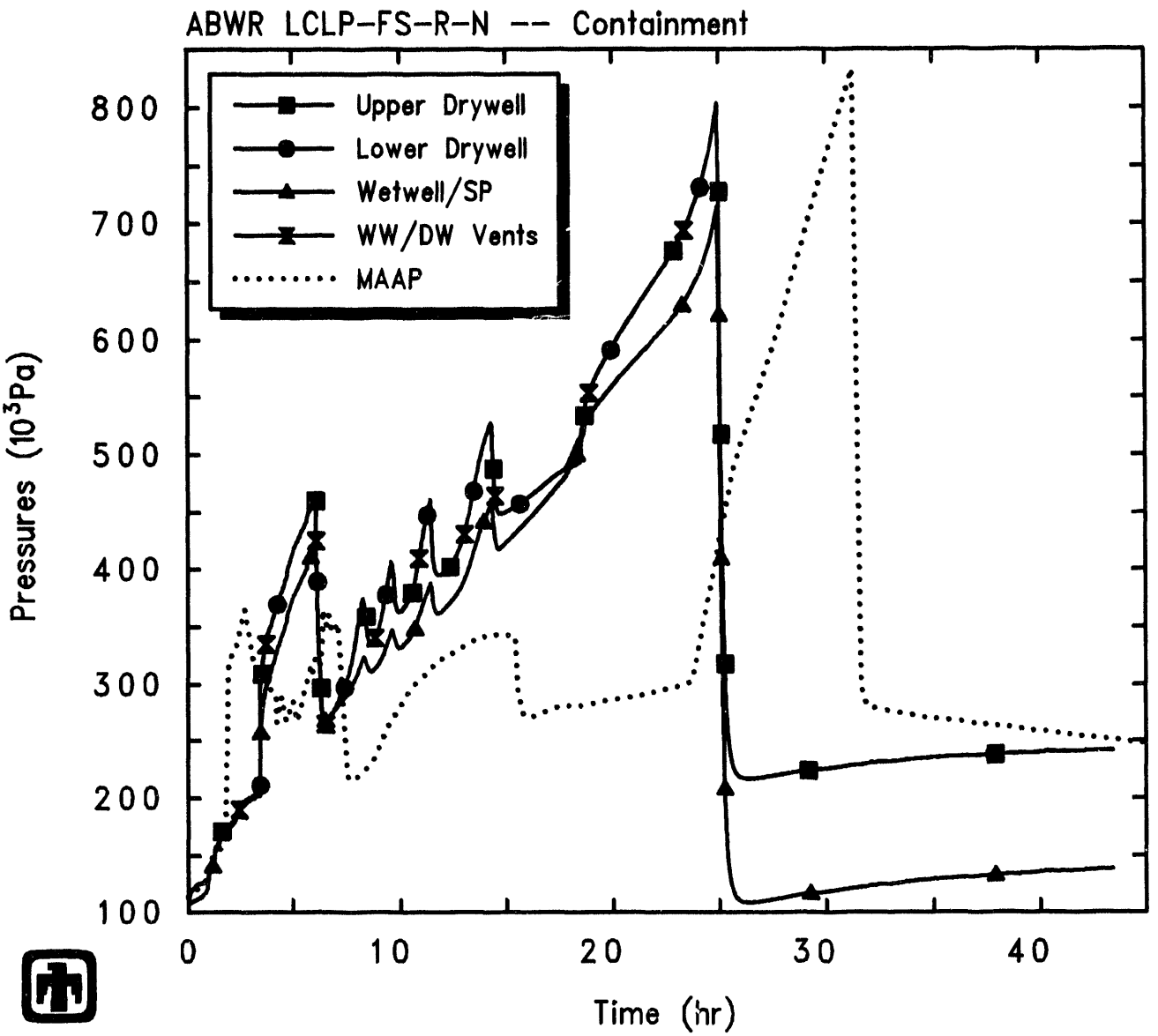

Figure 5.2.4. Containment Pressures Predicted by MELCOR for LCLP-FS-R-N Sequence, Compared to MAAP

cooler than the lower drywell while the firewater spray injection is activated, but with a much smaller temperature difference during spray injection and with the upper drywell then hotter than the lower drywell for the remainder of the transient calculated.

Figures 5.2.6 and 5.2.7 show the total and partial pressures, and the mole fractions, respectively, in the atmospheres of the four control volumes representing containment (*i.e.*, upper and lower drywell, wetwell and drywell/wetwell vents). The predicted conditions are somewhat different from those calculated for the LCLP-PF-R-N sequence (Figures 5.1.19 and 5.1.20). As in the LCLP-PF-R-N sequence results, the lower drywell and DW/WW vent atmospheres consist of almost all (>90%) steam from vessel failure at 3.3hr through spray initiation at 6hr, and later from containment rupture disk actuation at 25hr through calculation end. However, after spray injection begins at 6hr, there is first a series of oscillations with steam concentration dropping due to condensation (while hydrogen concentration rises), followed after about 14hr by a prolonged drop in steam concentration and increase in hydrogen concentration until COPS rupture at about 25hr. These oscillations in steam concentration and partial pressure cause the oscillations in overall containment pressures and temperatures shown in Figures 5.2.4 and 5.2.5.

In the upper drywell, steam begins accumulating after vessel failure at 3.3hr but that steam is effectively condensed and removed by the firewater spray from spray initiation after about 6hr until after spray injection was calculated to stop at 18.5hr; most ($\sim$60%) of the upper drywell atmosphere consists of hydrogen after spray initiation. Even after spray is stopped, the steam concentration builds up again quite slowly. The response of the wetwell vapor space is similar to that predicted for the LCLP-PF-R-N sequence: steam does not predominate until after containment rupture disk opening at 25hr, while most (50-60%) of the wetwell atmosphere between vessel failure and containment depressurization is hydrogen.

The containment continues to pressurize until the wetwell pressure reaches 0.72MPa (90psig) at 31.1hr in the MAAP analysis and at 25hr in the MELCOR calculation, when the rupture disk opens as shown in Figures 5.1.17. The flow out the COPS rupture disk in the MELCOR calculation is presented in Figure 5.2.8. No penetration leakage is predicted by either MAAP or MELCOR, since the temperature in the upper drywell remains below 533K (500°F) until well after the rupture disk opens (as illustrated in Figure 5.2.5).

The total mass of debris in the cavity, the mass of ejected core debris, the mass of ablated concrete and the mass of gases generated in the cavity calculated by MELCOR are illustrated in Figure 5.2.9. The mass of core debris in the cavity for this sequence is very similar to the results for the LCLP-PF-R-N sequence; both are basically an inversion of the masses retained in-vessel, presented in Figure 5.1.12. The debris ejection from the vessel can be seen to occur in discrete steps or stages, while the concrete mass ablated increases continuously with time; the mass of concrete ablated and the rate at which it is ablated predicted by MELCOR for the LCLP-FS-R-N sequence is quite similar to the LCLP-PF-R-N results calculated by MELCOR and given in Figure 5.1.22.

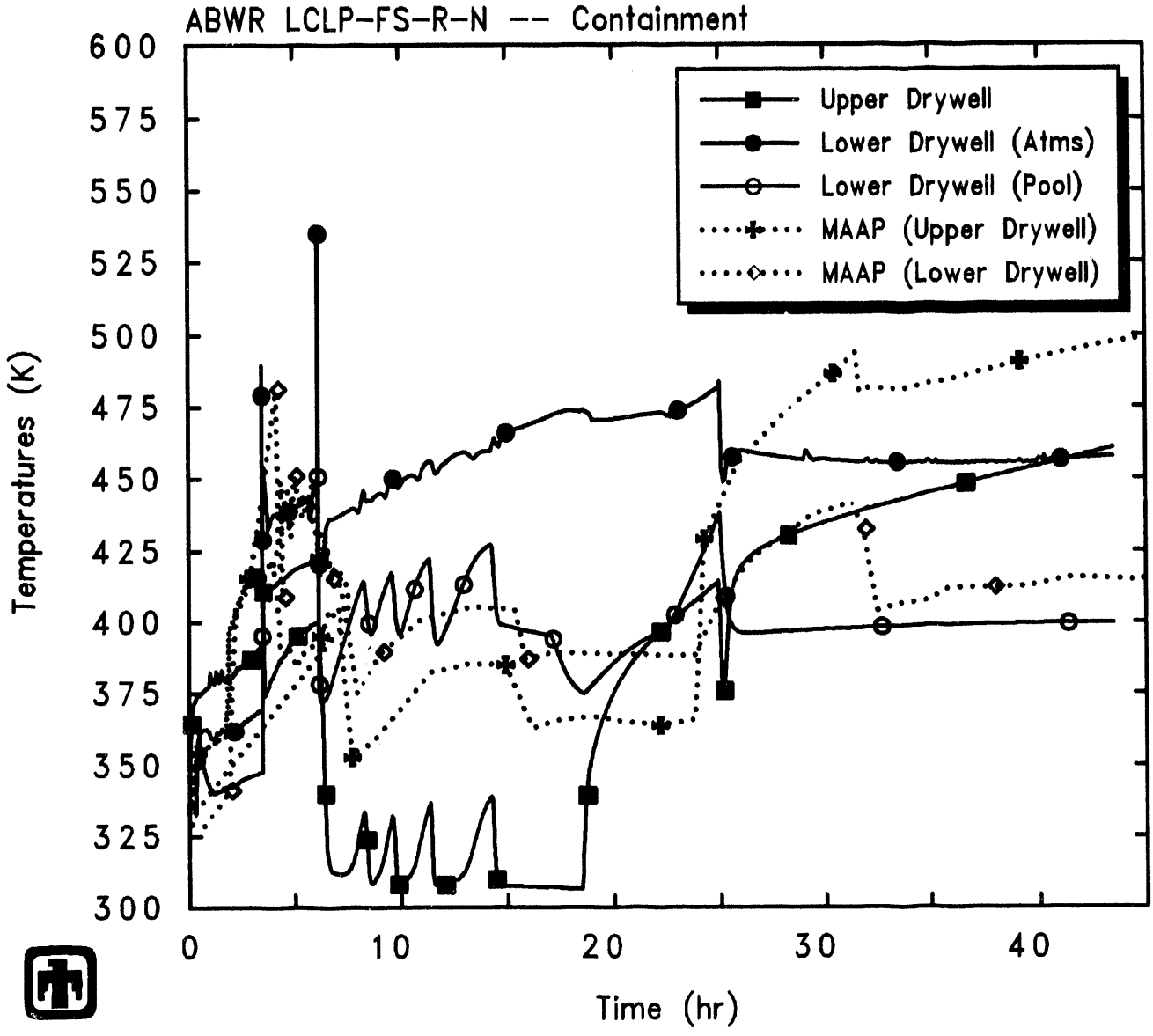

Figure 5.2.5. Containment Temperatures Predicted by MELCOR for LCLP-FS-R-N Sequence, Compared to MAAP

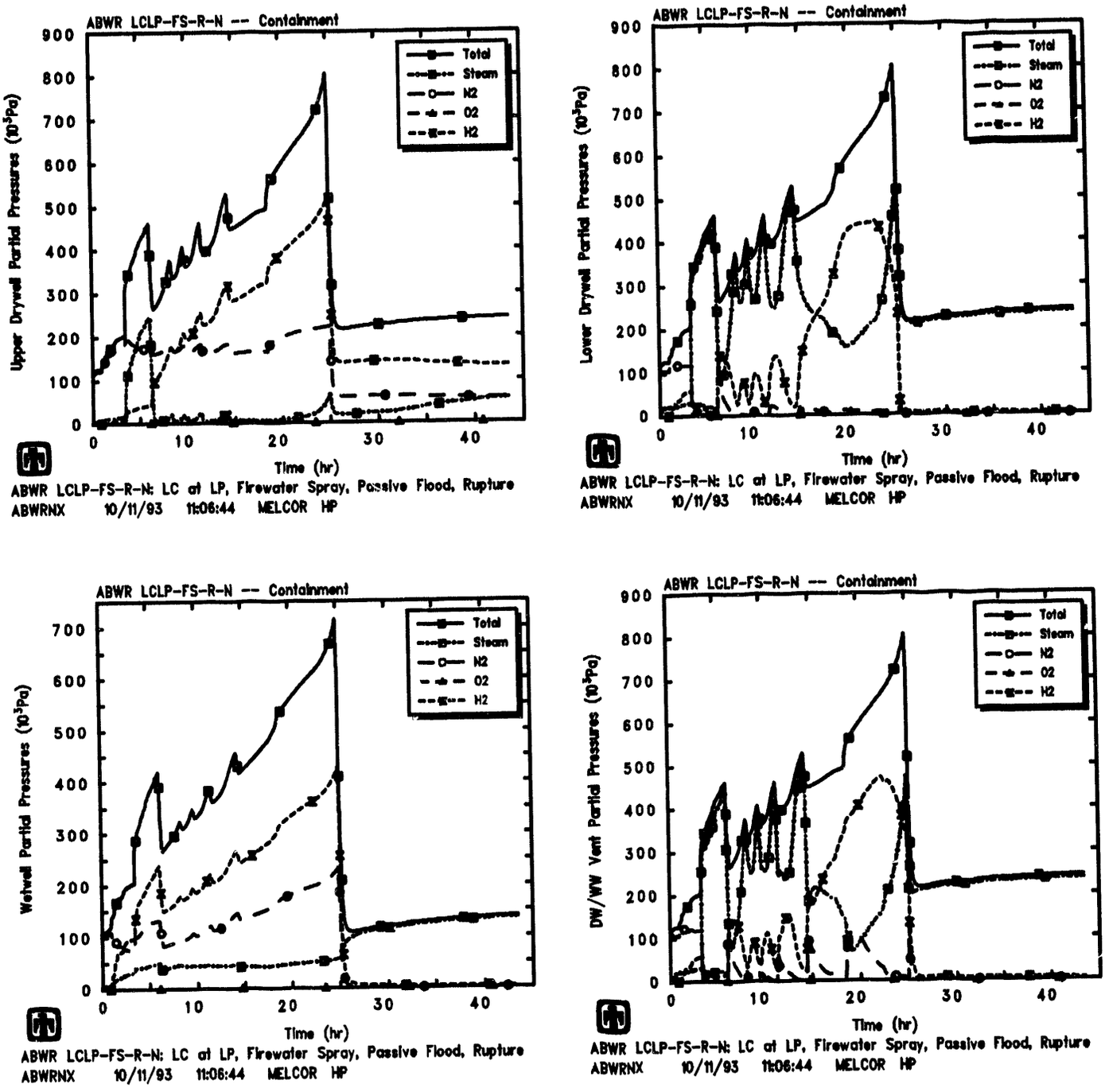

Figure 5.2.6. Containment Upper Drywell (upper left), Lower Drywell (upper right), Wetwell (lower left) and DW/WW Vent (lower right) Partial Pressures Predicted by MELCOR for LCLP-FS-R-N Sequence

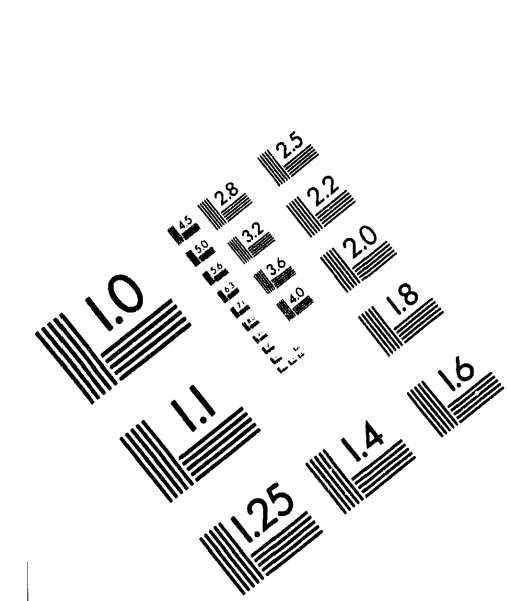

Association for Information and Image Management

1100 Wayne Avenue, Suite 1100
Silver Spring, Maryland 20910

301/587-8202

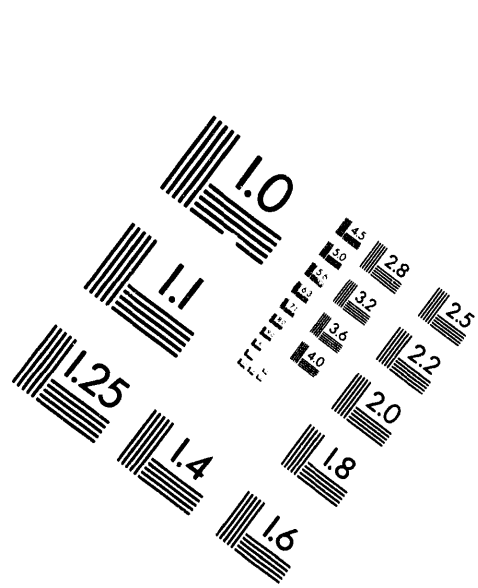

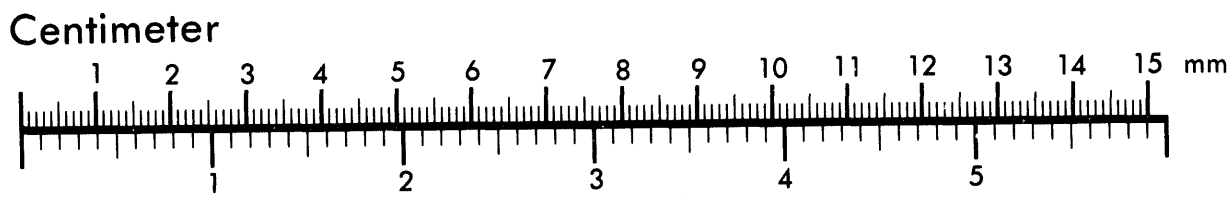

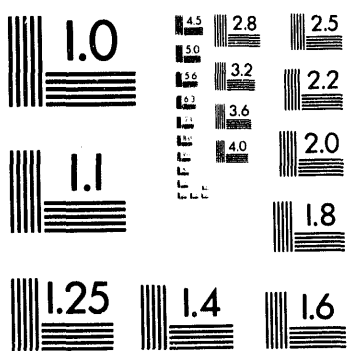

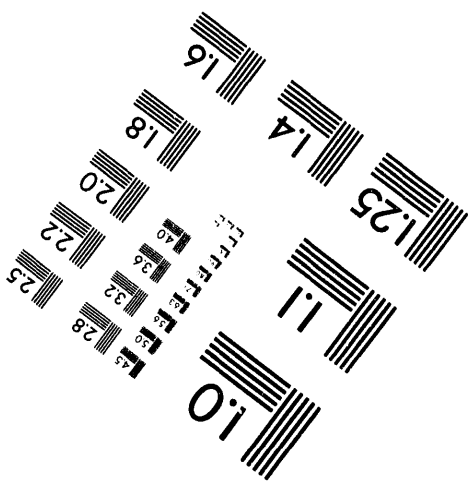

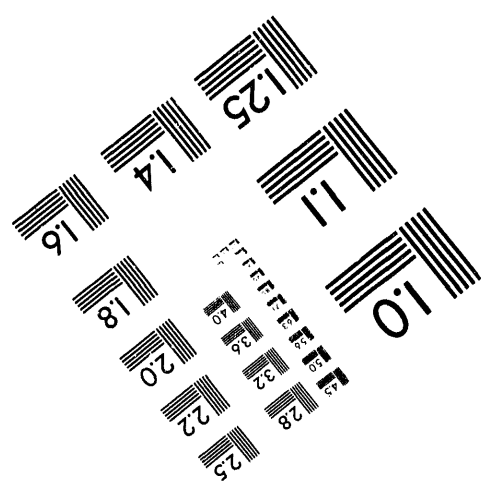

MANUFACTURED TO AIIM STANDARDS
BY APPLIED IMAGE, INC.

2 of 3

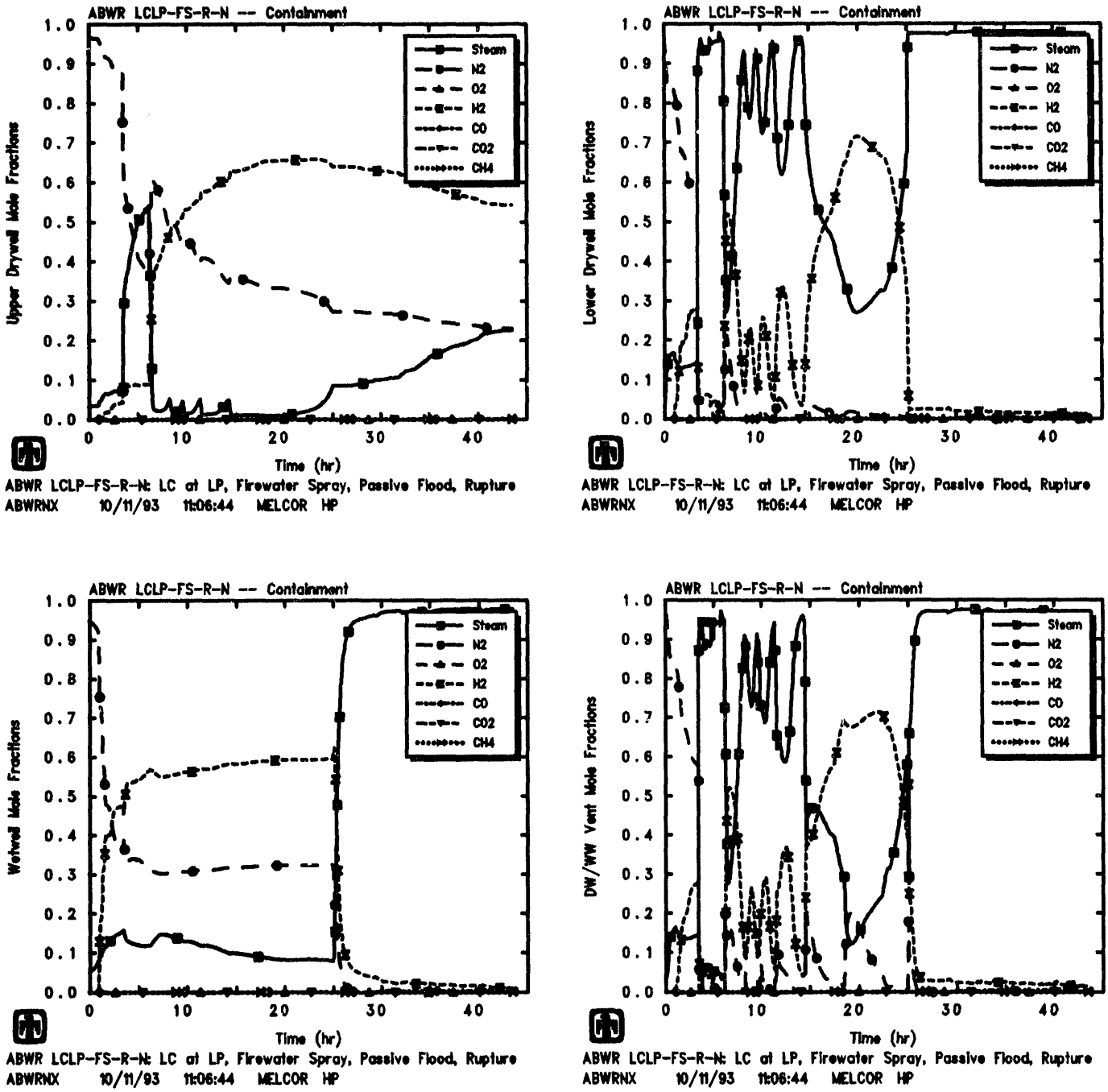

Figure 5.2.7. Containment Upper Drywell (upper left), Lower Drywell (upper right), Wetwell (lower left) and DW/WW Vent (lower right) Mole Fractions Predicted by MELCOR for LCLP-FS-R-N Sequence

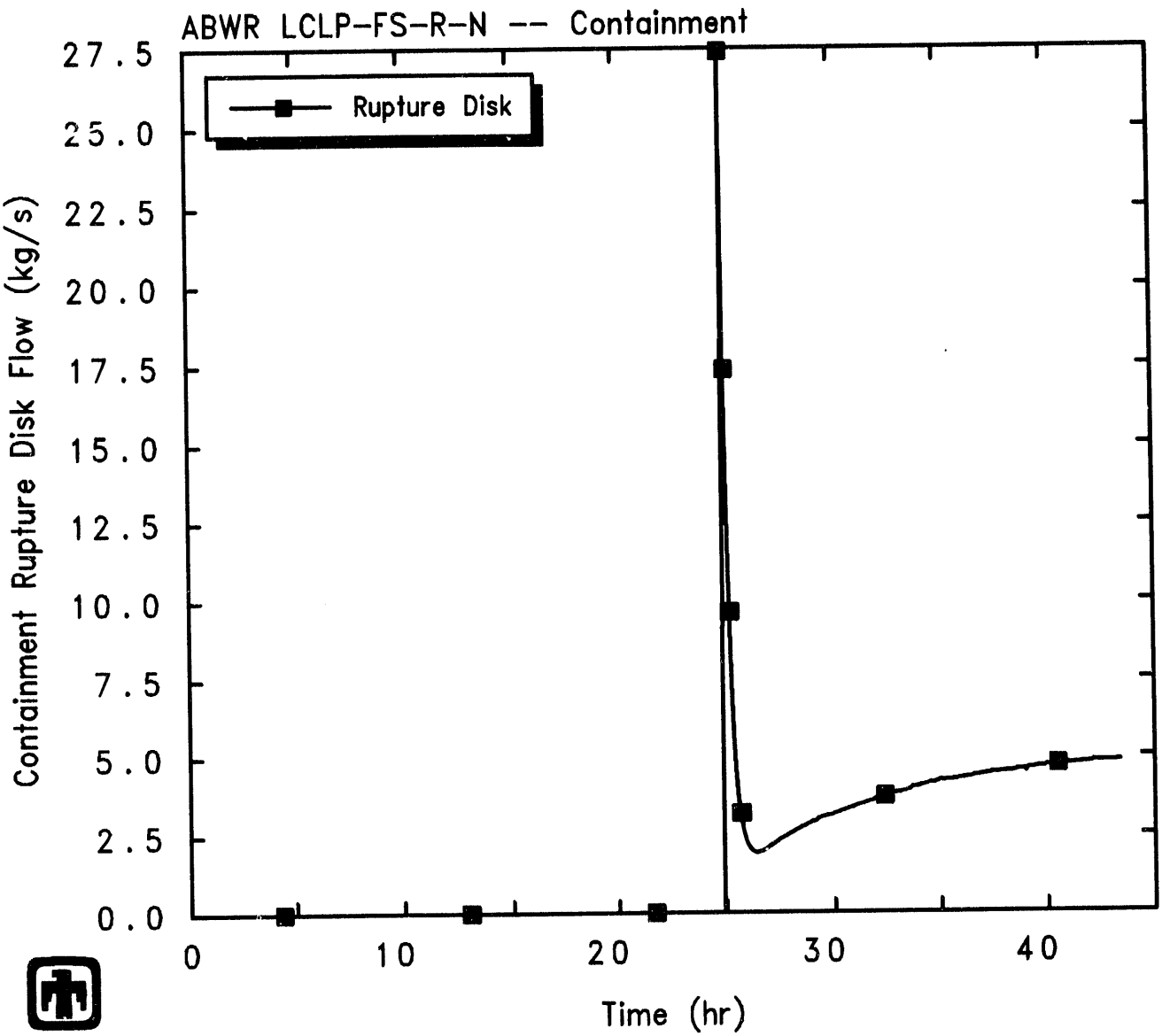

Figure 5.2.8. COPS Rupture Disk Mass Flow Predicted by MELCOR for LCLP-FS-R-N Sequence

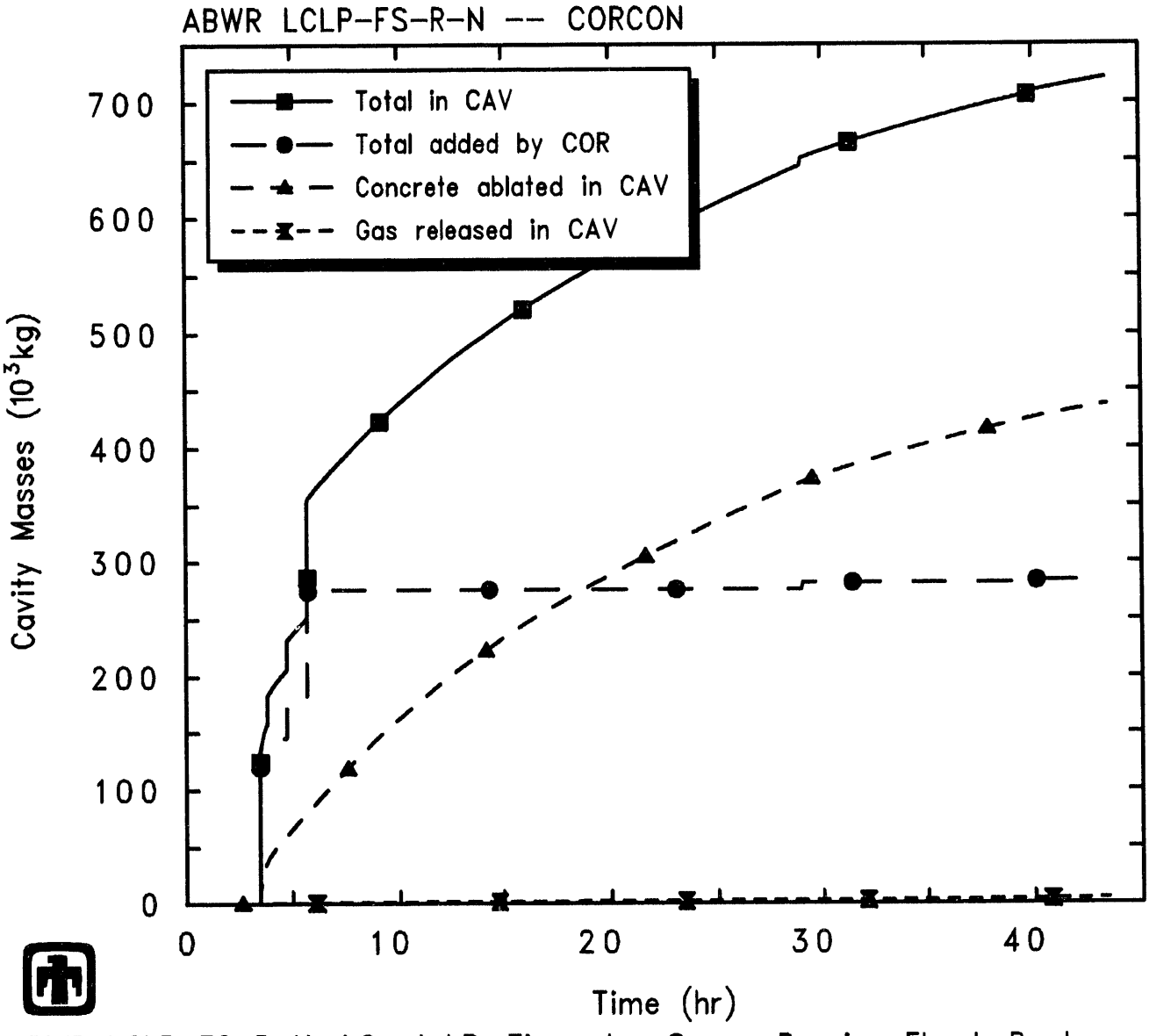

Figure 5.2.9. Cavity Material Masses Predicted by MELCOR for LCLP-FS-R-N Sequence

As seen by the ablated concrete mass given in Figure 5.2.9, as soon as the core debris was predicted to enter the cavity, core-concrete interaction began, resulting in the production of carbon dioxide and hydrogen; reduction of these gases by the molten metal also gave rise to carbon monoxide and hydrogen. Figure 5.2.10 presents the production of various noncondensable gases in the cavity due to core-concrete interaction, calculated by MELCOR. Throughout most of the transient period calculated, almost all of the cavity gas production is in the form of hydrogen; however, there is a rapid increase in CO production after 30hr. This is qualitatively the same as the MELCOR results for LCLP-PF-R-N, given in Figure 5.2.10, but significantly more CO is predicted to be produced in the LCLP-FS-R-N sequence prior to "cavity rupture" (*i.e.*, ablation of either the initial cavity thickness and/or depth at some point) and calculation end than in the LCLP-PF-R-N sequence analysis. In both cases, CO is produced only after all the zironium in the cavity is oxidized to ZrO_2, which happens at about 30hr in this case, because before that time Zr is assumed to reduce any CO_2 generated to pure carbon ("coking").

Figure 5.2.11 gives the calculated maximum cavity depth and radius. (Note that these represent maximum, not average, ablation distances.) Immediately after core debris is first ejected from the vessel to the cavity upon vessel breach in the MELCOR analysis, there is a brief period of rapid radial ablation, which stops after about 6cm of concrete loss. The bulk of the concrete ablation calculated is axially downward, with the MELCOR calculation stopping at 44hr due to "cavity rupture", when the axial ablation equals and tries to exceed the specified available concrete thickness of 2m.

Figure 5.2.12 shows the predicted masses, thicknesses, temperatures and densities of the light oxide, metallic and heavy oxide debris layers in the cavity. No heavy oxide layer is visible in these plots; MELCOR calculates a stable configuration of a light oxide layer above a metallic debris layer throughout the transient period calculated. The metallic layer remains nearly constant in mass and thickness, with a gradually increasing density; the light oxide layer mass and thickness increase continuously (and the density decreases) as ablating concrete (with its resultant low-density silicate oxides) continues to dilute the high-density zirc oxide and steel oxide debris to an average density value less than the metallic debris density. After a few initial oscillations, the temperatures of both layers remain nearly equal, at $\simeq$1500K, throughout the transient period calculated.

The heat transfer from the cavity debris pool in the MELCOR analysis, both downward and outward to the concrete surface and upward to the cavity volume atmosphere, is shown in Figure 5.2.13. The energy transfer from the debris in the cavity upward through the debris bed surface to the lower drywell atmosphere and/or overlying water pool is 2-4 times greater than the energy transferred downward (and sideways) to the concrete. In general, that upper surface of the debris bed is covered with a water pool, not exposed to atmosphere.

Tables 5.2.2 and 5.2.3 give the distribution of the released radionuclides at the end of the calculation (*i.e.*, at 44hr). Table 5.2.2 provides an overview of how much of the radionuclides remain bound up in fuel in either the core or the cavity, and of how much of the released radionuclides are retained in the primary system *vs* how much of the released radionuclides are released to, or released in, either the drywell or the

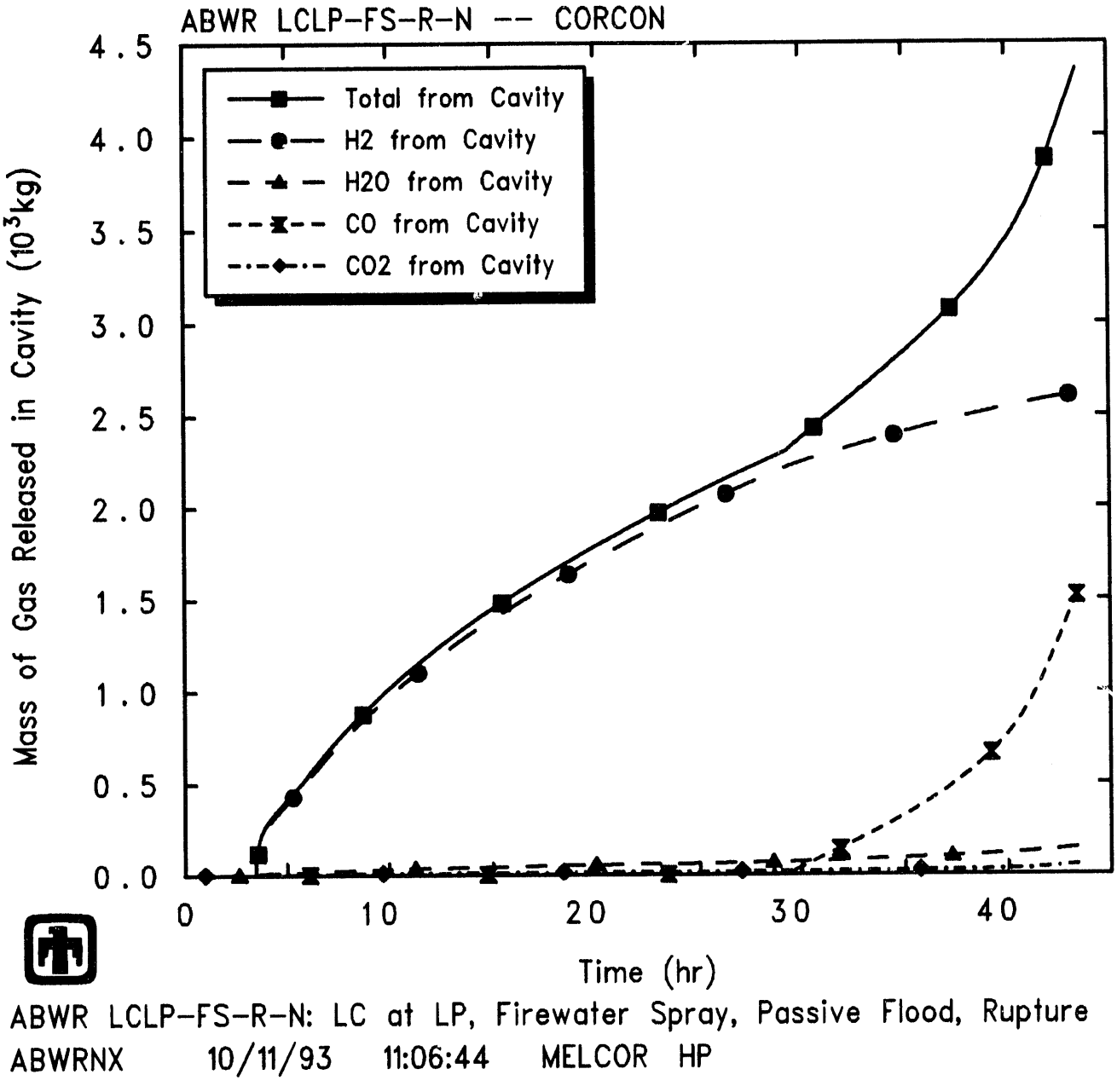

Figure 5.2.10. Cavity Gas Production Predicted by MELCOR for LCLP-FS-R-N Sequence

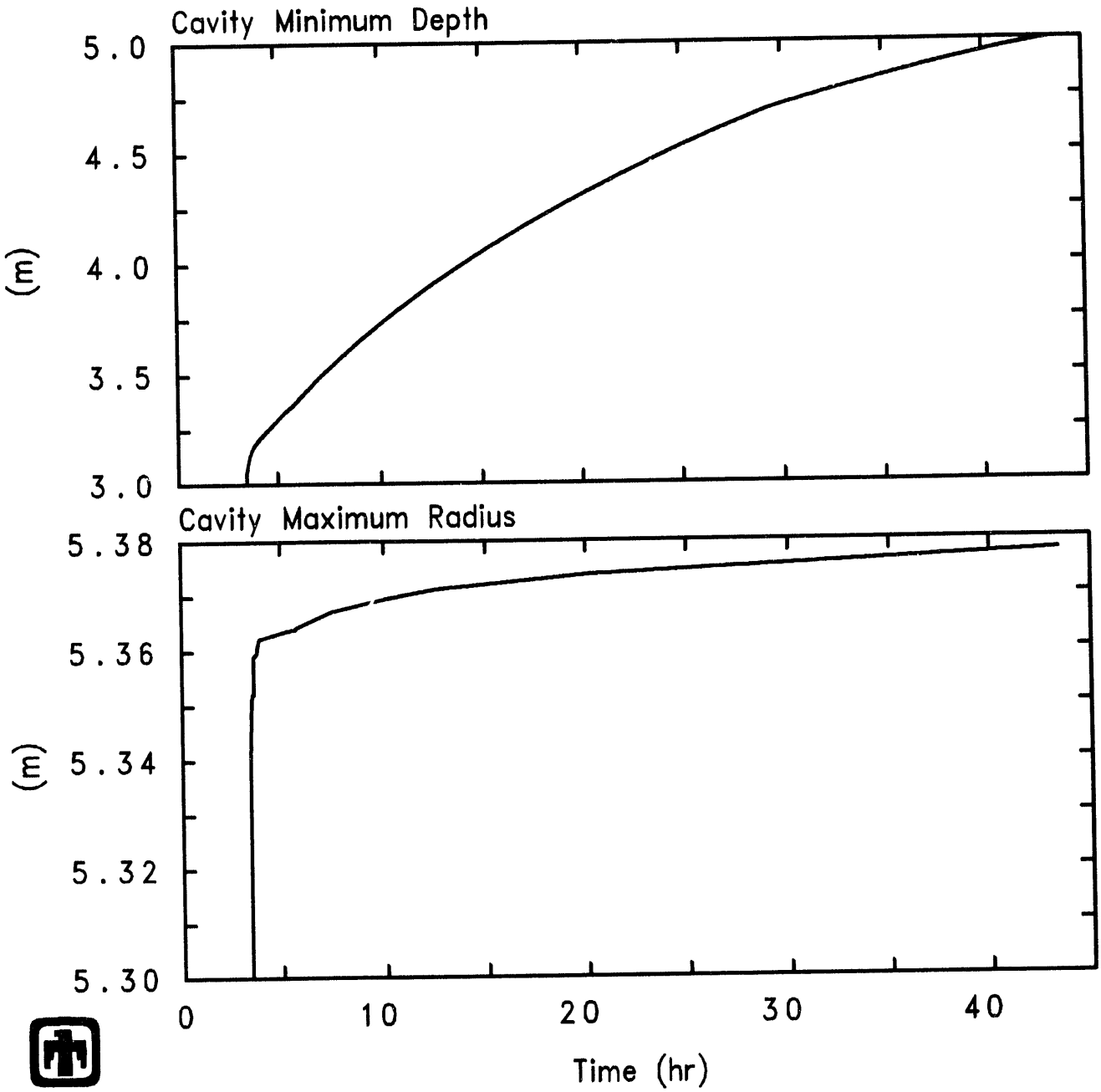

Figure 5.2.11. Cavity Maximum Radius and Depth Predicted by MELCOR for LCLP-FS-R-N Sequence

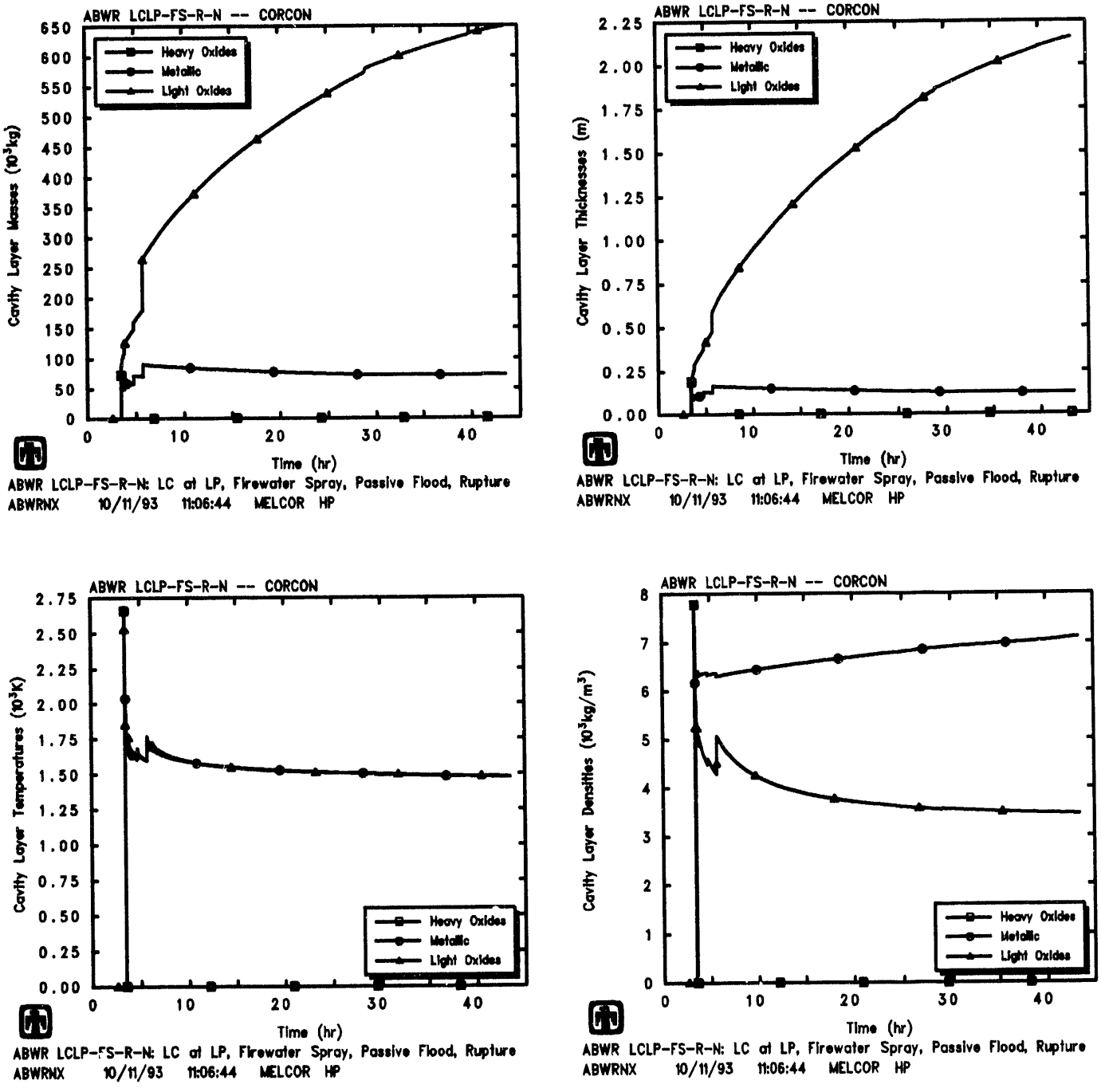

Figure 5.2.12. Cavity Layer Masses (upper left), Thicknesses (upper right), Temperatures (lower left) and Densities (lower right) Predicted by MELCOR for LCLP-FS-R-N Sequence

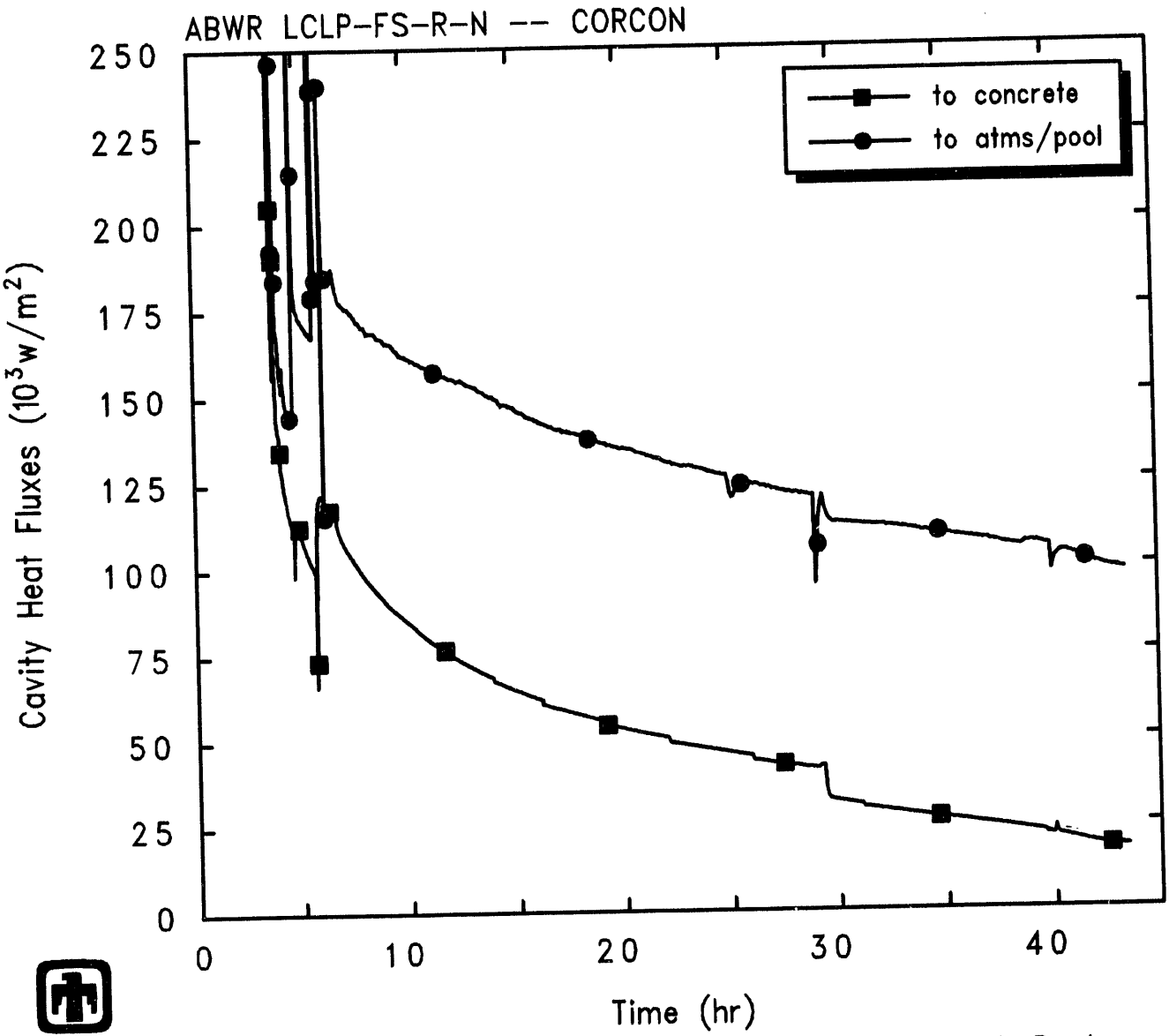

Figure 5.2.13. Cavity Heat Flows Predicted by MELCOR for LCLP-FS-R-N Sequence

wetwell in containment and the environment, all normalized to the initial inventories of each class. Table 5.2.3 gives a slightly different breakdown of the released radionuclide final distribution – the fractions of initial inventory released for each class from fuel in-vessel in the core, ex-vessel in the cavity and overall total are given, together with the distribution of the released radionuclides in the primary system, drywell, wetwell and environment normalized by the mass of each class released. (Note that these amounts generally consider only the release of radioactive forms of these classes, and not additional releases of nonradioactive aerosols from structural materials.)

The release behavior predicted by MELCOR can be grouped into several subdivisions. Almost all ($\simeq$100%) of the volatile Class 1 (noble gases), Class 2 (CsOH), Class 5 (Te) and Class 16 (CsI) radionuclide species are released, primarily in-vessel, as are most (80-90%) of the Class 3 (Ba) and Class 12 (Sn) inventories. The next major release fractions are of Ru and Mo, Ce and La, all between 2% and 4%. Finally, a total $\leq$0.1% of the initial inventory of uranium and Class 11 (Cd) are predicted to be released. This is very similar to the fission product release behavior predicted by MELCOR for the LCLP-PF-R-N sequence. (Note that the CORSOR-M fission product release model option used in these analyses has identically zero release in-vessel of Class 7, Class 9 and Class 11.)

Most of the released radionuclides remain in the primary system and/or the containment; only the noble gases show a significant release to the environment. Of the other radionuclides, <0.1% of the initial inventories are released to the environment. Of the species with significant (>80%) release from fuel, the wetwell retains most (65-75%) of the released CsOH, Te and CsI volatiles, while the Ba and Sn aerosols are held up both in the primary system (55%) and in the wetwell (30-40%). The predicted release to the environment of each radionuclide species is lower for the LCLP-FS-R-N sequence than calculated for the LCLP-PF-R-N sequence; the fractions retained in the wetwell are higher, and the fractions in the drywell generally lower, for the LCLP-FS-R-N sequence analysis than calculated for the LCLP-PF-R-N sequence, reflecting the sprays removing fission products from the containment atmosphere and/or structures (*via* draining condensate films) into the suppression pool.

Figures 5.2.14 and 5.2.15 give the retention factors for the various radionuclides calculated by MELCOR, for the primary system and for the overall containment, respectively. The retention factors are defined as the fraction of material released in, or transported into, a region which remains in that region. The vessel retention factors fall into three sets:

- essentially no retention for the noble gases and for I_2 (of which there is very little),
- a retention of 20-30% for the radionuclide species with non-zero vapor pressures (*i.e.*, CsOH, Te, and CsI), and
- a $\geq$50% retention of those classes which form aerosols only.

These are very similar to the values found in the LCLP-PF-R-N sequence, shown in Figure 5.2.14. The containment retention factors fall into several distinct categories also, and are very similar to the values for the LCLP-PF-R-N sequence, shown in Figure 5.2.15:

Table 5.2.2. Radionuclide Distribution Predicted at 44hr for LCLP-FS-R-N Sequence

Class	Fission Product Distribution (% Initial Inventory)					
	Remaining in Fuel		Released from Fuel			
	Core	Cavity	Primary System	Drywell	Wetwell	Environment
Noble Gases (Xe)	$\simeq 0$	0	0.0782	8.79	4.44×10^{-3}	91.1
Alkali Metals (CsOH)	$\simeq 0$	$\simeq 0$	18.2	6.39	75.3	0.0795
Alkaline Earths (Ba)	2.64×10^{-4}	18.0	47.1	7.65	27.2	1.75×10^{-3}
Halogens (I)	$\simeq 0$	$\simeq 0$	$\simeq 0$	$\simeq 0$	$\simeq 0$	$\simeq 0$
Chalcogens (Te)	$\simeq 0$	0.0274	28.8	5.75	65.4	0.0176
Platinoids (Ru)	1.11×10^{-3}	96.4	2.06	1.03	0.512	2.11×10^{-5}
Transition Metals (Mo)	1.11×10^{-3}	98.2	4.04×10^{-3}	0.513	1.27	1.38×10^{-3}
Tetravalents (Ce)	1.11×10^{-3}	95.4	2.58	1.41	0.628	2.30×10^{-5}
Trivalents (La)	1.11×10^{-3}	97.9	1.73×10^{-3}	1.06	1.07	4.86×10^{-4}
Uranium (U)	1.94×10^{-3}	99.9	0.0344	0.0175	9.81×10^{-3}	1.14×10^{-6}
More Volatile Main Group Elements (Cd)	1.11×10^{-3}	$\simeq 100$	1.70×10^{-5}	6.50×10^{-3}	5.47×10^{-3}	1.92×10^{-6}
Less Volatile Main Group Elements (Sn)	1.48×10^{-4}	8.99	47.5	6.49	37.1	1.74×10^{-3}
CsI	$\simeq 0$	7.52×10^{-6}	18.8	6.34	74.8	0.0241

Table 5.2.3. Radionuclide Release and Released Distribution Predicted at 44hr for LCLP-FS-R-N Sequence

Class	Released from Fuel (% Initial Inventory)			Distribution (% Released Mass)			
	Core	Cavity	Total	Primary System	Drywell	Wetwell	Environment
Noble Gases (Xe)	99.97	0.03	≃100	0.0782	8.79	4.44×10^{-3}	91.13
Alkali Metals (CsOH)	99.94	0.03	99.97	18.25	6.39	75.29	0.0795
Alkaline Earths (Ba)	80.28	1.75	82.04	57.45	9.33	33.21	0.002
Halogens (I)	≃0	≃0	≃0	0.057	8.57	4.32×10^{-3}	92.98
Chalcogens (Te)	99.98	7.56×10^{-3}	99.98	28.78	5.76	65.45	0.0176
Platinoids (Ru)	3.60	2.61×10^{-5}	3.60	36.06	17.98	8.96	3.70×10^{-4}
Transition Metals (Mo)	0	1.79	1.79	0.226	28.70	70.99	0.0769
Tetravalents (Ce)	4.61	4.60×10^{-4}	4.61	55.90	30.48	13.62	4.98×10^{-4}
Trivalents (La)	0	2.13	2.13	0.0814	49.55	50.35	0.0228
Uranium (U)	0.060	0.003	0.063	55.68	28.42	15.90	1.84×10^{-3}
More Volatile Main Group Elements (Cd)	0	0.012	0.012	0.142	54.24	45.60	0.016
Less Volatile Main Group Elements (Sn)	91.00	0.011	91.01	52.15	7.13	40.72	1.91×10^{-3}
CsI	99.97	0.032	≃100	18.81	6.34	74.83	0.0241

- essentially no retention for the noble gases and for I_2 after COPS rupture,
- a retention of 70-80% for the radionuclide species with non-zero vapor pressures (*i.e.*, CsOH, Te, and CsI), and
- for those classes which form aerosols only, there is a 40-50% retention for those which had some in-vessel release (Ba, Ru, Ce, U and Sn) and a ~100% retention of those with only ex-vessel release (Mo, La and Cd).

Figures 5.2.16 and 5.2.17 give the decontamination factors (DFs) for the various radionuclides calculated by MELCOR, for the suppression pool and for the overall containment, respectively. The period of interest in these plots is after ~25hr when the containment is calculated to depressurize due to rupture disk actuation. After containment rupture disk opening, the suppression pool and overall containment DFs are simply DF=1.0 for the noble gases and for I_2 (of which there is very little), not shown explicitly in these figures.

The suppression pool DFs after COPS actuation vary over two orders of magnitude,

- $DF_{SP} \leq 100$ for classes with no in-vessel release and no continuing ex-vessel release (*i.e.*, La and Cd),
- $DF_{SP} \geq 200$ for classes with no in-vessel release but continuous ex-vessel release (*i.e.*, Mo),
- $DF_{SP} \sim 600$ for classes with $\ll 1\%$ in-vessel release (U),
- $DF_{SP} \sim 900$ for the volatile CsOH,
- $DF_{SP} \geq 2000$ for the majority of classes (Ba, Te and CsI), and
- $DF_{SP} \geq 6000$ for the other classes (Ru, Ce and Sn).

The magnitude of the various DFs calculated by MELCOR for the LCLP-FS-R-N sequence are generally higher than those calculated by MELCOR for the LCLP-PF-R-N sequence, presented in Figure 5.1.29, reflecting the sprays removing fission products from the containment atmosphere and/or structures (*via* draining condensate films) into the suppression pool. The classes predicted to have relatively higher wetwell decontamination factors are also different in the two analyses, reflecting differences in release and distribution.

The overall containment DFs sequence also are generally higher than those calculated by MELCOR for the LCLP-PF-R-N sequence, presented in Figure 5.1.30, again reflecting the sprays removing fission products from the atmosphere and/or structures into the wetwell pool:

- $DF_{Cont} \sim 1000\text{-}6000$ for classes with no in-vessel release (*i.e.*, Mo, La and Cd) and for the volatiles (CsOH, Te and CsI),

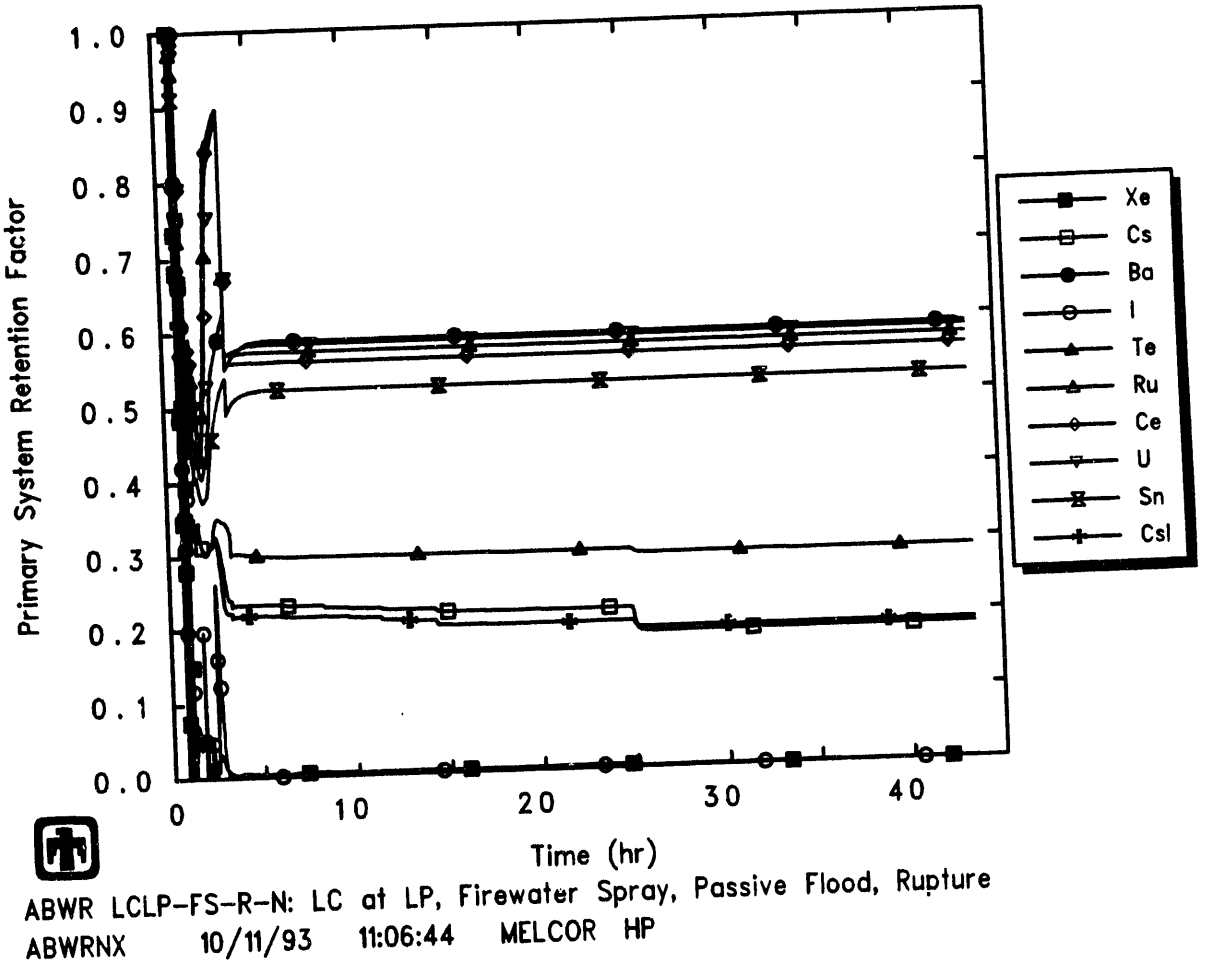

Figure 5.2.14. Primary System Retention Factors Predicted by MELCOR for LCLP-FS-R-N Sequence

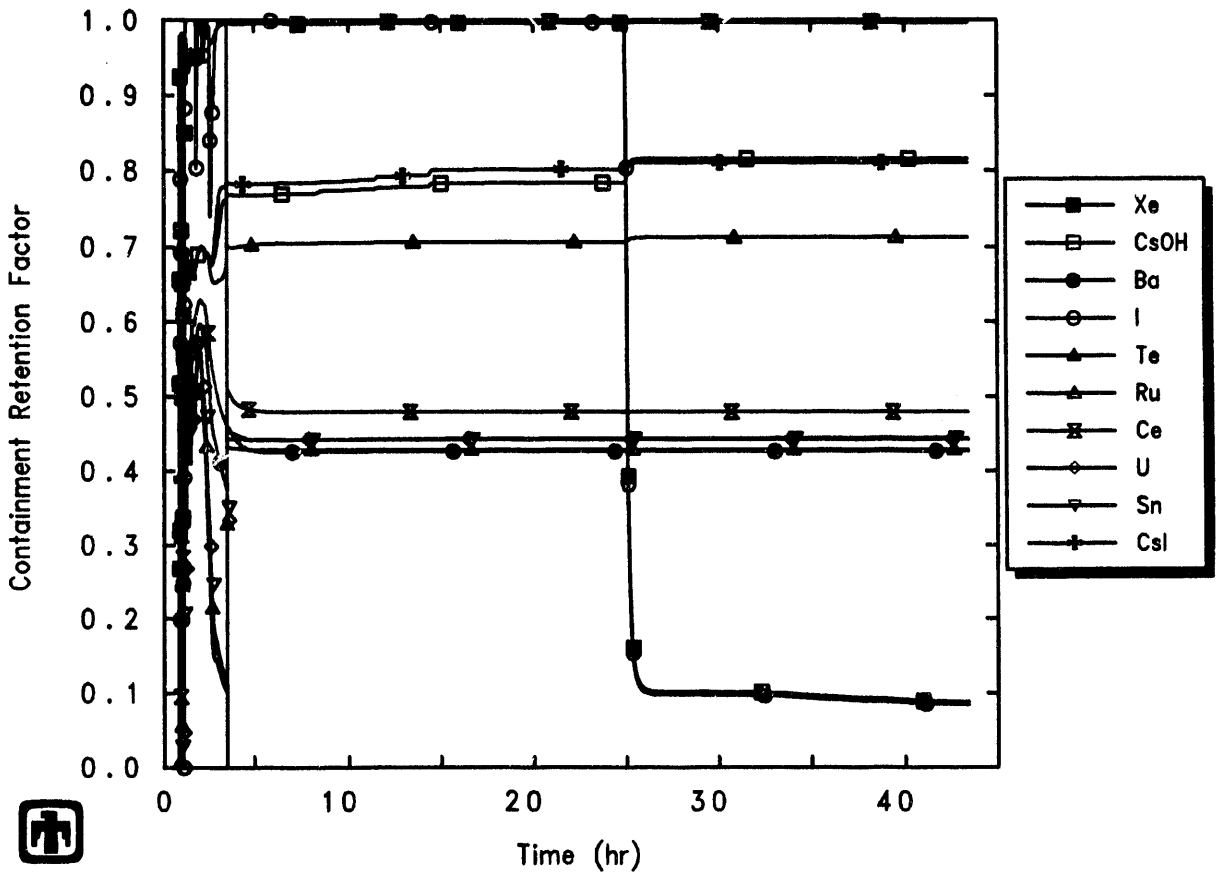

Figure 5.2.15. Containment Retention Factors Predicted by MELCOR for LCLP-FS-R-N Sequence

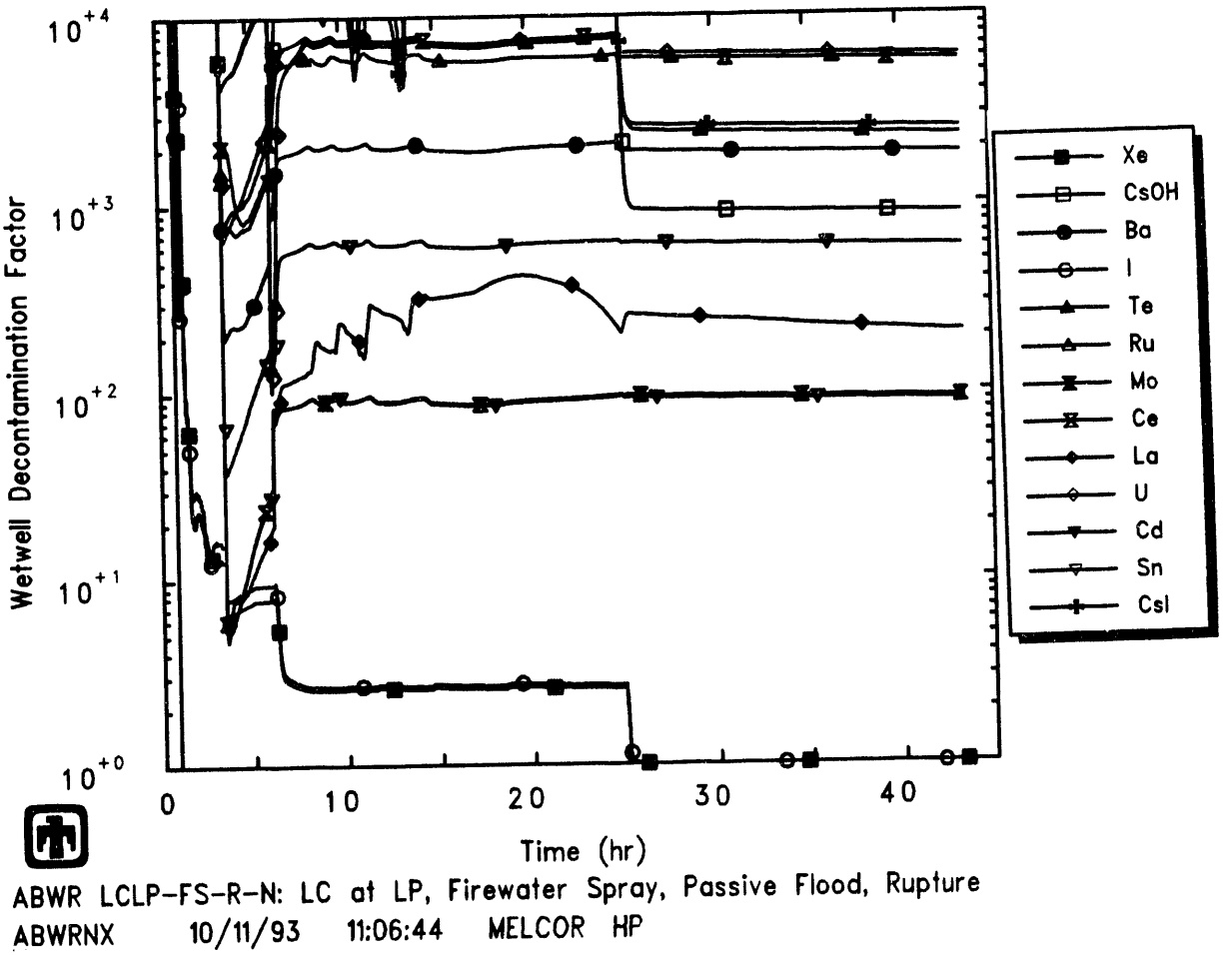

Figure 5.2.16. Suppression Pool Decontamination Factors Predicted by MELCOR for LCLP-FS-R-N Sequence

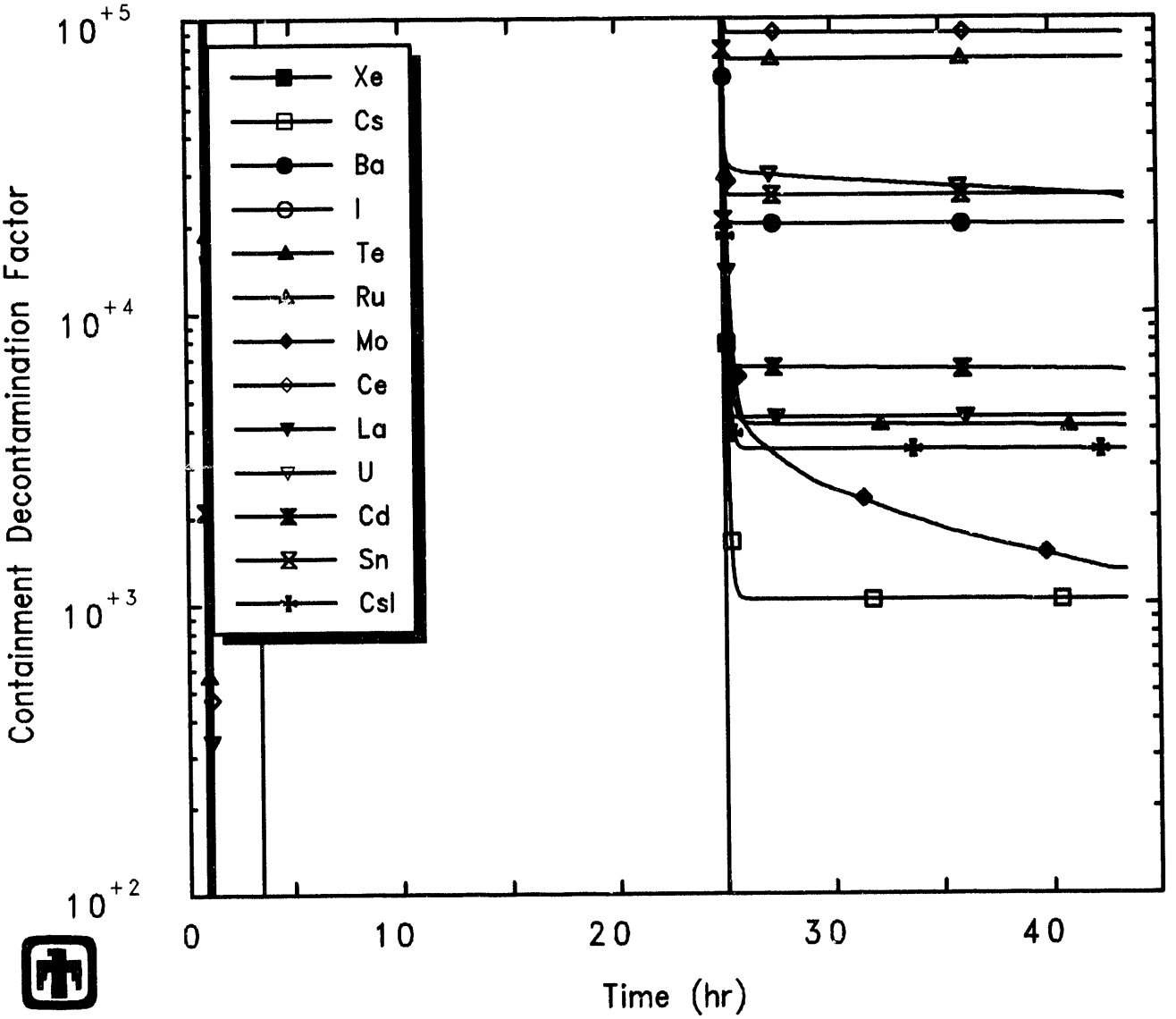

Figure 5.2.17. Overall Containment Decontamination Factors Predicted by MELCOR for LCLP-FS-R-N Sequence

- $DF_{Cont} \geq 20{,}000$ for several classes (Ba, U and Sn), and
- $DF_{Cont} \leq 100{,}000$ for Class 6 (Ru) and Class 8 (Ce).

While the overall containment decontamination factors predicted by MELCOR for the LCLP-FS-R-N are greater in magnitude than for the LCLP-PF-R-N sequence, the relative differences between DFs for various radionuclide classes are generally similar in the two calculations.

Note that both the suppression pool and overall containment decontamination factors remain nearly constant or drop very slowly for most classes after containment rupture disk actuation, but drop steadily for several radionuclide species (*i.e.*, CsOH, Te, Mo and CsI). These are the classes for which a continuing release to the environment is predicted, while for the other classes there is only a single step-like release at containment depressurization, as illustrated in Figure 5.2.18. That continuing release comes from two different causes. The non-zero vapor pressure of CsOH, Te and CsI causes continuous vaporization from the suppression pool and replenishment of these fission product vapors in the wetwell atmosphere as those fission product vapors in the wetwell atmosphere are lost out the COPS rupture. Class 7 (Mo) has no non-zero vapor pressure and therefore remains an aerosol throughout the problem. However, this class is the only one with substantial and continuing radionuclide release in the cavity, and a small fraction of that continuing release (while mostly remaining in the cavity and/or suppression pools) does survive pool scrubbing and get released to the wetwell atmosphere and then out the containment rupture disk to the environment.

Figure 5.2.18 does not include the release of the noble gases, to allow expansion of the scale for the environmental release of the other radionuclide classes. In the MAAP analysis, the release of noble gases is nearly complete one hour after the rupture disk opens (Figure 19E.2-3D in [1]; the release of the noble gases in the MELCOR calculation also occurs within a brief time after COPS actuation, and almost all of the noble gases are released. Figure 19.E.2-3E in [1] gives the release fractions of cesium iodide and cesium hydroxide as functions of time from the MAAP analysis. The release of the volatile species, CsI and CsOH, occurs over a much longer period of time than for the noble gases and is nearly complete at 76hr; the release fractions of CsOH and CsI at 70hr are $\leq 2 \times 10^{-7}$. It is not clear from Figure 19E.2-3E in [1] whether the release fractions of CsOH and CsI were normalized to their initial inventories or to their released inventories. This MELCOR calculation shows environment release fractions by the end of the calculation (44hr) of about 8×10^{-4} and 2×10^{-4} for CsOH and CsI, respectively, normalized to their total available inventory (Table 5.2.2; since ~99.9% of these radionuclides were predicted to be released, the same environment release fractions are obtained normalizing to released inventories (Table 5.2.3). The release fractions calculated by MELCOR are significantly higher than the values predicted by MAAP, primarily due to the continuing steaming of cavity water by non-quenched debris in MELCOR; however, the MELCOR release fractions are still very small fractions of the fission product inventories initially present, released but retained within containment even after containment rupture disk opening.

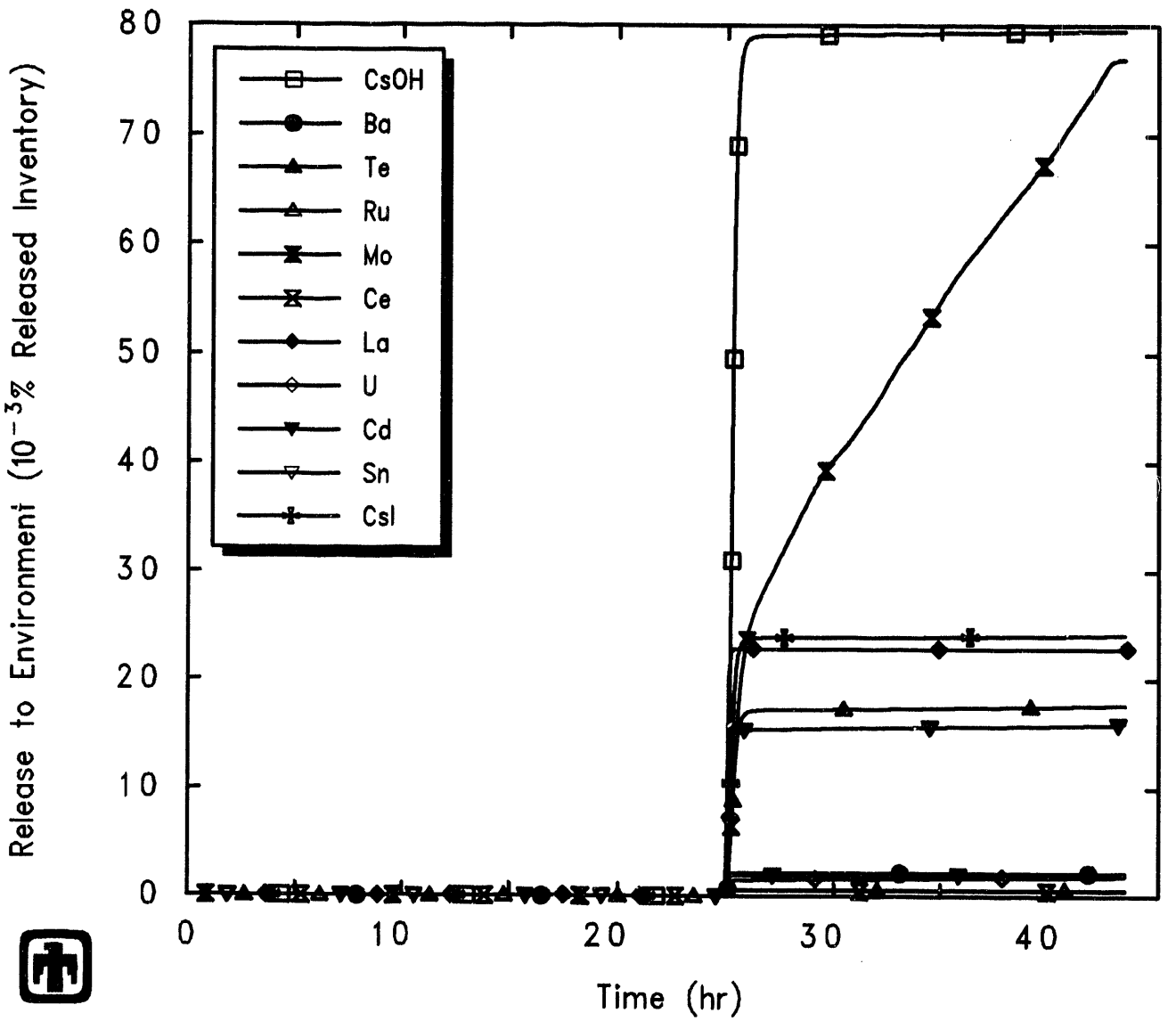

Figure 5.2.18. Radionuclide Environmental Releases Predicted by MELCOR for LCLP-FS-R-N Sequence

5.3 LCHP-PF-P-M Sequence

The initiator for this analysis is a station blackout with loss of all core cooling. The MSIV closes, followed by reactor scram. The feedwater trips, with a coastdown of 5s. The ECC injection systems fail. The operator is assumed to fail to depressurize the vessel. The safety relief valves (SRVs) cycle open and closed to relieve the steam pressure.

The sequence of events predicted by MELCOR for this accident is given in Table 5.3.1, with the timings of the various events as calculated by MAAP (taken from Table 19E.2-8 in [1]) included for comparison.

The swollen and collapsed liquid levels predicted by MELCOR in the vessel control volumes are given in Figure 5.3.1. Less than 30min after accident initiation, decay heat has been sufficient to lower the water level in the vessel to uncover the channel control volume, as shown in Figure 5.3.1, slightly later in the MELCOR analysis than in the MAAP analysis. Comparison to vessel liquid levels predicted by MELCOR for the corresponding low-pressure sequence, shown in Figure 5.3.1, illustrates that the core uncovers more s owly in the high-pressure boiloff than when the ADS is actuated. With failure to depressurize, the vessel pressure continues to cycle on the SRV setpoint, as illustrated by the primary system pressure history presented in Figure 5.3.2, while the water in the core boils away and the core melts.

The core plate and lower head are not predicted to fail immediately after core uncovery is completed; core uncovery is complete at 1hr, while core plate failure and lower head penetration failure are first calculated to occur at about 4.5hr. Between those times, the core is maintained in a degraded configuration by steam cooling from boiling off water in the lower plenum. Note that both MAAP and MELCOR predict that the core can be maintained in this degraded condition longer in the high-pressure sequence than in the low-pressure LCLP-PF-R-N sequence, so that vessel failure is calculated to occur later in the high-pressure sequence than in the corresponding low-pressure sequence by both codes.

Figure 5.3.3 shows core clad temperatures in the various axial levels in the active fuel region for each of the four radial rings used in the MELCOR core model; Figure 5.3.4 gives core particulate debris temperatures in the same axial levels, in the active fuel region, for each of the four radial rings. Core particulate debris temperatures in the five axial levels in the lower plenum (with the core support plate in level 5) are presented in Figure 5.3.5.

The majority of material in the active fuel region (*i.e.*, above the core support plate) heats up without interruption through melt and relocation to debris formation. Most of the fuel and clad in the innermost, highest-powered ring have collapsed into a debris bed by about 1hr, and all has collapsed into a debris bed by 1.5hr. Most of the fuel and clad in the middle two rings have collapsed into a debris bed by 1.5-2.5hr, and all has collapsed into a debris bed by 3-4hr. None of the fuel and clad in the outermost, lowest-powered ring have collapsed into a debris bed by the time of vessel failure at 4.5hr, unlike the results calculated for the low-pressure LCLP-PF-R-N sequence where MELCOR predicts

Table 5.3.1. Sequence of Events Predicted by MELCOR for LCHP-PF-P-M Sequence, Compared to MAAP

Event	Time	
	MAAP	MELCOR
Accident initiation (MSIV Closure)	0.0	0.0
Reactor scrammed	4.2s	
Core uncovery begins	0.3hr	1,637.5s (0.45hr)
Clad failure/Gap release		
(Ring 1)		3,203.3s (0.83hr)
(Ring 2)		4,322.8s (1.20hr)
(Ring 3)		5,144.0s (1.43hr)
(Ring 4)		8,279.6s (2.30hr)
Core plate failed		
(Ring 1)		16,325.7s (4.53hr)
(Ring 2)		18,072.6s (5.02hr)
(Ring 3)		21,940.1s (6.09hr)
(Ring 4)		30,660.2s (8.52hr)
Vessel bottom head failed	2.0hr	
Vessel LH penetration failed		
(Ring 1)		16,389.6s (4.55hr)
(Ring 2)		16,393.2s (4.55hr)
(Ring 3)		16,404.2s (4.56hr)
(Ring 4)		16,412.9s (4.56hr)
Commence debris ejection		16,389.6s (4.55hr)
End of HPME/DCH		16,565.8s (4.60hr)
Passive flooder opens	2.0hr	16,401.0s (4.56hr)
Seal degradation temperature reached	2.1hr	16,401.2s (4.56hr)
Leakage through movable penetrations begins	18.1hr	21,780s (6.05hr)
Concrete ablation $\geq$2m		209,736s (58.26hr)
End of calculation	100hr	209,736s (58.26hr)

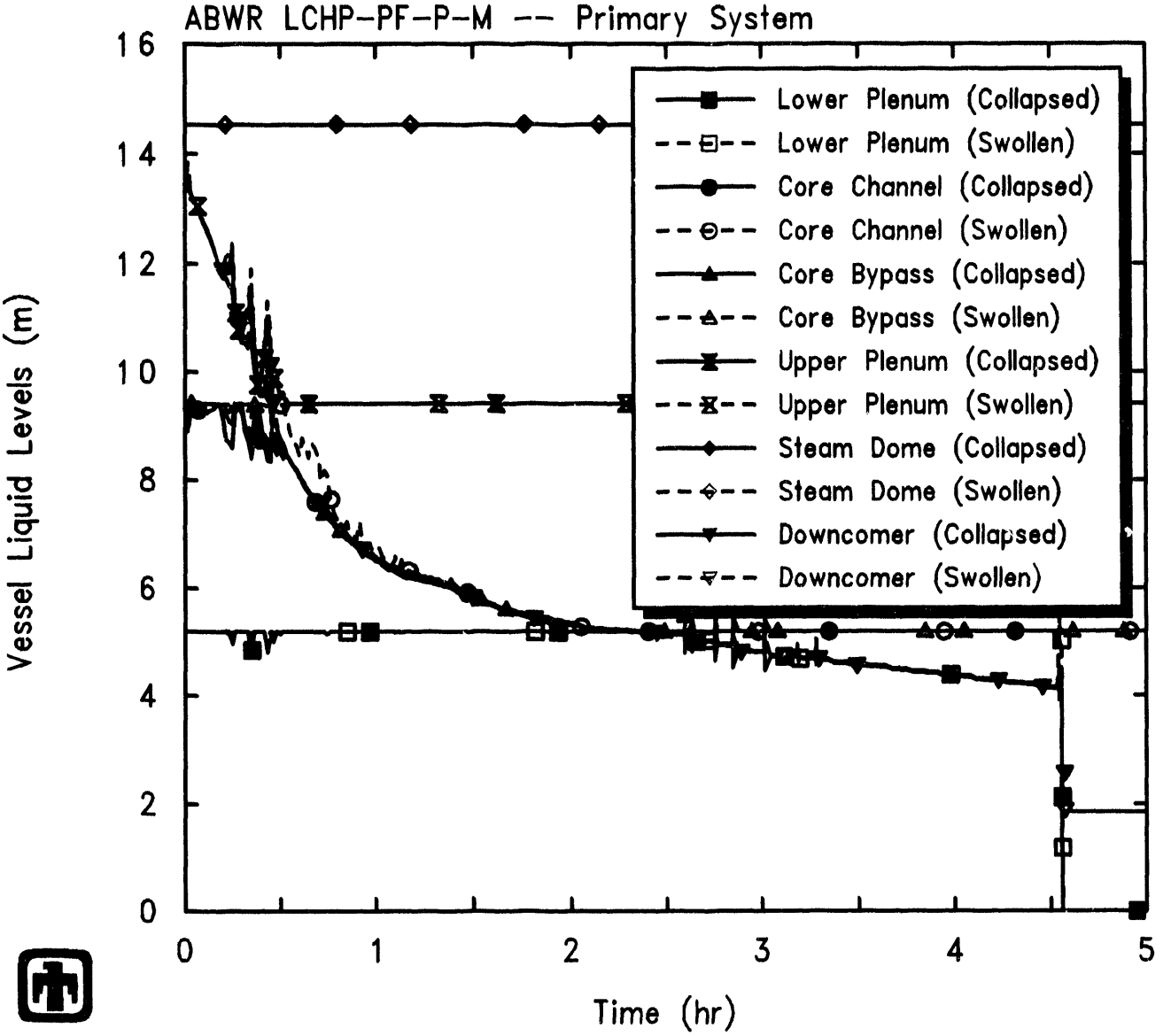

Figure 5.3.1. Vessel Swollen and Collapsed Liquid Levels Predicted by MELCOR for LCHP-PF-P-M Sequence

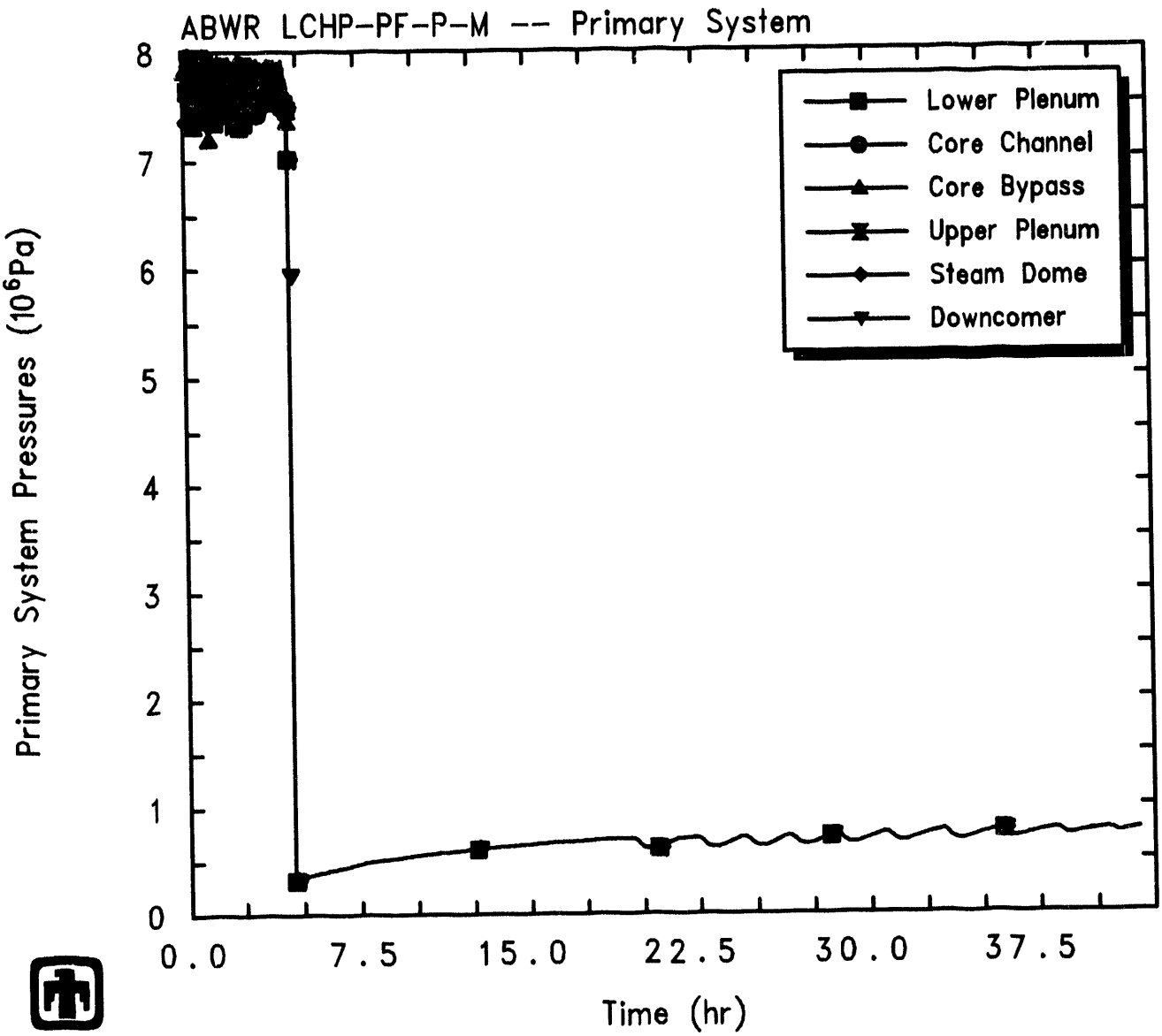

Figure 5.3.2. Primary System Pressures Predicted by MELCOR for LCHP-PF-P-M Sequence

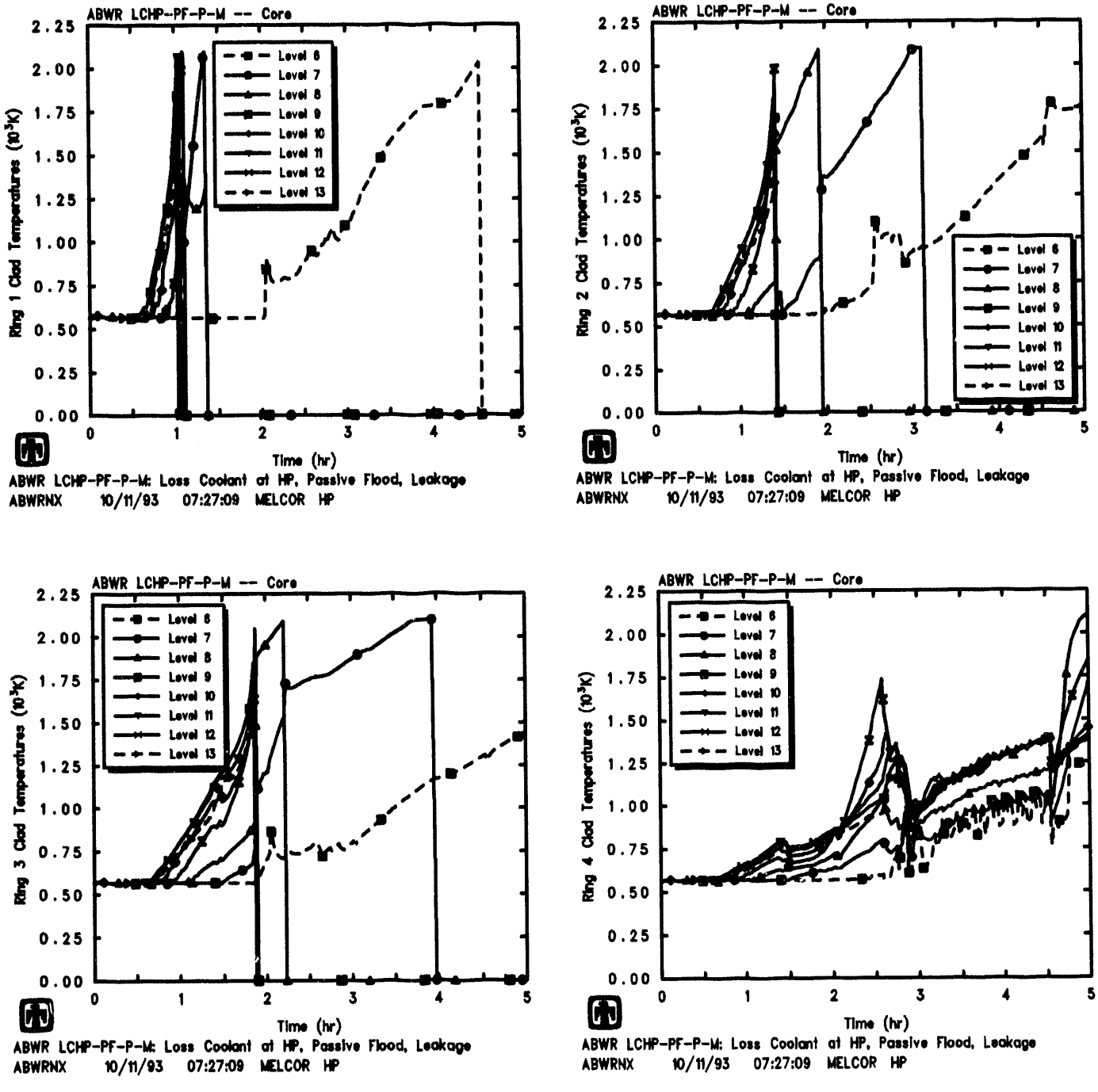

Figure 5.3.3. Core Ring 1 (upper left), Ring 2 (upper right), Ring 3 (lower left) and Ring 4 (lower right) Clad Temperatures Predicted by MELCOR for LCHP-PF-P-M Sequence

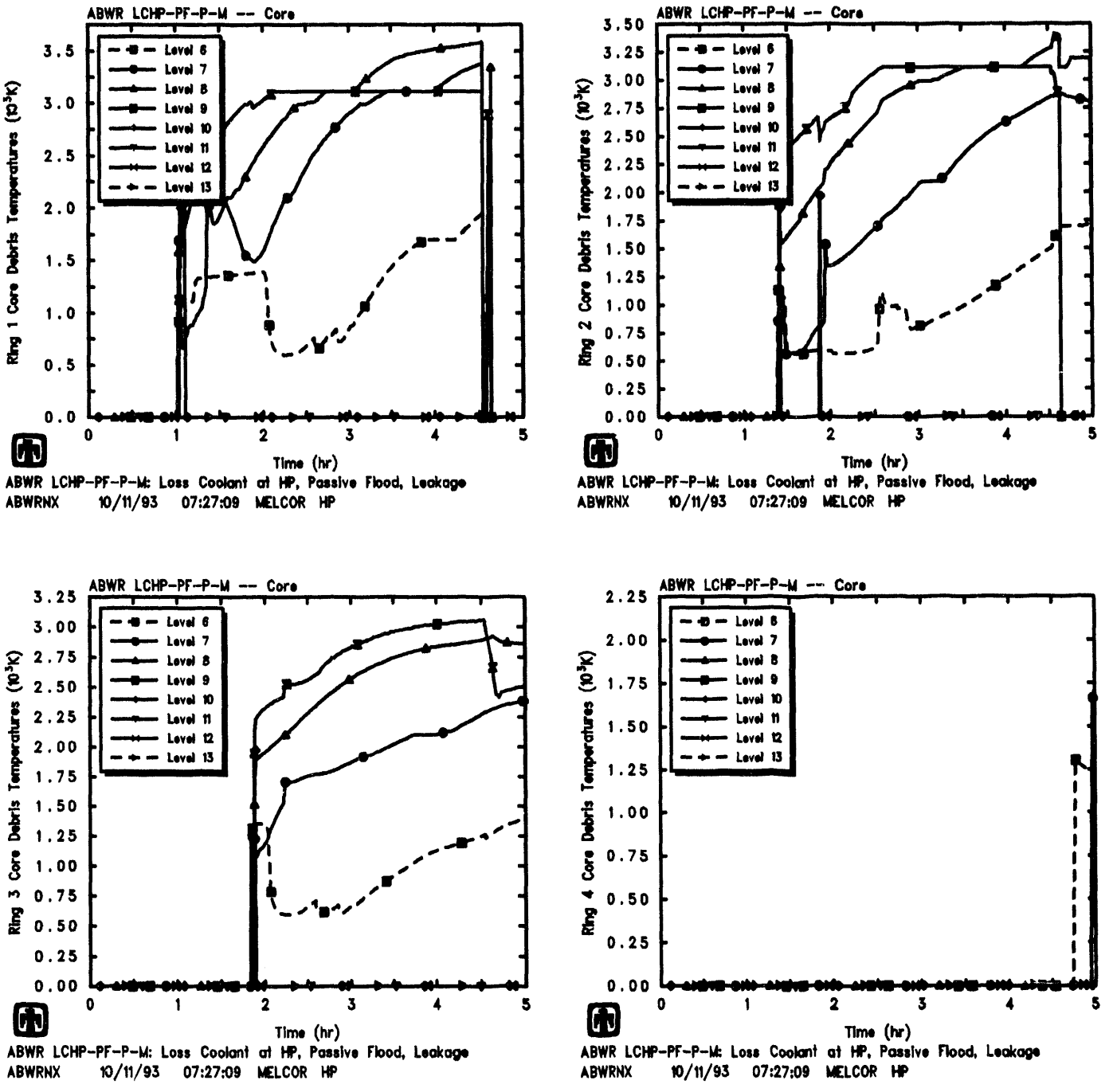

Figure 5.3.4. Core Ring 1 (upper left), Ring 2 (upper right), Ring 3 (lower left) and Ring 4 (lower right) Debris Temperatures in the Active Fuel Region Predicted by MELCOR for LCHP-PF-P-M Sequence

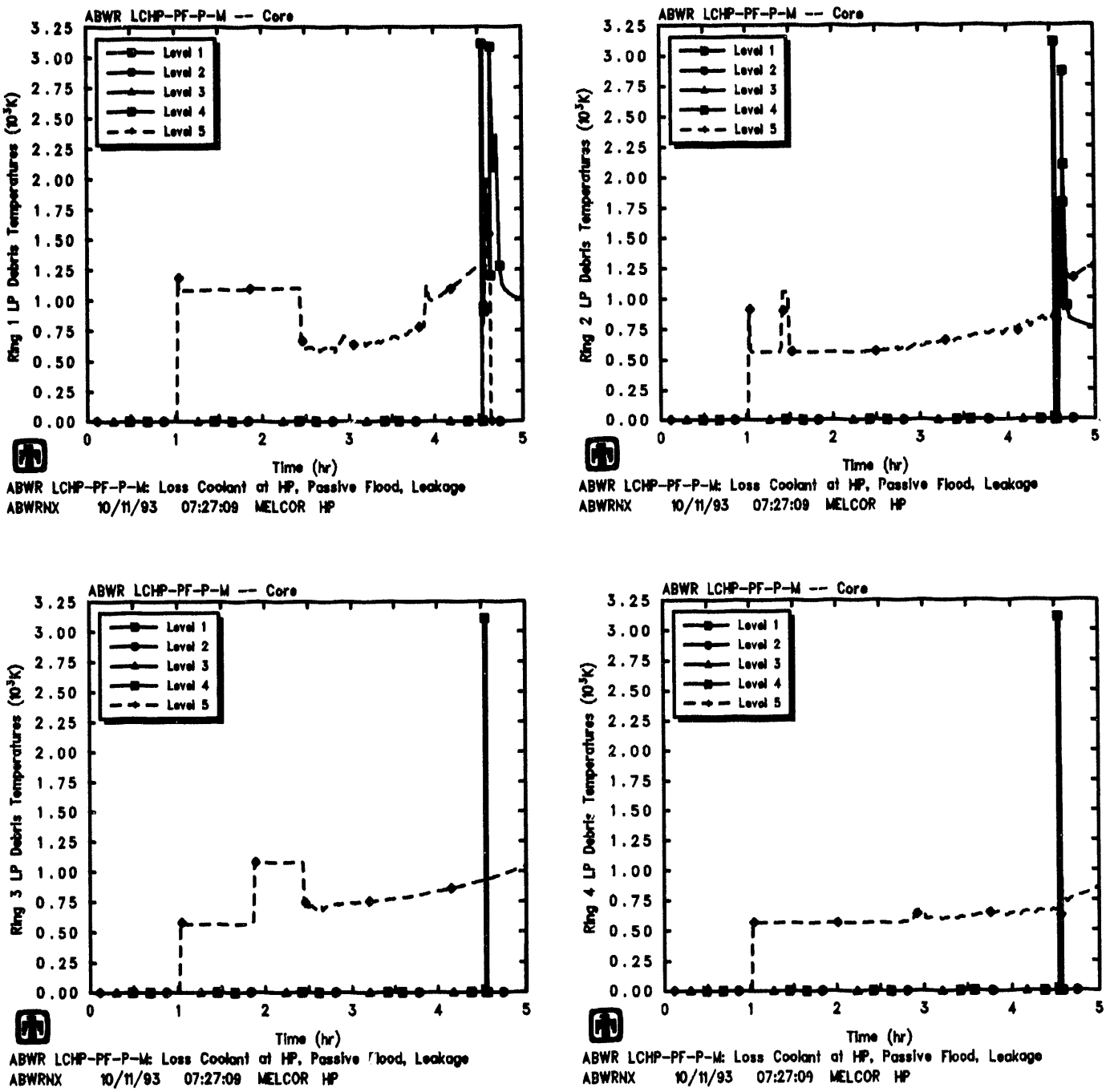

Figure 5.3.5. Core Ring 1 (upper left), Ring 2 (upper right), Ring 3 (lower left) and Ring 4 (lower right) Debris Temperatures in the Lower Plenum Predicted by MELCOR for LCHP-PF-P-M Sequence

all of the fuel and clad in the outermost, lowest-powered ring collapsed into a debris bed by the time of vessel failure at 3.3hr. The debris beds in the active fuel region are held up for several hours by the core support plate and by still-intact support structures in the lowermost, non-fueled level in the active fuel region (*i.e.*, level 6), as illustrated in the temperatures in Figures 5.3.3 and 5.3.4.

The temperatures calculated for the core support plate (*i.e.*, the "other structure" in level 5) are given in Figure 5.3.6. The core support plate begins to heat up as soon as the bottom of the core is uncovered, at 2hr, and then heats up at a generally steady, slow rate due to conduction and/or radiation heat transfer from the hot debris in the active fuel region levels above the core plate. The core support plate first fails at 4.53hr, in the innermost ring where the debris was hottest. Even before the core support plate fails, some debris has fallen through the core support plate into the lowest lower plenum level, just above the lower head, as indicated by the debris temperatures given in Figure 5.3.5. That falling debris falls into a water pool in the lower plenum, and the water in the lower plenum is boiled off slowly by that hot debris, as visible in Figure 5.3.1. The steam generated flows upward through the core and temporarily significantly increases the steam cooling of the material remaining in the core region, helping to slow the core plate heatup and to maintain the integrity of the core support plate and lower core support structures.

The core support plate in the innermost ring failed by reaching the failure criterion of 1273K at 16,326s (4.53hr), allowing any particulate debris and remaining intact material in the active fuel region and core plate level to fall through into the lower plenum. The lower head surface and penetration temperatures are presented in Figure 5.3.7. The temperature of the lower head penetrations in all four rings quickly rose well above the weld failure temperature of 1273K. The penetrations were assumed to have failed and vessel breach occurred at 16,390s (4.55hr); this compares to an earlier vessel failure time of about 2hr after transient start in the MAAP analysis. Although the times of vessel failure predicted by MAAP and by MELCOR are different, both codes show later vessel failure in sequences with high-pressure boiloff than in sequences where the ADS functions as intended. The core support plate in the other three rings failed 0.5 to 3hr later in this LCHP-PF-P-M sequence analysis; this is largely a result of the new debris radial relocation model allowing debris formed in the outer rings to move laterally to the first, failed ring and fall through the failed core plate and lower head penetration in the first ring, rather than remain on and continue to heat the core support plate in the other rings.

The calculated core state at vessel failure (*i.e.*, at 16,389.6s or 4.55hr) is illustrated in Figures 5.3.8 through 5.3.11, for the four rings in the MELCOR ABWR core model. The content of these figures is explained in Section 5.1 when discussing Figures 5.1.8 through 5.1.11, which give corresponding results for the core state calculated at vessel failure in the low-pressure LCLP-PF-R-N sequence. These core material configurations at the time of vessel failure also should be compared to the initial core material configuration given in Figure 4.4, to aid in visualize the amount of material degradation and relocation.

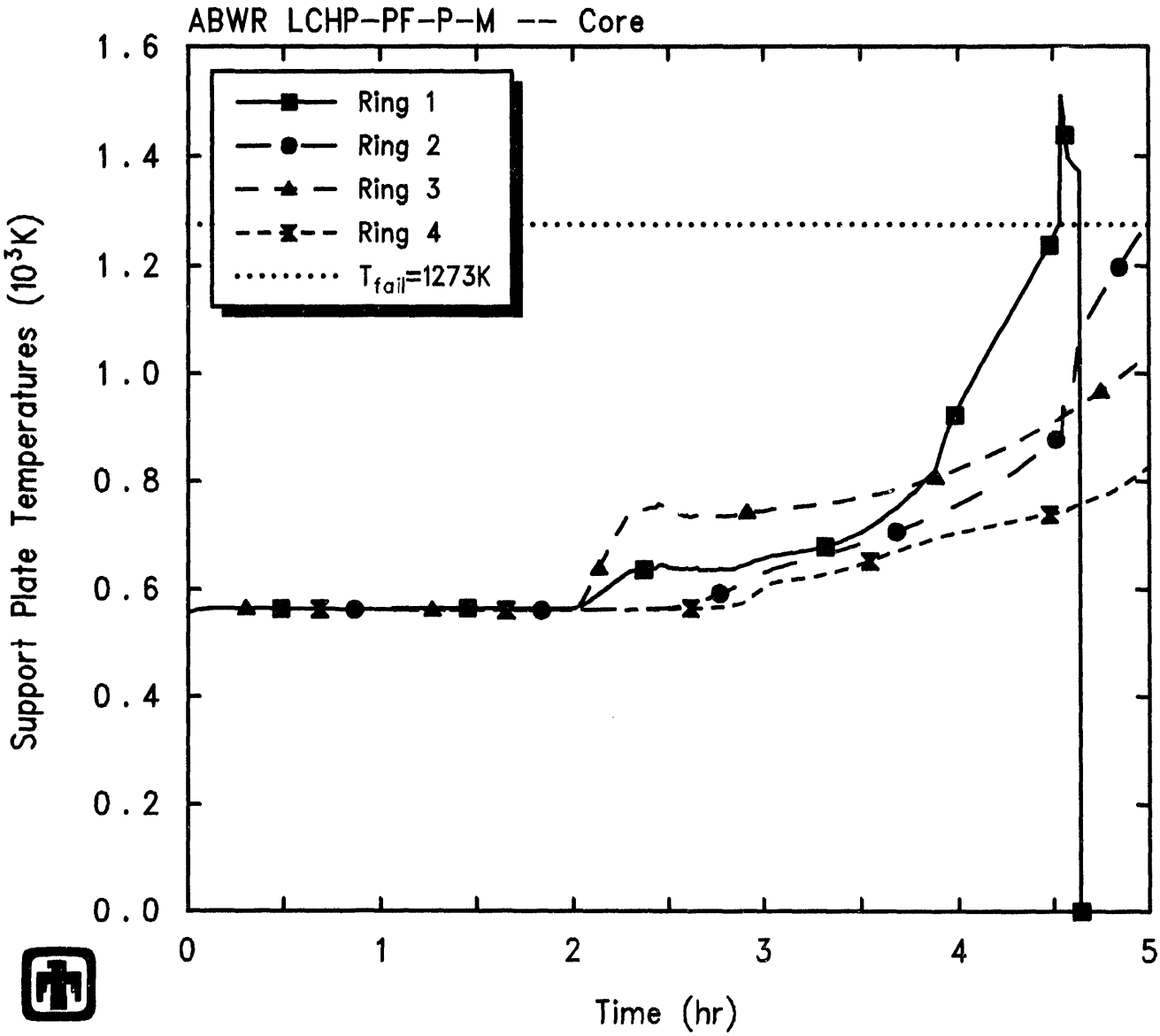

Figure 5.3.6. Core Support Plate Temperatures Predicted by MELCOR for LCHP-PF-P-M Sequence

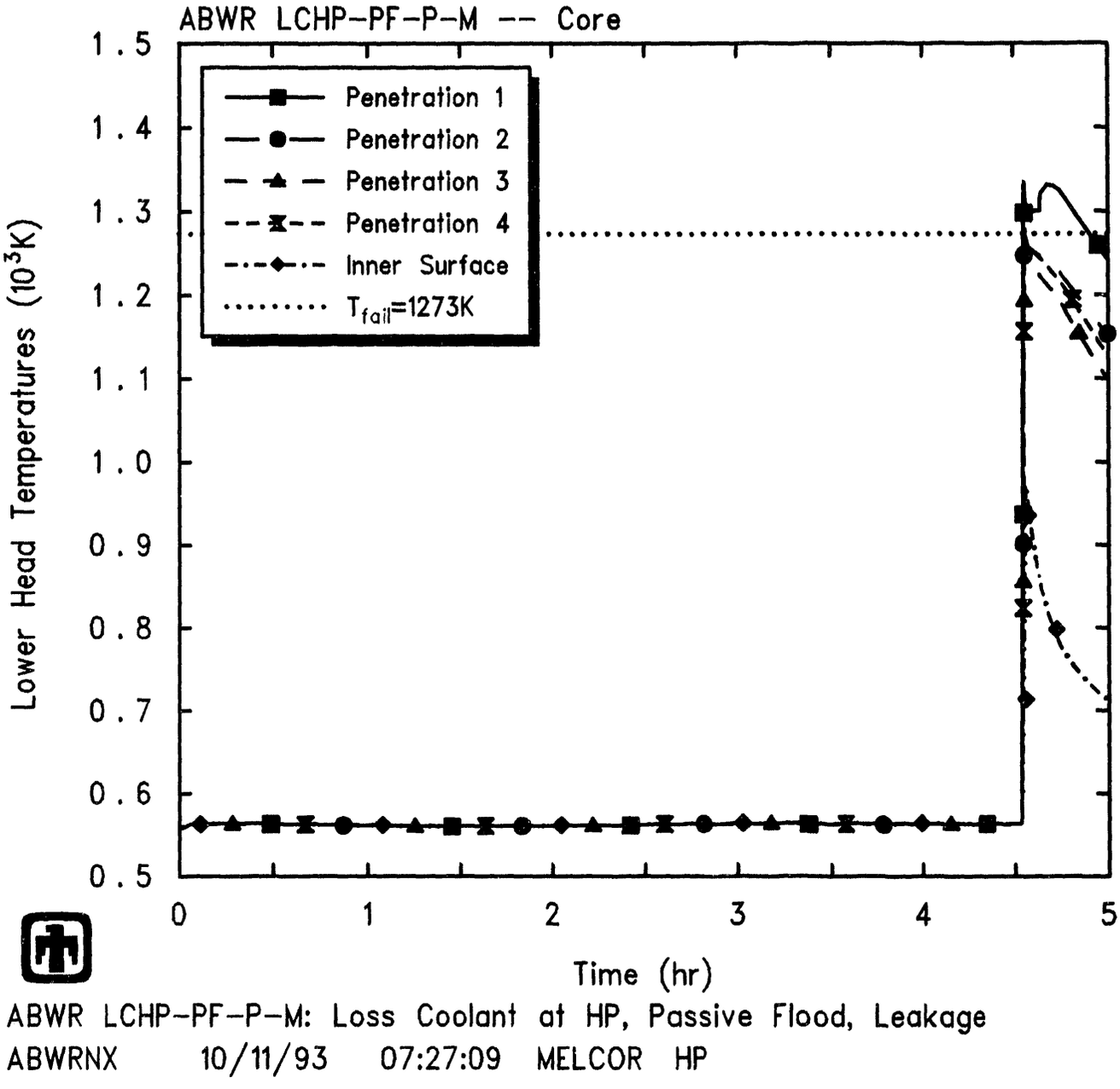

Figure 5.3.7. Lower Head Inner Surface and Penetration Temperatures Predicted by MELCOR for LCHP-PF-P-M Sequence

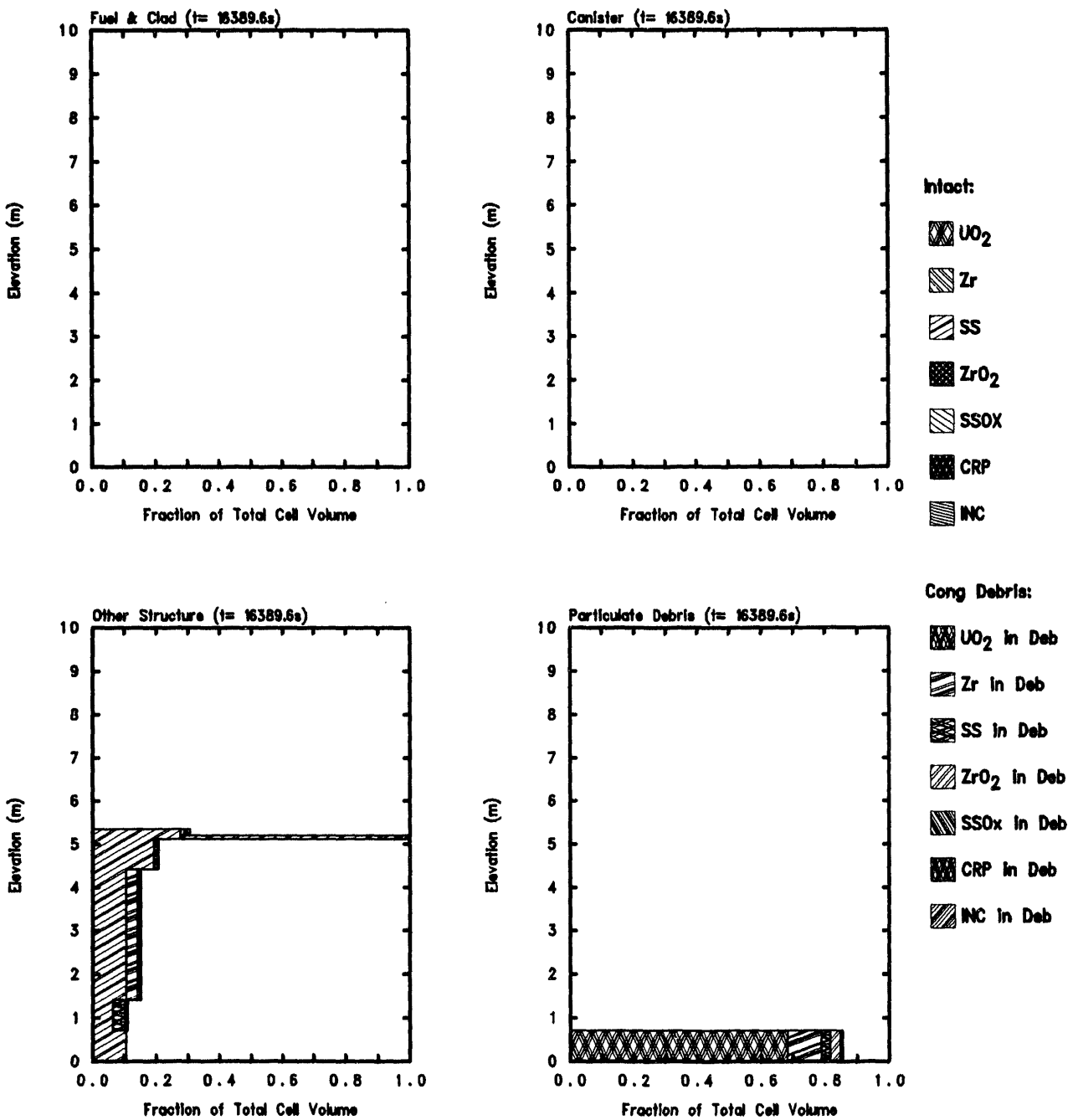

Figure 5.3.8. Core Ring 1 Fuel/Clad (upper left), Canister (upper right), Other Structure (lower left) and Particulate Debris (lower right) Component Material Masses Predicted by MELCOR for LCHP-PF-P-M Sequence

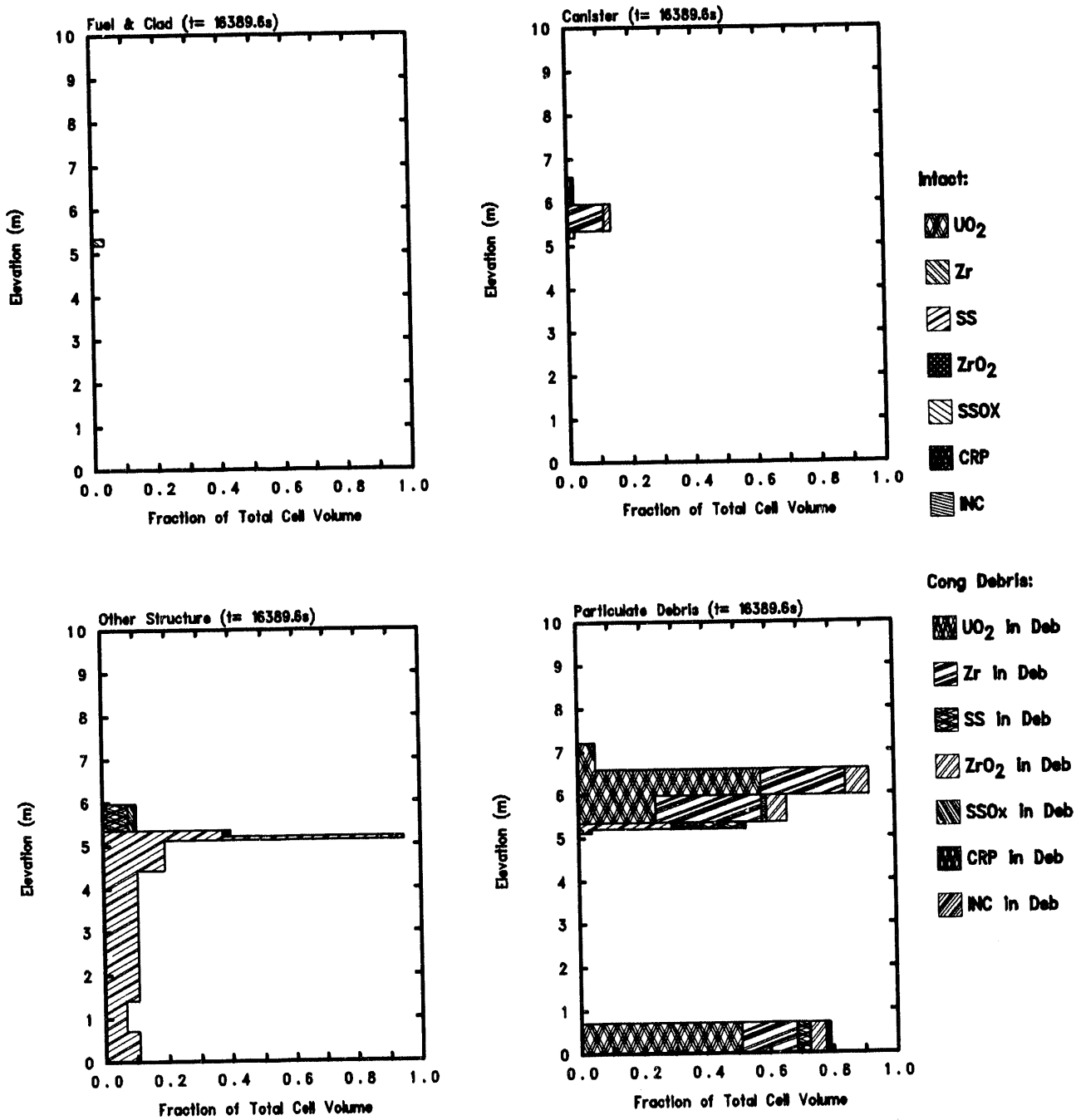

Figure 5.3.9. Core Ring 2 Fuel/Clad (upper left), Canister (upper right), Other Structure (lower left) and Particulate Debris (lower right) Component Material Masses Predicted by MELCOR for LCHP-PF-P-M Sequence

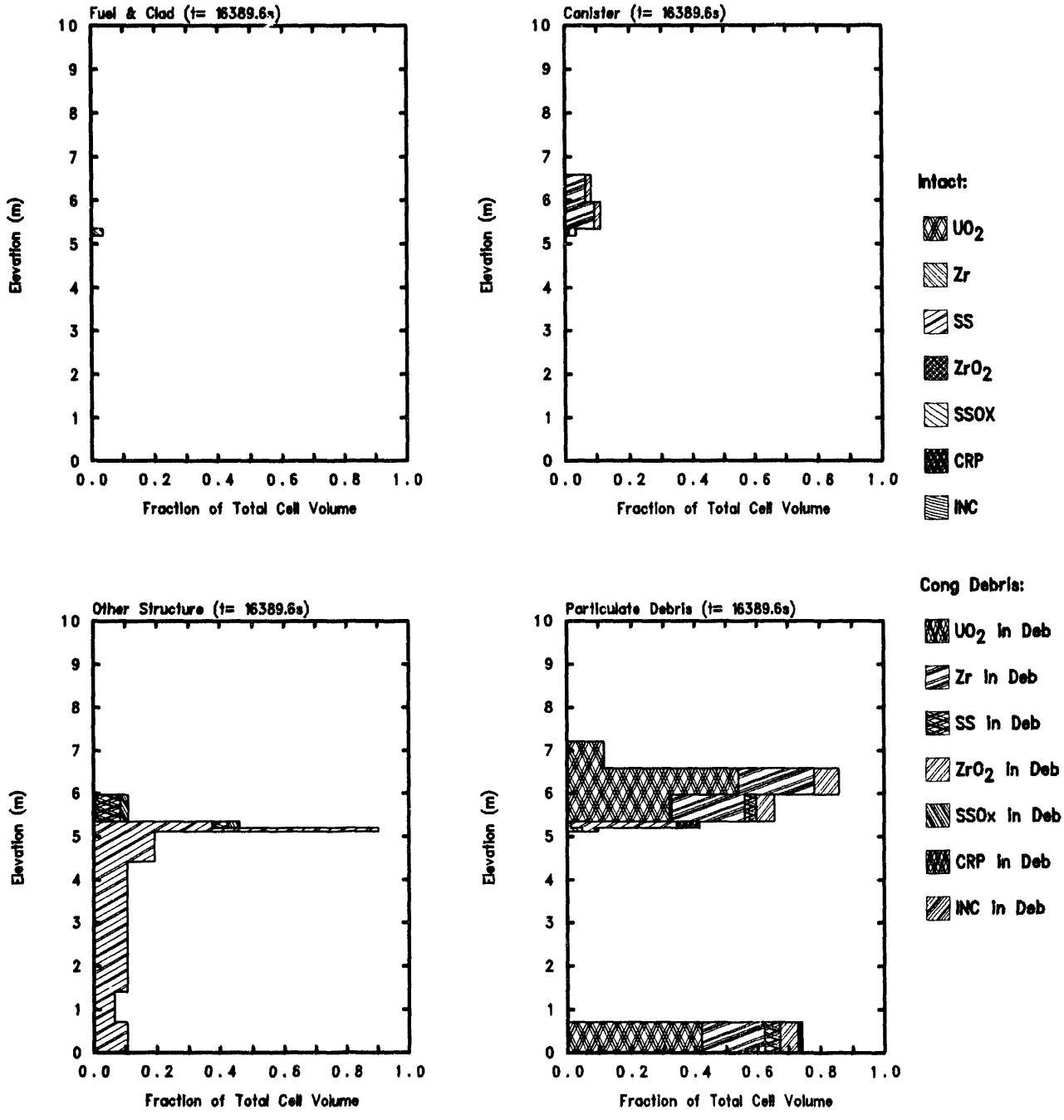

Figure 5.3.10. Core Ring 3 Fuel/Clad (upper left), Canister (upper right), Other Structure (lower left) and Particulate Debris (lower right) Component Material Masses Predicted by MELCOR for LCHP-PF-P-M Sequence

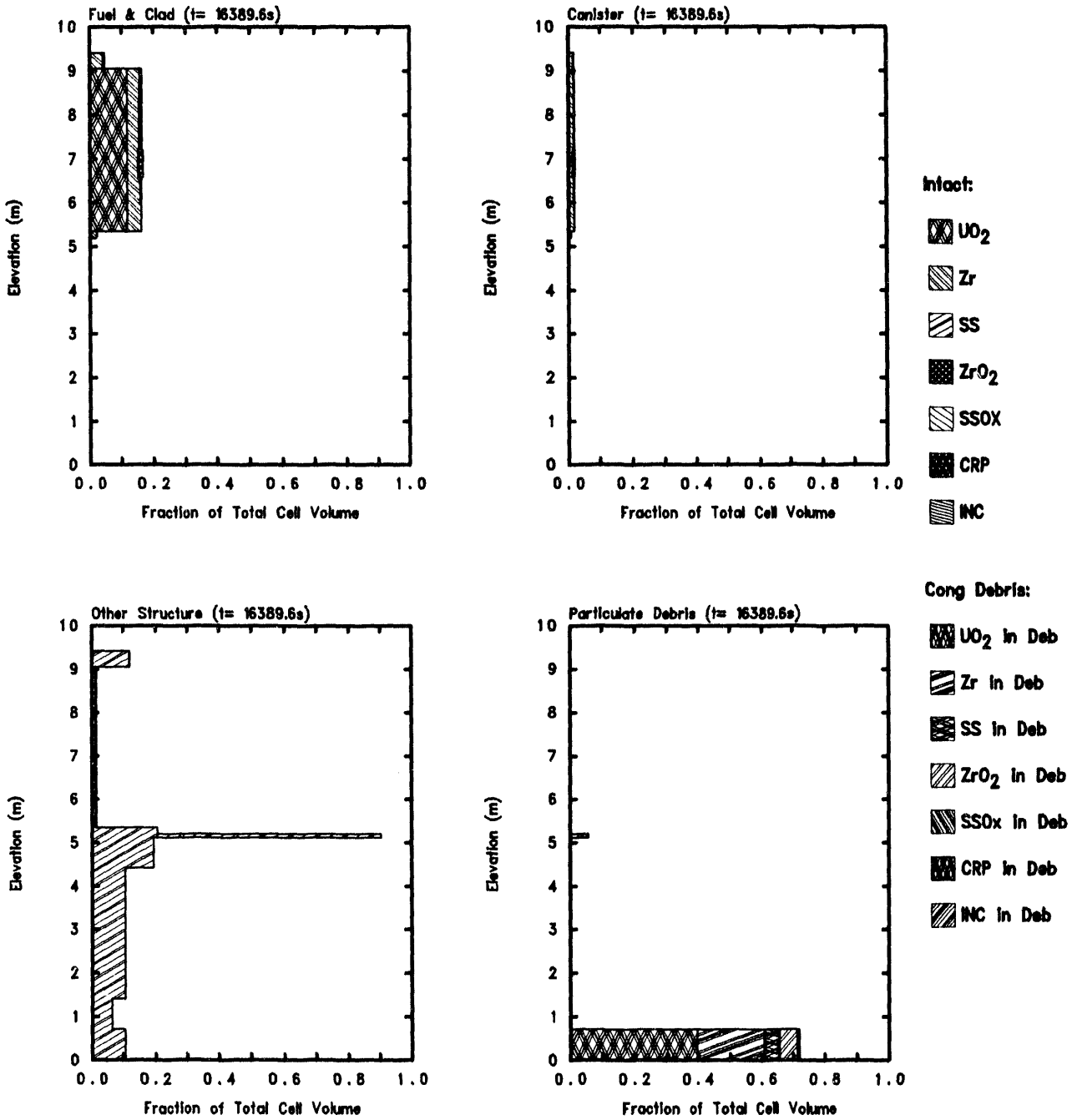

Figure 5.3.11. Core Ring 4 Fuel/Clad (upper left), Canister (upper right), Other Structure (lower left) and Particulate Debris (lower right) Component Material Masses Predicted by MELCOR for LCHP-PF-P-M Sequence

As visible in Figure 5.3.8, the innermost ring has no intact structure in the active fuel region at all at the time of vessel failure, but there is a substantial debris bed visible in the lowest axial level in the lower plenum. In the second and third rings (Figures 5.3.9 and 5.3.10), a very small intact clad mass is visible, corresponding to the non-fueled core support material in level 6; also in the second and third rings, a small intact canister mass is visible in several levels just above the core support plate. Most of the material in these middle two rings is in the particulate debris bed, held up by the core support plate in level 5 (at >5m) and the non-fueled core material in level 6. Note that there is a significant debris bed also present in the lower plenum; that debris comes from the failure of the innermost ring, through the debris radial relocation model. The material in the outermost ring at the time of vessel failure (Figure 5.3.11) is still mostly intact.

Tables 5.3.2 and5.3.3 summarize the state of the various materials in the core active fuel region, core plate and lower plenum at vessel breach. Masses of intact components and of debris components are presented for each region in Table 5.3.2; in Table 5.3.3 the average debris temperatures and the fraction of debris material molten at the time of vessel failure are included.

Compared to corresponding results for the low-pressure LCLP-PF-R-N sequence, given in Tables 5.1.2 and5.1.3, MELCOR predicts more intact material remaining in the active fuel region at the time the vessel fails at high pressure (mostly in the outermost, low-powered ring as illustrated in Figure 5.3.11); there is also more particulate debris in the active fuel region and less in the lower plenum predicted in that low-pressure sequence than for this high-pressure sequence. In both sequences, the core support plate and lower plenum structural steel is basically intact at vessel failure.

Figure 5.3.12 shows the total masses of core materials (UO_2, Zircaloy and ZrO_2, stainless steel and steel oxide, and control rod poison) remaining in the vessel. As noted in Table 5.3.1, debris ejection began immediately after lower head failure. This figure illustrates that the core material was lost from the vessel to the cavity in step-like stages. Almost all of the UO_2 was transferred to the cavity within 10.5hr after the start of the transient, as was the unoxidized zircaloy, the associated zirc oxide and the control rod poison. About half of the structural steel in the lower plenum was predicted to remain unmelted and in place throughout the entire transient period calculated, together with some associated steel oxide.

Zircaloy oxidation began at about 1-2hr, as indicated by the production of hydrogen in the core illustrated in Figure 5.3.13. No other gases were calculated to be generated in the core. The hydrogen produced by the time the vessel failed at 4.55hr corresponds to oxidation of 17% of the total zircaloy mass initially present in the core, and 4% and 0.9% of the structural steel in the core and lower plenum regions, respectively.

In the low-pressure LCLP sequence analyses discussed in Sections 5.1 and 5.2, all of the debris lost from the core simply fell directly into the cavity. In the high-pressure LCHP analyses, in contrast, the potential exists for high-pressure melt ejection (HPME) to disperse core debris throughout containment, with direct containment heating (DCH) possible. The MAAP analyses assumed that "the initial discharge of corium and water

Table 5.3.2. Core Masses at Vessel Failure Predicted during LCHP-PF-P-M Sequence

	Intact	Debris
Active Fuel Region Masses (kg)		
UO_2	42,900	59,377
Zircaloy	28,681	20,632
ZrO_2	4,415	4,535
Steel	19,288	6,480
Steel oxide	1,066	77
Control rod poison	355	350
Total	96,705	91,380
Core Support Plate Masses (kg)		
UO_2	0	0
Zircaloy	255	164
ZrO_2	63	0
Steel	11,616	315
Steel oxide	12	1
Control rod poison	0	37
Total	11,946	517
Lower Plenum Masses (kg)		
UO_2	23	69,298
Zircaloy	1,443	14,279
ZrO_2	142	3,438
Steel	49,240	4,192
Steel oxide	149	328
Control rod poison	0	166
Total	50,997	91,701

Table 5.3.3. Core State at Vessel Failure Predicted during LCHP-PF-P-M Sequence

Region	Average Debris Temperature (K)	Fraction of Debris Material Molten
Active Fuel	2810	47%
Core Support Plate	833	0%
Lower Plenum	3113	100%

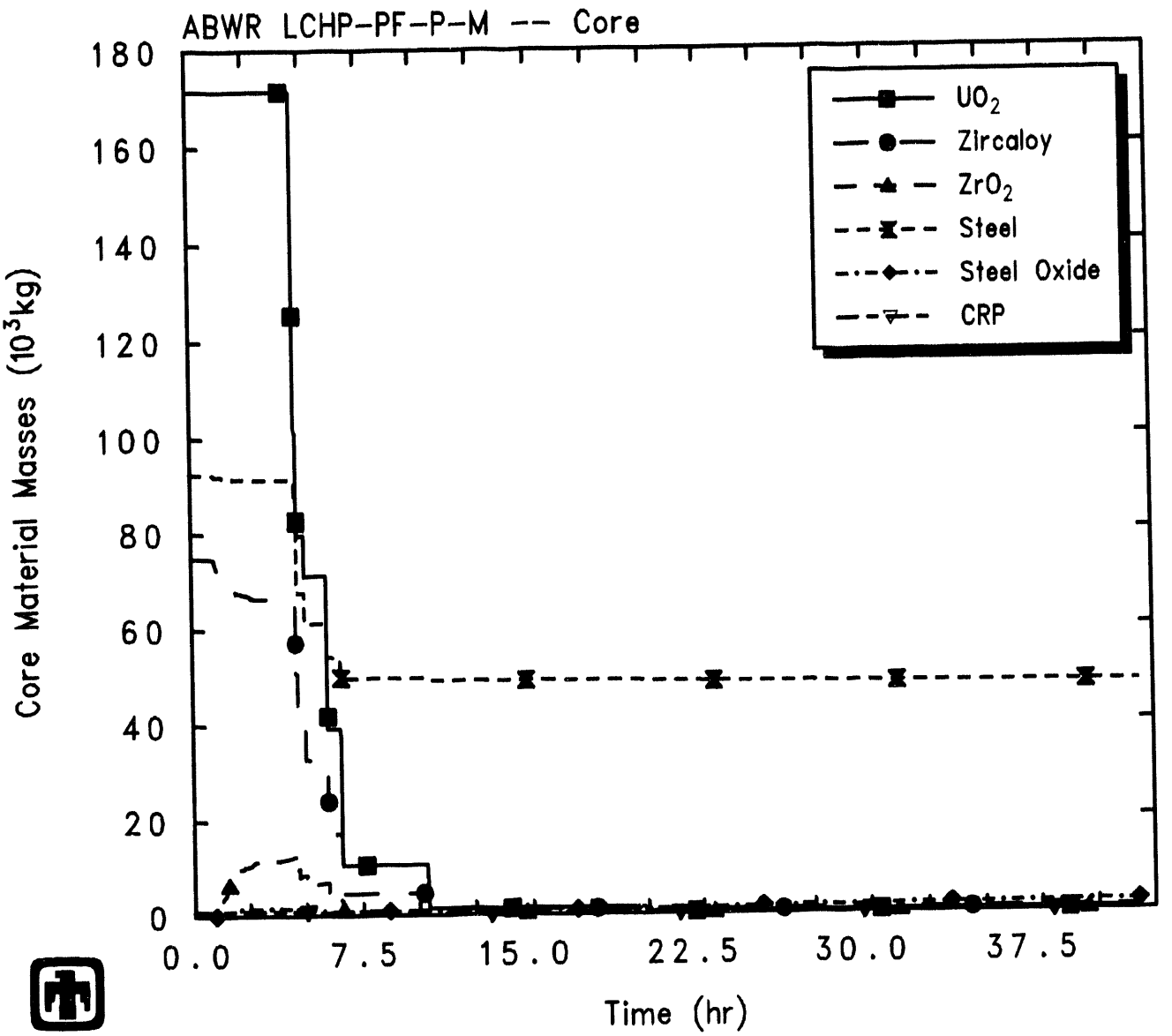

Figure 5.3.12. Core Material Masses Predicted by MELCOR for LCHP-PF-P-M Sequence

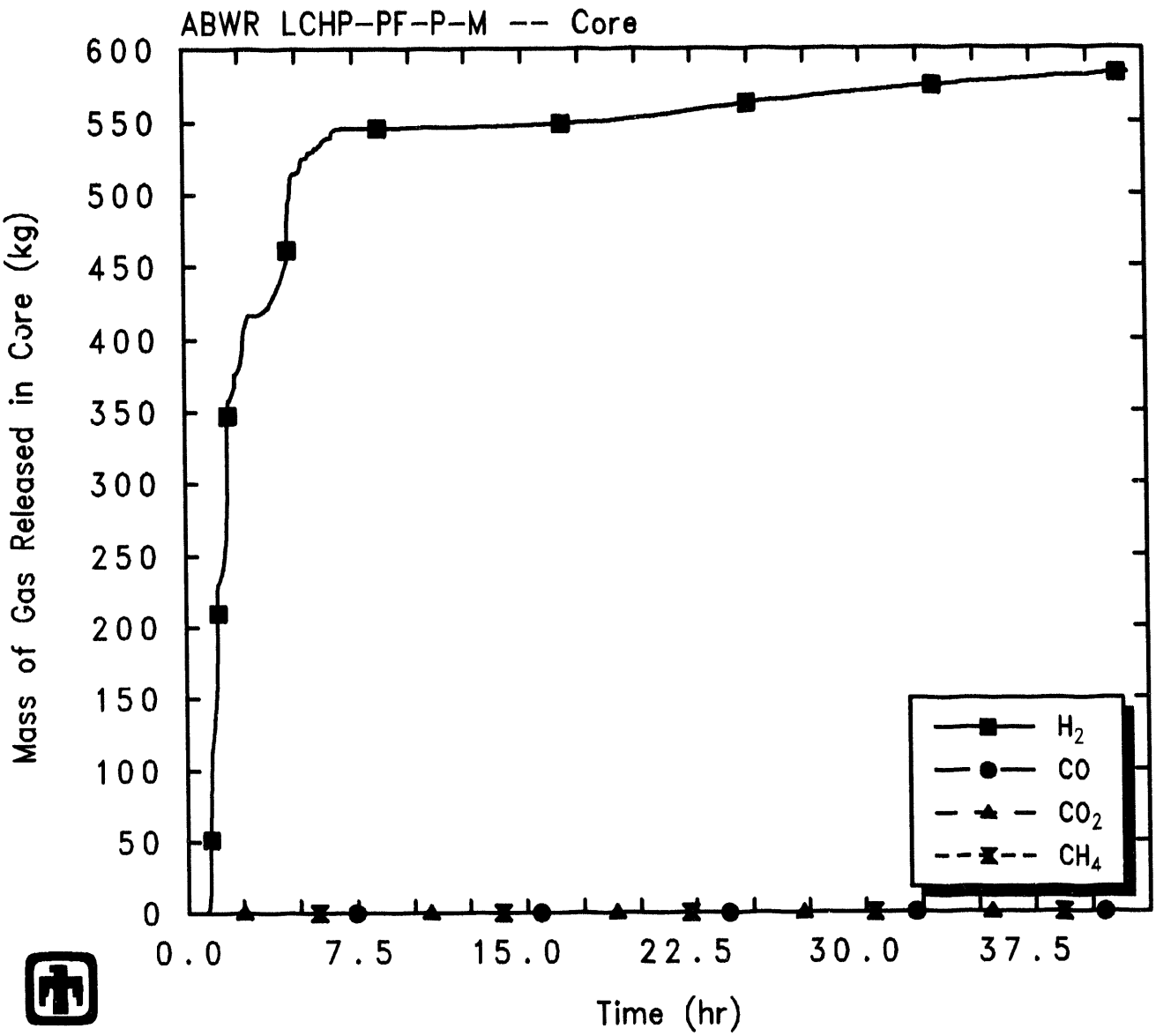

Figure 5.3.13. In-Vessel Hydrogen Production Predicted by MELCOR for LCHP-PF-P-M Sequence

from the lower plenum is entrained by the steam from the vessel into the upper drywell and wetwell because the vessel fails at high pressure" [1]. MELCOR calculations were done with and without high-pressure debris dispersal assumed, and the results showed that it was necessary to assume some hot core debris entrained into the upper drywell for the upper drywell to heat up sufficiently (to 533K) for penetration leakage to occur. However, the amount of debris entrained into the upper drywell must be limited so that in the high-pressure sequences with spray injection (discussed in the next two subsections) the sprays can cool the drywell sufficiently that that failure temperature is not reached. Also, the high-pressure melt ejection and associated direct containment heating must be benign enough not to pressurize containment to the rupture disk setpoint immediately upon vessel failure and HPME/DCH interactions. The debris distribution and interaction times used in these MELCOR ABWR analyses are not necessarily "correct"; they simply satisfy these constraint criteria. The total amount of core debris ejected during high-pressure melt ejection and the amounts carried to various containment volumes in this LCHP-PF-P-M analysis are shown in Figure 5.3.14, and correspond to about 15% of the material eventually lost from the vessel. The remainder of the core debris ejected from the vessel is assumed to fall directly into the cavity as a low-pressure melt ejection or pour, as in the low-pressure scenarios.

Figure 5.3.15 shows the collapsed liquid level in the lower drywell (cavity) control volume in the MELCOR calculation; the level given is referenced to 0 at the bottom of the vessel lower plenum, and the bottom of the cavity control volume is indicated in the figure. The sudden rise in liquid level at about 4.5hr corresponds to the remaining lower plenum water pouring out the vessel breach and to the passive flooder opening; MELCOR predicts the passive flooder to open almost immediately (~25s) after vessel failure in this LCHP-PF-P-M sequence. Note that Table 5.3.1 shows that MAAP also predicts the passive flooder opening immediately after vessel failure in this sequence. Water pours from the wetwell into the drywell and the cavity liquid level settles to a pool depth of about 2m, the level of the upper horizontal vent, almost immediately. Later in the transient the pool depth in the lower drywell oscillates between 2m and 5-5.5m, as cycling of the DW/WW vents occasionally pushes water from the suppression pool over to the lower drywell.

The lower drywell and wetwell atmosphere and pool temperatures are presented in Figure 5.3.16. As soon as the vessel fails and core debris is ejected into the cavity, the lower drywell atmosphere temperature spikes rapidly and reaches the 533K (500°F) setpoint for passive flooder actuation. The hot debris in the cavity in the MELCOR calculation keeps the lower drywell pool temperature 25-75K hotter than the suppression pool temperature; the cavity pool temperature remains nearly constant at ~425K while the suppression pool temperature slowly rises. Prior to vessel breach, the wetwell atmosphere is about 20K hotter than the suppression pool, and the wetwell atmosphere temperature remains more nearly constant while the suppression pool continually heats up. The cavity atmosphere remains 25-50K hotter than the cavity pool throughout the transient, with the differential increasing with time.

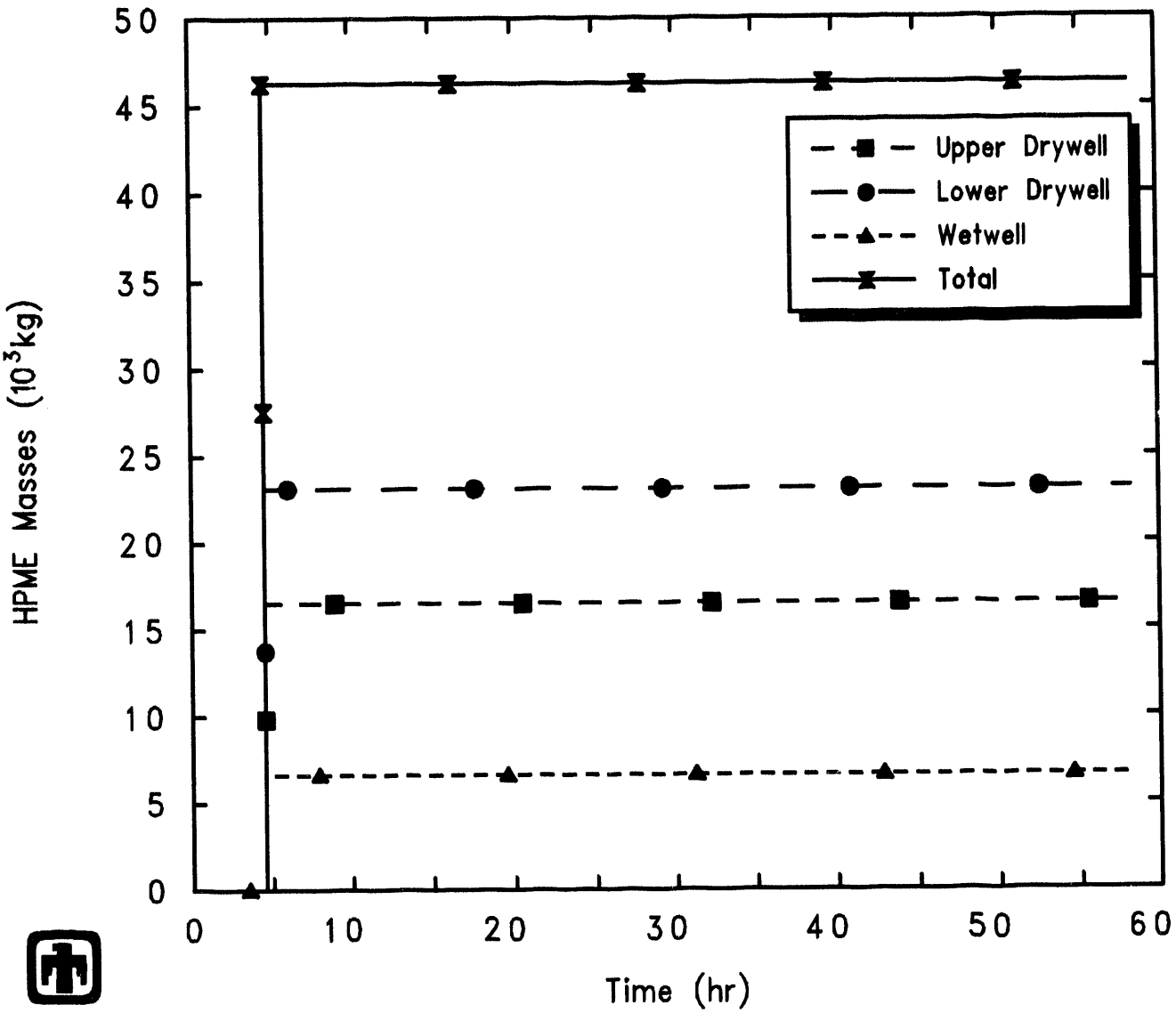

Figure 5.3.14. High-Pressure Melt Ejection Predicted by MELCOR for LCHP-PF-P-M Sequence

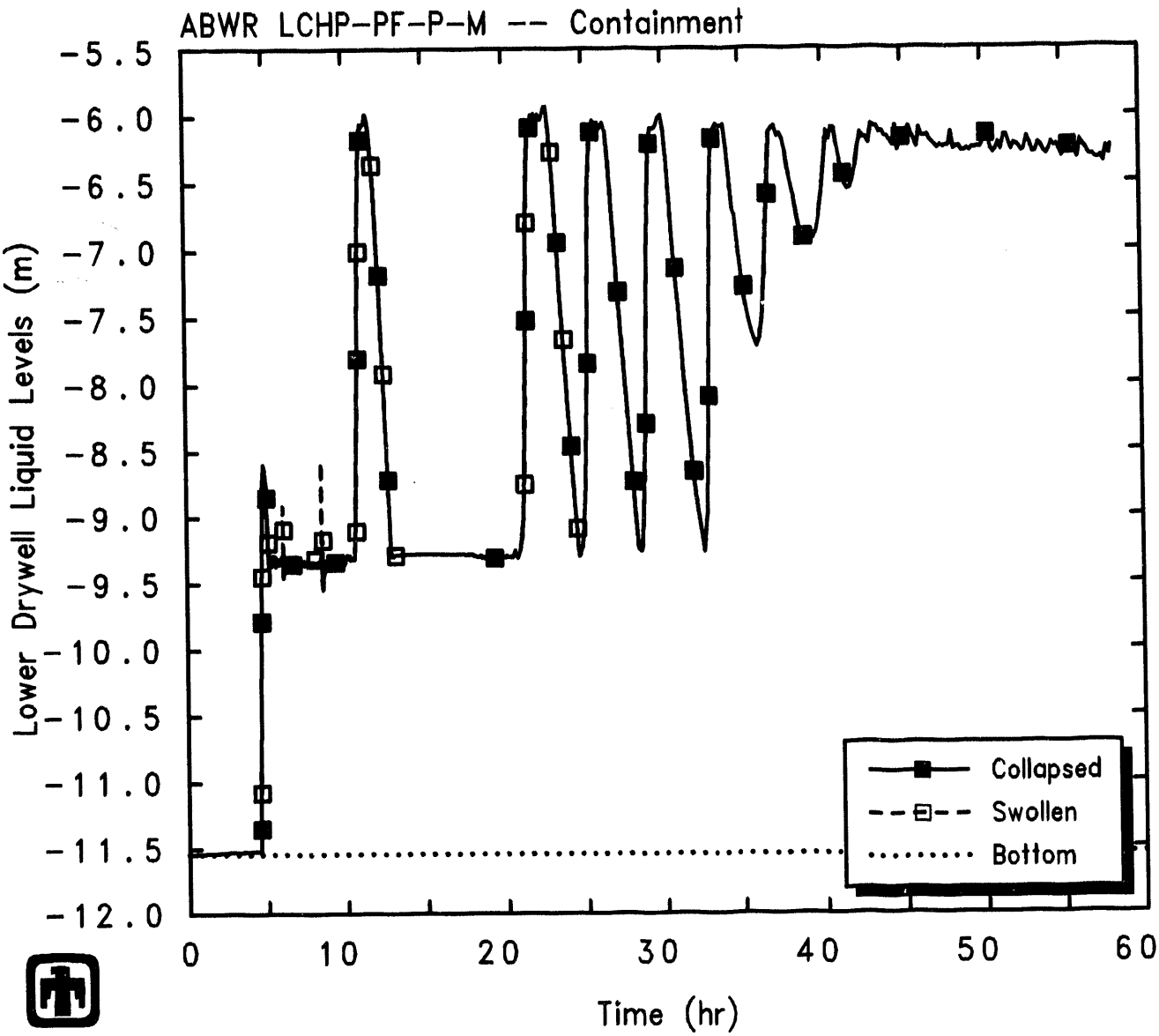

Figure 5.3.15. Lower Drywell Liquid Level Predicted by MELCOR for LCHP-PF-P-M Sequence

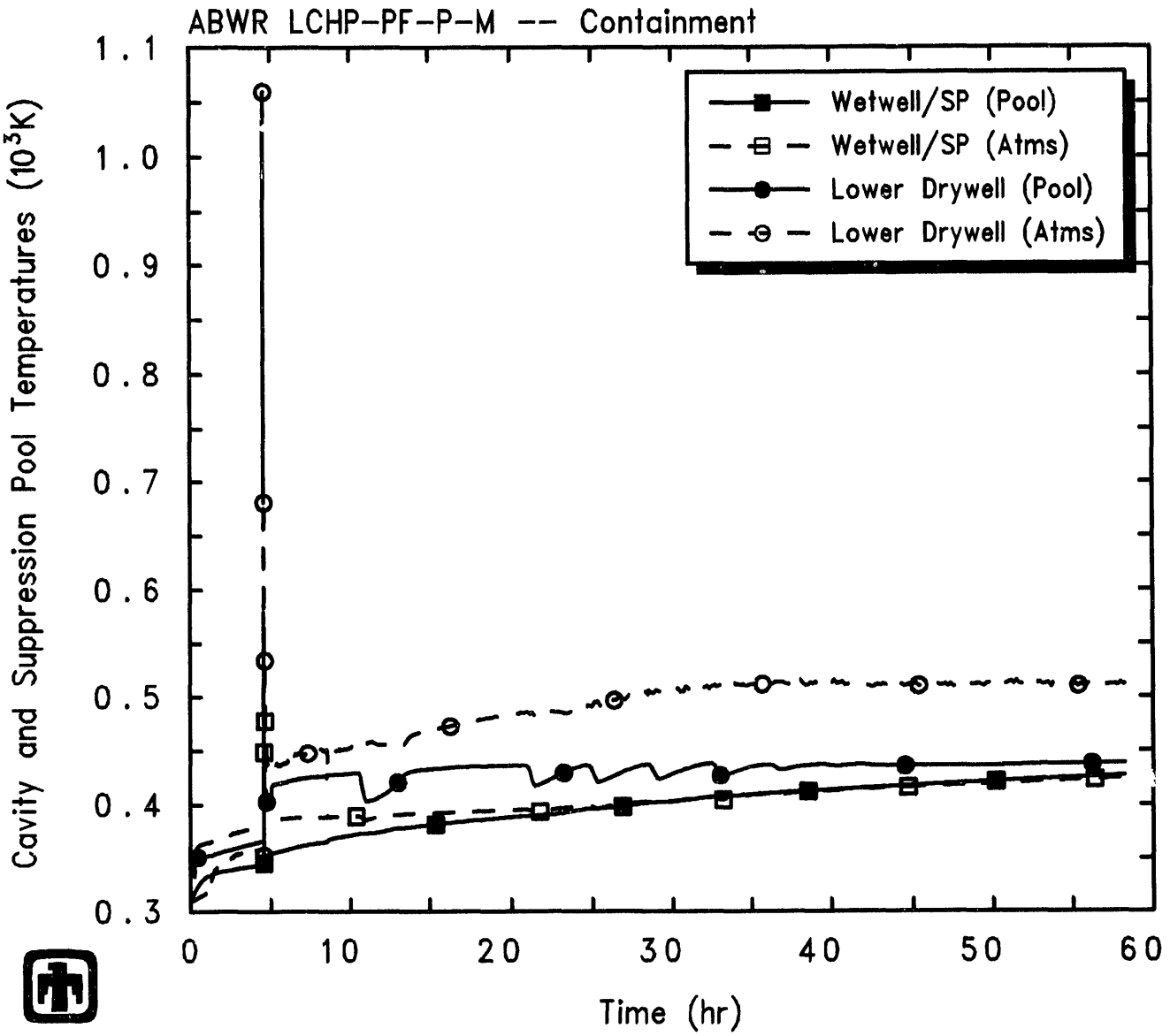

Figure 5.3.16. Lower Drywell and Suppression Pool Temperatures Predicted by MELCOR for LCHP-PF-P-M Sequence

Figure 5.3.17 give the drywell and wetwell pool masses for the MELCOR analysis, compared to the pool masses calculated by MAAP (taken from Figure 19E.2-5D in [1]). There appears to be a small difference in the suppression pool initial mass (and/or level) in the two calculations. Also, MELCOR predicts a gradual, long-term drop in suppression pool level with some intermittent transfers of water to the lower drywell superimposed on the slow level decline, while MAAP predicts more constant suppression pool and lower drywell pool masses after passive flooder opening, with no drops in suppression pool mass and corresponding jumps in cavity pool mass until about 40hr (with another at ~60hr).

The pressures calculated by MELCOR in the various containment control volumes are depicted in Figure 5.3.18, together with the containment pressure from the MAAP analysis (taken from Figure 19E.2-5A in [1]). The results from the two codes are generally similar qualitatively, but with a number of quantitative differences and shifts in timing. Both codes predict a rapid pressure increase in containment immediately after vessel failure, due to steam generation from hot debris and water falling into the cavity from the lower plenum. That initial containment pressurization is greater in the MELCOR analysis than in the MAAP analysis, probably due to direct containment heating associated with high-pressure melt ejection in the MELCOR analysis. Both codes then predict a gradual pressurization of containment to around 700kPa, with MELCOR showing multiple brief depressurizations and repressurizations associated with water being displaced from the suppression pool to the lower drywell (as indicated in Figures 5.3.15 and 5.3.17) and MAAP showing fewer such pressure pulses, at about 40hr and at about 60hr.

Figure 5.3.19 gives the upper and lower drywell temperatures calculated by MELCOR, compared to corresponding MAAP results. (The MAAP curves included in this plot were taken from Figure 19E.2-5B in [1].) Large temperature spikes are predicted at vessel failure by both codes, at 2hr by MAAP and at 4.5hr by MELCOR. The spike in the lower drywell temperature at vessel failure triggers the passive flooder to open; the spike in the upper drywell temperature at vessel failure causes the seals in the movable penetrations to degrade, so that penetration leakage can occur. In both codes the upper drywell temperature reaches this failure temperature due to heat transfer from hot core debris assumed to have been swept into the upper drywell due to vessel failure at high pressure. As seen in the pressure comparison presented in Figure 5.3.18, that initial spike is greater in the MELCOR analysis than in the MAAP analysis, probably due to direct containment heating associated with high-pressure melt ejection in the MELCOR analysis. Both codes then predict the upper drywell significantly hotter than the lower drywell throughout the rest of this sequence. The lower drywell temperature calculated by MAAP agrees very well with the cavity pool temperature predicted by MELCOR, while the lower drywell atmosphere temperature calculated by MELCOR is hotter. The upper drywell temperature from MELCOR is significantly lower than the corresponding MAAP value after the initial spike, probably due partly to less debris assumed ejected into the upper drywell and partly to more rapid heat transfer from that debris to the upper drywell in the MELCOR direct containment heating model.

Figures 5.3.20 and 5.3.21 show the total and partial pressures, and the mole fractions, respectively, in the atmospheres of the four containment control volumes. The lower

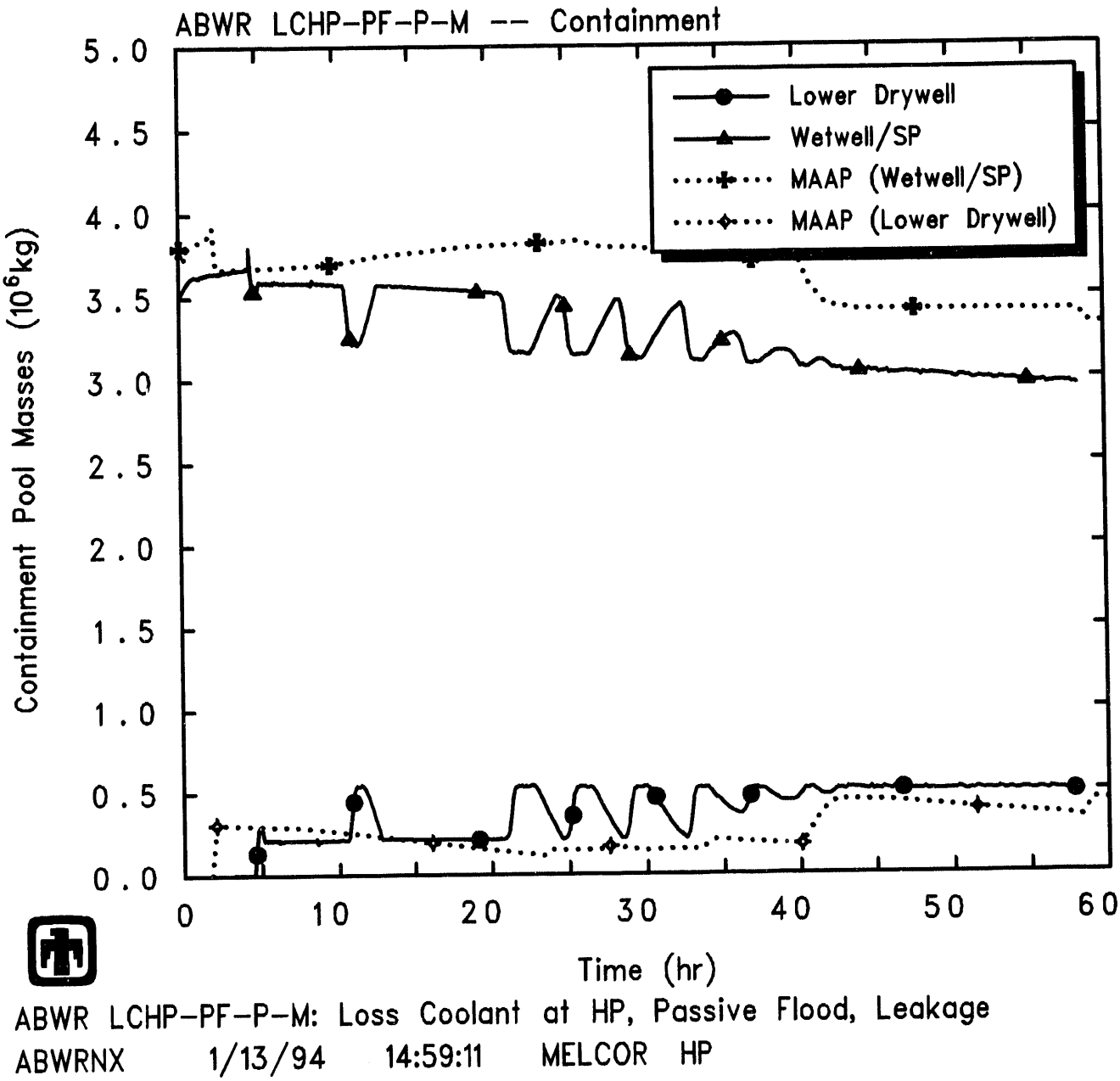

Figure 5.3.17. Lower Drywell and Suppression Pool Masses Predicted by MELCOR for LCHP-PF-P-M Sequence, Compared to MAAP

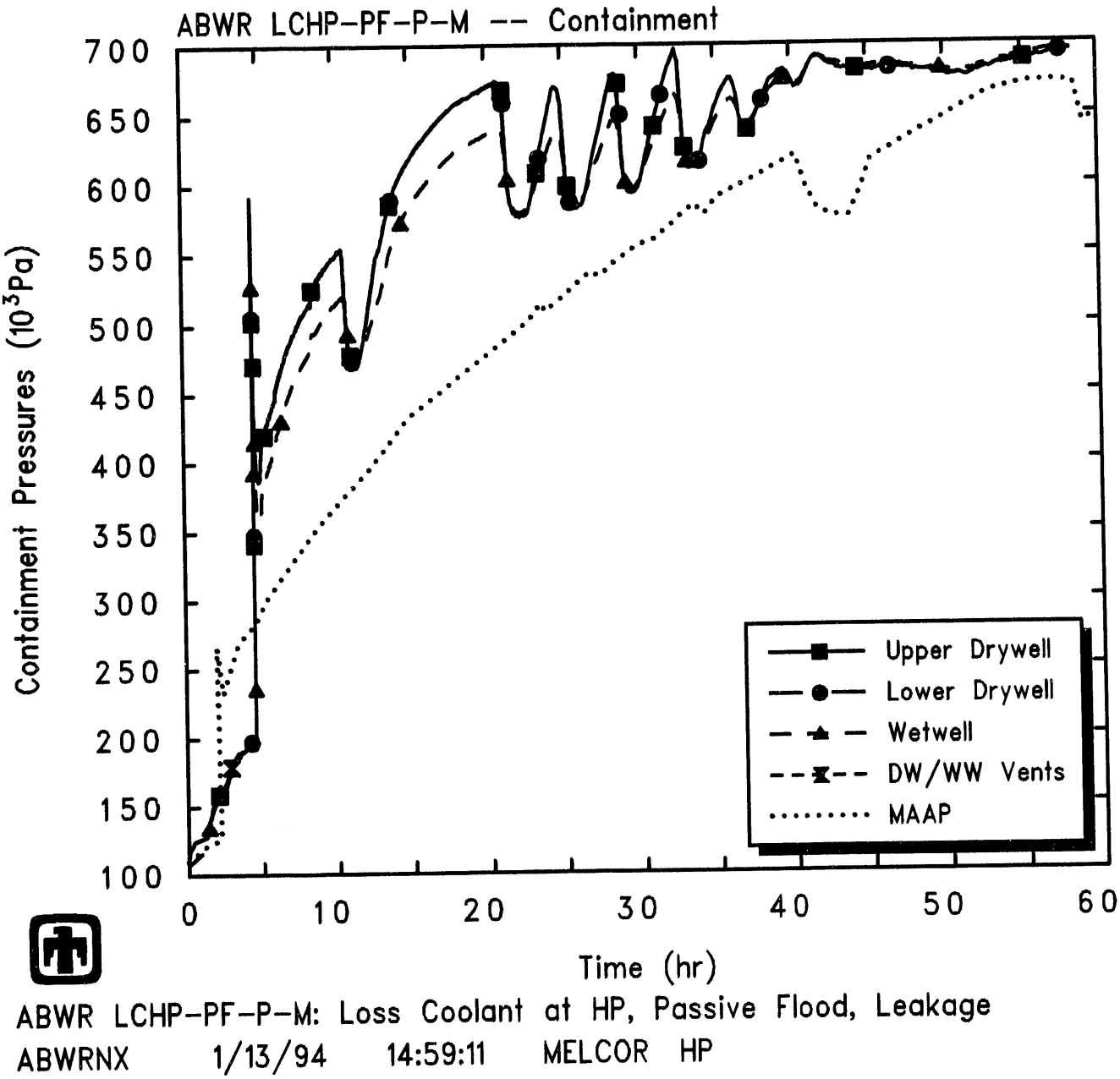

Figure 5.3.18. Containment Pressures Predicted by MELCOR for LCHP-PF-P-M Sequence, Compared to MAAP

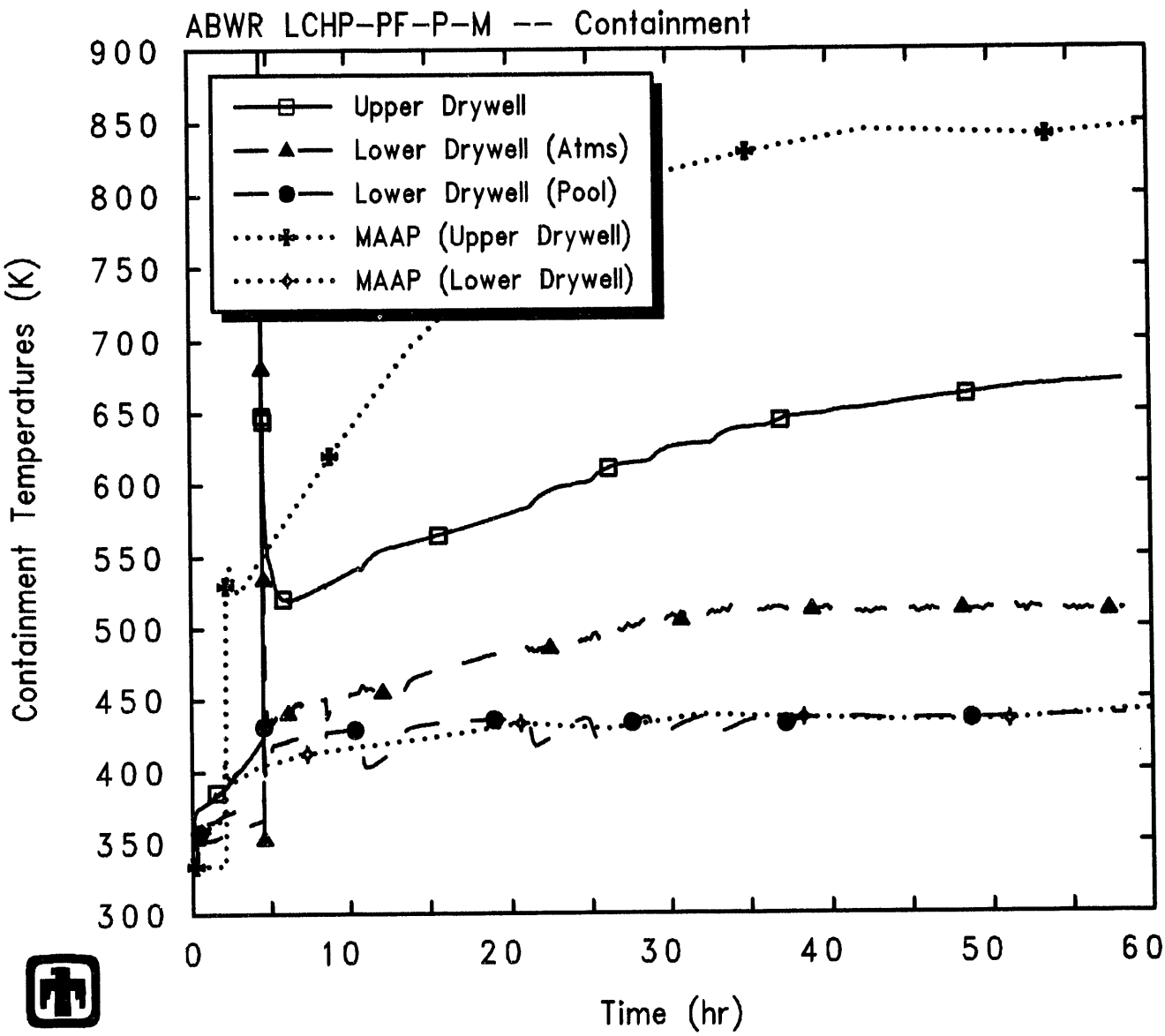

Figure 5.3.19. Containment Temperatures Predicted by MELCOR for LCHP-PF-P-M Sequence, Compared to MAAP

drywell and DW/WW vent atmospheres consist of almost all (80-90%) steam from vessel failure through calculation end; in the upper drywell, the concentration of steam increases a little more slowly after vessel failure, taking about 15hr to reach >90%. At about 12hr and after about 22hr, there are oscillations visible in both the lower drywell and the DW/WW vents (and in the upper drywell, but much smaller in magnitude) with steam concentration dropping due to condensation while hydrogen concentration rises. These oscillations in steam concentration and partial pressure cause the oscillations in overall containment pressures and temperatures shown in Figures 5.3.18 and 5.3.19. In the suppression pool, most (50-60%) of the wetwell atmosphere after vessel failure is hydrogen, although the concentration of hydrogen is dropping and the concentration of steam increasing after penetration leakage begins.

The flow out the movable penetrations in the MELCOR calculation is presented in Figure 5.3.22. Both MAAP and MELCOR predict penetration leakage in this sequence, since the temperature in the upper drywell rises above 533K (500°F), as illustrated in Figure 5.3.19). Note that, in both codes, the upper drywell temperature reaches this penetration seal leakage temperature only because hot core debris was assumed swept into the upper drywell due to vessel failure at high pressure.

The total mass of debris in the cavity, the mass of ejected core debris, the mass of ablated concrete and the mass of gases generated in the cavity calculated by MELCOR are illustrated in Figure 5.3.23. The core debris in the cavity includes both debris ejected directly into the cavity during high-pressure melt ejection, debris ejected into the lower drywell atmosphere during high-pressure melt ejection which then settles into the cavity, and debris subsequently poured directly into the cavity during low-pressure melt ejection. The mass of core debris in the cavity is basically an inversion of the masses retained in-vessel, presented in Figure 5.3.12, and the debris ejection can be seen to occur in discrete steps or stages. The mass of core debris in the cavity includes most of the core debris lost from the vessel, since Figure 5.3.14 shows that only ~10% of the total core debris lost from the vessel is dispersed to the upper drywell or wetwell in this MELCOR analysis. Little concrete ablation occurs before about 12hr; after that time, the mass of concrete ablated increases continuously with time.

Core-concrete interaction results in the production of carbon dioxide and hydrogen; reduction of these gases by the molten metal also gave rise to carbon monoxide and hydrogen. Figure 5.3.24 presents the production of various noncondensable gases in the cavity due to core-concrete interaction in this LCHP-PF-P-M sequence, calculated by MELCOR. Almost all of the cavity gas production before about 35-40hr is in the form of hydrogen, with a growing amount of CO produced after that time. CO is produced only after all the zironium in the cavity is oxidized to ZrO_2, which happens at about 35hr in this case, because before that time Zr is assumed to reduce any CO_2 generated to pure carbon ("coking"); this reaction can be disabled in MELCOR, but is enabled by default.

Figure 5.3.25 gives the calculated maximum cavity depth and radius. (Note that these represent maximum, not average, ablation distances.) Immediately after core debris is first ejected from the vessel to the cavity upon vessel breach in the MELCOR analysis, there is a brief period of rapid radial ablation lasting less than 1hr, which stops after about

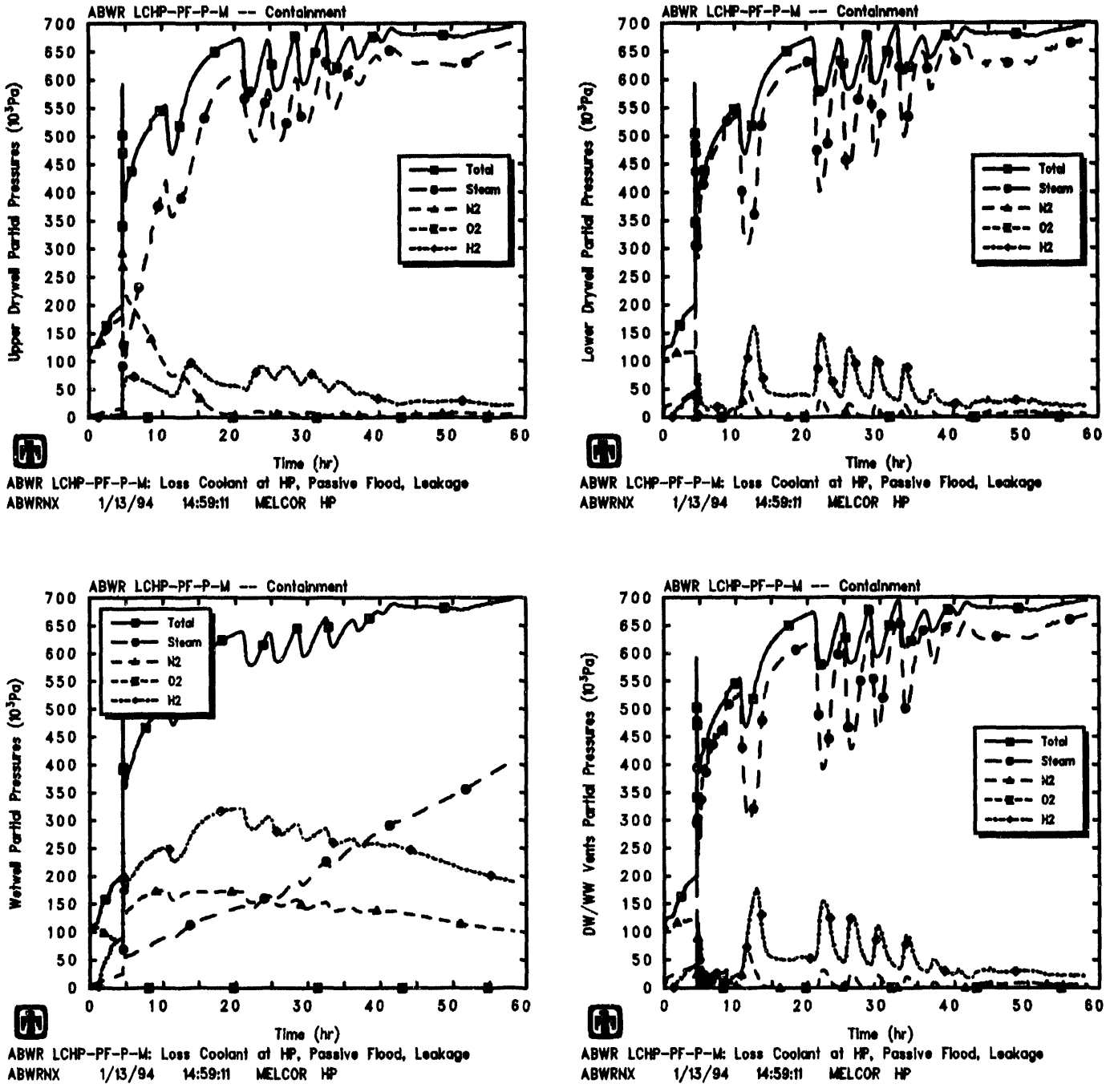

Figure 5.3.20. Containment Upper Drywell (upper left), Lower Drywell (upper right), Wetwell (lower left) and DW/WW Vent (lower right) Partial Pressures Predicted by MELCOR for LCHP-PF-P-M Sequence

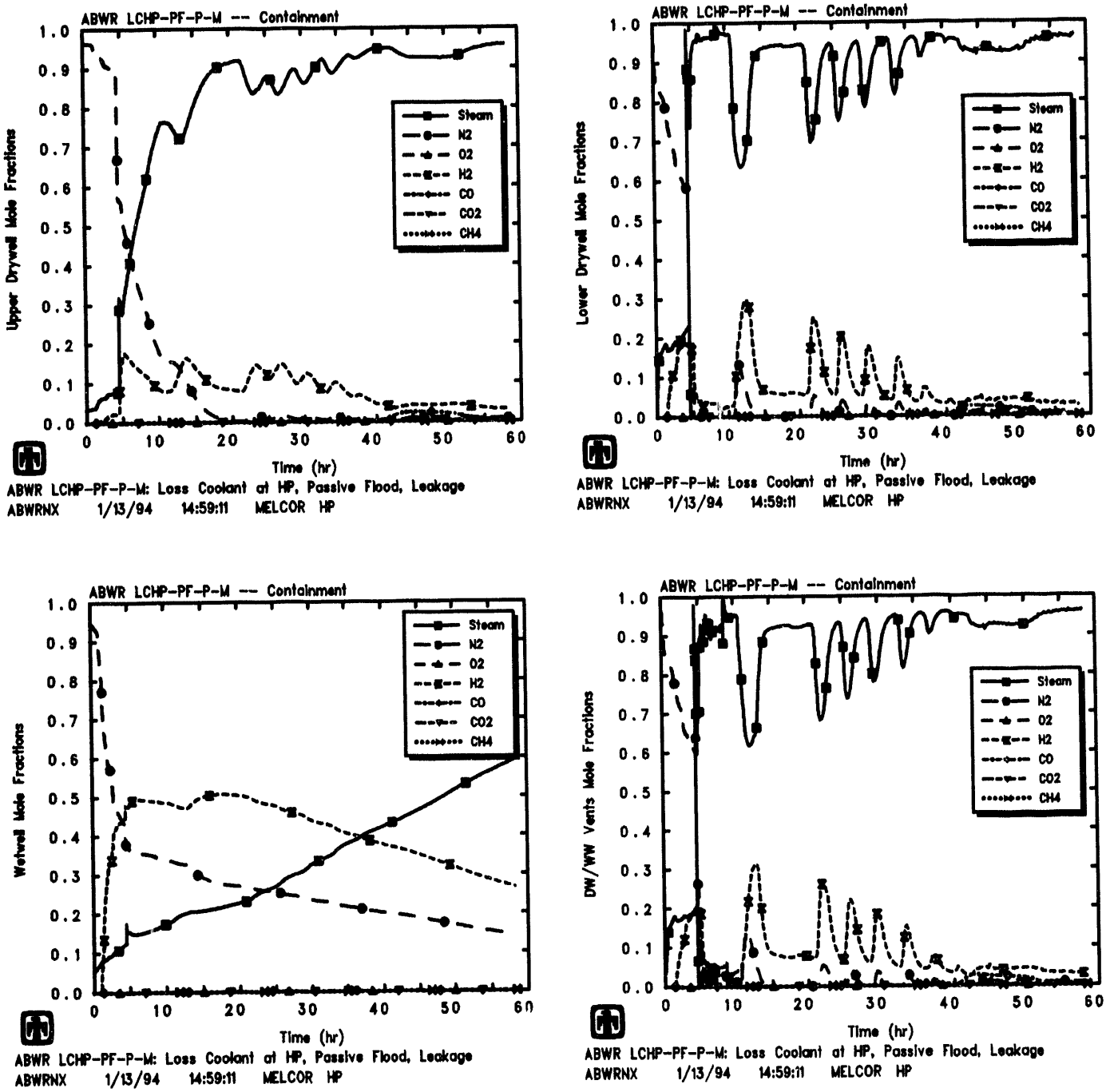

Figure 5.3.21. Containment Upper Drywell (upper left), Lower Drywell (upper right), Wetwell (lower left) and DW/WW Vent (lower right) Mole Fractions Predicted by MELCOR for LCHP-PF-P-M Sequence

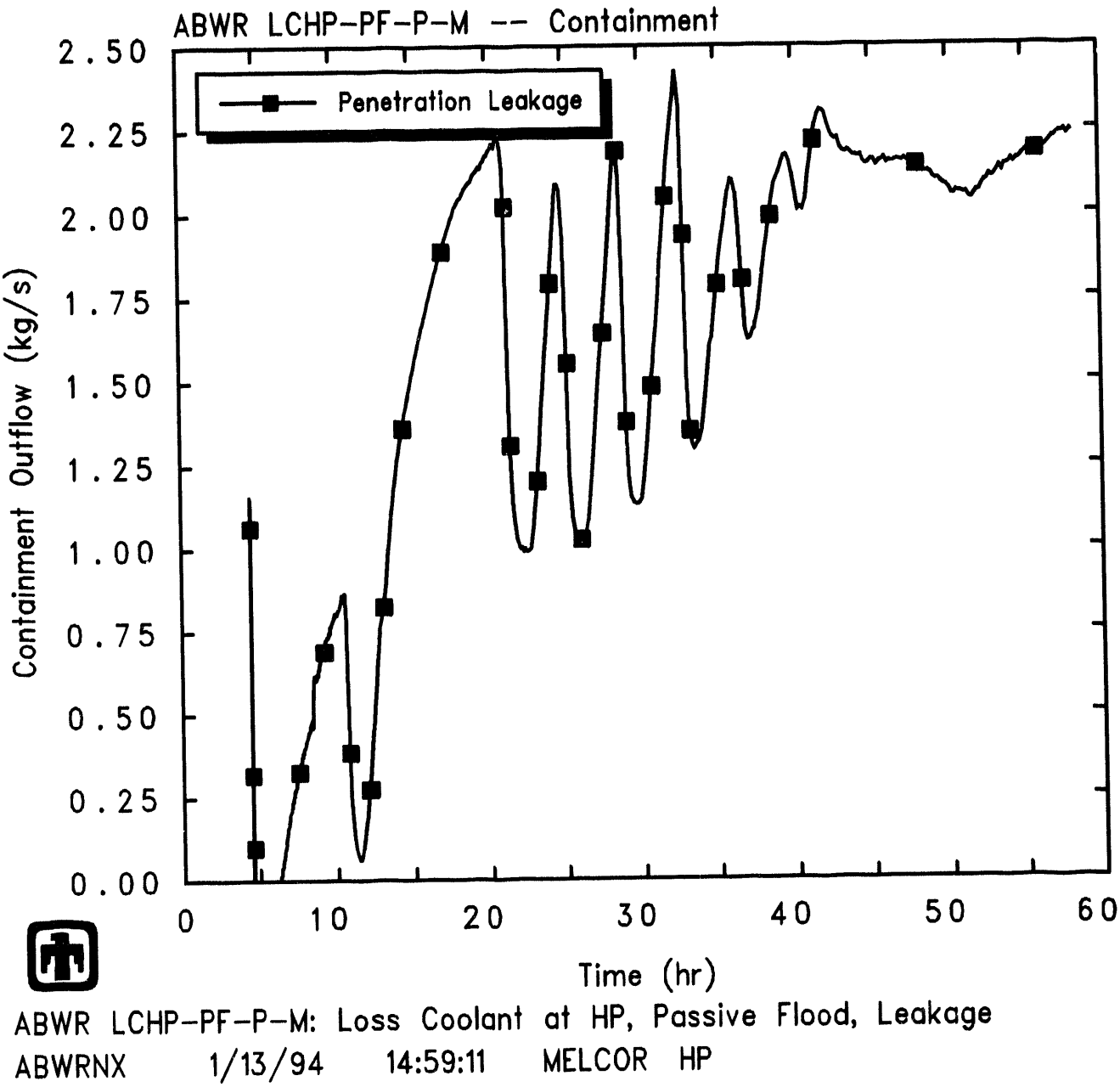

Figure 5.3.22. Movable Penetrations Leakage Mass Flow Predicted by MELCOR for LCHP-PF-P-M Sequence

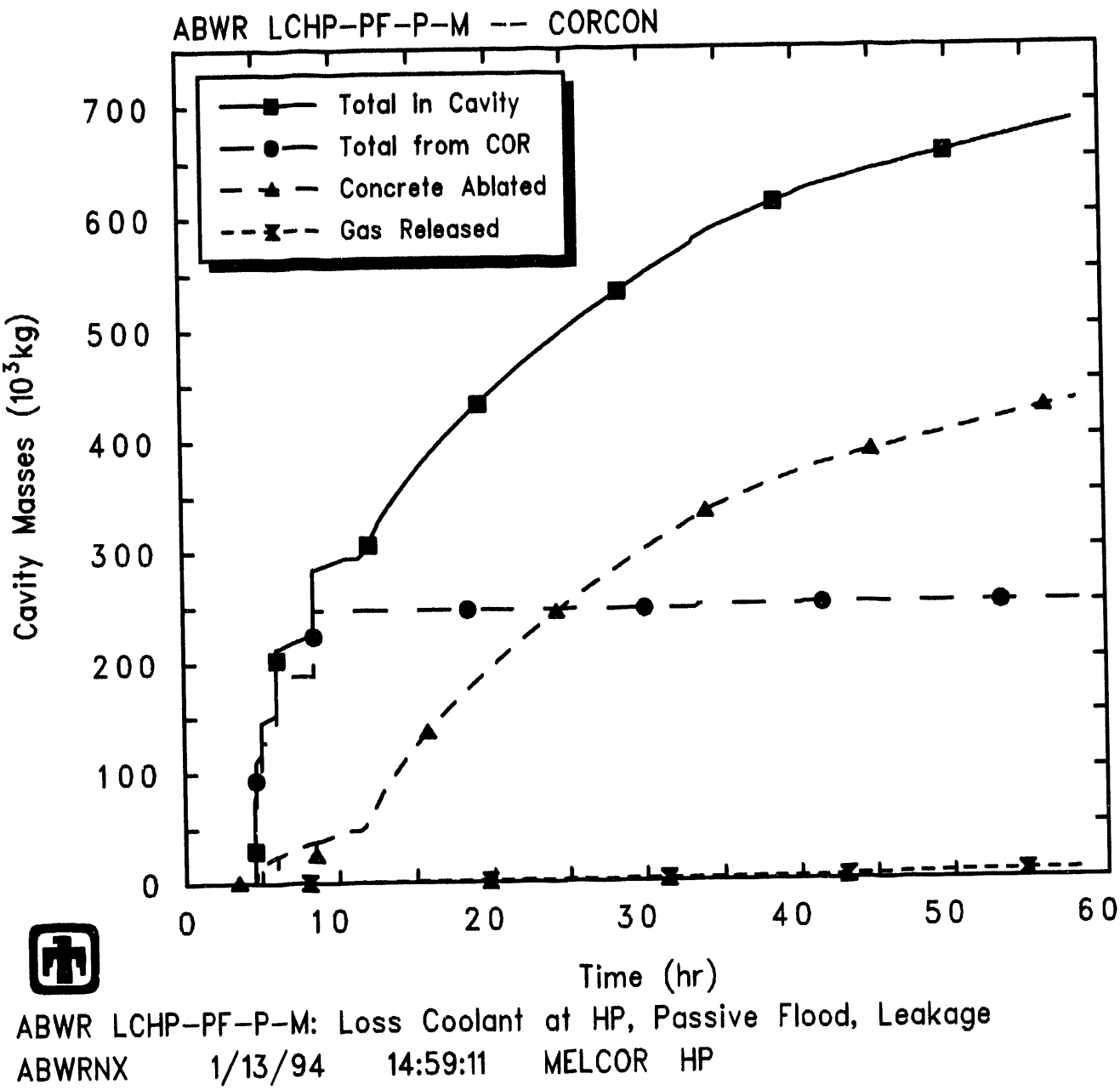

Figure 5.3.23. Cavity Material Masses Predicted by MELCOR for LCHP-PF-P-M Sequence

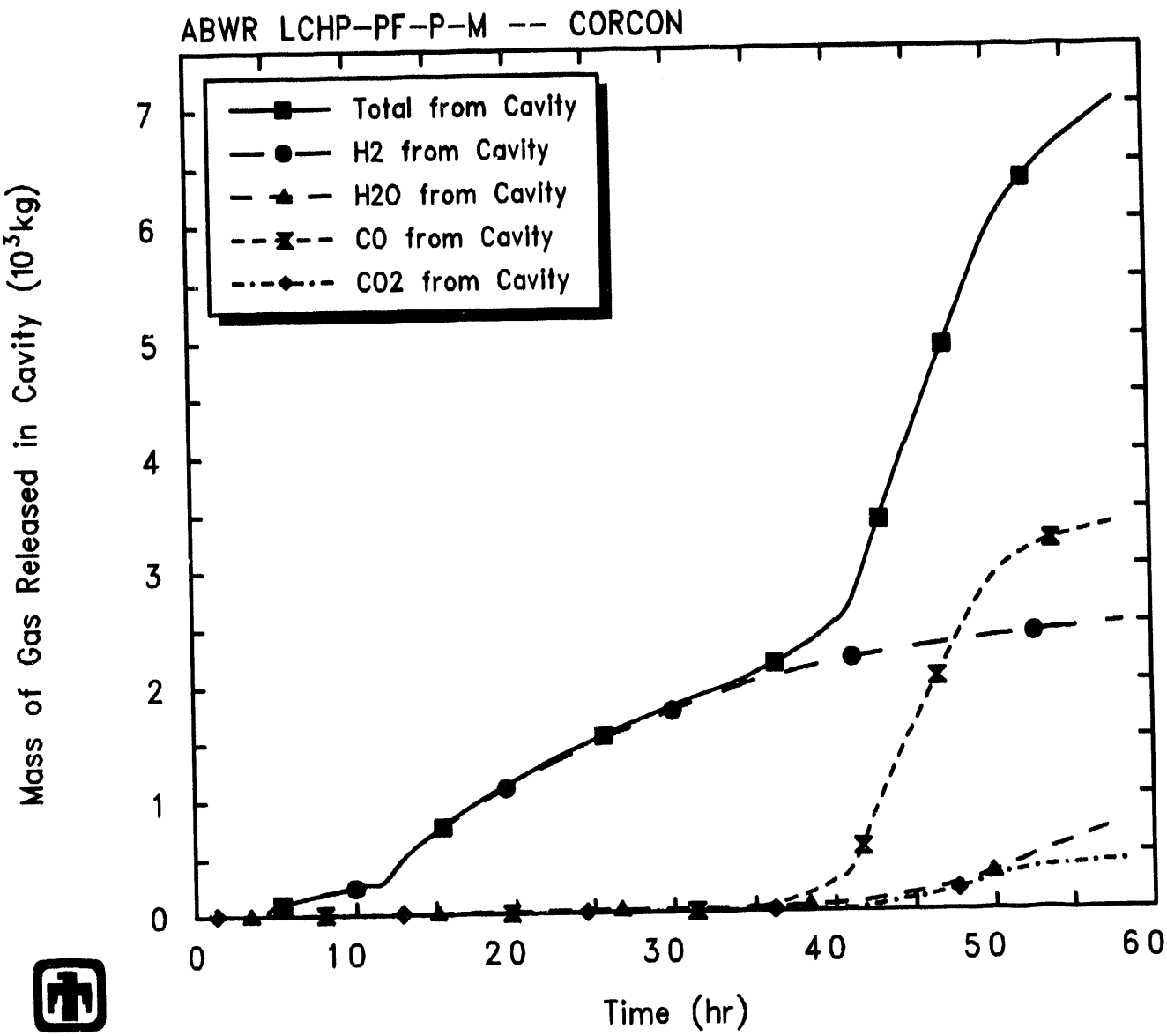

Figure 5.3.24. Cavity Gas Production Predicted by MELCOR for LCHP-PF-P-M Sequence

2cm of concrete loss. The bulk of the concrete ablation calculated is axially downward, with the MELCOR calculation stopping at 58hr when the axial ablation equals and tries to exceed the specified available concrete thickness of 2m.

Figure 5.3.26 shows the predicted masses, thicknesses, temperatures and densities of the light oxide, metallic and heavy oxide debris layers in the cavity. A heavy oxide layer is present for only a brief period of time, after which MELCOR calculates a stable configuration of a light oxide layer above a metallic debris layer throughout the remainder of the transient period calculated. The transition from a metallic layer over a heavy oxide layer to a light oxide layer over a metallic layer at 10-12hr corresponds to the time when the concrete ablation rate increases (as illustrated in Figures 5.3.23 and 5.3.25). The metallic layer remains nearly constant in mass and thickness, with a gradually increasing density; the light oxide layer mass and thickness increase continuously (and the density decreases) as ablating concrete (with its resultant low-density silicate oxides) continues to dilute the high-density zirc oxide and steel oxide debris to an average density value less than the metallic debris density. After some initial oscillations, the temperatures of both layers remain nearly equal, at $\simeq$1500K, throughout the transient period calculated.

The heat transfer from the cavity debris pool in the MELCOR analysis, both downward and outward to the concrete surface and upward to the cavity volume atmosphere, is shown in Figure 5.3.27. The energy transfer from the debris in the cavity upward through the debris bed surface to the lower drywell atmosphere and/or overlying water pool is several times greater than the energy transferred downward (and sideways) to the concrete before about 10hr and after about 12hr. In general, that upper surface of the debris bed is covered with a water pool, not exposed to atmosphere.

Tables 5.3.4 and 5.3.5 give the distribution of the released radionuclides at the end of the calculation (*i.e.*, at 58hr). Note that these amounts generally consider only the release of radioactive forms of these classes, and not additional releases of nonradioactive aerosols from structural materials.

Table 5.3.4 provides an overview of how much of the radionuclides remain bound up in fuel in either the core or the cavity, and of how much of the released radionuclides are retained in the primary system *vs* how much of the released radionuclides are released to, or released in, either the drywell or the wetwell in containment and the environment, all normalized to the initial inventories of each class. Table 5.3.5 gives a slightly different breakdown of the released radionuclide final distribution – the fractions of initial inventory released for each class from fuel in-vessel in the core, ex-vessel in the cavity and overall total are given, together with the distribution of the released radionuclides in the primary system, drywell, wetwell and environment normalized by the mass of each class released.

The release behavior predicted by MELCOR can be grouped into the same several subdivisions as already noted for the low-pressure sequence results. Almost all ($\simeq$100%) of the volatile Class 1 (noble gases), Class 2 (CsOH), Class 5 (Te) and Class 16 (CsI) radionuclide species are released, primarily in-vessel, as are most (80-90%) of the Class 3 (Ba) and Class 12 (Sn) inventories. The next major release fractions are of Ru and Mo, Ce and La, all between 0.5% and 2%. Finally, a total $\leq$0.1% of the initial inventory

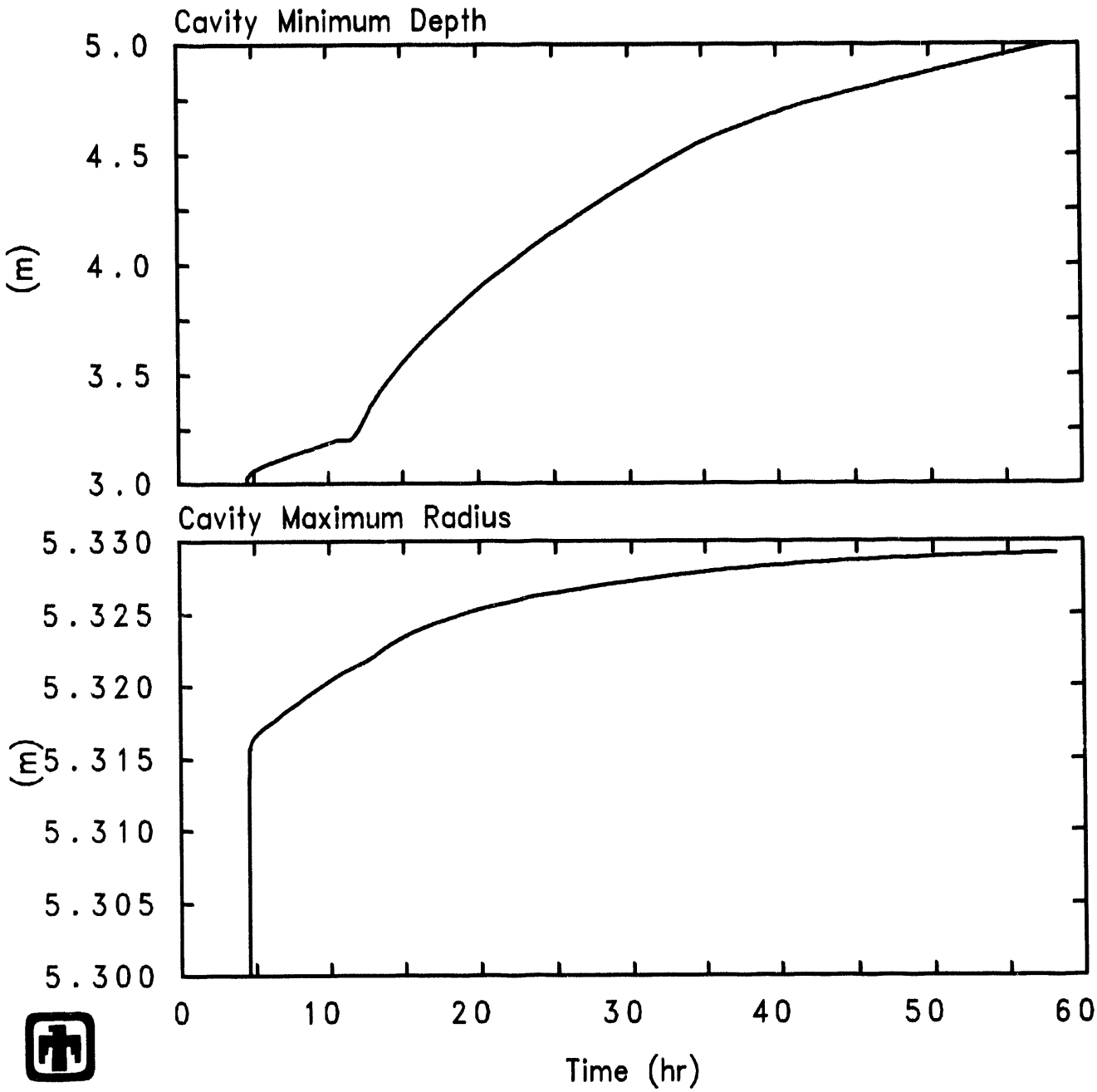

Figure 5.3.25. Cavity Maximum Radius and Depth Predicted by MELCOR for LCHP-PF-P-M Sequence

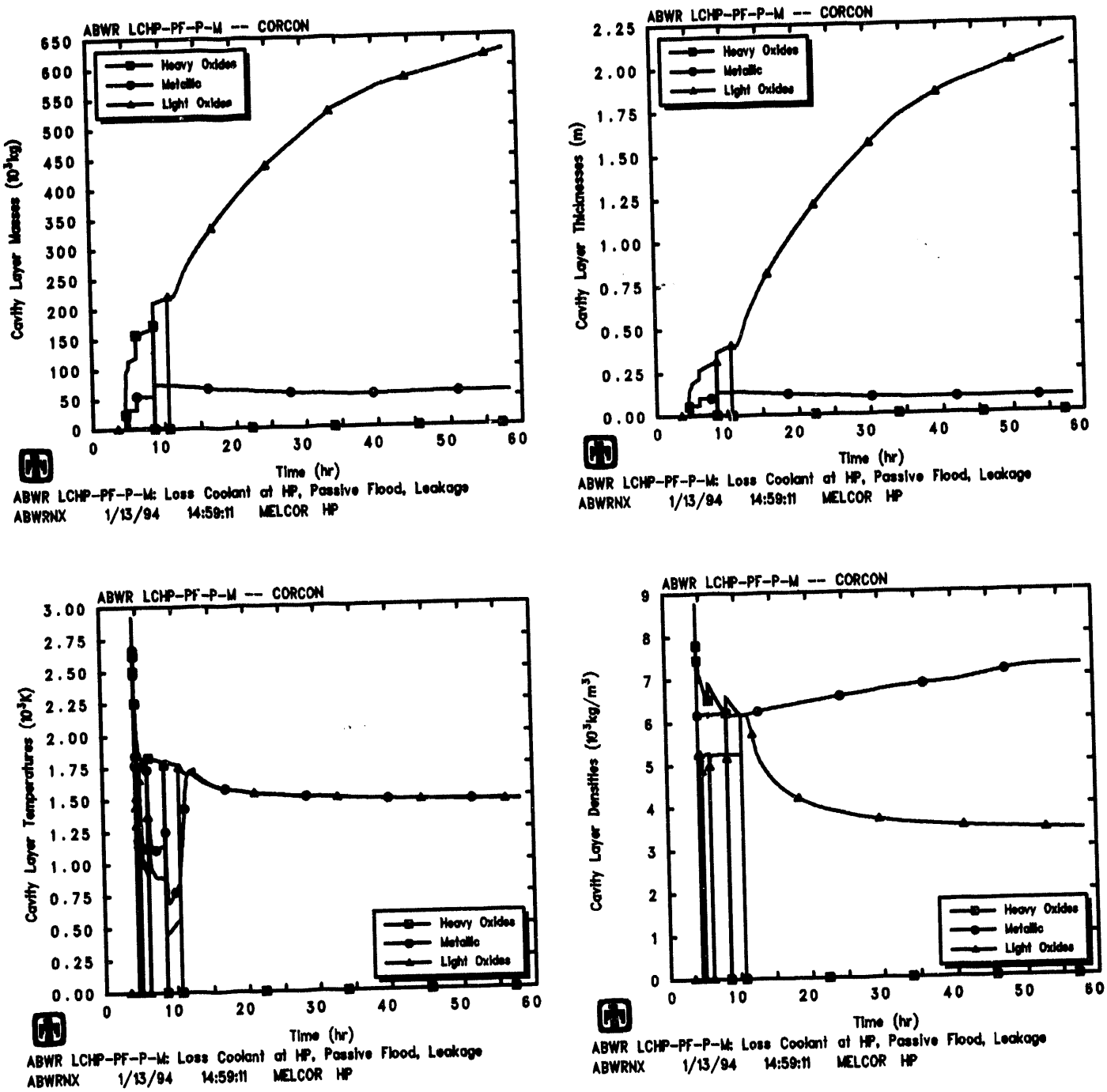

Figure 5.3.26. Cavity Layer Masses (upper left), Thicknesses (upper right), Temperatures (lower left) and Densities (lower right) Predicted by MELCOR for LCHP-PF-P-M Sequence

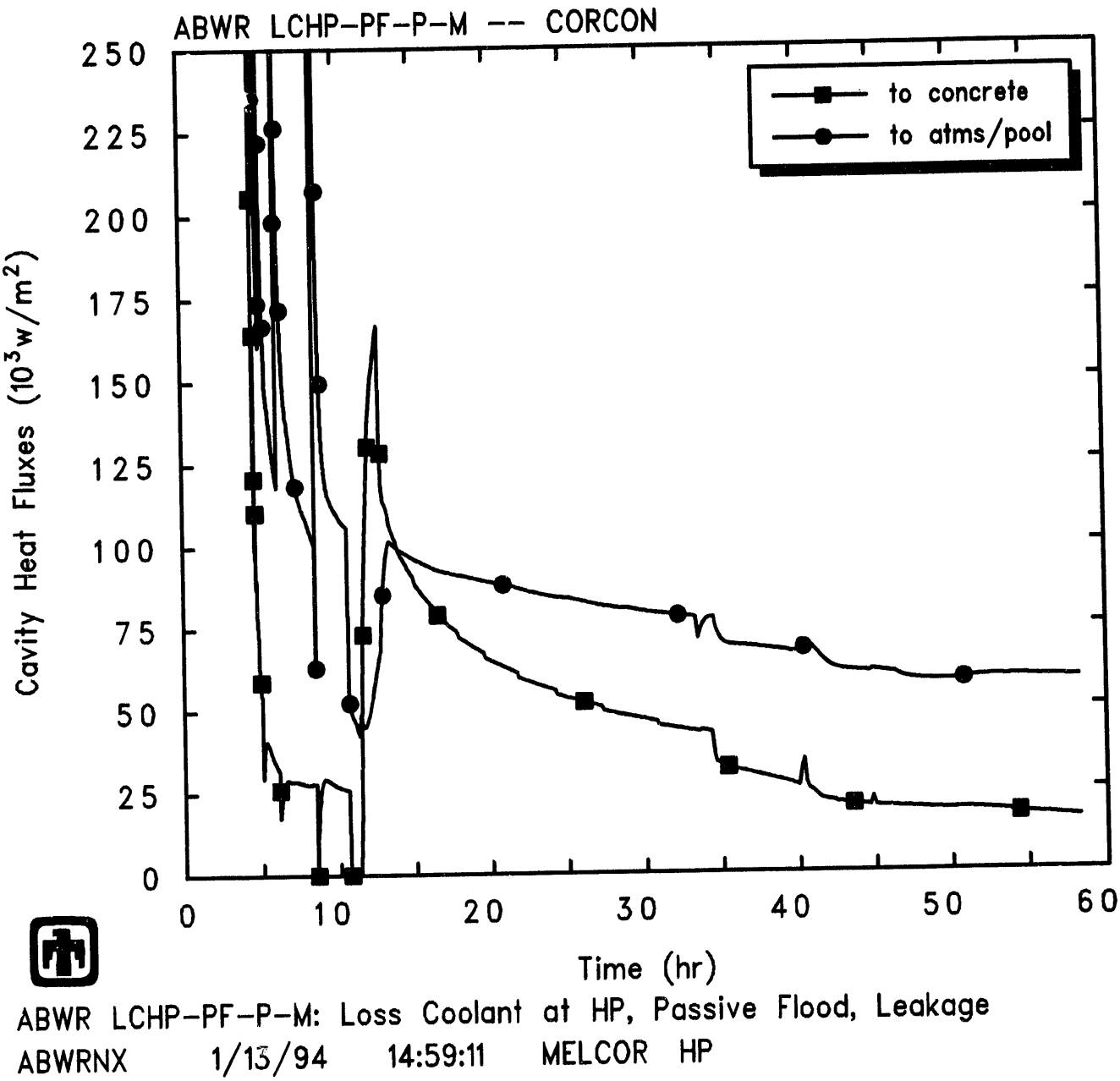

Figure 5.3.27. Cavity Heat Flows Predicted by MELCOR for LCHP-PF-P-M Sequence

Table 5.3.4. Radionuclide Distribution Predicted at 58hr for LCHP-PF-P-M Sequence

Class	Fission Product Distribution (% Initial Inventory)					
	Remaining in Fuel		Released from Fuel			
	Core	Cavity	Primary System	Drywell	Wetwell	Environment
Noble Gases (Xe)	1.18×10^{-8}	0	0.0934	1.81	51.5	46.6
Alkali Metals (CsOH)	1.26×10^{-8}	1.91×10^{-13}	19.6	24.8	42.6	13.1
Alkaline Earths (Ba)	1.43×10^{-8}	12.3	53.4	5.50	28.8	0.018
Halogens (I)	$\simeq0$	$\simeq0$	$\simeq0$	$\simeq0$	$\simeq0$	$\simeq0$
Chalcogens (Te)	8.36×10^{-9}	6.41×10^{-3}	19.6	25.8	39.3	15.3
Platinoids (Ru)	1.32×10^{-9}	98.8	0.794	0.0750	0.379	1.59×10^{-4}
Transition Metals (Mo)	1.18×10^{-9}	97.4	7.98×10^{-3}	0.658	1.76	0.154
Tetravalents (Ce)	1.37×10^{-9}	98.9	0.687	0.0658	0.331	1.76×10^{-4}
Trivalents (La)	2.80×10^{-9}	97.4	4.57×10^{-4}	0.516	2.03	3.72×10^{-3}
Uranium (U)	1.55×10^{-9}	~100	0.0168	3.32×10^{-3}	0.0132	6.69×10^{-5}
More Volatile Main Group Elements (Cd)	2.23×10^{-9}	99.9	3.95×10^{-5}	0.0240	0.0716	3.81×10^{-4}
Less Volatile Main Group Elements (Sn)	2.12×10^{-9}	7.07	56.3	5.83	30.8	3.81×10^{-4}
CsI	$\simeq0$	1.79×10^{-5}	0.0390	34.8	48.5	16.7

Table 5.3.5. Radionuclide Release and Released Distribution Predicted at 58hr for LCHP-PF-P-M Sequence

Class	Released from Fuel (% Initial Inventory)			Distribution (% Released Mass)			
	Core	Cavity	Total	Primary System	Drywell	Wetwell	Environment
Noble Gases (Xe)	99.991	0.006	$\simeq$100	0.093	1.81	51.54	46.56
Alkali Metals (CsOH)	99.986	0.006	$\simeq$100	19.55	24.77	42.59	13.09
Alkaline Earths (Ba)	81.0	0.497	81.52	60.91	6.27	32.80	0.020
Halogens (I)	$\simeq$0	$\simeq$0	$\simeq$0	0.095	1.84	52.51	45.55
Chalcogens (Te)	99.997	0.0007	$\sim$100	19.57	25.85	39.32	15.27
Platinoids (Ru)	0.86	0.0004	0.86	63.63	6.01	30.35	0.013
Transition Metals (Mo)	0	1.78	1.78	0.310	25.56	68.16	5.98
Tetravalents (Ce)	0.75	1.35×10^{-3}	0.75	63.38	6.07	30.53	0.016
Trivalents (La)	0	1.76	1.76	0.018	20.21	79.62	0.146
Uranium (U)	0.018	0.005	0.023	50.23	9.94	39.63	0.002
More Volatile Main Group Elements (Cd)	0	0.066	0.066	0.041	24.96	74.60	0.397
Less Volatile Main Group Elements (Sn)	89.11	5.79×10^{-3}	89.12	60.57	6.28	33.13	0.016
CsI	99.997	5.92×10^{-3}	$\sim$100	0.039	34.77	48.46	16.73

of uranium and Class 11 (Cd) are predicted to be released. Note that the CORSOR-M fission product release model option used in these analyses has identically zero release in-vessel of Class 7 (Mo), Class 9 (La) and Class 11 (Cd).

These are significantly higher release fractions of Ba, Te, Ru, Ce, La and Sn than seen in MELCOR analyses of severe accidents in current, conventional LWR plants [8, 9, 10], reflecting the high debris temperatures calculated during in-vessel core degradation (shown in Figures 5.3.4 and 5.3.5 and in Table 5.3.3).

As in the other sequences analyzed, most of the released radionuclides do remain in the primary system and/or the containment. Only the noble gases show a significant release to the environment; that release ($\leq$50% of the total inventory) is smaller than seen for any of the other sequences analyzed because the penetration leakage flow in this sequence is much slower than the rupture disk flow in the other scenarios. However, of the other radionuclides, $\sim$10-20% of the total masses of other volatiles (CsOH, Te and CsI) are released to the environment, orders of magnitude more than in either the two low-pressure sequences or the other two high-pressure scenarios. There is also more release of Ba and Mo in this sequence than in any other (although still $\ll$1% of their initial inventories), while $\ll$0.1% of the other radionuclides' initial inventory is released to the environment, as in the other accidents considered. Of the species with significant (>80%) release from fuel, the wetwell retains a significant fraction (40-50%) of the released CsOH, Te and CsI volatiles, while the Ba and Sn aerosols are held up both in the primary system (60%) and in the wetwell (30-35%).

The retention in-vessel and in the containment, and the release to the environment, are quite different for this LCHP-PF-P-M sequence than calculated for either of the two low-pressure sequence analyses described in Sections 5.1 and 5.2 (and also quite different than the results found for the other two high-pressure sequence analyses done, described in Sections 5.4 and 5.5). This is due to the release in this sequence occurring from the upper drywell through the movable penetration leakage, rather than through the containment rupture disk opening as in all the other sequences considered. Although the rupture disk is a significantly larger opening, its location in the wetwell vapor space allows fission products to escape only after scrubbing in the suppression pool. Penetration leakage in the upper drywell, in contrast, allows fission products to escape containment without having to pass through the suppression pool first.

Figures 5.3.28 and 5.3.29 give the retention factors for the various radionuclides calculated by MELCOR, for the primary system and for the overall containment, respectively. The retention factors are defined as the fraction of material released in, or transported into, a region which remains in that region. The vessel retention factors fall into three sets:

- essentially no retention for the noble gases and for I_2 (of which there is very little),
- for the radionuclide species with non-zero vapor pressures (*i.e.*, CsOH, Te, and CsI), a retention of 50-60% before significant penetration leakage, falling to 20% later in the transient (and to 0 for CsI), and

- a $\geq$60% retention of those classes which form aerosols only.

This is similar to the results found in the low-pressure sequences, except for the change in the time-dependent retention factor for the volatile species.

The containment retention factors fall into several distinct categories also:

- a slowly decreasing retention for the noble gases and for I_2, from >90% before penetration leakage begins to <60% by the end of the transient,
- an increasing retention for the radionuclide species with non-zero vapor pressures (*i.e.*, CsOH, Te, and CsI) from 40-50% before penetration leakage begins to 60-80% by the end of the transient,
- for those classes which form aerosols only, there is a ~50% retention for those which had some in-vessel release (Ba, Ru, Ce, U and Sn) and a ~100% retention of those with only ex-vessel release (Mo, La and Cd).

The retention factors for the species which form aerosol forms only are very similar to the results found for the two low-pressure sequences, while the results for the noble gases and for the volatiles differ both in magnitude and in time dependence.

Figures 5.3.30 and 5.3.31 give the decontamination factors (DFs) for the various radionuclides calculated by MELCOR, for the suppression pool and for the overall containment, respectively. The period of interest in these plots is after ~10hr when significant leakage through the degraded containment penetration seals is calculated to occur (Figure 5.3.22). After significant leakage flow occurs, the suppression pool and overall containment DFs for the noble gases and for I_2 (of which there is very little), and for the other radionuclide volatile species (*i.e.*, CsOH, Te, and CsI) continually decrease as these species continue to be release out the leakage path in the upper drywell. For radionuclide species with only aerosol forms in MELCOR, the suppression pool and overall containment DFs remain nearly constant after significant leakage flow occurs.

As with the retention factors, the suppression pool DF falls into subdivisions:

- DF_{SP}~2-5 for the noble gases, for I_2 (of which there is very little), and for the other radionuclide volatile species (*i.e.*, CsOH, Te, and CsI), after significant leakage flow occurs,
- DF_{SP}~10 for classes with very little or no in-vessel release (*i.e.*, Mo, La, U and Cd),
- $DF_{SP}\geq$100 for classes with somewhat greater in-vessel release (*i.e.*, Ba, Ru, Ce and Sn).

Classes with aerosol-only forms and large in-vessel releases have the highest wetwell decontamination factors (DF_{SP} ~200-300). The overall containment DFs also fall into several, somewhat different subdivisions:

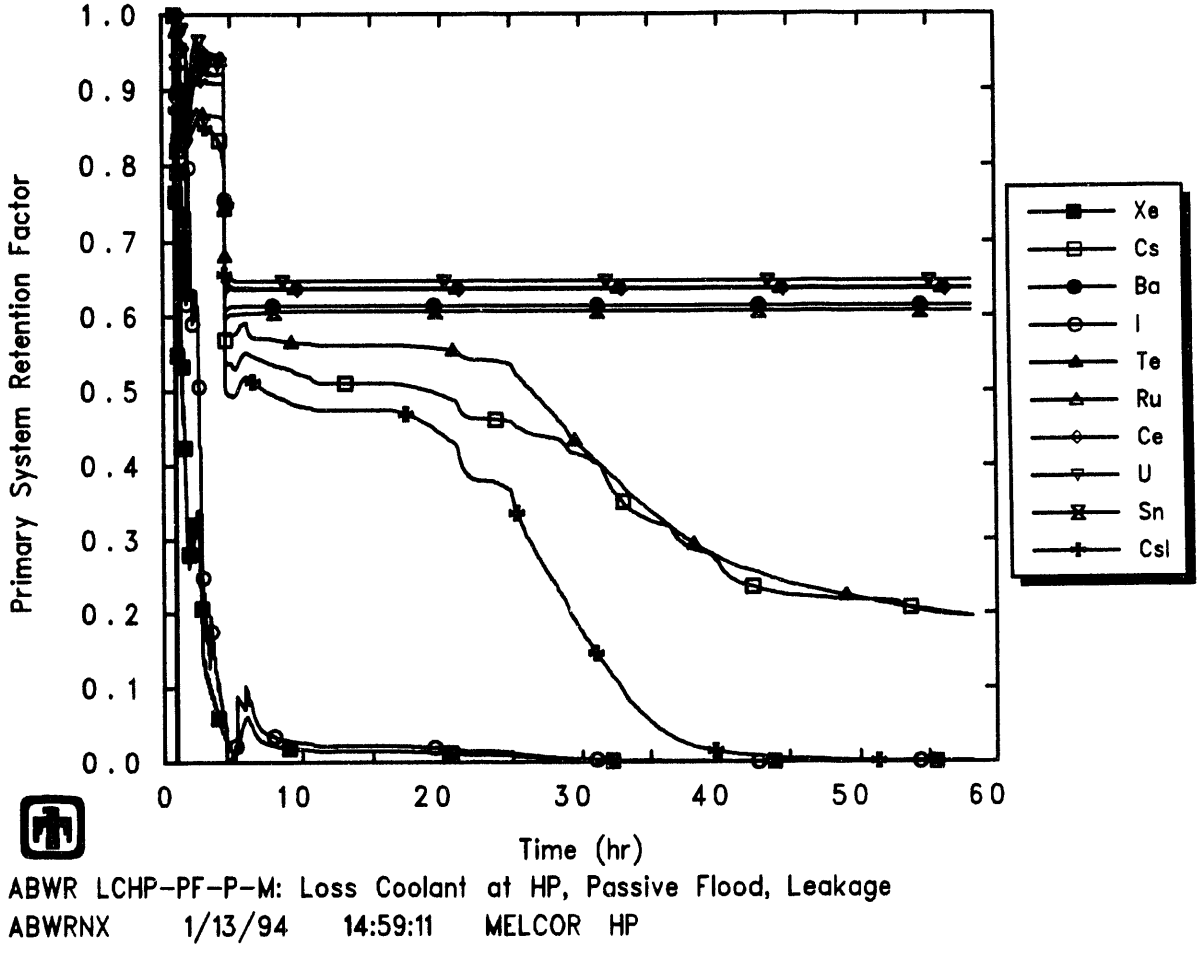

Figure 5.3.28. Primary System Retention Factors Predicted by MELCOR for LCHP-PF-P-M Sequence

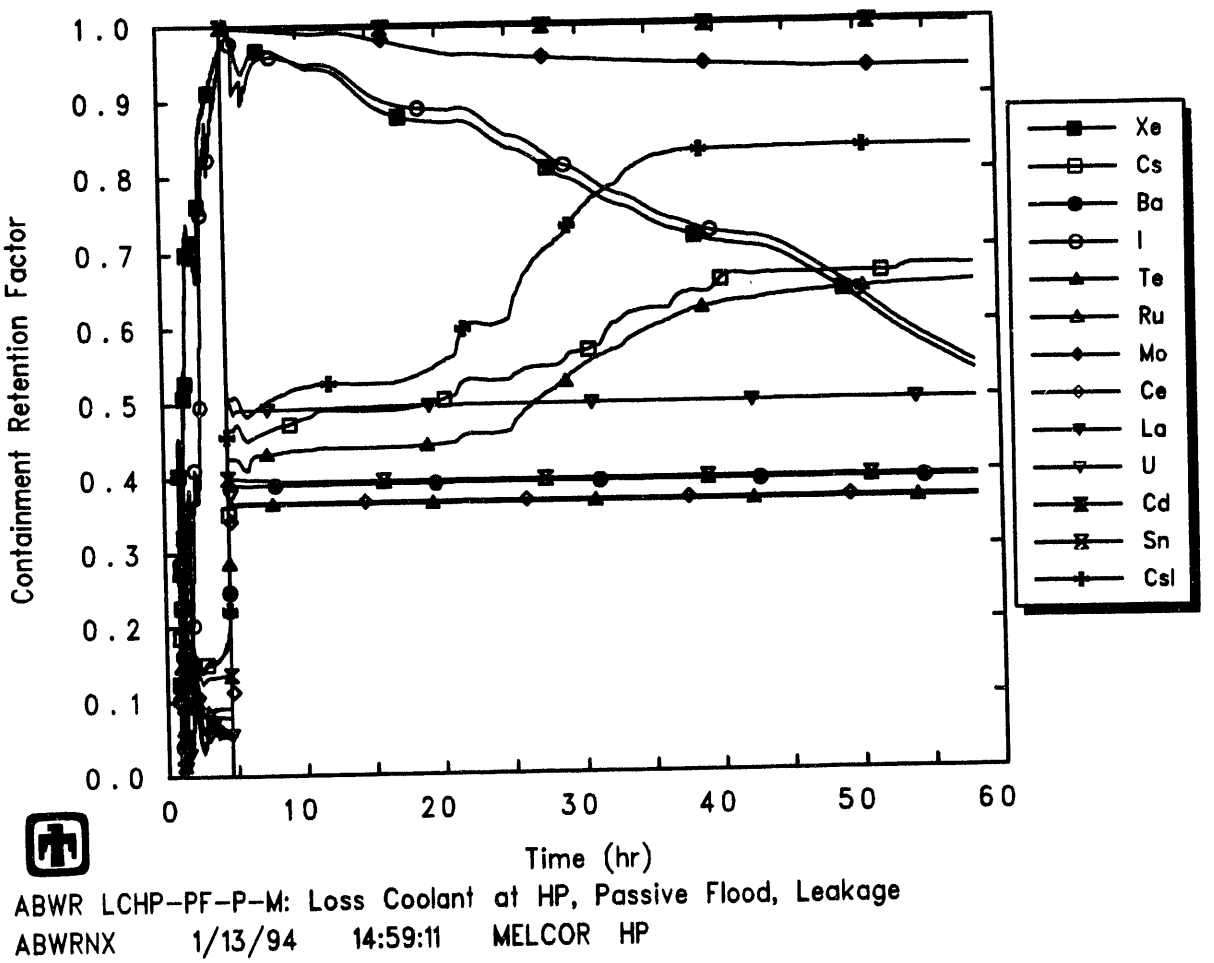

Figure 5.3.29. Containment Retention Factors Predicted by MELCOR for LCHP-PF-P-M Sequence

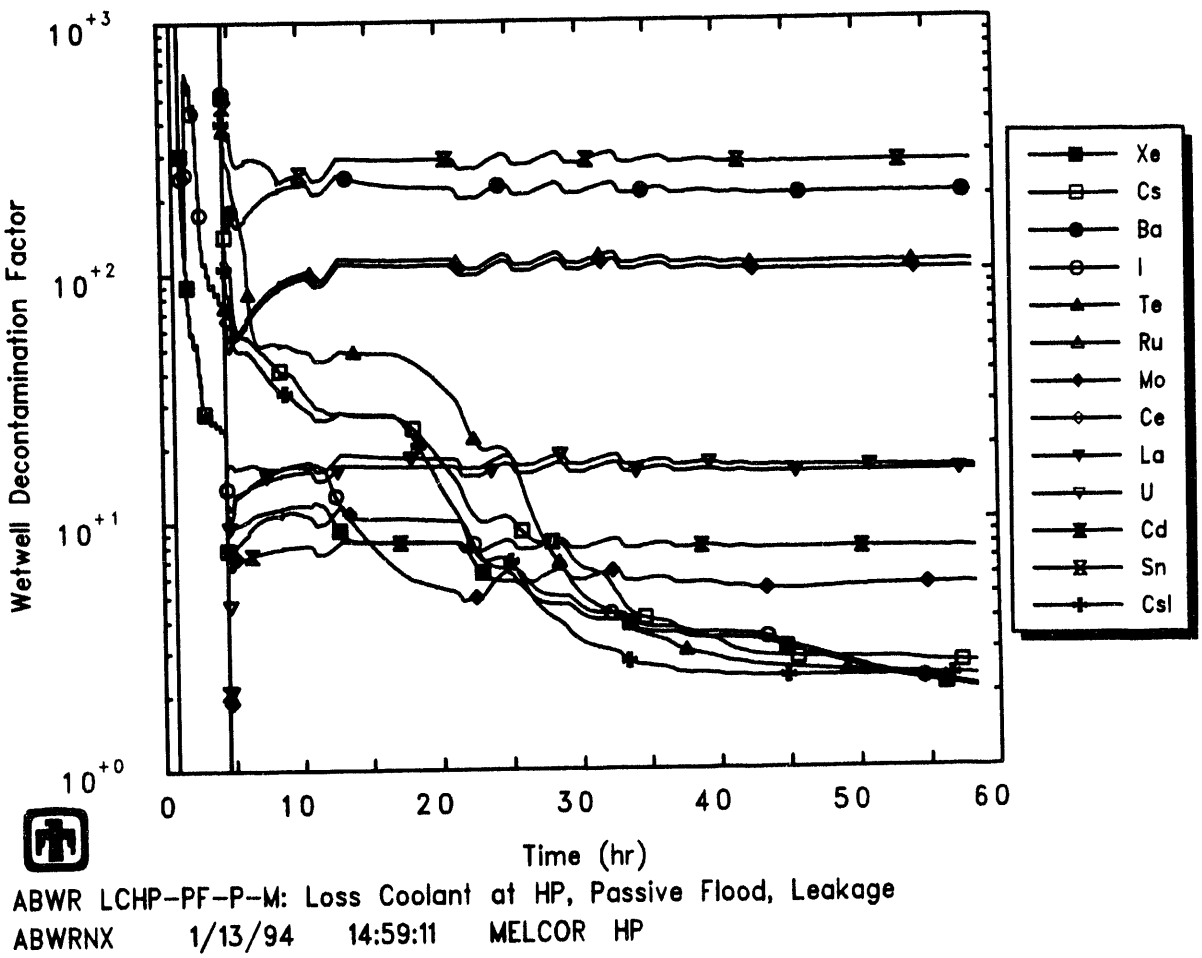

Figure 5.3.30. Suppression Pool Decontamination Factors Predicted by MELCOR for LCHP-PF-P-M Sequence

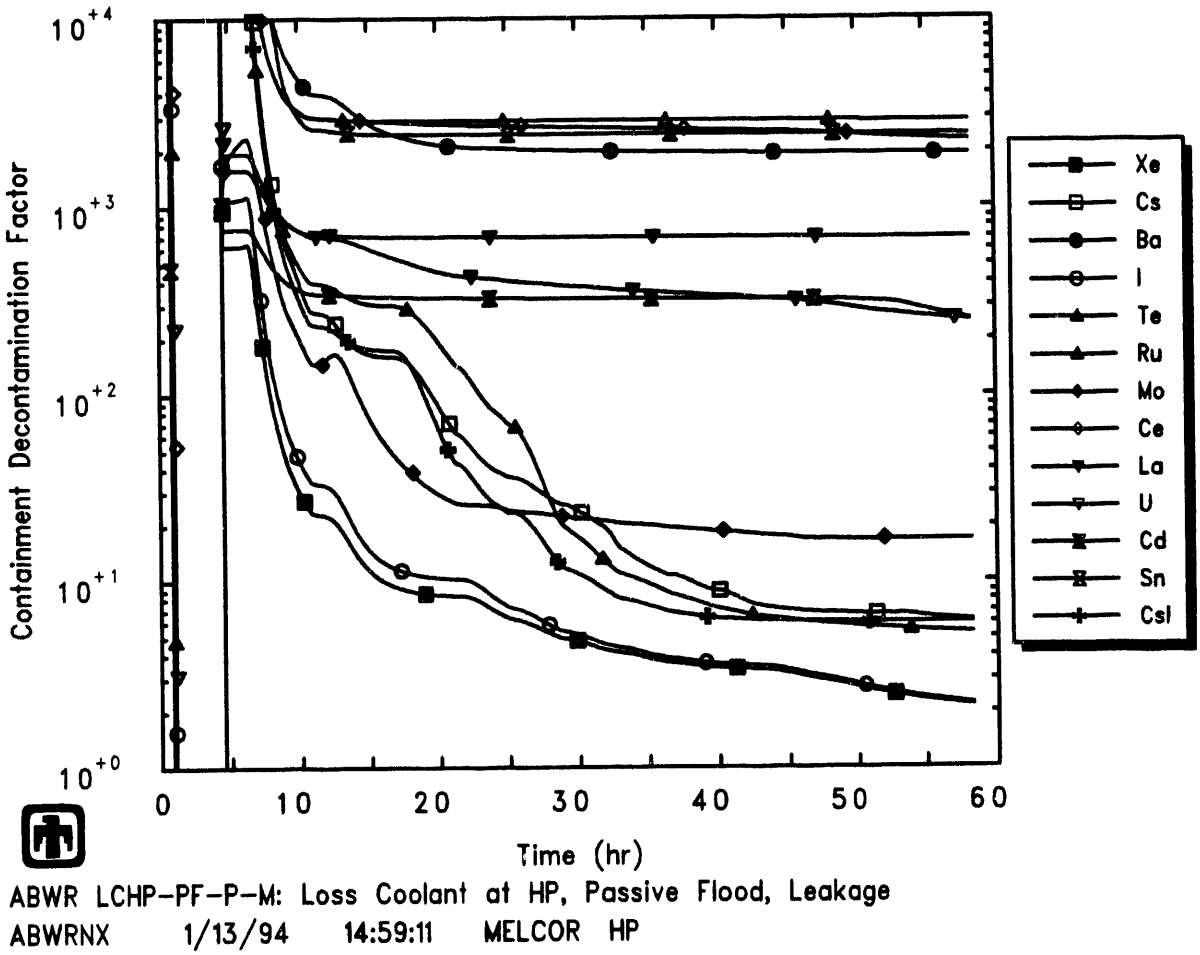

Figure 5.3.31. Overall Containment Decontamination Factors Predicted by MELCOR for LCHP-PF-P-M Sequence

- DF_{Cont}<10 for the noble gases, for I_2 (of which there is very little), and for the other radionuclide volatile species (*i.e.*, CsOH, Te, and CsI), late in the transient after significant leakage flow occurs,
- $DF_{Cont}\leq$20 for Class 7 (Mo), also decreasing with time until late in the transient after significant leakage flow occurs,
- $DF_{Cont}\sim$200-700 for other classes with very little or no in-vessel release (*i.e.*, La, U and Cd), and
- $DF_{Cont}\geq$2000 for the other classes (Ba, Ru, Ce and Sn).

Note that both the suppression pool and overall containment decontamination factors remain nearly constant or drop very slowly for most classes after containment leakage begins, but drop steadily for several radionuclide species (*i.e.*, noble gases and I, CsOH, Te, Mo and CsI). These are the classes for which a continuing release to the environment is predicted, while for the other classes there is only a single step-like release at the start of containment leakage, as illustrated in Figure 5.3.32. That continuing release comes from several different causes.

The release of the noble gases and of any I_2 which may be present is limited by the slow flow out the small area of the penetration leakage. The non-zero vapor pressure of CsOH, Te and CsI causes continuous vaporization and replenishment of these fission product vapors in the containment atmosphere as those fission product vapors are lost out the penetration leakage. Class 7 (Mo) has no non-zero vapor pressure and therefore remains an aerosol throughout the problem. However, this class is the only one with substantial and continuing radionuclide release in the cavity, and a small fraction of that continuing release (while mostly remaining in the cavity and/or suppression pools) gets released to the atmosphere and then out through the containment penetration leakage to the environment.

Figure 5.3.32 includes the release of the noble gases, unlike corresponding results presented for the two low-pressure sequences in Figures 5.1.31 and 5.2.18. In the MAAP analysis, the fission product release begins at 18.1hr (Figure 19E.2-5E in [1]), and the noble gas release continues well beyond 5 days, while the volatile fission product release is nearly complete at 70hr. The release fraction of CsI at 72hr is 8.8×10^{-2}. The release of the noble gases in the MELCOR calculation also occurs much more slowly for this scenario than in any of the other sequences analyzed, due to the limited flow out the penetration leakage.

Figure 5.3.33 gives the release fractions of nobles gases, cesium iodide and cesium hydroxide as functions of time, compared with corresponding MAAP results (taken from Figure 19E.2-5E in [1]). For this sequence, the release fraction of the noble gases predicted by MAAP is $\leq$50% at 100hr, quite similar to the MELCOR result of about 45% of the noble gas inventory released to the environment by about 60hr. The release fractions of CsOH and CsI at 100hr in the MAAP analysis are $\sim$0.1, while this MELCOR calculation shows environment release fractions for both CsOH and CsI by the end of the calculation

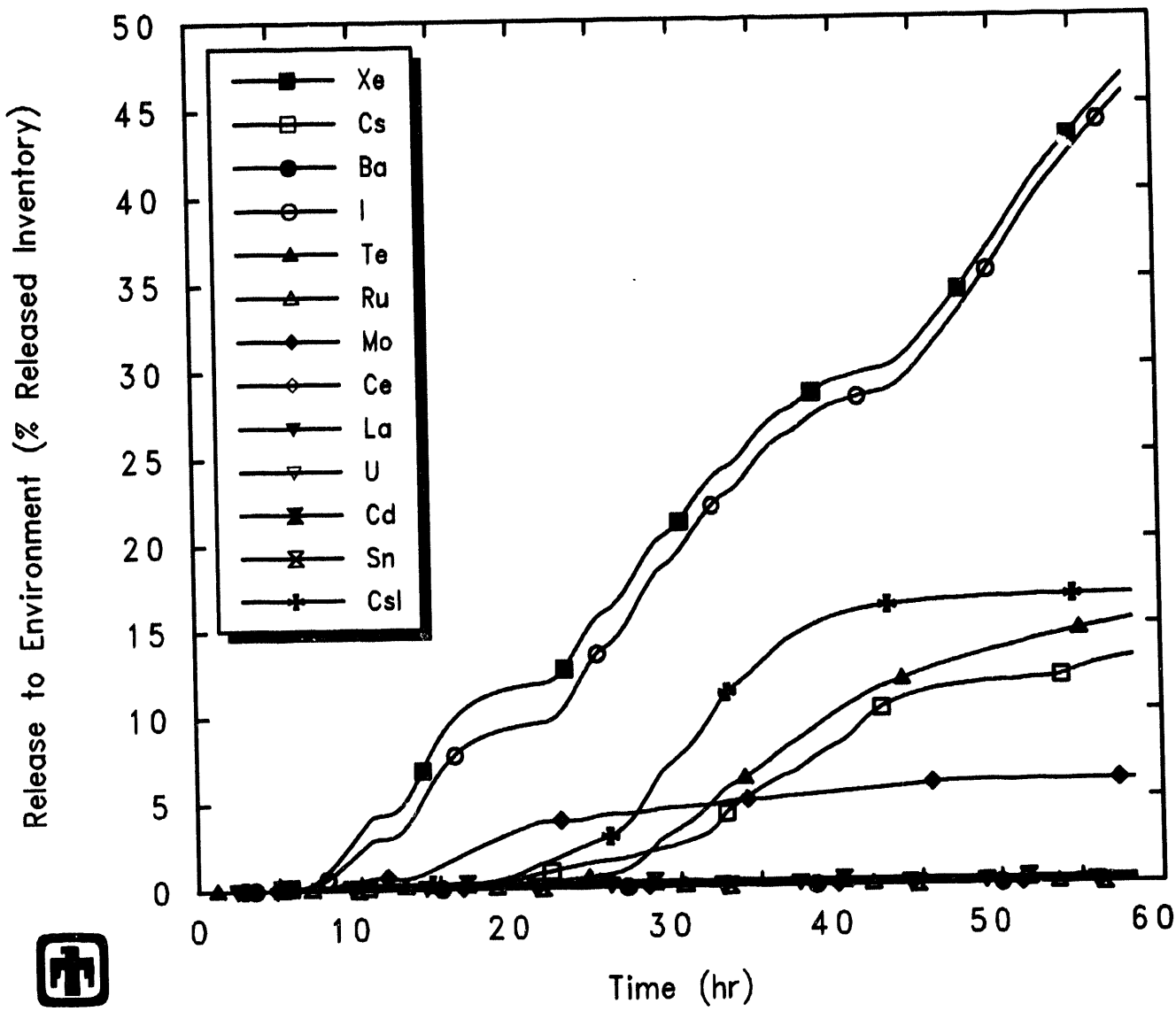

Figure 5.3.32. Radionuclide Environmental Releases Predicted by MELCOR for LCHP-PF-P-M Sequence

(58hr) of about 15%. MELCOR also shows the release of noble gases still increasing at the end of the calculation, while the releases of CsOH and CsI have plateaued; this is the same trend as found in the corresponding MAAP results. This overall qualitative and quantitative agreement is judged to be excellent, given the differences in code and input models and in cavity response in the MAAP and MELCOR analyses.

5.4 LCHP-FS-R-N Sequence

The first part of this sequence, through core uncovery, heatup and degradation, and vessel lower head failure, is identical to the LCHP-PF-P-M sequence discussed in Section 5.3. The difference is that the firewater system is used in spray mode to add external water to the containment after vessel failure. (This sequence is the high-pressure counterpart of the low-pressure LCLP-FS-R-N sequence discussed in Section 5.2.)

The sequence of events predicted by MELCOR for this accident sequence is given in Table 5.4.1, with the timings of the various events up to vessel failure as calculated by MAAP (taken from Tables 19E.2-7 and 19E.2-8 in [1]) included for comparison; no later-time tabular or plotted MAAP results were given in [1] for this sequence, just a brief discussion of the results.

Before the spray system begins injection, the results of this sequence are almost identical to those for the LCHP-PF-P-M sequence discussed in Section 5.3; the small differences are due to slightly different time steps and other numerical effects.

It is assumed in the MAAP calculation that the operator turns on the firewater addition spray system 1.9hr after the start of the accident, just before the passive flooder would operate (as stated in Section 19E.2.2.2(b) in [1]). When the suppression pool water level reaches the bottom of the vessel, at about 22hr, the operator is assumed to turn off the firewater system. The corium in the upper drywell then causes the temperature in the upper drywell to increase. When the temperature in the upper drywell again reaches 500K (440°F) the operator restarts the drywell spray. This causes the pressure and the upper drywell temperature to decrease. After 15min, the operator turns the system off in order to minimize excess water addition to the containment. The cycle is repeated many times.

In the MELCOR calculation, the firewater spray was assumed to turn and/or stay on if:

1. the lower drywell temperature exceeds 500K (first time only), or
2. the upper drywell temperature exceeds 500K, or
3. the spray has been on less than 15min, or
4. the sprays are on and the suppression pool level has never reached the elevation of the bottom of the reactor vessel.

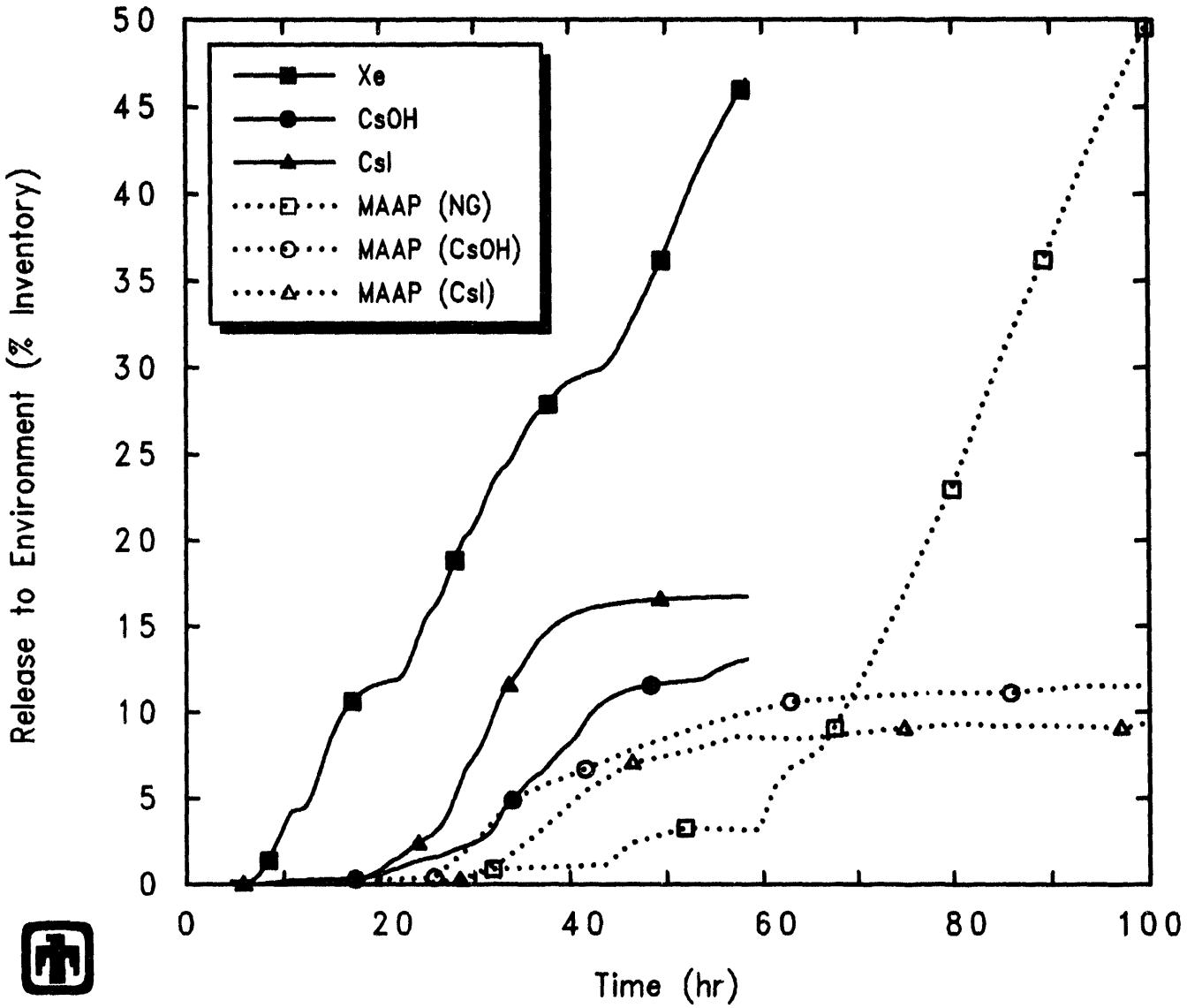

Figure 5.3.33. Noble Gas, CsOH and CsI Environmental Releases Predicted by MELCOR for LCHP-PF-P-M Sequence, Compared to MAAP

Table 5.4.1. Sequence of Events Predicted by MELCOR for LCHP-FS-R-N Sequence, Compared to MAAP

Event	Time	
	MAAP	MELCOR
Accident initiation (MSIV Closure)	0.0	0.0
Reactor scrammed	4.2s	
Core uncovery begins	0.3hr	1,626.1s (0.45hr)
Clad failure/Gap release		
(Ring 1)		3,198.4s (0.83hr)
(Ring 2)		4,328.0s (1.20hr)
(Ring 3)		5,157.9s (1.43hr)
(Ring 4)		8,168.0s (2.27hr)
Core plate failed		
(Ring 1)		15,765.4s (4.38hr)
(Ring 2)		20,800.3s (5.78hr)
(Ring 3)		22,257.0s (6.18hr)
(Ring 4)		22,114.6s (6.14hr)
Vessel bottom head failed	2.0hr	
Vessel LH penetration failed		
(Ring 1)		15,827.4s (4.40hr)
(Ring 2)		15,831.5s (4.40hr)
(Ring 3)		15,842.7s (4.40hr)
(Ring 4)		15,854.8s (4.40hr)
Commence debris ejection		15,827.4s (4.40hr)
End of HPME/DCH		16,002.7s (4.45hr)
Firewater spray started	1.9hr	15,833.0s (4.40hr)
Passive flooder opens	2.0hr	15,835.8s (5.40hr)
Firewater spray stopped	22hr	60,647.5s (16.85hr)
Rupture disk opens	50hr	81,172.5s (22.55hr)
Concrete ablation $\geq$2m		224,471s (62.35hr)
End of calculation	100hr	224,471s (62.35hr)

This is the logic in the MELCOR ABWR deck as received from BNL and used for LCHP-PF-D-H sequence analyses in 1990 [3]. The spray thus begins on a high-temperature trip, stays on at least 15min, and then turns off when the suppression pool level reaches the elevation of the bottom of the reactor vessel. This logic caused the spray in the MELCOR calculation to begin injection at 4.4hr and stop at 16.85hr. (The firewater spray would have resumed cycling on and off after about 23hr in the MELCOR calculation, based upon the upper drywell temperature, but those later spray cycles were suppressed to keep the suppression pool liquid level below the bottom of the drywell-wetwell vacuum breakers and, more importantly, to keep the spray from filling the suppression pool to the rupture disk elevation and causing liquid outflow.)

Figure 5.4.1 shows the collapsed liquid level in the lower drywell (cavity) control volume in the MELCOR calculation, for comparison to the LCHP-PF-P-M sequence results given in Figure 5.3.15 and the LCLP-FS-R-N sequence results in Figure 5.2.1. The spray flow starts as soon as the vessel fails but, since the flow from the sprays does not initially enter the lower drywell, the passive flooder opens as soon as core debris falls into the cavity and begins heating the lower drywell. The sudden rise in liquid level at $\geq$4.4hr thus corresponds to the remaining lower plenum water pouring out the vessel breach and to suppression pool water through the passive flooder opening. The additional water added by the firewater spray actuating at 4.4hr is initially directed to the suppression pool. Water continues to flow from the suppression pool into the cavity as the suppression pool mass increases, until the sprays are turned off just before 17hr. After the spray stops adding water to the containment, the water level in the cavity then drops to the elevation of the top horizontal vent (a depth of about 2m).

Figure 5.4.2 gives the corresponding drywell and wetwell pool masses for the MELCOR analysis. Since the firewater spray is operating in injection mode, the suppression pool mass increases while the spray is on, and then begins gradually decreasing after the containment rupture disk is predicted to open at about 22.5hr.

The lower drywell and wetwell atmosphere and pool temperatures are presented in Figure 5.4.3. There is a large temperature spike at vessel failure, partly due simply to melt ejection and partly due to direct containment heating; this temperature spike triggers the passive flooder opening and the firewater spray actuation. The hot debris in the cavity in the MELCOR calculation keeps the lower drywell pool temperature ($\sim$400K) somewhat hotter than the suppression pool temperature ($\sim$350K). The wetwell atmosphere temperature is slightly hotter than the suppression pool temperature throughout most of this sequence. The cavity atmosphere remains significantly hotter than the cavity pool throughout the transient, even after containment rupture disk actuation.

The pressures calculated by MELCOR in the various containment control volumes are depicted in Figure 5.4.4. MELCOR predicts a pressure spike in containment immediately after vessel failure, due to steam generation from hot debris and water falling into the cavity from the lower plenum and due to direct containment heating. The MELCOR HPME/DCH input parameters were selected so as not to actuate the rupture disk during this pressure spike. The containment pressure then continues to rise as hot, unquenched core debris continues to boil off the cavity water pool. After the firewater spray is

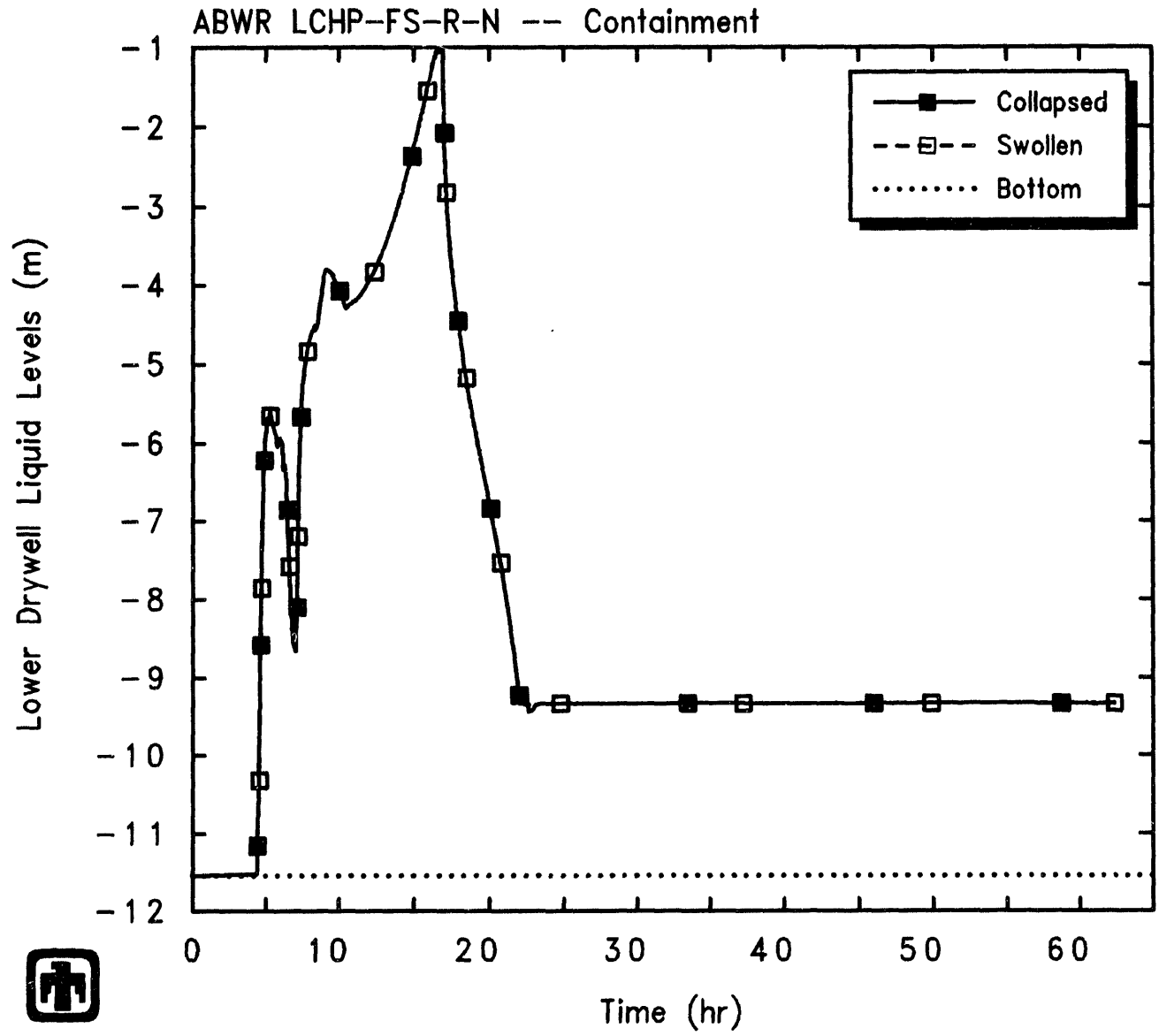

Figure 5.4.1. Lower Drywell Liquid Level Predicted by MELCOR for LCHP-FS-R-N Sequence

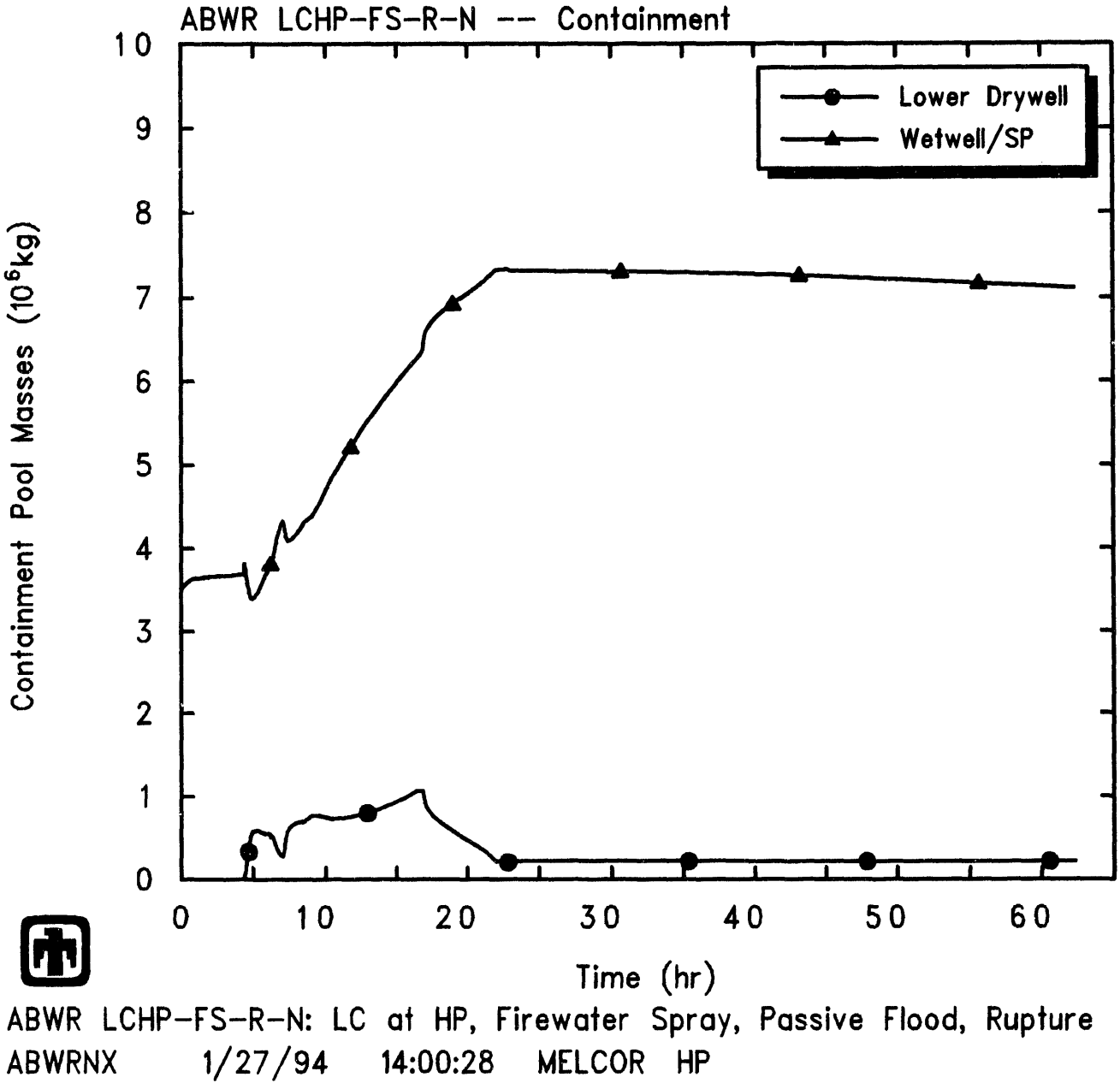

Figure 5.4.2. Lower Drywell and Suppression Pool Masses Predicted by MELCOR for LCHP-FS-R-N Sequence

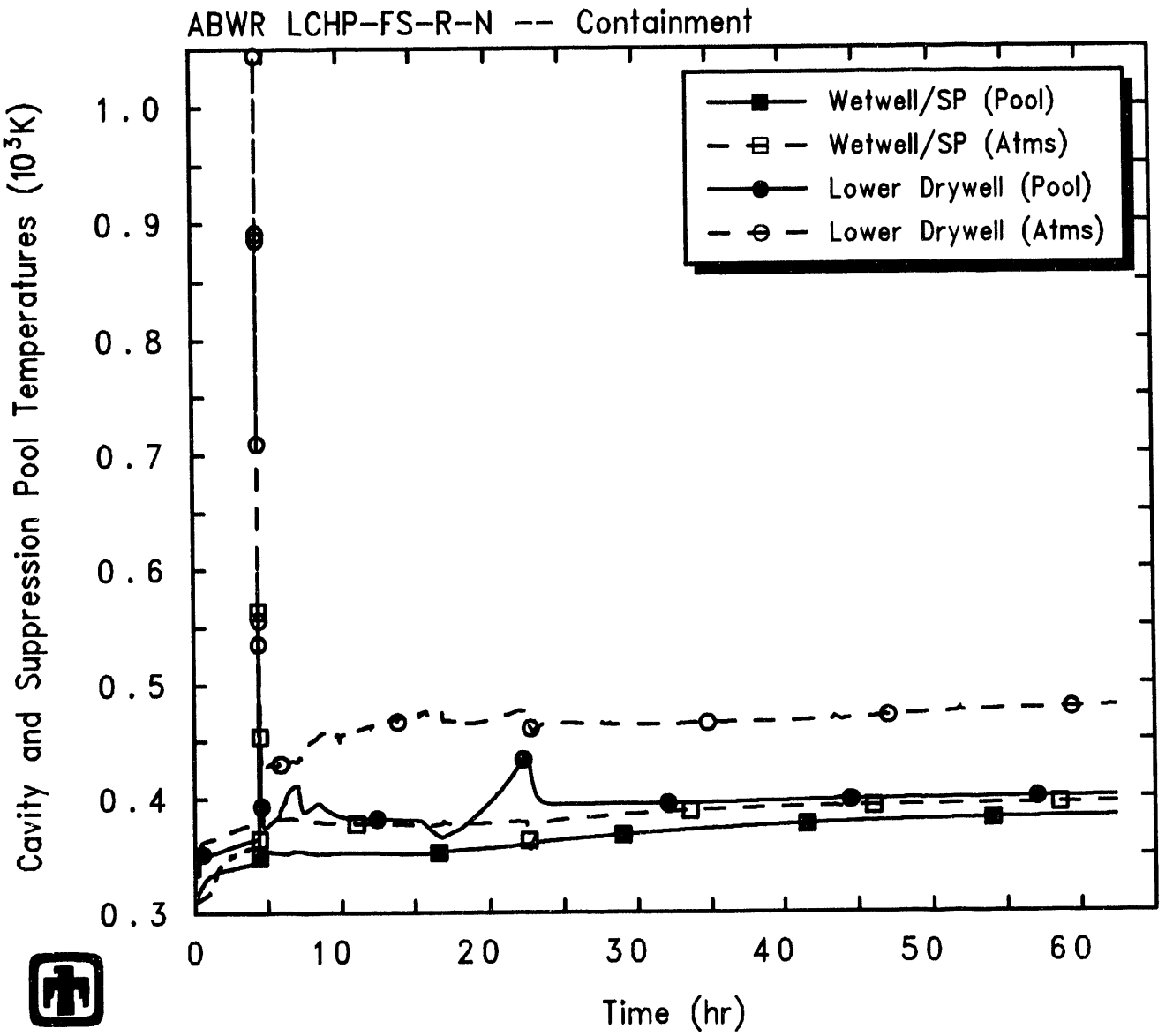

Figure 5.4.3. Lower Drywell and Suppression Pool Temperatures Predicted by MELCOR for LCHP-FS-R-N Sequence

turned off, at 16.85hr in the MELCOR calculation, the pressures continue to increase as steam is generated by corium in the lower drywell, until the containment rupture disk opening setpoint is reached, at about 23.5hr in the MELCOR calculation, after which the containment depressurizes.

Figure 5.4.5 gives the upper and lower drywell temperatures calculated by MELCOR. In the MELCOR calculation, the lower drywell temperature spikes up when debris first falls into the cavity at 4.4hr, triggering the spray initiation and passive flooder opening. The upper drywell temperature in the MELCOR calculation almost reached the penetration seal degradation temperature of 533K (500°F), but the HPME/DCH input parameters were selected so as not to degrade the penetrations during this temperature spike in the two high-pressure sequences with sprays, to prevent containment leakage rather than rupture disk actuation (to match the MAAP scenario). The spray keeps the upper drywell temperature low (310-315K). After the spray injection is stopped, the upper drywell temperature increases throughout the remainder of the transient. Note that the firewater spray would have resumed cycling on and off after about 23hr in the MELCOR calculation, based upon the upper drywell temperature, but those later spray cycles were suppressed to keep the suppression pool liquid level below the bottom of the drywell-wetwell vacuum breakers and, more importantly, to keep the spray from filling the suppression pool to the rupture disk elevation and causing liquid outflow.

Figures 5.4.6 and 5.4.7 show the total and partial pressures, and the mole fractions, respectively, in the atmospheres of the four control volumes representing containment (*i.e.*, upper and lower drywell, wetwell and drywell/wetwell vents). The predicted conditions are generally quite similar to those calculated for the LCLP-FS-R-N sequence (Figures 5.2.6 and 5.2.7). As in the LCLP-FS-R-N sequence results, the lower drywell and DW/WW vent atmospheres consist of almost all (>90%) steam after vessel failure and spray initiation at 4.5hr. In the upper drywell, steam begins accumulating after vessel failure at $\geq$4.5hr but almost all of that steam is condensed and removed by the firewater spray from spray initiation until after spray injection was calculated to stop at 22.5hr when the rupture disk opens. Even after spray injection ends, the steam concentration builds up again quite slowly and remains quite low. The response of the wetwell vapor space is similar to that predicted for the LCLP-FS-R-N sequence: steam does not predominate until after containment rupture disk actuation at 22.5hr, while most (about 50%) of the wetwell atmosphere between vessel failure and containment depressurization is hydrogen.

The containment continues to pressurize until the wetwell pressure reaches 0.72MPa (90psig) at 22.5hr in the MELCOR calculation, when the rupture disk opens as shown in Figure 5.3.18. The flow out the COPS rupture disk in the MELCOR calculation is presented in Figure 5.4.8. No penetration leakage is predicted by MELCOR, since the input was adjusted to keep the temperature in the upper drywell below 533K (500°F) until well after the rupture disk opens as illustrated in Figure 5.4.5. The upper drywell temperature in the MELCOR calculation almost reached the penetration seal degradation temperature of 533K (500°F) due to heat transfer from high-pressure debris ejection at vessel failure, but the HPME/DCH input parameters were selected so as not to degrade

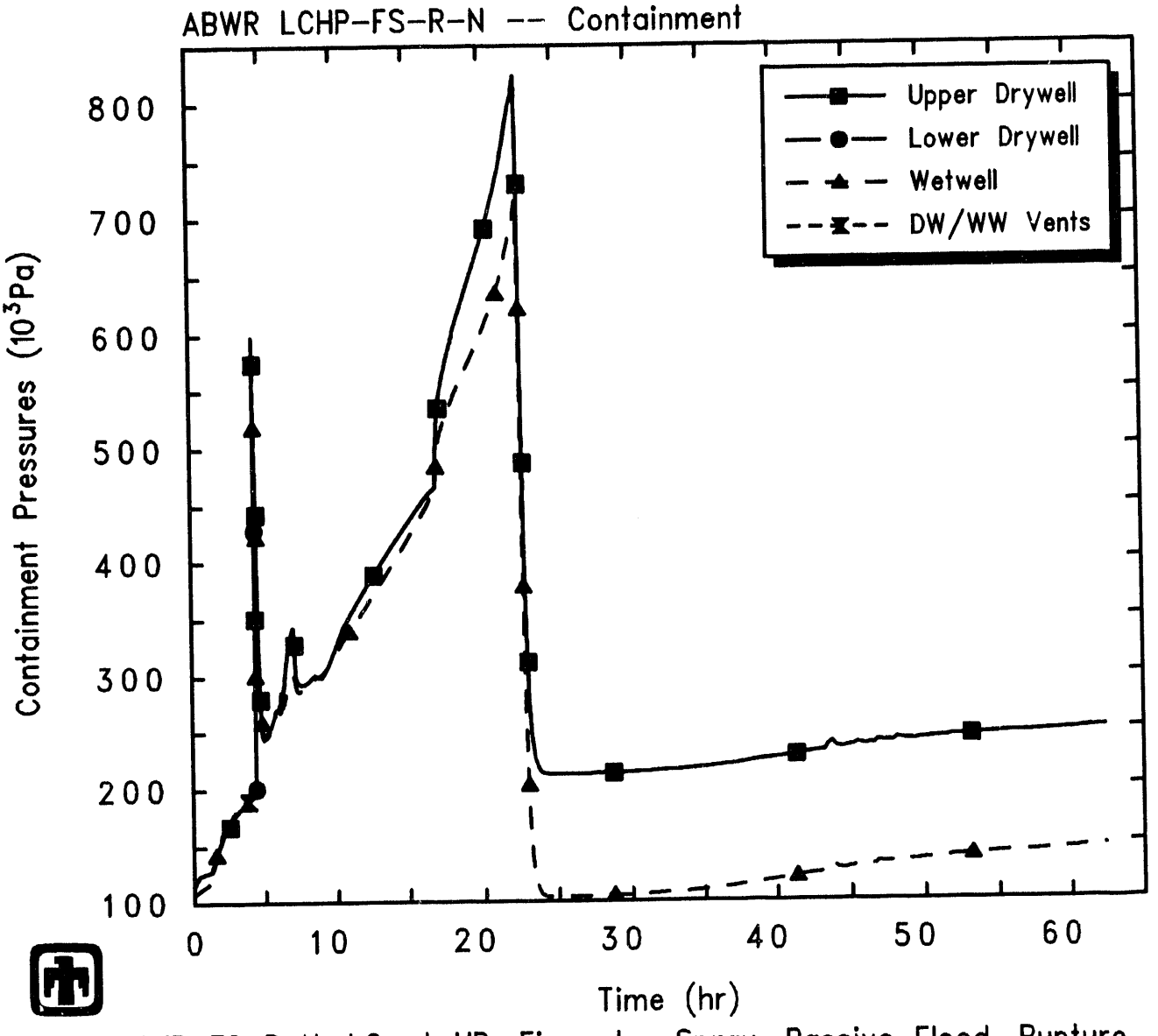

Figure 5.4.4. Containment Pressures Predicted by MELCOR for LCHP-FS-R-N Sequence

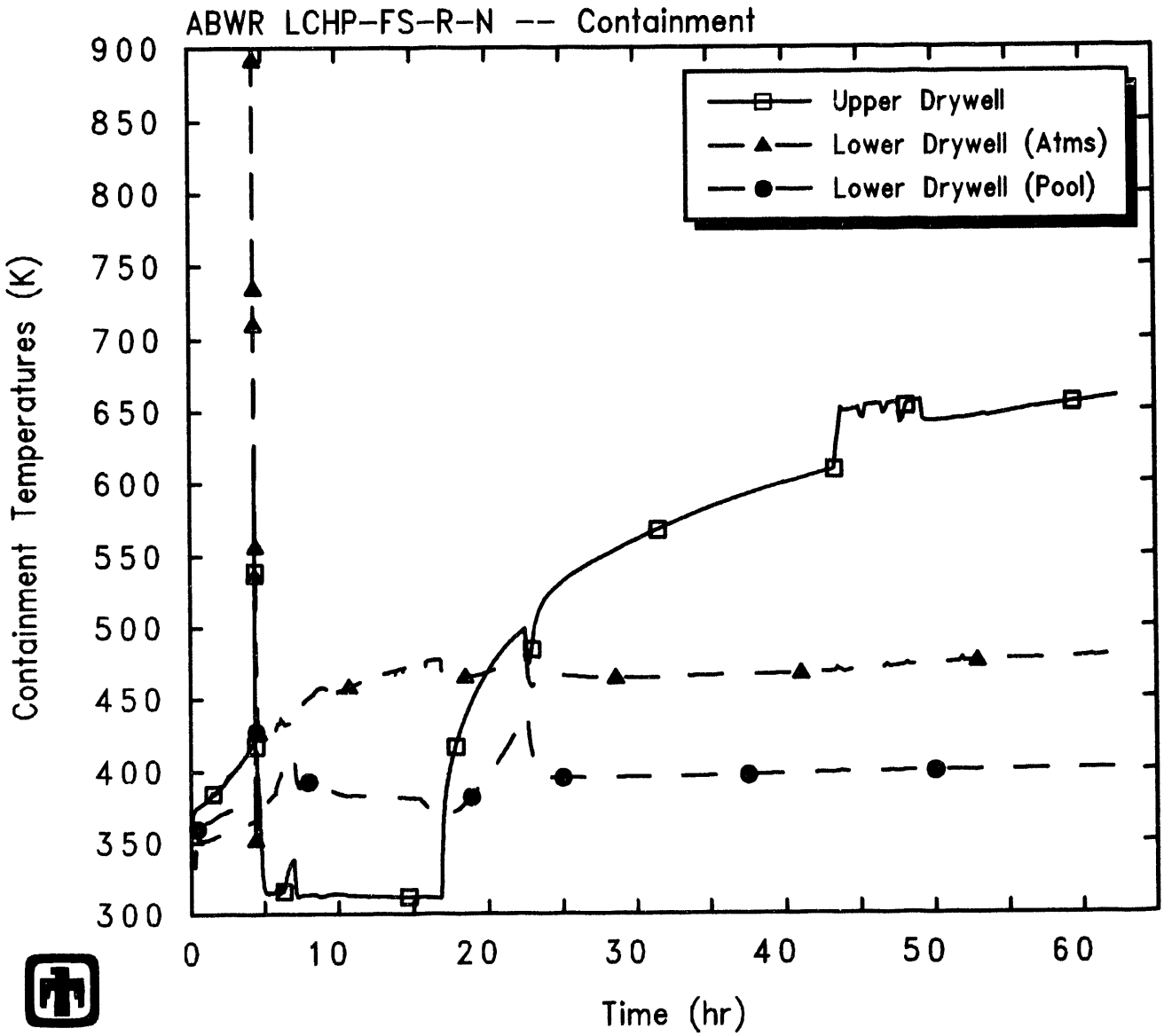

Figure 5.4.5. Containment Temperatures Predicted by MELCOR for LCHP-FS-R-N Sequence

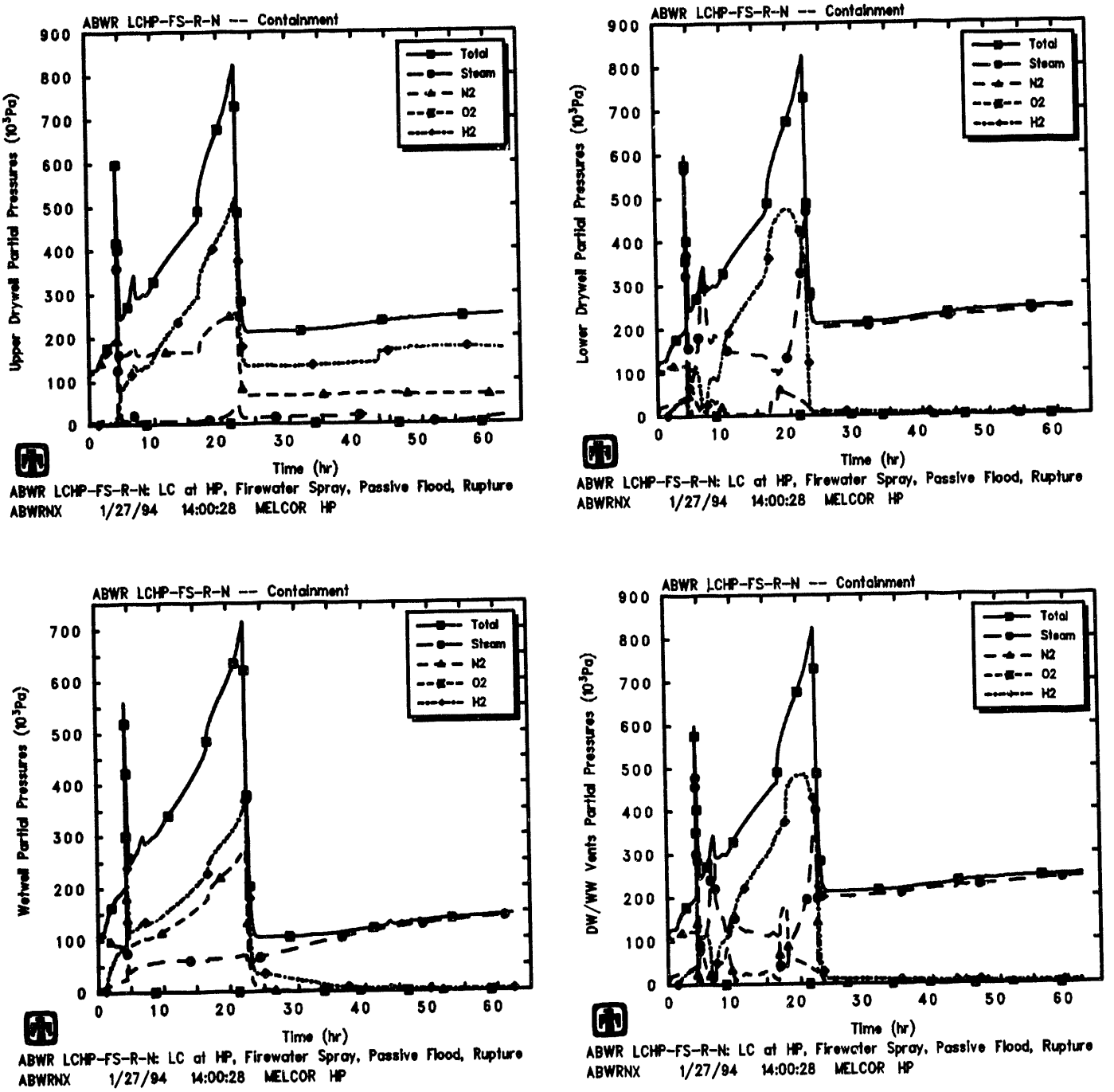

Figure 5.4.6. Containment Upper Drywell (upper left), Lower Drywell (upper right), Wetwell (lower left) and DW/WW Vent (lower right) Partial Pressures Predicted by MELCOR for LCHP-FS-R-N Sequence

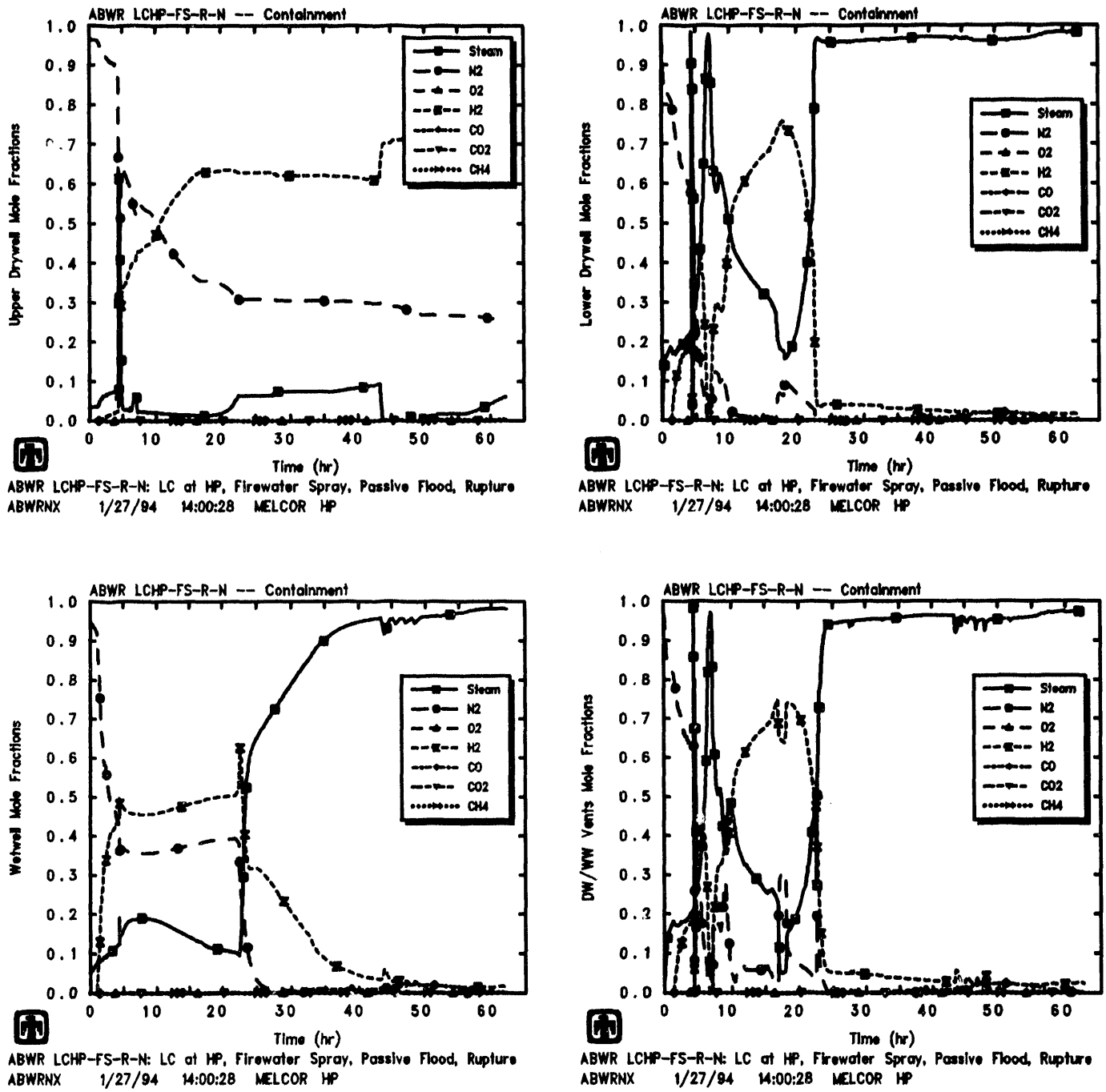

Figure 5.4.7. Containment Upper Drywell (upper left), Lower Drywell (upper right), Wetwell (lower left) and DW/WW Vent (lower right) Mole Fractions Predicted by MELCOR for LCHP-FS-R-N Sequence

the penetrations during this temperature spike in the two high-pressure sequences with sprays, to prevent containment leakage rather than rupture disk actuation (to match the MAAP scenario).

The total mass of debris in the cavity, the mass of ejected core debris, the mass of ablated concrete and the mass of gases generated in the cavity calculated by MELCOR are illustrated in Figure 5.4.9. The mass of core debris in the cavity for this sequence is very similar to the results for the LCHP-PF-P-M sequence; both are basically an inversion of the masses retained in-vessel, presented in Figure 5.3.12, with a small fraction of the debris mass (~10%) dispersed to either the upper drywell or the wetwell during high-pressure melt ejection. The debris ejection from the vessel can be seen to occur in discrete steps or stages, while the concrete mass ablated increases continuously with time. The mass of concrete ablated and the rate at which it is ablated predicted by MELCOR for the LCHP-FS-R-N sequence is quite similar to the LCHP-PF-P-M results calculated by MELCOR and given in Figure 5.3.23; the mass of concrete ablated predicted by MELCOR for this sequence is quite similar to the LCLP-FS-R-N results calculated by MELCOR and given in Figure 5.2.9, but the concrete is calculated to be ablated more slowly in this high-pressure sequence than in the corresponding low-pressure accident. (The similarity in the mass of concrete ablated by transient end in all these MELCOR analyses is not surprising, since all of these MELCOR analyses ran until stopped by "cavity rupture", *i.e.*, ablation of the initial specified 2m cavity depth, which required ablating about the same amount of material.)

As seen by the ablated concrete mass given in Figure 5.4.9, as soon as the core debris was predicted to enter the cavity, core-concrete interaction began, resulting in the production of carbon dioxide and hydrogen; reduction of these gases by the molten metal also gave rise to carbon monoxide and hydrogen. Figure 5.4.10 presents the production of various noncondensable gases in the cavity due to core-concrete interaction, calculated by MELCOR. Throughout the first half of the transient period calculated, almost all of the cavity gas production is in the form of hydrogen; however, there is a rapid increase in CO production after about 35hr. This is very similar to the MELCOR results for both the LCLP-FS-R-N sequence, illustrated in Figure 5.2.10, and the LCHP-PF-P-M scenario, shown in Figure 5.4.10 (although the low-pressure sequence analysis did not show as much CO generated, probably because of the earlier problem end time of ~40hr in that case). In all cases, CO is produced only after all the zironium in the cavity is oxidized to ZrO_2, because before that time Zr is assumed to reduce any CO_2 generated to pure carbon ("coking").

Figure 5.4.11 gives the calculated maximum cavity depth and radius. (Note that these represent maximum, not average, ablation distances.) Immediately after core debris is first ejected from the vessel to the cavity upon vessel breach in the MELCOR analysis, there is a brief period of rapid radial ablation, which stops after about 2.5cm of concrete loss. The bulk of the concrete ablation calculated is axially downward, with the MELCOR calculation stopping at 62hr due to "cavity rupture", when the axial ablation equals and tries to exceed the specified available concrete thickness of 2m.

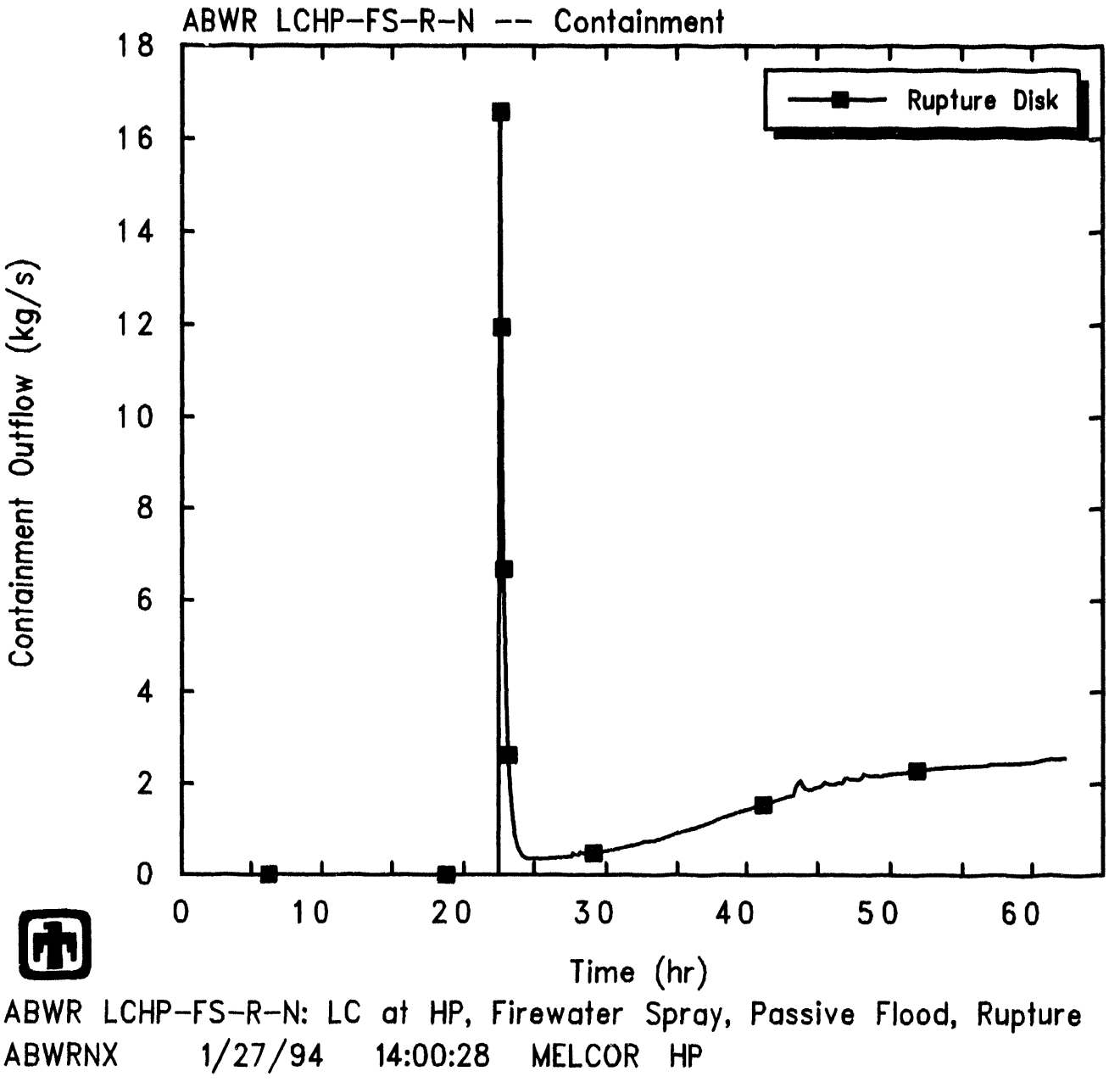

Figure 5.4.8. COPS Rupture Disk Mass Flow Predicted by MELCOR for LCHP-FS-R-N Sequence

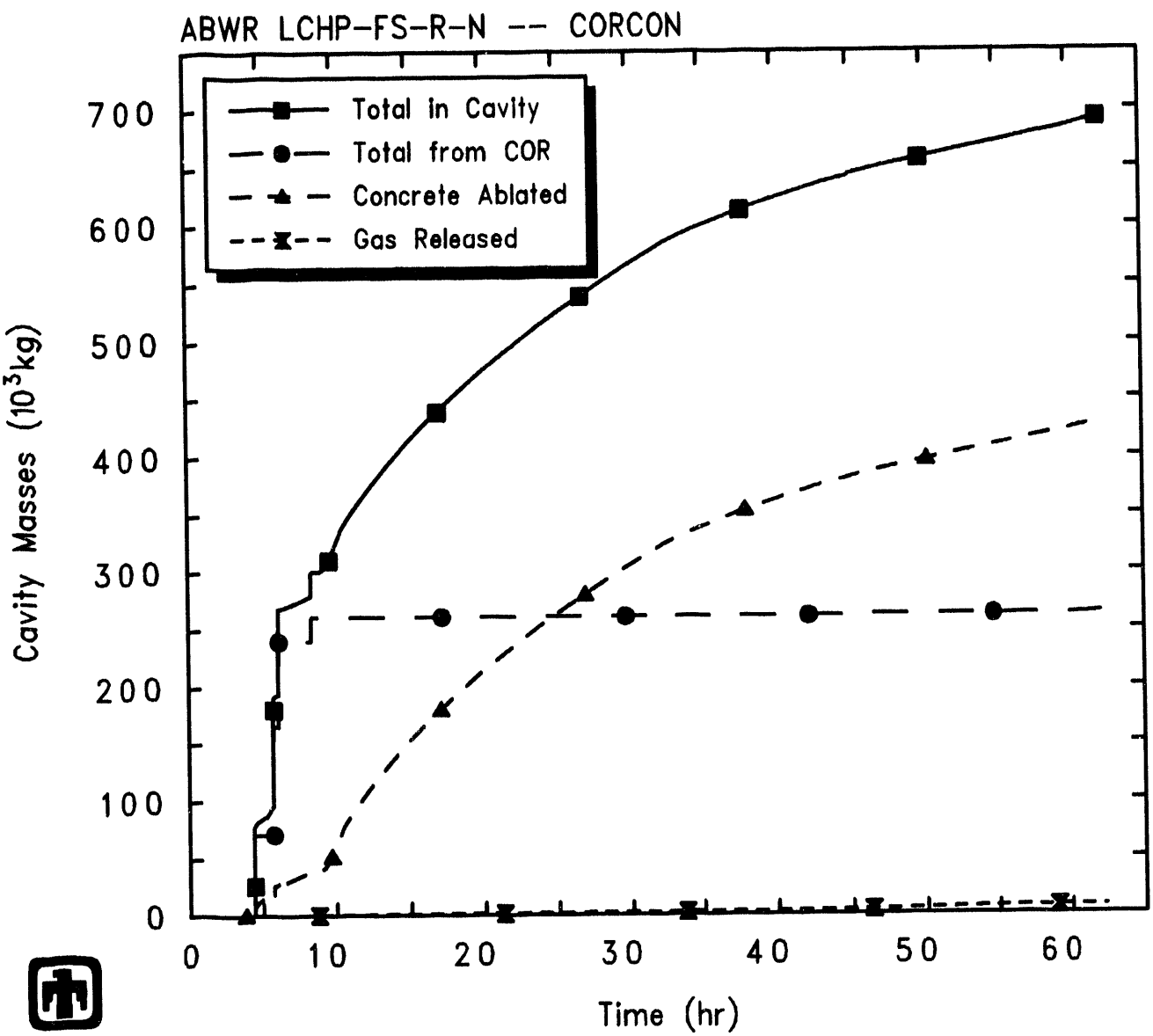

Figure 5.4.9. Cavity Material Masses Predicted by MELCOR for LCHP-FS-R-N Sequence

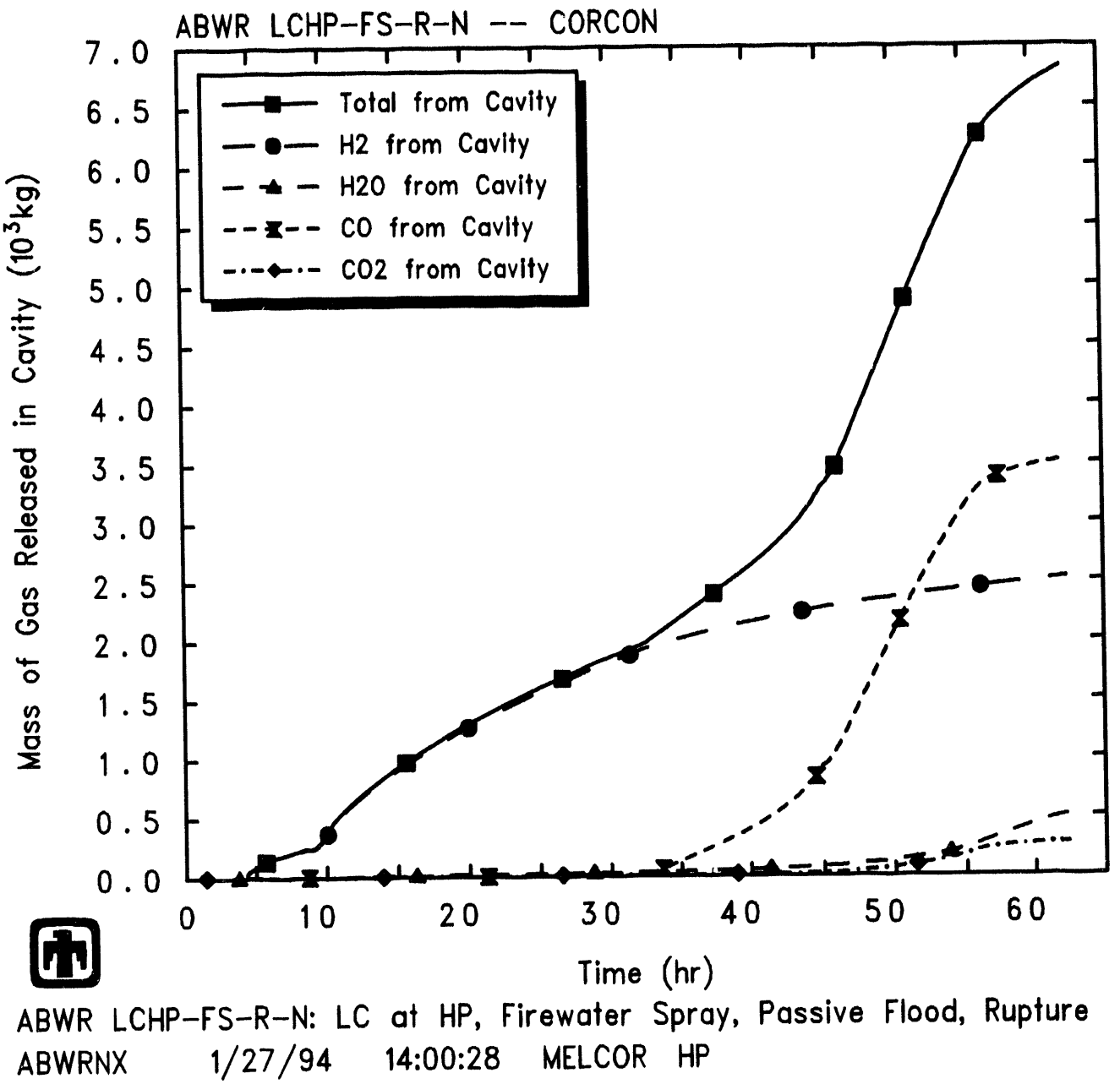

Figure 5.4.10. Cavity Gas Production Predicted by MELCOR for LCHP-FS-R-N Sequence

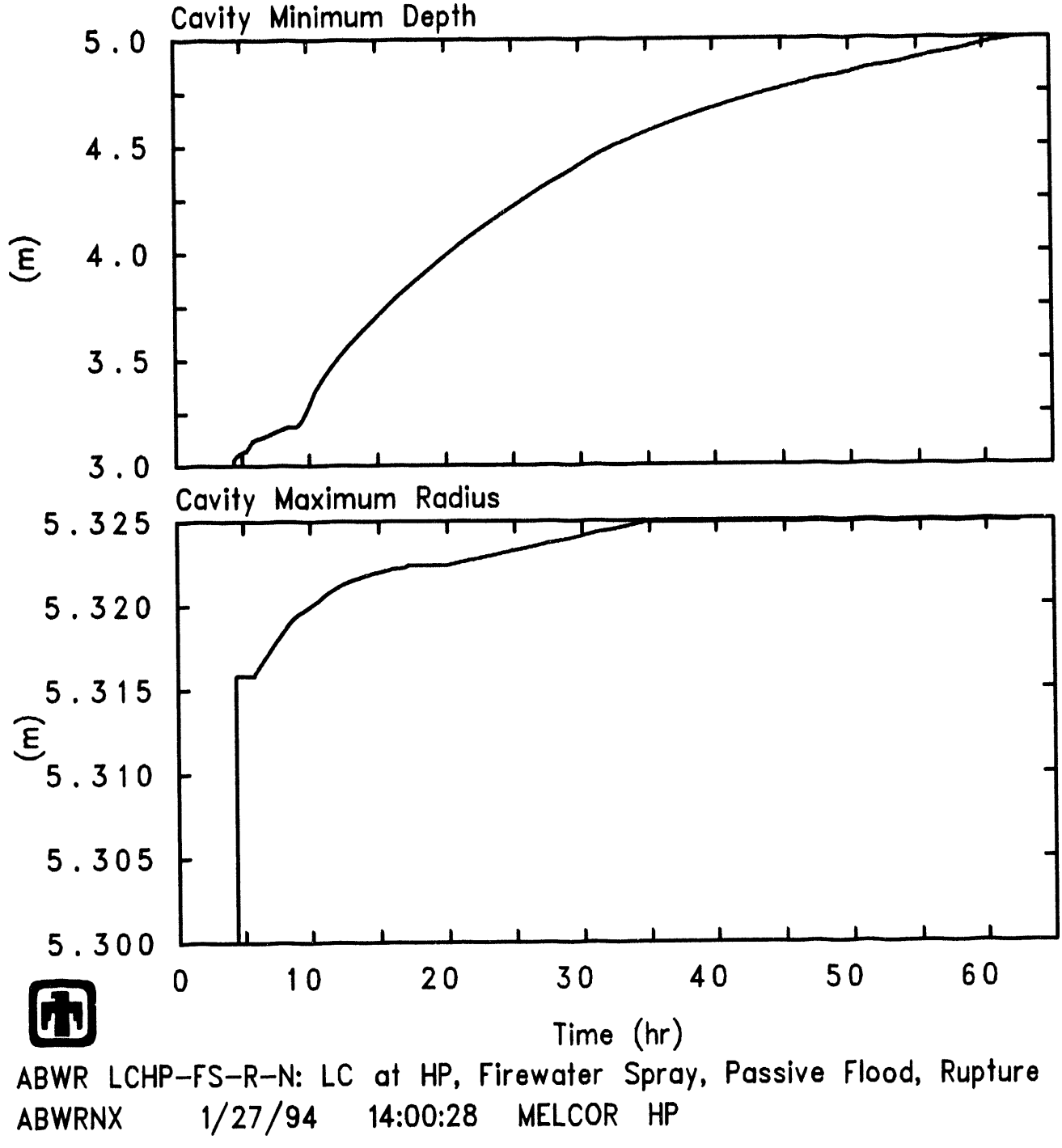

Figure 5.4.11. Cavity Maximum Radius and Depth Predicted by MELCOR for LCHP-FS-R-N Sequence

Figure 5.4.12 shows the predicted masses, thicknesses, temperatures and densities of the light oxide, metallic and heavy oxide debris layers in the cavity. A heavy oxide layer is present for only a brief period of time, after which MELCOR calculates a stable configuration of a light oxide layer above a metallic debris layer throughout the remainder of the transient period calculated. The transition from a metallic layer over a heavy oxide layer to a light oxide layer over a metallic layer at 10hr corresponds to the time when the concrete ablation rate increases (as illustrated in Figures 5.4.9 and 5.4.11). The metallic layer remains nearly constant in mass and thickness, with a gradually increasing density; the light oxide layer mass and thickness increase continuously (and the density decreases) as ablating concrete (with its resultant low-density silicate oxides) continues to dilute the high-density zirc oxide and steel oxide debris to an average density value less than the metallic debris density. After some initial oscillations, the temperatures of both layers remain nearly equal, at $\simeq$1500K, throughout the transient period calculated.

The heat transfer from the cavity debris pool in the MELCOR analysis, both downward and outward to the concrete surface and upward to the cavity volume atmosphere, is shown in Figure 5.4.13. The energy transfer from the debris in the cavity upward through the debris bed surface to the lower drywell atmosphere and/or overlying water pool is several times greater than the energy transferred downward (and sideways) to the concrete before about 9hr and after about 12hr. In general, that upper surface of the debris bed is covered with a water pool, not exposed to atmosphere.

Tables 5.4.2 and 5.4.3 give the distribution of the released radionuclides at the end of the calculation (*i.e.*, at ~62hr). Table 5.4.2 provides an overview of how much of the radionuclides remain bound up in fuel in either the core or the cavity, and of how much of the released radionuclides are retained in the primary system *vs* how much of the released radionuclides are released to, or released in, either the drywell or the wetwell in containment and the environment, all normalized to the initial inventories of each class. Table 5.4.3 gives a slightly different breakdown of the released radionuclide final distribution – the fractions of initial inventory released for each class from fuel in-vessel in the core, ex-vessel in the cavity and overall total are given, together with the distribution of the released radionuclides in the primary system, drywell, wetwell and environment normalized by the mass of each class released. (Note that these amounts generally consider only the release of radioactive forms of these classes, and not additional releases of nonradioactive aerosols from structural materials.)

The release behavior predicted by MELCOR can be grouped into the same several subdivisions as found in the other MELCOR sequence analyses. Almost all ($\simeq$100%) of the volatile Class 1 (noble gases), Class 2 (CsOH), Class 5 (Te) and Class 16 (CsI) radionuclide species are released, primarily in-vessel, as are most (80-90%) of the Class 3 (Ba) and Class 12 (Sn) inventories. The next major release fractions are of Ru and Mo, Ce and La, all between about 0.5% and 2%. Finally, $\leq$0.1% of the initial inventory of uranium and Class 11 (Cd) are predicted to be released. This is very similar to the fission product release behavior predicted by MELCOR for the LCHP-PF-P-M sequence. (Note that the CORSOR-M fission product release model option used in these analyses has identically zero release in-vessel of Class 7, Class 9 and Class 11.)

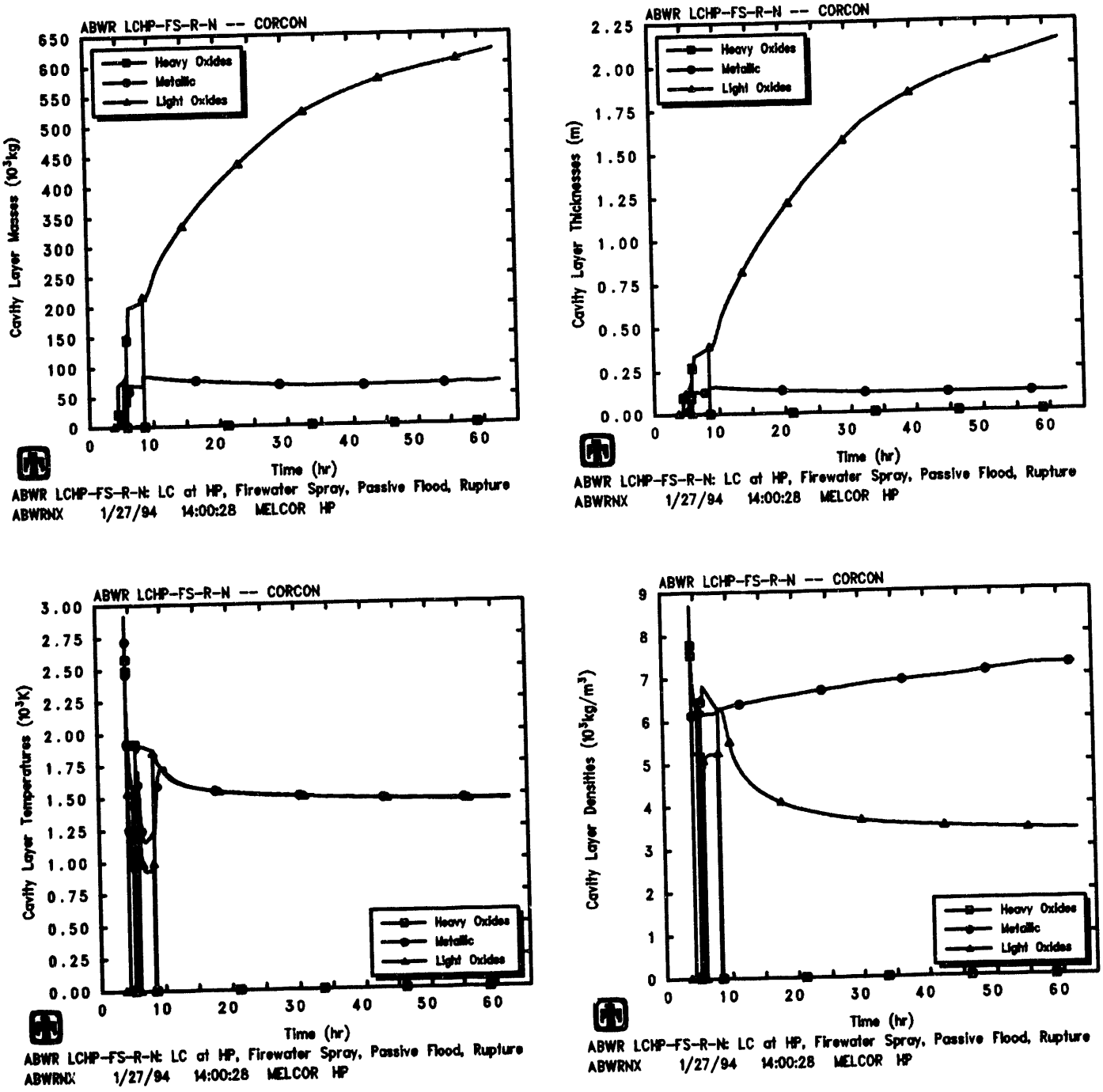

Figure 5.4.12. Cavity Layer Masses (upper left), Thicknesses (upper right), Temperatures (lower left) and Densities (lower right) Predicted by MELCOR for LCHP-FS-R-N Sequence

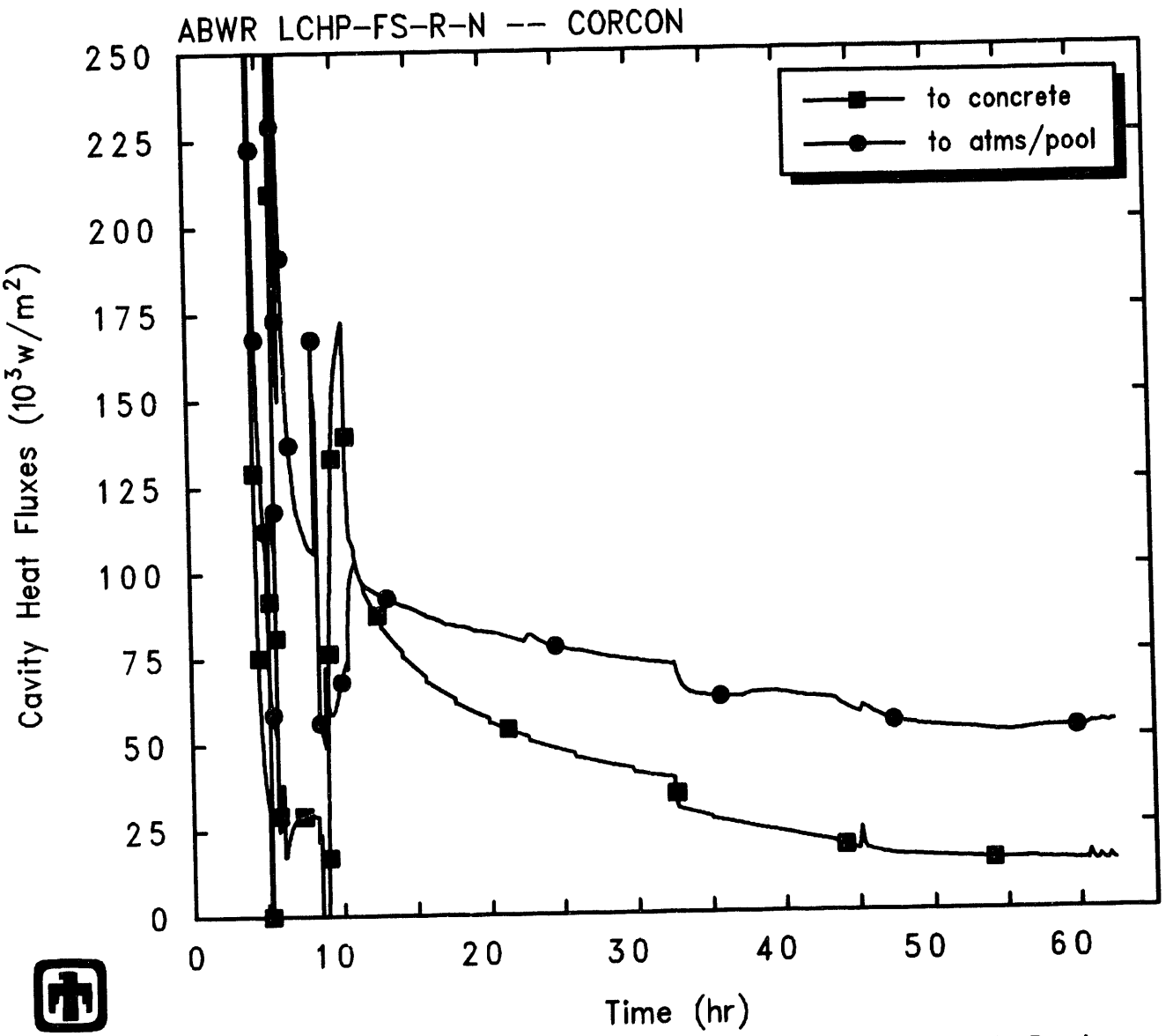

Figure 5.4.13. Cavity Heat Flows Predicted by MELCOR for LCHP-FS-R-N Sequence

Table 5.4.2. Radionuclide Distribution Predicted at 62hr for LCHP-FS-R-N Sequence

Class	Fission Product Distribution (% Initial Inventory)					
	Remaining in Fuel		Released from Fuel			
	Core	Cavity	Primary System	Drywell	Wetwell	Environment
Noble Gases (Xe)	7.12×10^{-3}	0	0.0562	8.41	0.0157	91.5
Alkali Metals (CsOH)	7.60×10^{-3}	$\simeq$0	22.9	10.5	66.5	0.0771
Alkaline Earths (Ba)	0.246	13.6	53.9	2.38	29.9	6.45×10^{-5}
Halogens (I)	$\simeq$0	$\simeq$0	$\simeq$0	$\simeq$0	$\simeq$0	$\simeq$0
Chalcogens (Te)	0.0207	0.436	50.3	5.09	44.1	0.0255
Platinoids (Ru)	0.367	98.7	0.635	0.0236	0.281	8.82×10^{-7}
Transition Metals (Mo)	0.368	97.2	0.0111	0.450	1.99	1.22×10^{-3}
Tetravalents (Ce)	0.368	98.9	0.490	0.0185	0.217	2.35×10^{-6}
Trivalents (La)	0.369	96.7	6.05×10^{-4}	0.247	2.65	1.43×10^{-4}
Uranium (U)	1.14	98.8	0.0143	1.27×10^{-3}	0.0132	1.93×10^{-6}
More Volatile Main Group Elements (Cd)	0.368	99.5	4.32×10^{-5}	0.0103	0.0987	1.02×10^{-5}
Less Volatile Main Group Elements (Sn)	0.220	7.61	57.0	2.56	32.6	2.86×10^{-5}
CsI	$\simeq$0	2.51×10^{-4}	15.9	11.1	73.0	0.149

Table 5.4.3. Radionuclide Release and Released Distribution Predicted at 62hr for LCHP-FS-R-N Sequence

Class	Released from Fuel (% Initial Inventory)			Distribution (% Released Mass)			
	Core	Cavity	Total	Primary System	Drywell	Wetwell	Environment
Noble Gases (Xe)	99.71	0.106	99.82	0.0562	8.41	0.0157	91.52
Alkali Metals (CsOH)	99.71	0.164	99.87	22.90	10.49	66.53	0.0771
Alkaline Earths (Ba)	79.00	0.605	79.61	62.50	2.76	34.75	7.48×10^{-5}
Halogens (I)	$\simeq$0	$\simeq$0	$\simeq$0	0.0248	6.99	0.0129	92.98
Chalcogens (Te)	98.89	0.046	98.94	50.57	5.11	44.29	0.0257
Platinoids (Ru)	0.588	3.82×10^{-4}	0.588	67.59	2.51	29.90	9.38×10^{-5}
Transition Metals (Mo)	0	1.50	1.50	0.454	18.37	81.13	0.0497
Tetravalents (Ce)	0.452	5.18×10^{-4}	0.453	67.53	2.55	29.92	3.24×10^{-4}
Trivalents (La)	0	1.81	1.81	0.021	8.52	91.46	4.92×10^{-3}
Uranium (U)	0.013	5.17×10^{-3}	0.018	49.58	4.41	46.01	6.69×10^{-3}
More Volatile Main Group Elements (Cd)	0	0.068	0.068	0.040	9.447	90.50	9.38×10^{-3}
Less Volatile Main Group Elements (Sn)	88.22	7.07×10^{-3}	88.23	61.82	2.78	35.41	3.11×10^{-5}
CsI	99.72	0.170	99.89	15.94	10.95	72.96	0.149

Most of the released radionuclides remain in the primary system and/or the containment. Most (>90%) of the noble gases show a significant release to the environment. Of the other volatile radionuclides, $\leq$0.1-0.2% of the total masses of CsOH and CsI and 0.025% of Class 5 (Te) are released to the environment, similar to the release predicted in either the two low-pressure sequences but much smaller than for the LCHP-PF-P-M high-pressure scenario. As in the corresponding LCLP-FS-R-N low-pressure accident, $\ll$0.01% of the other radionuclides' initial inventory is released to the environment. Of the species with significant (>80%) release from fuel, the wetwell retains a significant fraction (65-75%) of the released CsOH and CsI volatiles, while the Ba and Sn aerosols, and Te, are held up both in the primary system (50-70%) and in the wetwell (35-45%); this is the same pattern as found for the other scenarios analyzed.

Except for noble gases, the predicted release to the environment of each radionuclide species is much lower for the LCHP-FS-R-N sequence than calculated for the LCHP-PF-P-M sequence, reflecting the sprays removing fission products from the containment atmosphere and/or structures (*via* draining condensate films) into the suppression pool; the much lower releases calculated for the LCHP-FS-R-N sequence also reflect the additional scrubbing due to deliberately venting the containment in the wetwell vapor space through the rupture disk rather than bypassing the suppression pool by leaking through the movable containment penetrations in the upper drywell. The predicted release to the environment of all radionuclide species for the LCHP-FS-R-N sequence is generally similar to that calculated for the LCLP-FS-R-N sequence, the corresponding low-pressure scenario with automatic vessel depressurization.

Figures 5.4.14 and 5.4.15 give the retention factors for the various radionuclides calculated by MELCOR, for the primary system and for the overall containment, respectively. The retention factors are defined as the fraction of material released in, or transported into, a region which remains in that region. The vessel retention factors fall into three sets:

- essentially no retention for the noble gases and for I_2 (of which there is very little),
- a retention of 20-30% for the cesium radionuclide species (*i.e.*, CsOH and CsI),
- a retention of 50% for the other radionuclide species with non-zero vapor pressure (*i.e.*, Te), and
- a $\geq$50% retention of those classes which form aerosols only.

These are qualitatively very similar to, but quantitatively somewhat higher than, the values found in the LCLP-FS-R-N sequence, shown in Figure 5.2.14. The containment retention factors fall into several distinct categories also, and are very similar to the values for the LCLP-FS-R-N sequence, shown in Figure 5.2.15:

- <10% retention for the noble gases and for I_2 after COPS rupture,

- a retention of about 80% for the cesium radionuclide species (*i.e.*, CsOH and CsI),
- a retention of ~50% for Te, which also has both aerosol and vapor forms, and for uranium, and
- for the other classes which form aerosols only, there is a 30-40% retention for those which had some in-vessel release (Ba, Ru, Ce and Sn) and a ~100% retention of those with only ex-vessel release (Mo, La and Cd).

These are also generally quite similar to the values found in the LCLP-FS-R-N sequence, shown in Figure 5.2.15 except for Class 5 (Te), which had a higher containment retention factor in the corresponding low-pressure LCLP-FS-R-N sequence (~70%) than in the LCHP-FS-R-N sequence.

Figures 5.4.16 and 5.4.17 give the decontamination factors (DFs) for the various radionuclides calculated by MELCOR, for the suppression pool and for the overall containment, respectively. The period of interest in these plots is after 23.55hr when the containment rupture disk is predicted to open. After containment depressurization, the suppression pool and overall containment DFs are simply DF=1.0 for the noble gases and for I_2 (of which there is very little), not shown in these plots to highlight the region of interest.

The suppression pool DFs after containment rupture disk actuation vary over almost two orders of magnitude,

- $DF_{SP} \leq 100$ for Cd, La and U,
- $DF_{SP} \sim 200\text{-}600$ for most classes (CsOH, Te, Ru, Mo, Ce and CsI), and
- $DF_{SP} > 1000$ for the other classes (Ba and Sn).

The magnitude of the various wetwell DFs calculated by MELCOR for the LCHP-FS-R-N sequence are generally much higher than those calculated by MELCOR for the LCHP-PF-P-M sequence, presented in Figure 5.3.30, reflecting the sprays removing fission products from the containment atmosphere and/or structures (*via* draining condensate films) into the suppression pool. The much higher decontamination factors calculated for the LCHP-FS-R-N sequence also reflect the additional scrubbing due to deliberately venting the containment in the wetwell vapor space through the rupture disk rather than bypassing the suppression pool by leakage through movable penetrations in the upper drywell. The various DFs calculated by MELCOR for the LCHP-FS-R-N sequence are generally slightly lower than those calculated by MELCOR for the LCLP-FS-R-N sequence, presented in Figure 5.2.16. The classes predicted to have relatively higher wetwell decontamination factors are also different in the various analyses, reflecting differences in release and distribution.

The overall containment DFs predicted for the LCHP-FS-R-N sequence also are much higher than those calculated by MELCOR for the LCHP-PF-P-M sequence, presented in Figure 5.3.31, and generally similar to those calculated by MELCOR for the LCLP-FS-R-N sequence, presented in Figure 5.2.17:

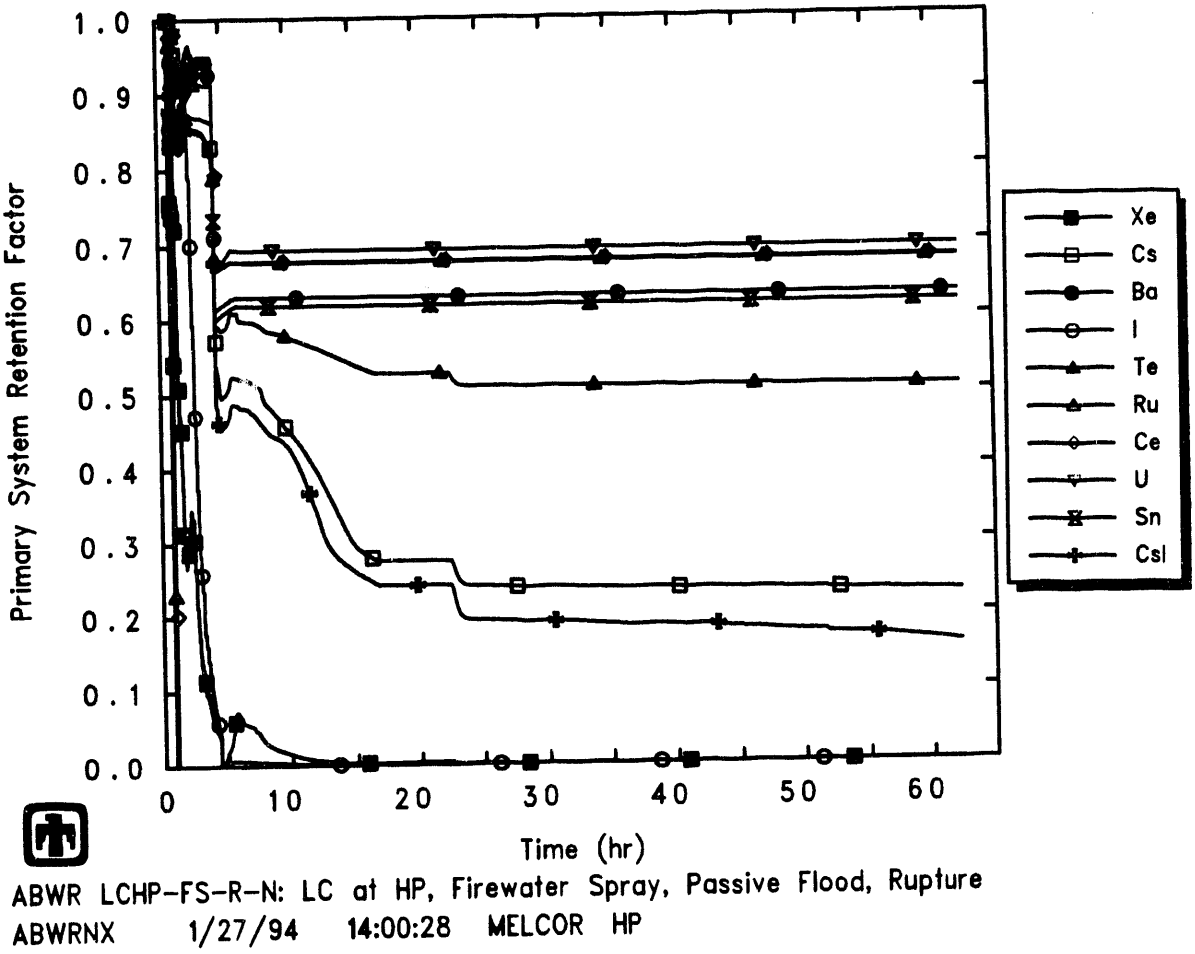

Figure 5.4.14. Primary System Retention Factors Predicted by MELCOR for LCHP-FS-R-N Sequence

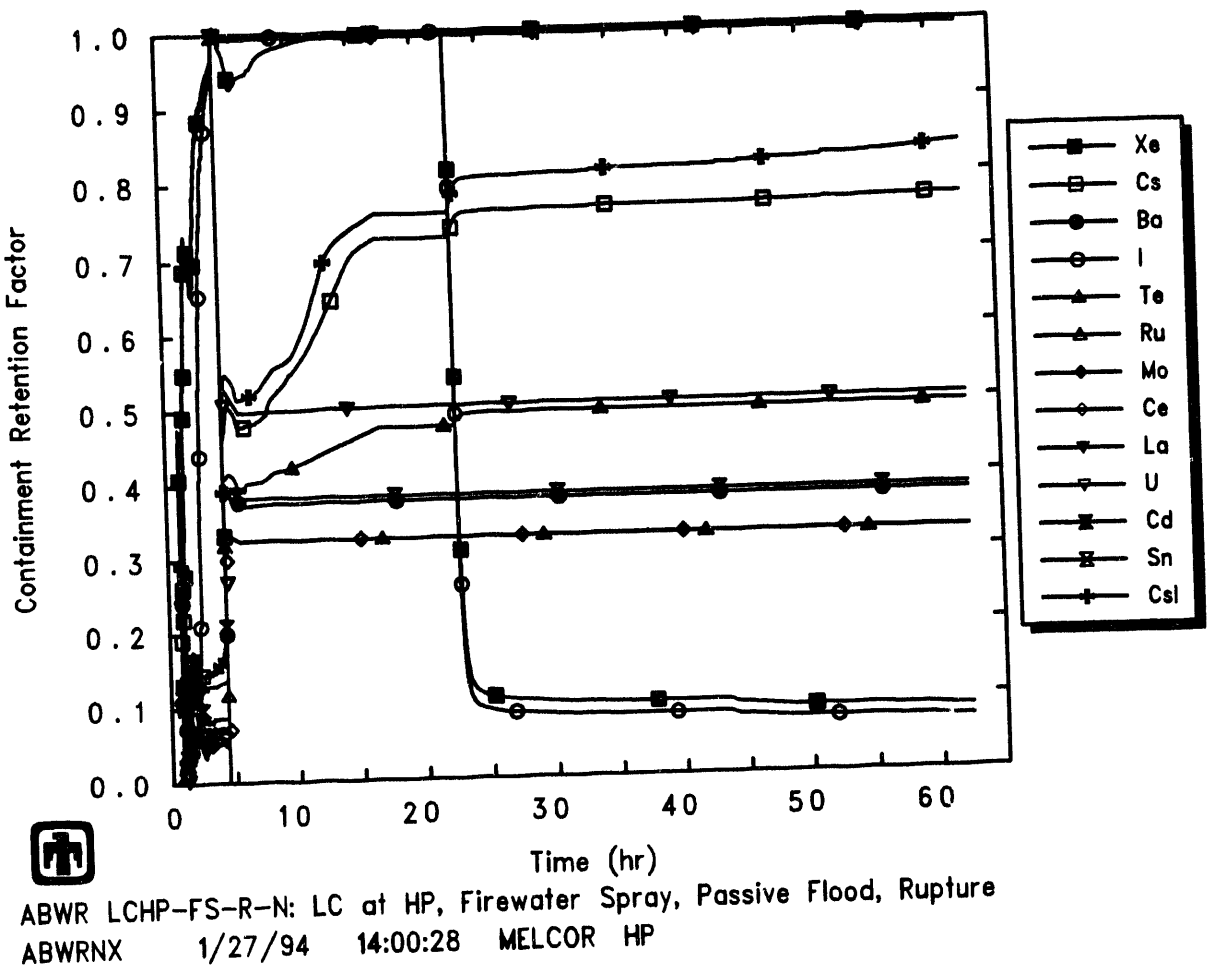

Figure 5.4.15. Containment Retention Factors Predicted by MELCOR for LCHP-FS-R-N Sequence

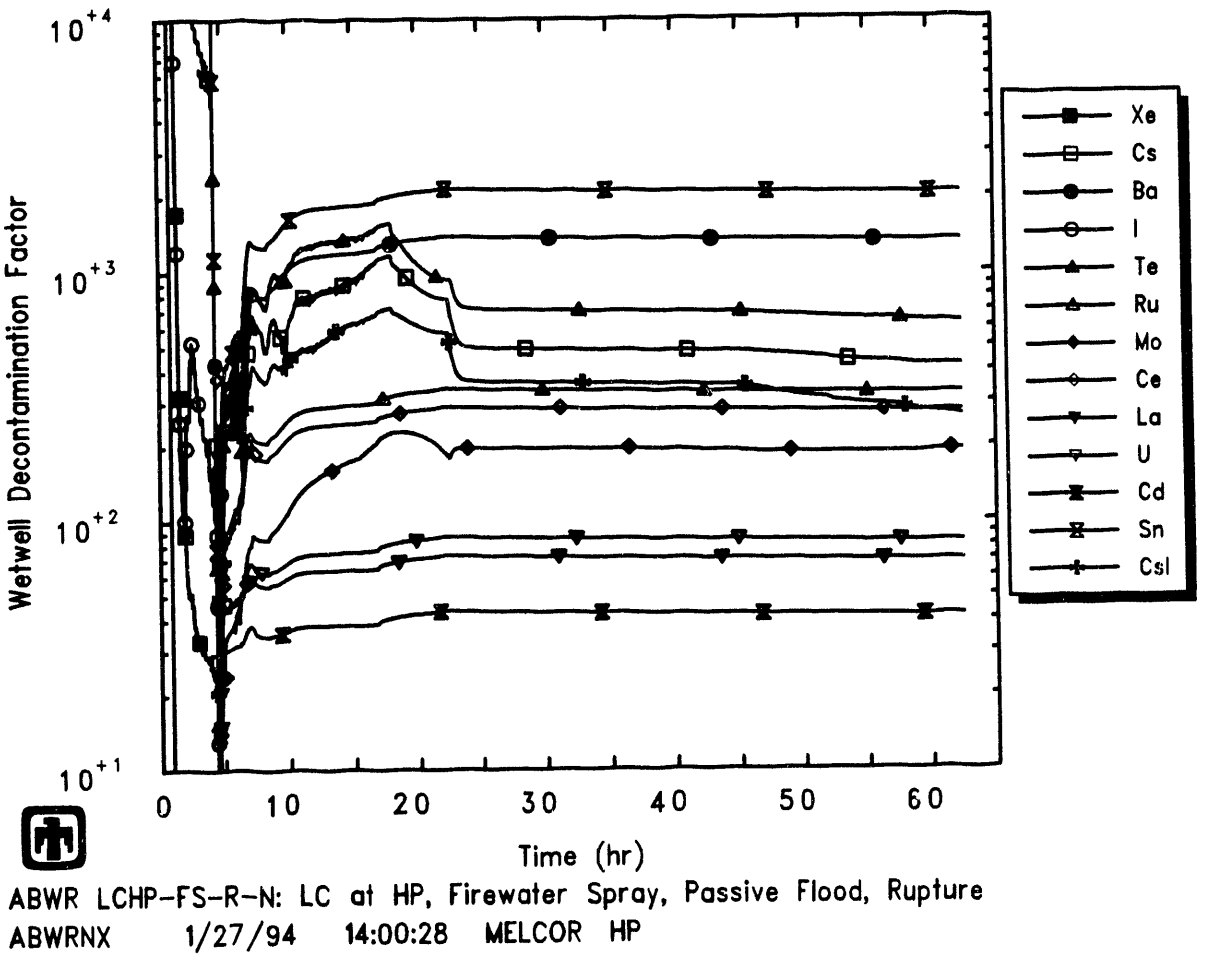

Figure 5.4.16. Suppression Pool Decontamination Factors Predicted by MELCOR for LCHP-FS-R-N Sequence

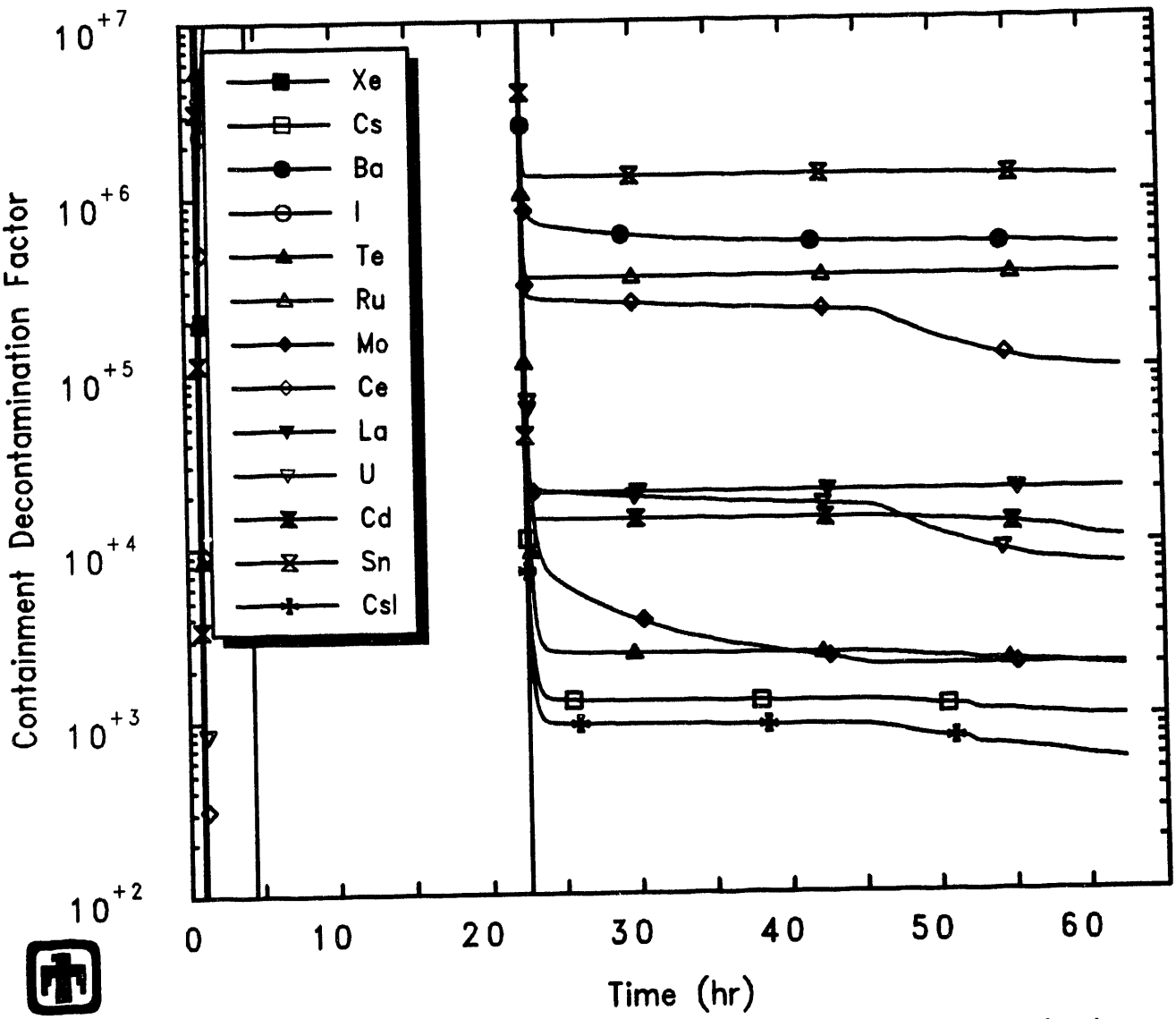

Figure 5.4.17. Overall Containment Decontamination Factors Predicted by MELCOR for LCHP-FS-R-N Sequence

- $DF_{Cont} \leq 1000$ for the cesium radionuclide classes (CsOH and CsI),
- $DF_{Cont} \sim 2000$ for the other volatile class (Te) and for Mo,
- $DF_{Cont} \sim 10{,}000$ for several classes (La, U and Cd),
- $DF_{Cont} \geq 100{,}000$ for Class 3 (Ba), Class 6 (Ru) and Class 8 (Ce), and
- $DF_{Cont} \geq 1{,}000{,}000$ for Class 12 (Sn).

Note that both the suppression pool and overall containment decontamination factors remain nearly constant for most classes after containment rupture disk opening, but drop noticeably for several radionuclide species, either continually after rupture disk opening at 23.5hr (Mo) or late in the transient after about 40hr (Ce, U, CsI). These are generally the classes for which a varying release to the environment is predicted, while for the other classes there is only a single step-like release at COPS opening, as illustrated in Figure 5.4.18.

Figure 5.4.18 does not include the release of the noble gases, to allow expansion of the scale for the environmental release of the other radionuclide classes; the release of the noble gases in the MELCOR calculation occurs within a brief time after containment rupture disk opening, and almost all of the noble gases are released. The rupture disk opens at 50hr in the MAAP calculation and the volatile fission product release continues for the next 75hr and the CsI release fraction at 72hr is less than 10^{-7} [1]. This MELCOR calculation shows environment release fractions by the end of the calculation (62hr) of about 8×10^{-4} and 1.5×10^{-3} for CsOH and CsI, respectively, normalized to their total available inventory (Table 5.4.2; since ~99.9% of these radionuclides were predicted to be released, the same environment release fractions are obtained normalizing to released inventories (Table 5.4.3). The release fractions calculated by MELCOR are significantly higher than the values predicted by MAAP, primarily due to the continuing steaming of cavity water by non-quenched debris in MELCOR; however, the MELCOR release fractions are still very small fractions of the fission product inventories initially present, released but retained within containment even after COPS actuation.

5.5 LCHP-PS-R-N Sequence

The first part of this sequence, through core uncovery, heatup and degradation, and vessel lower head failure, is almost identical to the behavior discussed for the LCHP-PF-P-M sequence in Section 5.3. The sequence of events predicted by MELCOR for this accident sequence is given in Table 5.5.1, with the timings of the various events as calculated by MAAP (taken from Table 19E.2-7 in [1]) included for comparison.

Before the spray system begins injection, the results of this sequence are identical to those for the LCHP-PF-P-M sequence discussed in Section 5.3. The drywell sprays were assumed to be turned on at 4hr in this MELCOR calculation, which was the same time as in the MAAP analysis (Section 19E.2.2.2(a) and Table 19E.2-7 in [1]). Note that this

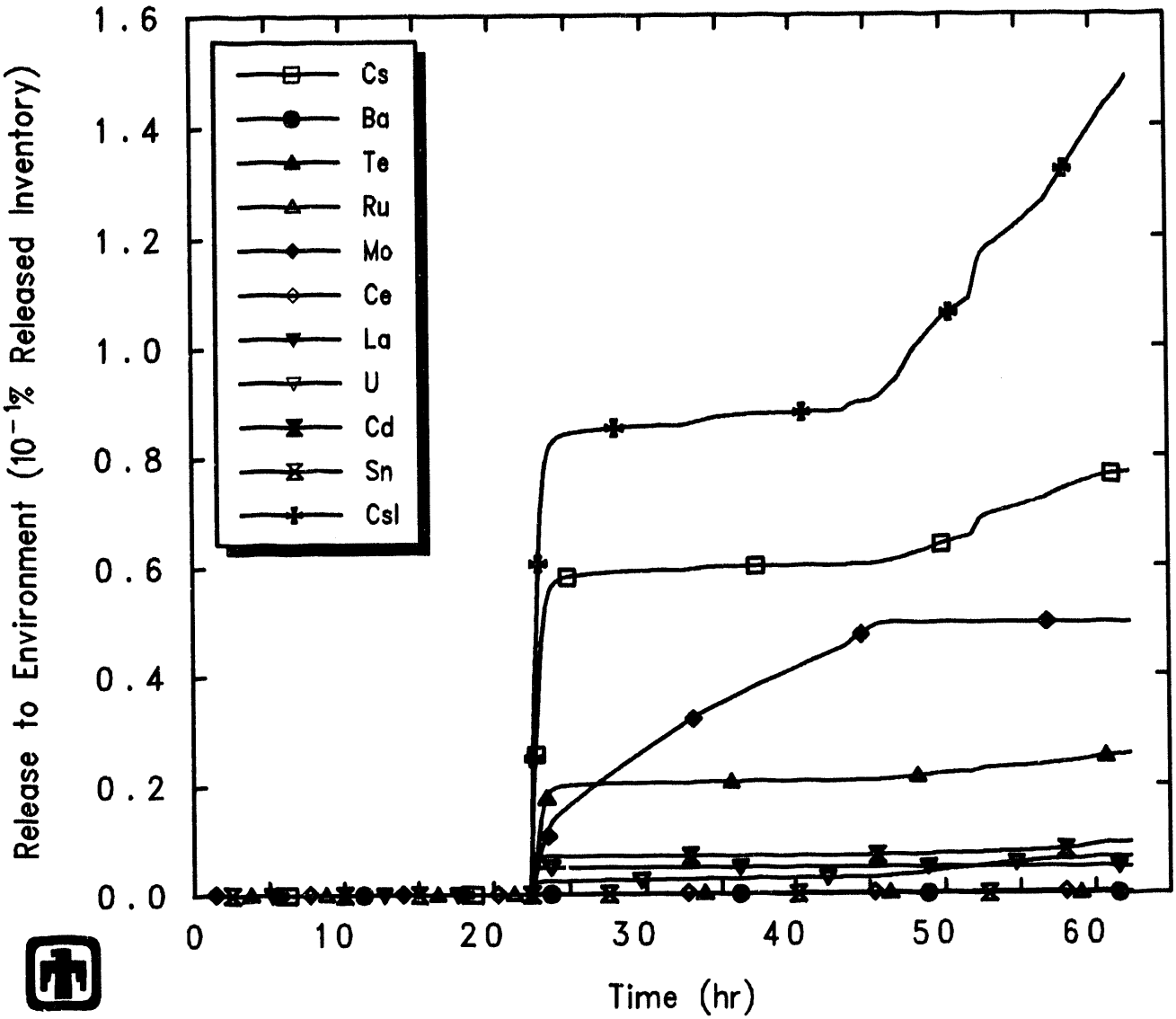

Figure 5.4.18. Radionuclide Environmental Releases Predicted by MELCOR for LCHP-FS-R-N Sequence

Table 5.5.1. Sequence of Events Predicted by MELCOR for LCHP-PS-R-N Sequence, Compared to MAAP

Event	Time	
	MAAP	MELCOR
Accident initiation (MSIV Closure)	0.0	0.0
Reactor scrammed	4.2s	
Core uncovery begins	0.3hr	1,637.5s (0.45hr)
Clad failure/Gap release		
(Ring 1)		3,203.3s (0.83hr)
(Ring 2)		4,322.8s (1.20hr)
(Ring 3)		5,144.0s (1.43hr)
(Ring 4)		8,279.6s (2.30hr)
Core plate failed		
(Ring 1)		16,325.9s (4.53hr)
(Ring 2)		19,945.2s (5.54hr)
(Ring 3)		21,997.4s (6.11hr)
(Ring 4)		28,763.6s (7.99hr)
Vessel bottom head failed	2.0hr	
Vessel LH penetration failed		
(Ring 1)		16,385.7s (4.55hr)
(Ring 2)		16,395.3s (4.55hr)
(Ring 3)		16,408.3s (4.56hr)
(Ring 4)		16,416.8s (4.56hr)
Commence debris ejection		16,385.7s (4.55hr)
End of HPME/DCH		16,559.0s (4.60hr)
Passive flooder opens	2.0hr	16,391.5s (4.55hr)
Drywell spray started	4.0hr	14,400.0s (4.00hr)
Drywell spray stopped		78,014.8s (21.67hr)
Rupture disk opens	25.0hr	78,014.8s (21.67hr)
Concrete ablation $\geq$2m		203,278s (56.47hr)
End of calculation	100hr	203,278s (56.47hr)

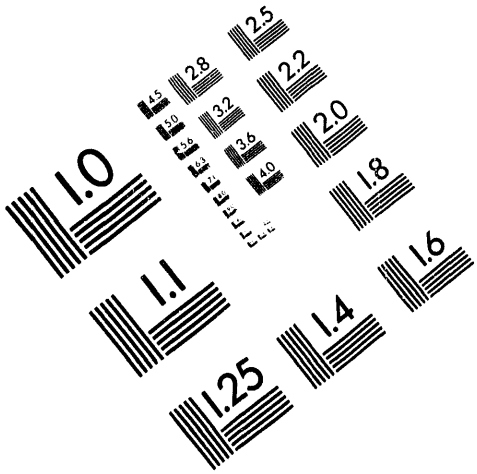

Association for Information and Image Management
1100 Wayne Avenue, Suite 1100
Silver Spring, Maryland 20910
301/587-8202

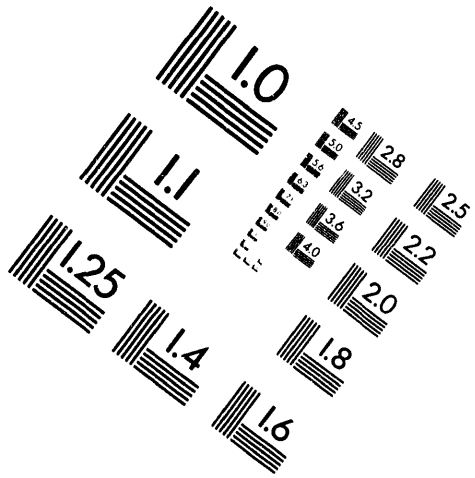

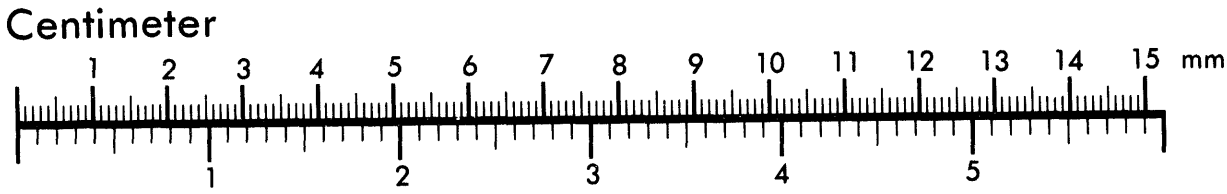

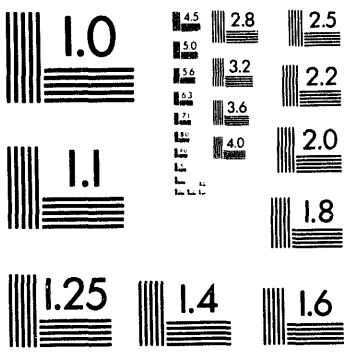

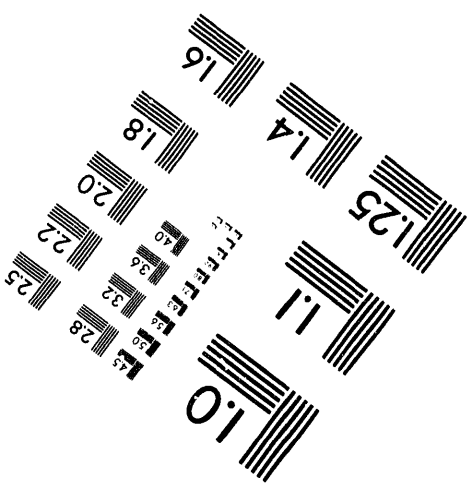

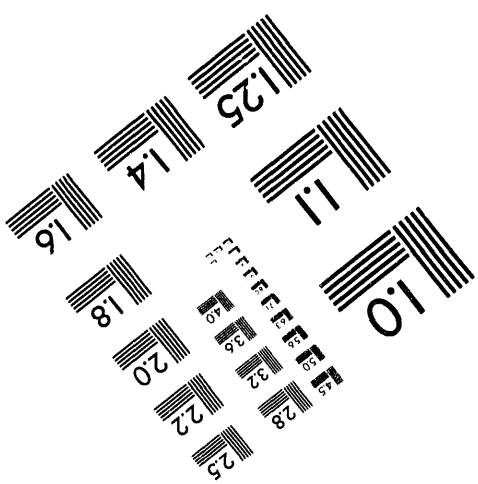

MANUFACTURED TO AIIM STANDARDS
BY APPLIED IMAGE, INC.

3 of 3

is after vessel failure (at 2hr) in the MAAP analysis, but before vessel failure (at 4.5hr) in the MELCOR analysis. However, turning on the drywell spray before vessel failure has little or no effect on the subsequent in-vessel accident progression predicted, as can be seen by comparing timings in Tables 5.3.1 and 5.5.1. (If the drywell spray were assumed to turn on according to the same actuation logic as used for the firewater spray in the LCHP-FS-R-N sequence, described in Section 5.4, the spray would have been turned on at 4.55hr, a small timing difference which would have little or no effect on the results calculated.)

Figure 5.5.1 shows the collapsed liquid level in the lower drywell (cavity) control volume in the MELCOR calculation, for comparison to the LCHP-PF-P-M and LCHP-FS-R-N sequence results given in Figures 5.3.15 and 5.4.1.

The spray flow starts shortly as the vessel fails but, since the flow from the sprays does not initially enter into and cool the lower drywell, the passive flooder opens as soon as core debris falls into the cavity and begins heating the lower drywell. The sudden rise in liquid level at 4.55hr thus corresponds to the remaining lower plenum water pouring out the vessel breach and to suppression pool water entering through the passive flooder opening. Water then pours from the wetwell into the drywell to the level of the upper horizontal vent. After an initial transient, the cavity liquid level settles to a constant pool depth of about 2m for the remainder of the transient.

Figure 5.5.2 give the drywell and wetwell pool masses for the MELCOR analysis, compared to the pool masses calculated by MAAP (taken from Figure 19E.2-4F in [1]). There appears to be a small difference in the suppression pool initial mass (and/or level) in the two calculations, and MELCOR predicts a bigger short-term drop in suppression pool level and corresponding rise in cavity pool level upon opening the passive flooder. However, the results are generally in very good agreement, with both codes showing no net change in suppression pool level due to drywell spray injection (because the drywell spray is modelled as operating in recirculation rather than injection mode), followed by a gradual drop in suppression pool level after the containment rupture disk opens and the drywell spray was assumed to stop. The lower drywell pool masses predicted by both codes are also somewhat similar, although MELCOR predicts a constant cavity pool mass after an initial transient while MAAP calculates a similar initial value after passive flooder opening but followed by a gradual decrease in lower drywell pool mass.

The lower drywell and wetwell atmosphere and pool temperatures are presented in Figure 5.5.3. These results are quite similar to those calculated for the LCHP-PF-P-M and LCHP-FS-R-N sequence results given in Figures 5.3.16 and 5.4.3. As soon as the vessel fails and core debris is ejected into the cavity, the lower drywell atmosphere temperature spikes rapidly and reaches the 533K (500°F) setpoint for passive flooder actuation. The hot debris in the cavity in the MELCOR calculation keeps the lower drywell pool temperature 25-75K hotter than the suppression pool temperature before rupture disk actuation at about 23hr, during the spray recirculation; after the rupture disk opens and the spray stops, the lower drywell and suppression pool temperatures become almost the same. The wetwell atmosphere is ~20K hotter than the suppression pool during the first portion of the transient, but the wetwell atmosphere temperature

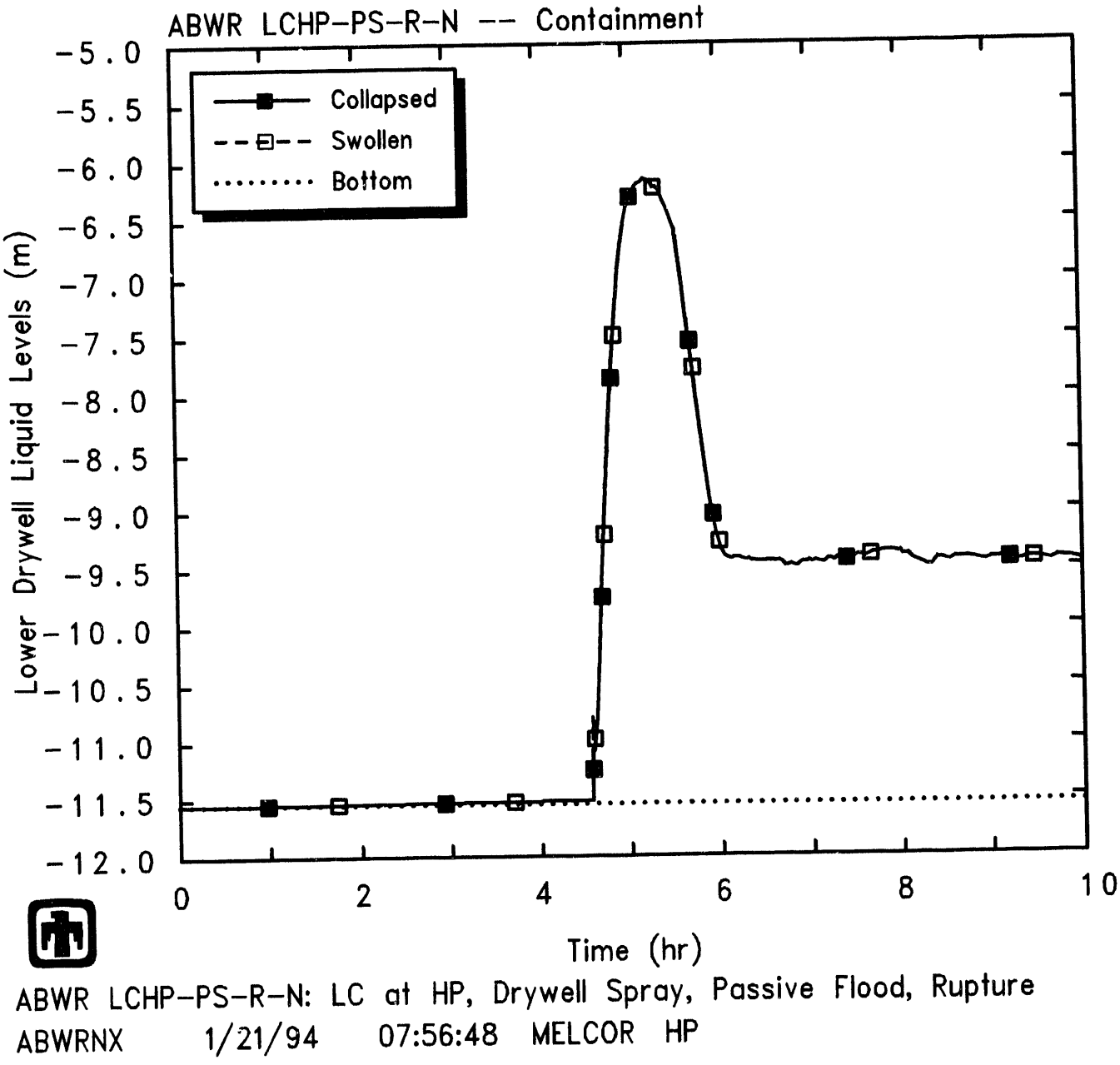

Figure 5.5.1. Lower Drywell Liquid Level Predicted by MELCOR for LCHP-PS-R-N Sequence

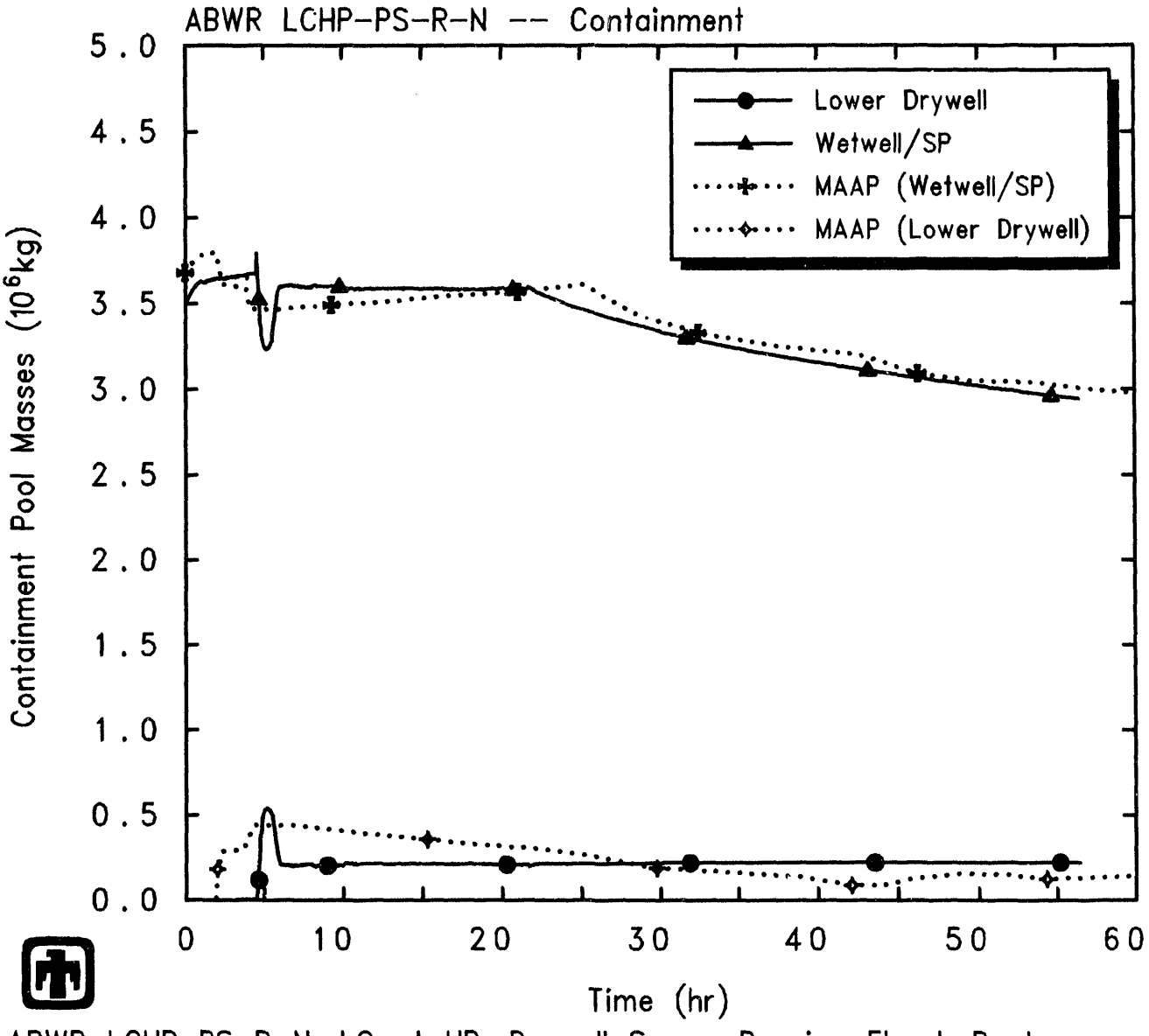

Figure 5.5.2. Lower Drywell and Suppression Pool Masses Predicted by MELCOR for LCHP-PS-R-N Sequence, Compared to MAAP

remains more nearly constant while the suppression pool continually heats up. The cavity atmosphere remains 25-75K hotter than the cavity pool throughout the transient, with the differential increasing with time until rupture disk opening then remaining about constant.

The pressures calculated by MELCOR in the various containment control volumes are depicted in Figure 5.5.4, together with the containment pressure from the MAAP analysis (taken from Figure 19E.2-4B in [1]). The results from the two codes are generally quite similar qualitatively, but with a number of quantitative differences and shifts in timing. Both codes predict a rapid pressure increase in containment immediately after vessel failure, due to steam generation from hot debris and water falling into the cavity from the lower plenum. That initial containment pressurization is greater in the MELCOR analysis than in the MAAP analysis, probably due to direct containment heating associated with high-pressure melt ejection in the MELCOR analysis. The MELCOR HPME/DCH input parameters were selected so as not to open the rupture disk during this pressure spike. The containment pressure then continues to rise as hot core debris continues to boil off the cavity water pool until the containment rupture disk actuation setpoint of 0.72MPa (90psig) is reached, at about 21-22hr in the MELCOR calculation and about 25hr in the MAAP calculation, after which the containment depressurizes. MELCOR calculates a faster containment pressurization between about 5hr and 20hr both because it begins from a higher containment pressure after vessel failure than MAAP (due to the direct containment heating associated with high-pressure melt ejection in MELCOR) and because the unquenched core debris in the cavity in MELCOR boils off the lower drywell water pool more rapidly than the quenched core debris in the cavity in MAAP.

Figure 5.5.5 gives the upper and lower drywell temperatures calculated by MELCOR, compared to corresponding MAAP results. (The MAAP curves included in this plot were taken from Figure 19E.2-4D in [1].) Large temperature spikes are predicted at vessel failure by both codes, at 2hr by MAAP and at about 4.5hr by MELCOR. The spike in the lower drywell temperature at vessel failure triggers the passive flooder to open; the upper drywell temperature in the MELCOR calculation almost reached the penetration seal degradation temperature of 533K (500°F), but the HPME/DCH input parameters were selected so as not to degrade the penetrations during this temperature spike in the two high-pressure sequences with sprays, to prevent containment leakage rather than rupture disk opening (to match the MAAP scenario). The upper drywell slowly heats up even during the drywell spray injection, since that spray is being recirculated from a slowly heating suppression pool. MELCOR predicts significantly higher lower drywell temperatures than in the upper drywell prior to containment depressurization, while the MAAP results shows the two regions at nearly equal temperature. This may again be due to the unquenched core debris in the cavity in MELCOR *vs* the quenched core debris in the cavity in MAAP. After the rupture disk opens and spray injection is stopped, the upper drywell temperature increases substantially in both the MAAP and MELCOR analyses.

Figures 5.5.6 and 5.5.7 show the total and partial pressures, and the mole fractions, respectively, in the atmospheres of the four control volumes representing containment

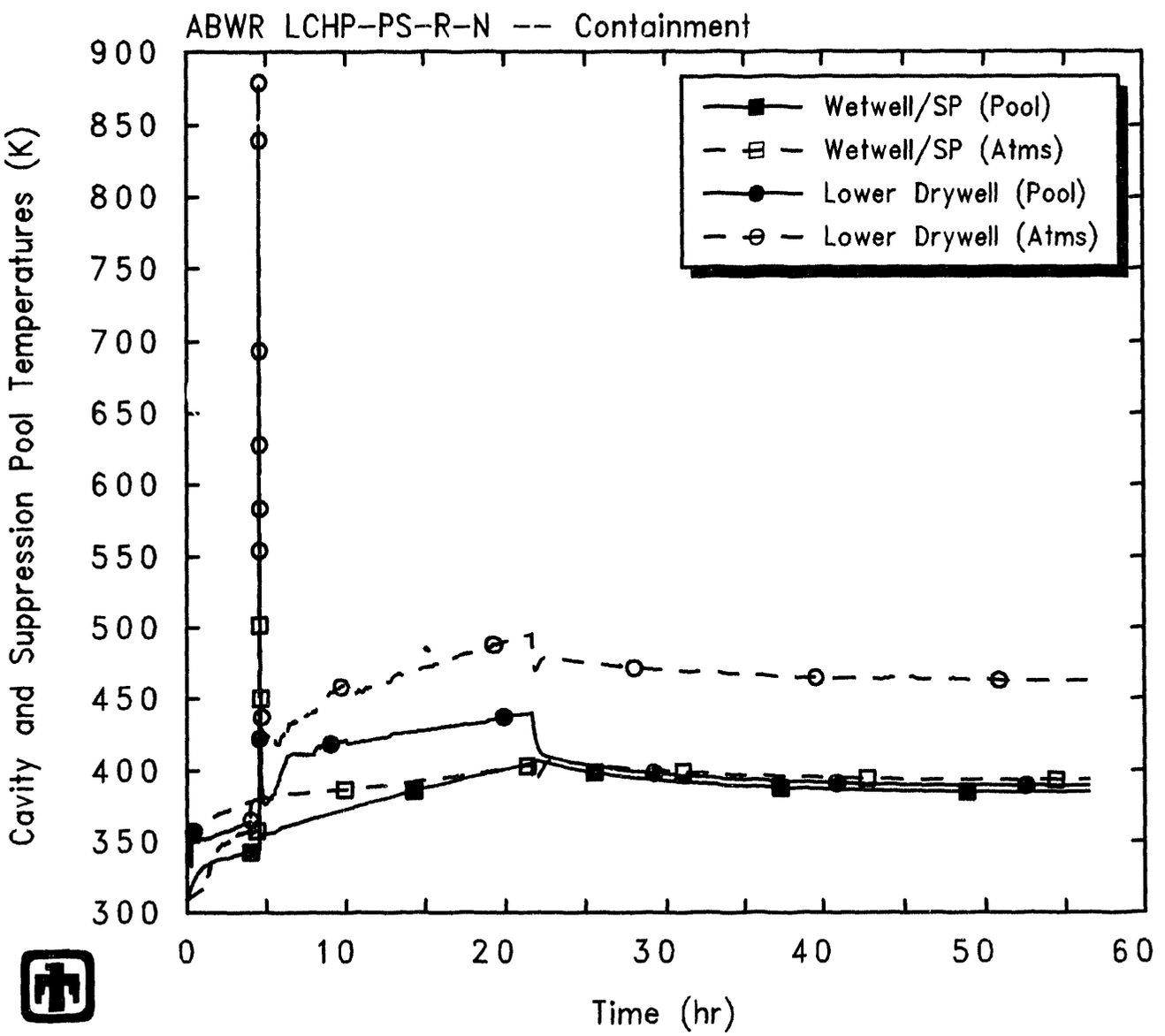

Figure 5.5.3. Lower Drywell and Suppression Pool Temperatures Predicted by MELCOR for LCHP-PS-R-N Sequence

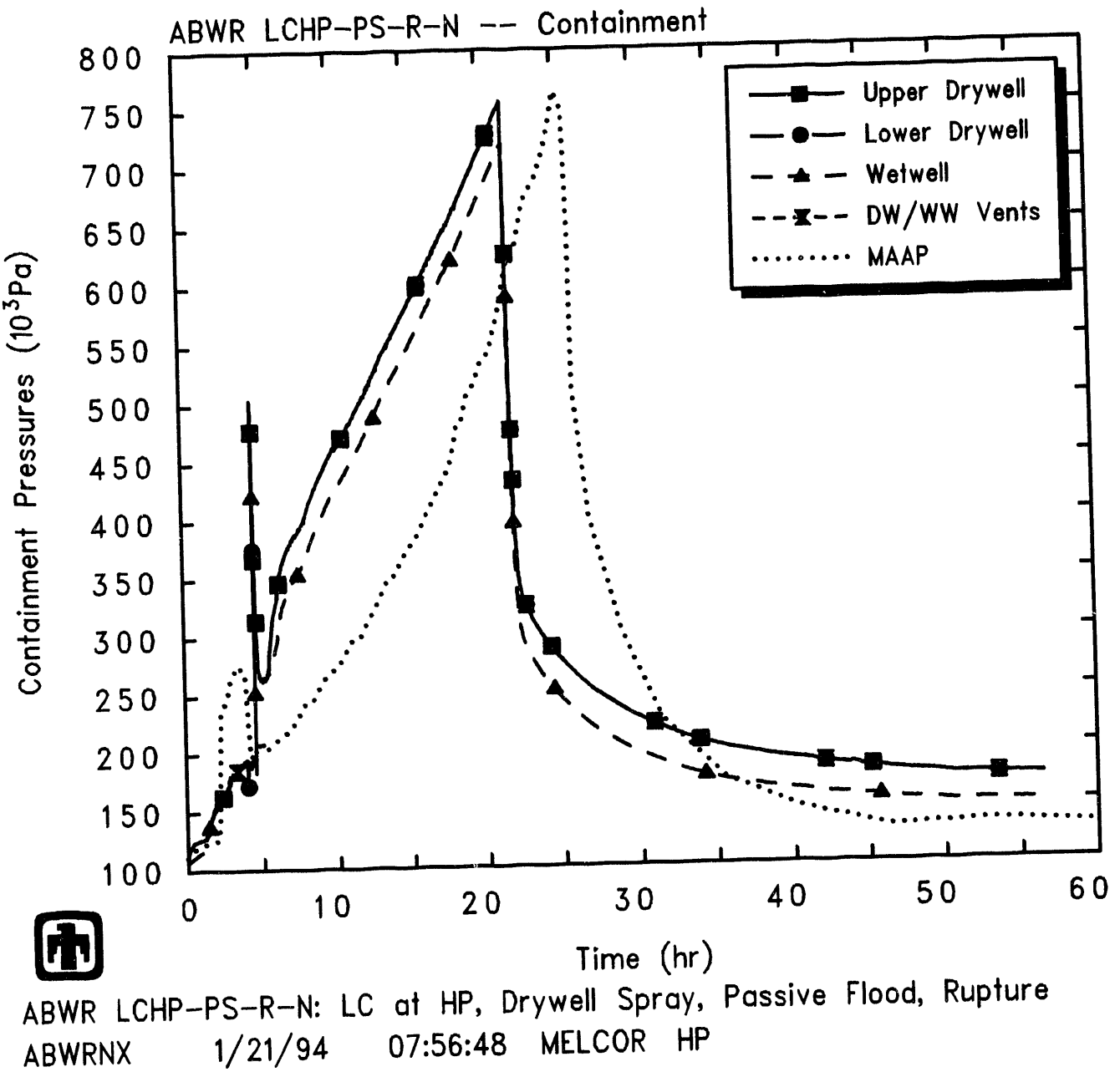

Figure 5.5.4. Containment Pressures Predicted by MELCOR for LCHP-PS-R-N Sequence, Compared to MAAP

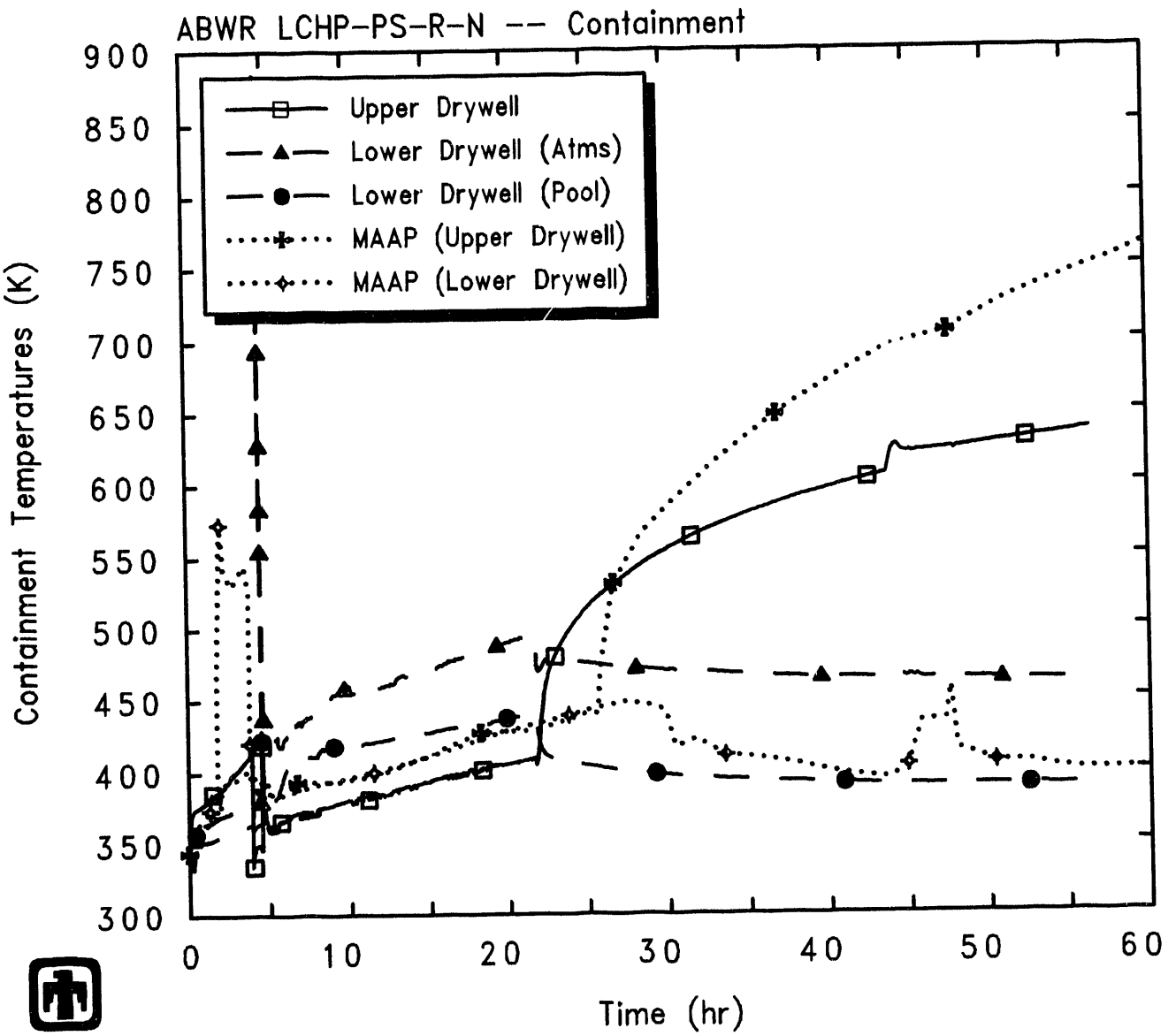

Figure 5.5.5. Containment Temperatures Predicted by MELCOR for LCHP-PS-R-N Sequence, Compared to MAAP

(*i.e.*, upper and lower drywell, wetwell and drywell/wetwell vents). The predicted conditions are generally quite similar to those calculated for the LCHP-FS-R-N sequence (Figures 5.4.6 and 5.4.7). As in the LCHP-FS-R-N sequence results, the lower drywell and DW/WW vent atmospheres consist of almost all (>90%) steam after vessel failure and spray initiation at 4-4.5hr. In the upper drywell, steam begins accumulating after vessel failure after 4.5hr but much of that steam is condensed and removed by the drywell spray from spray initiation until after spray injection was calculated to stop at 21.6hr when the rupture disk opens. Even during spray injection, the steam concentration builds up again quite slowly. The response of the wetwell vapor space is similar to that predicted for the LCHP-FS-R-N sequence: steam does not predominate until after containment rupture disk actuation at 22hr, while most (about 50%) of the wetwell atmosphere between vessel failure and containment depressurization is hydrogen.

The containment continues to pressurize until the wetwell pressure reaches 0.72MPa (90psig) at 25hr in the MAAP analysis and at 21.67hr in the MELCOR calculation, when the rupture disk opens as shown in Figures 5.3.18. The flow out the COPS rupture disk in the MELCOR calculation is presented in Figure 5.5.8. No penetration leakage is predicted by either MAAP or MELCOR, since the temperature in the upper drywell remains below 533K (500°F) until well after the rupture disk opens (as illustrated in Figure 5.5.5). The upper drywell temperature in the MELCOR calculation almost reached the penetration seal degradation temperature of 533K (500°F) due to heat transfer from high-pressure debris ejection at vessel failure, but the HPME/DCH input parameters were selected so as not to degrade the penetrations during this temperature spike in the two high-pressure sequences with sprays, to prevent containment leakage rather than rupture disk opening (to match the MAAP scenario).

The total mass of debris in the cavity, the mass of ejected core debris, the mass of ablated concrete and the mass of gases generated in the cavity calculated by MELCOR are illustrated in Figure 5.5.9. The mass of core debris in the cavity for this sequence is very similar to the results for the LCHP-PF-P-M and LCHP-FS-R-N sequences given in Figures 5.3.23 and 5.4.9; both are basically an inversion of the masses retained in-vessel, presented in Figure 5.3.12. The debris ejection from the vessel can be seen to occur in discrete steps or stages and ends within a few hours after vessel failure, while the concrete mass ablated increases continuously with time until "cavity rupture" (*i.e.*, ablation of the specified initial cavity depth of 2m at some point).

As seen by the ablated concrete mass given in Figure 5.5.9, as soon as the core debris was predicted to enter the cavity, core-concrete interaction began, resulting in the production of carbon dioxide and hydrogen; reduction of these gases by the molten metal also gave rise to carbon monoxide and hydrogen. Figure 5.5.10 presents the production of various noncondensable gases in the cavity due to core-concrete interaction, calculated by MELCOR. Throughout most of the transient period calculated, almost all of the cavity gas production is in the form of hydrogen; however, there is a rapid increase in CO production after 30hr. This is very similar to the MELCOR results for the LCHP-PF-P-M and LCHP-FS-R-N scenarios, given in Figures 5.5.10 and 5.4.10. MELCOR shows more CO produced for all the high-pressure sequences analyzed than for the two

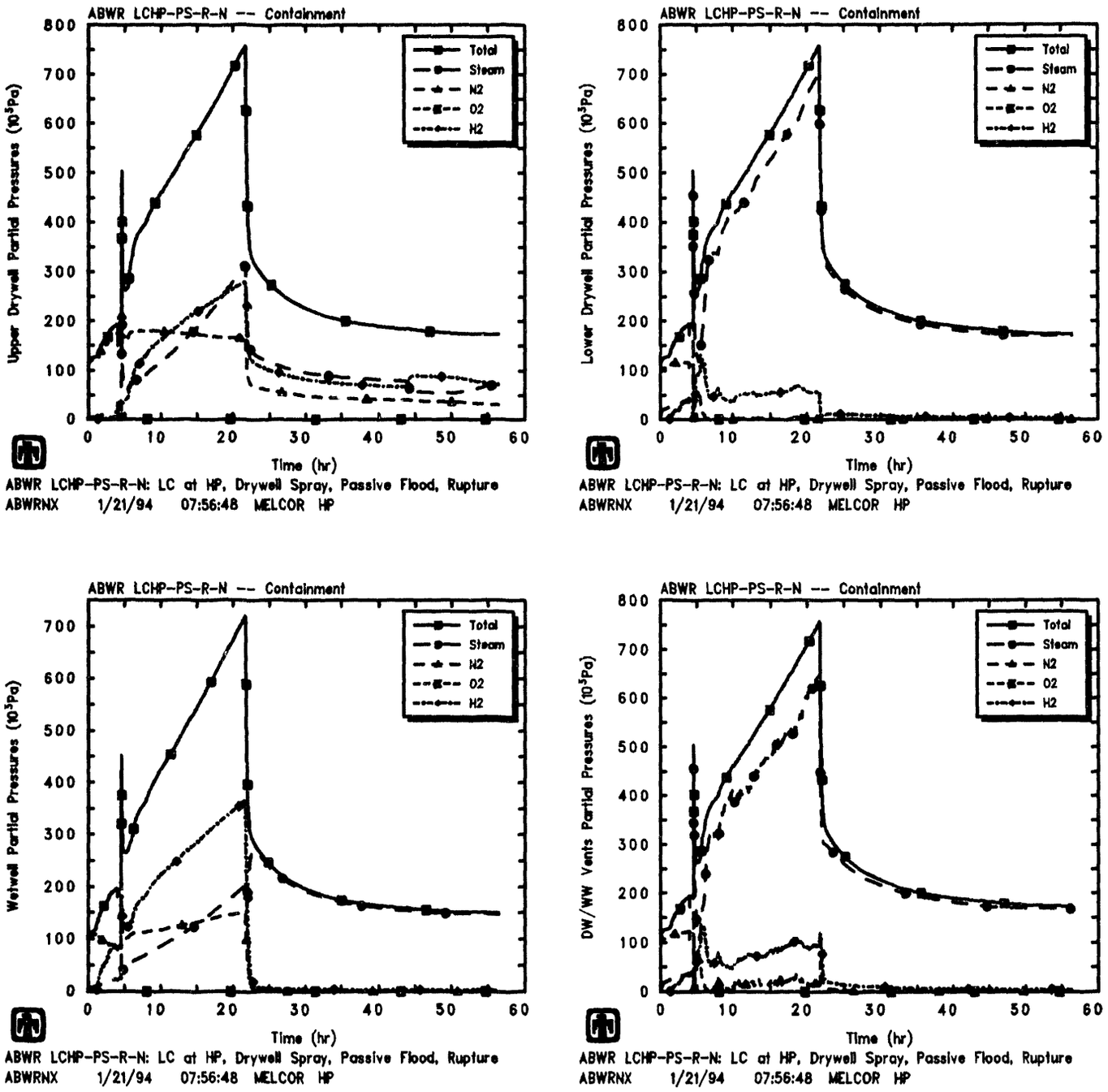

Figure 5.5.6. Containment Upper Drywell (upper left), Lower Drywell (upper right), Wetwell (lower left) and DW/WW Vent (lower right) Partial Pressures Predicted by MELCOR for LCHP-PS-R-N Sequence

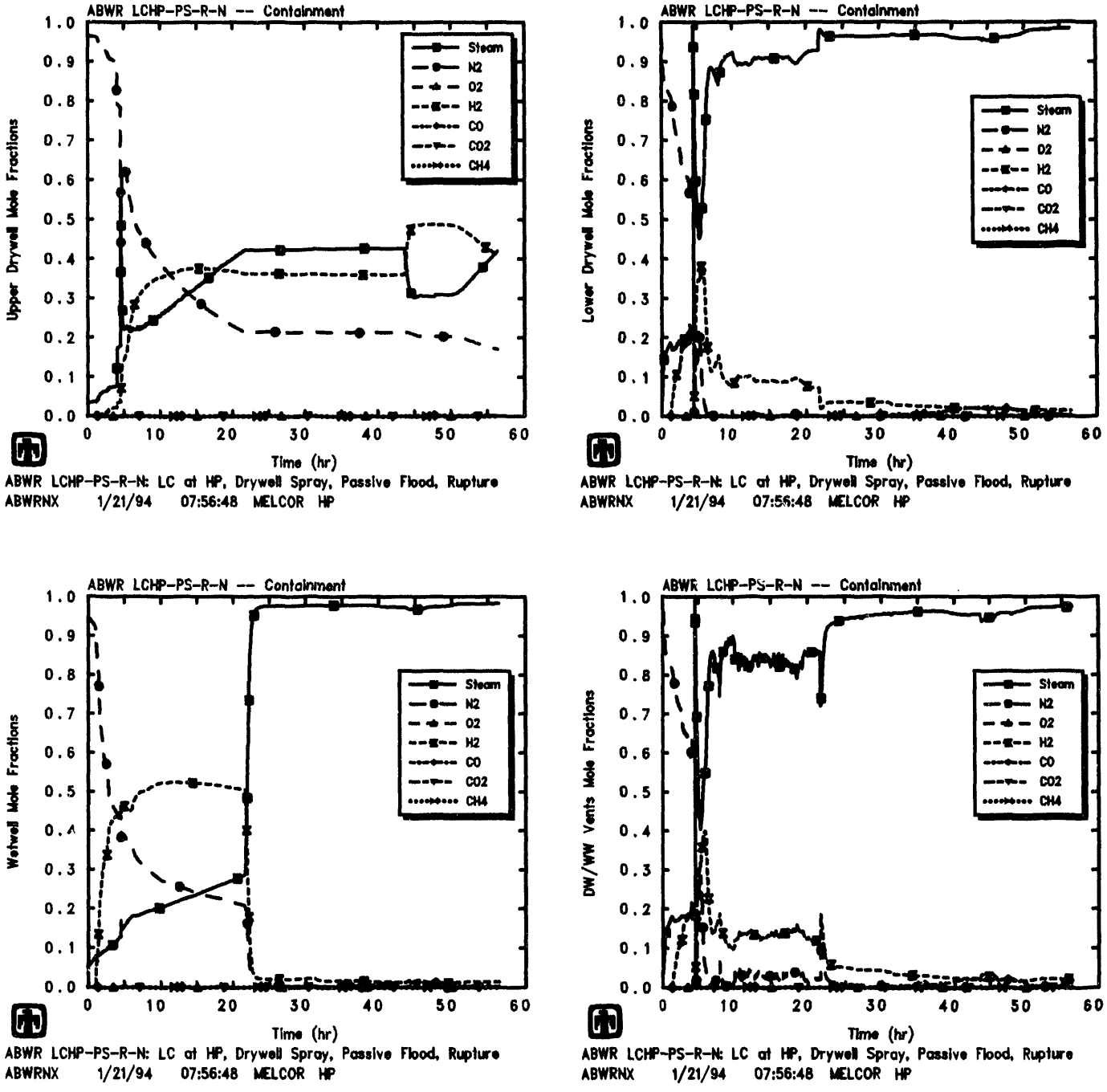

Figure 5.5.7. Containment Upper Drywell (upper left), Lower Drywell (upper right), Wetwell (lower left) and DW/WW Vent (lower right) Mole Fractions Predicted by MELCOR for LCHP-PS-R-N Sequence

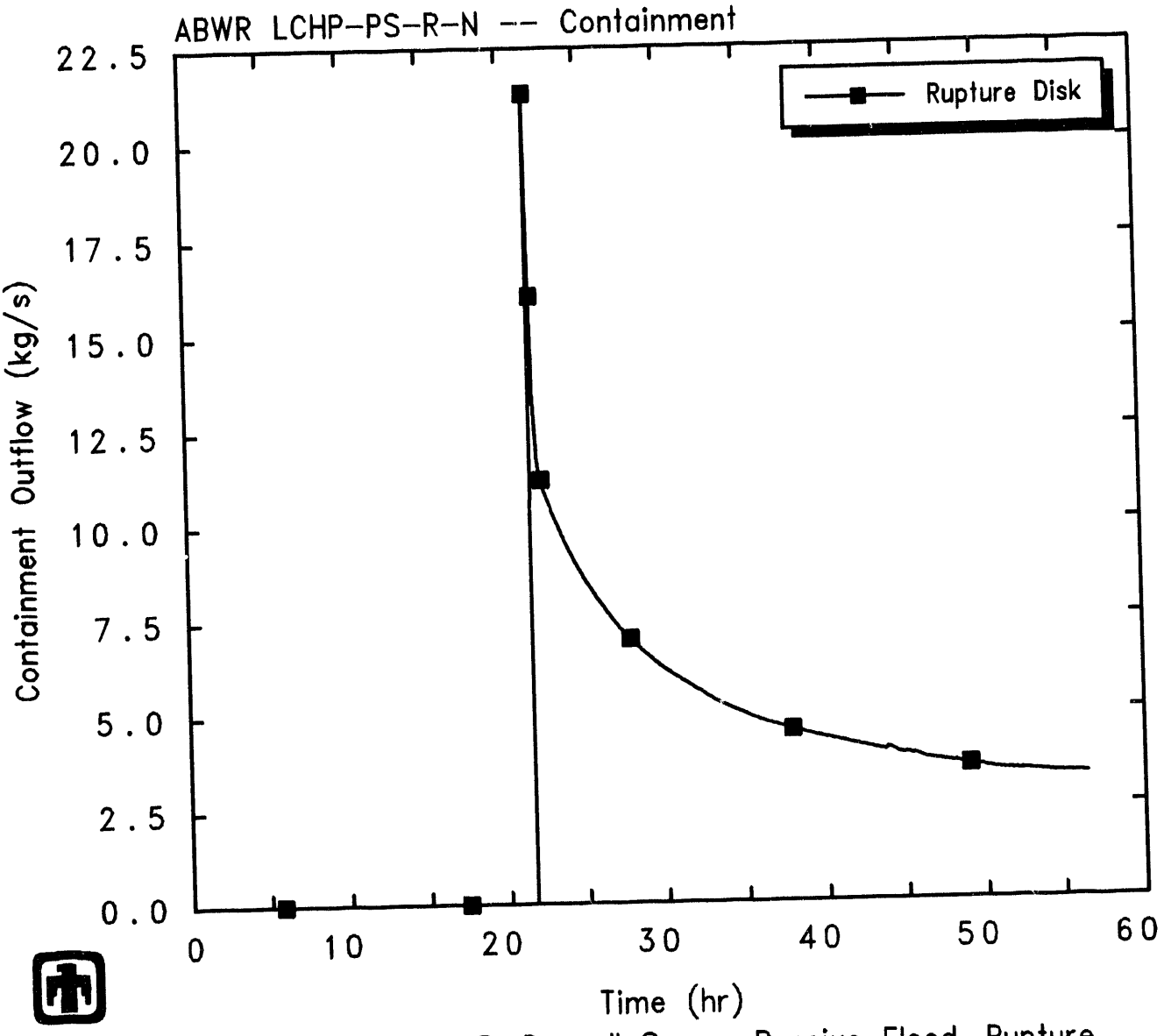

Figure 5.5.8. COPS Rupture Disk Mass Flow Predicted by MELCOR for LCHP-PS-R-N Sequence

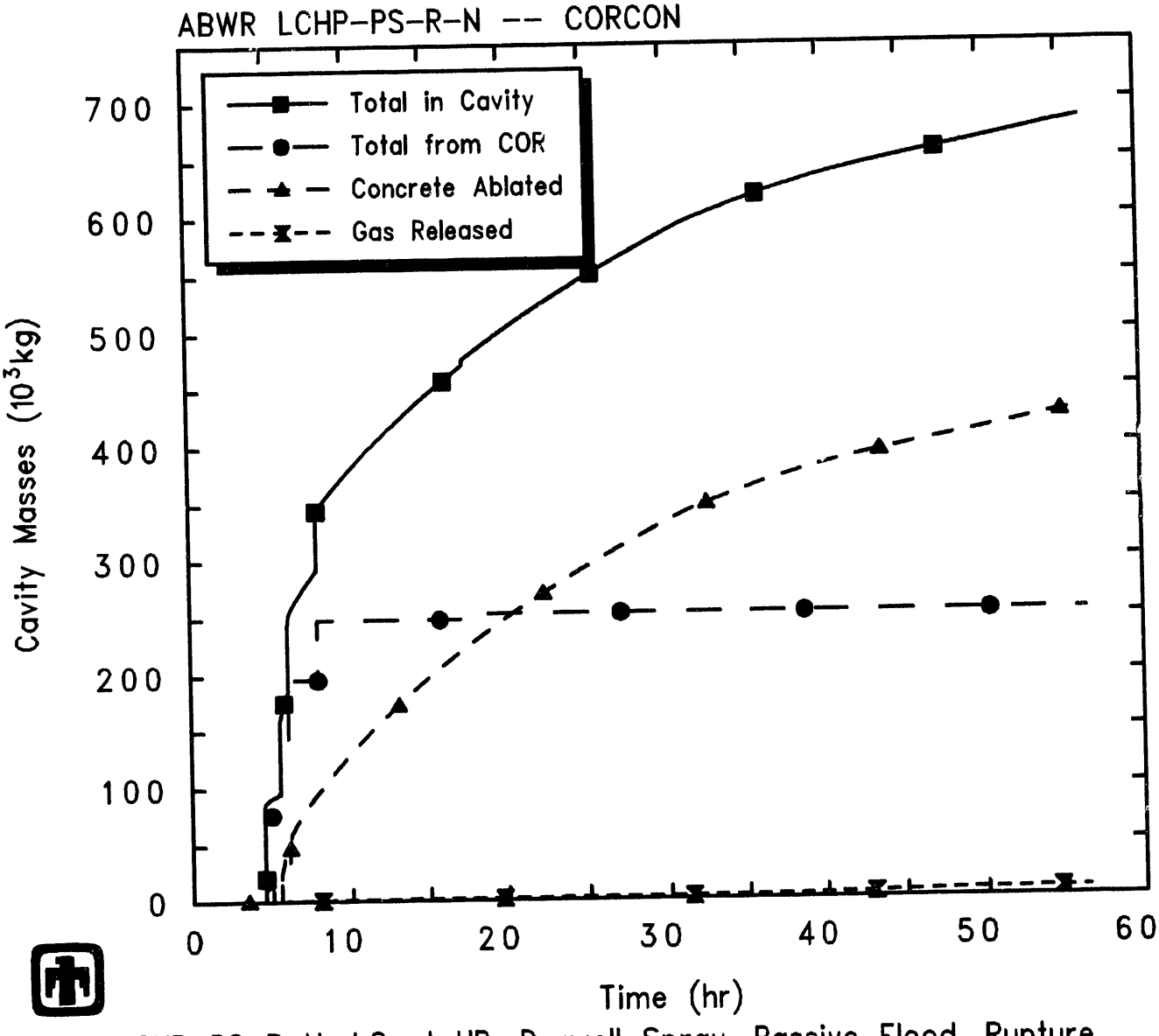

Figure 5.5.9. Cavity Material Masses Predicted by MELCOR for LCHP-PS-R-N Sequence

low-pressure sequences simulated. In all cases, CO is produced only after all the zironium in the cavity is oxidized to ZrO_2, because before that time Zr is assumed to reduce any CO_2 generated to pure carbon ("coking").

Figure 5.5.11 gives the calculated maximum cavity depth and radius. (Note that these represent maximum, not average, ablation distances.) Immediately after core debris is first ejected from the vessel to the cavity upon vessel breach in the MELCOR analysis, there is a brief period of rapid radial ablation, which stops after about 3cm of concrete loss. The bulk of the concrete ablation calculated is axially downward, with the MELCOR calculation stopping at around 56hr due to "cavity rupture", when the axial ablation equals and tries to exceed the specified available concrete thickness of 2m.

Figure 5.5.12 shows the predicted masses, thicknesses, temperatures and densities of the light oxide, metallic and heavy oxide debris layers in the cavity. A heavy oxide layer is present for only a brief time after vessel failure at 4.5hr; throughout most of the transient MELCOR calculates a stable configuration of a light oxide layer above a metallic debris layer. The metallic layer remains nearly constant in mass and thickness, with a gradually increasing density; the light oxide layer mass and thickness increase continuously (and the density decreases) as ablating concrete (with its resultant low-density silicate oxides) continues to dilute the high-density zirc oxide and steel oxide debris to an average density value less than the metallic debris density. After a few initial oscillations, the temperatures of both layers remain nearly equal, at $\simeq$1500K, throughout the transient period calculated.

The heat transfer from the cavity debris pool in the MELCOR analysis, both downward and outward to the concrete surface and upward to the cavity volume atmosphere, is shcwn in Figure 5.5.13. The energy transfer from the debris in the cavity upward through the debris bed surface to the lower drywell atmosphere and/or overlying water pool is 2-4 times greater than the energy transferred downward (and sideways) to the concrete. In general, that upper surface of the debris bed is covered with a water pool, not exposed to atmosphere.

Tables 5.5.2 and 5.5.3 give the distribution of the released radionuclides at the end of the calculation (*i.e.*, at 56hr). Table 5.5.2 provides an overview of how much of the radionuclides remain bound up in fuel in either the core or the cavity, and of how much of the released radionuclides are retained in the primary system *vs* how much of the released radionuclides are released to, or released in, either the drywell or the wetwell in containment and the environment, all normalized to the initial inventories of each class. Table 5.5.3 gives a slightly different breakdown of the released radionuclide final distribution – the fractions of initial inventory released for each class from fuel in-vessel in the core, ex-vessel in the cavity and overall total are given, together with the distribution of the released radionuclides in the primary system, drywell, wetwell and environment normalized by the mass of each class released. (Note that these amounts generally consider only the release of radioactive forms of these classes, and not additional releases of nonradioactive aerosols from structural materials.)

The release behavior predicted by MELCOR again falls into the same several subdivisions as found for all the other sequences analyzed. Almost all ($\simeq$100%) of the volatile

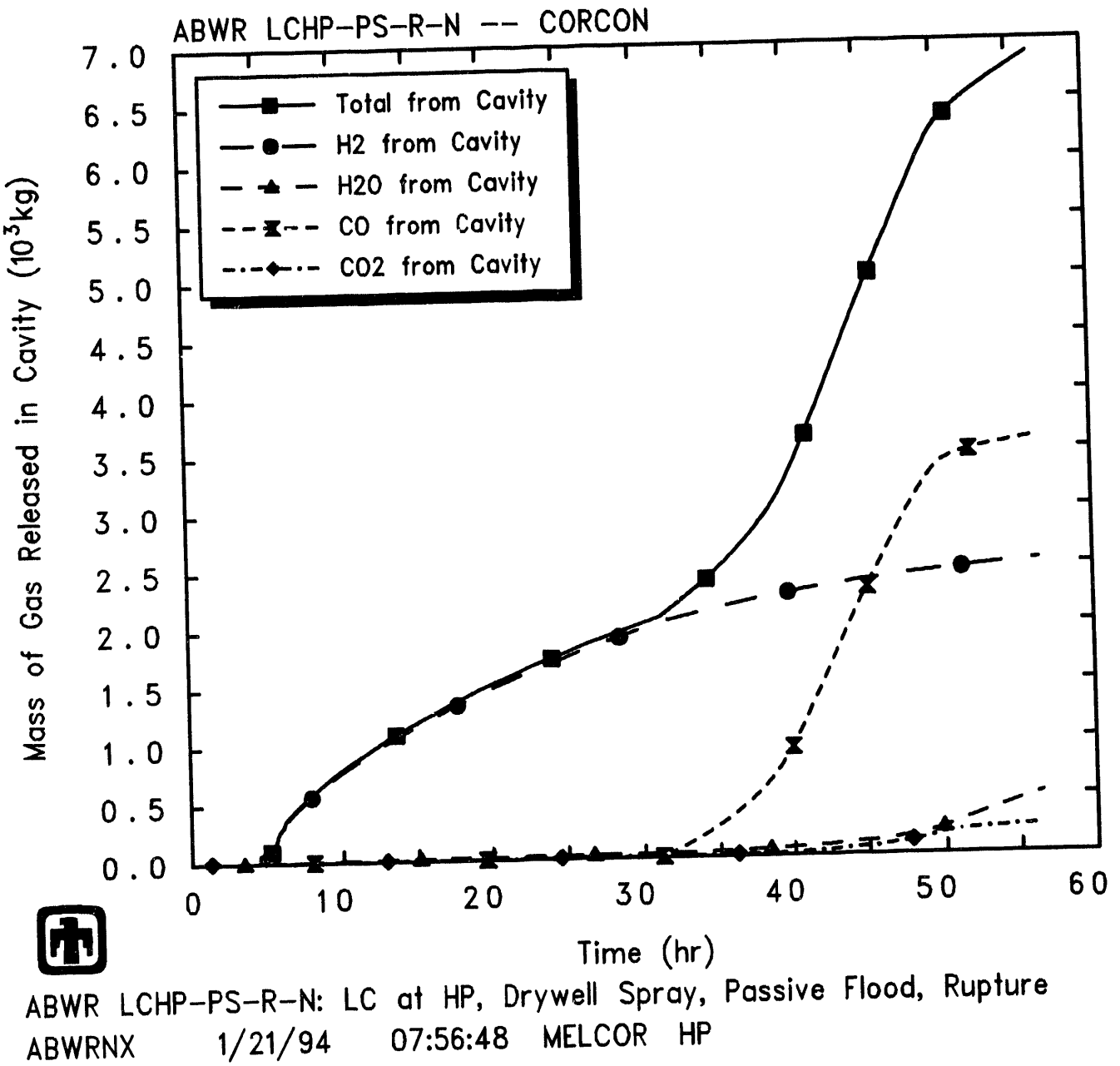

Figure 5.5.10. Cavity Gas Production Predicted by MELCOR for LCHP-PS-R-N Sequence

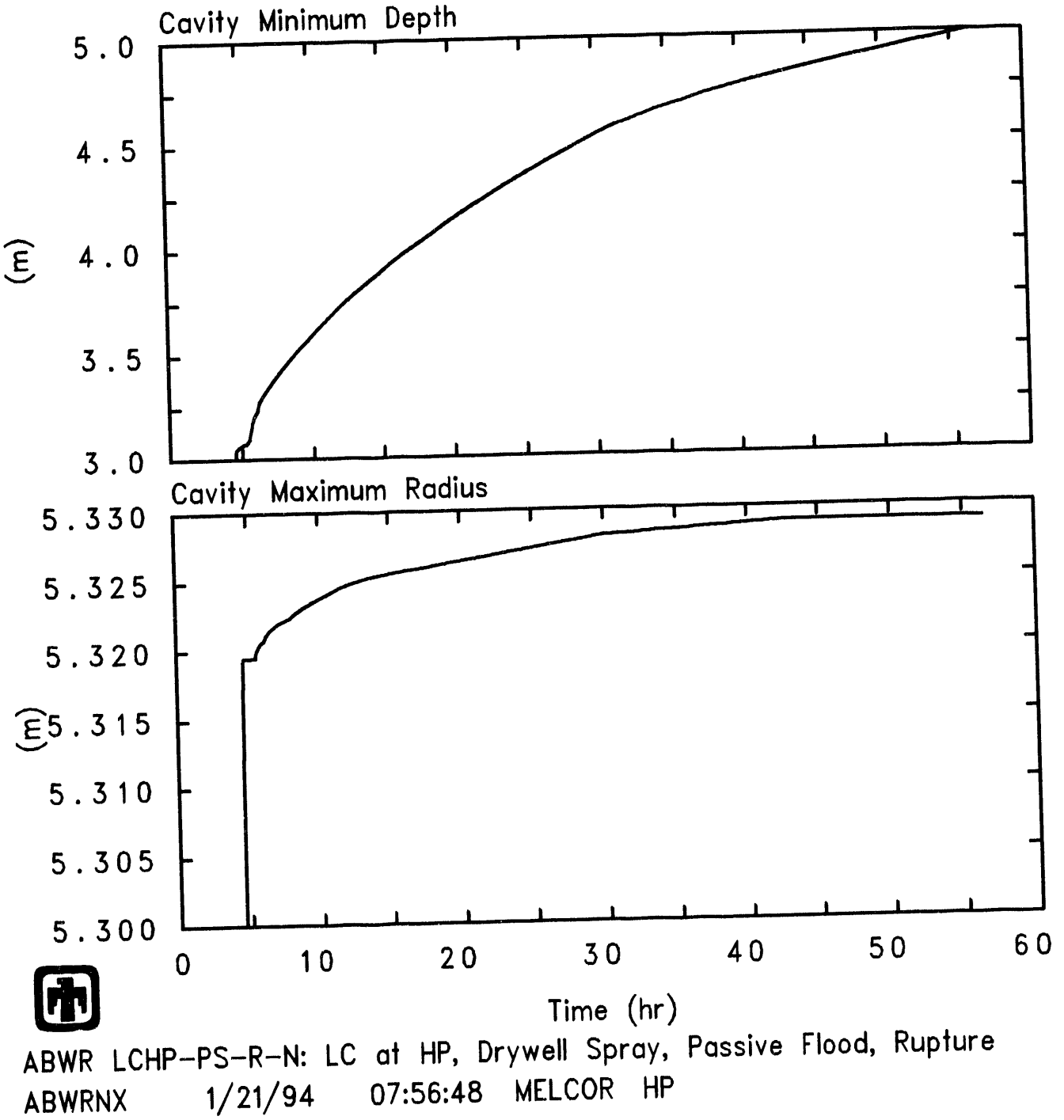

Figure 5.5.11. Cavity Maximum Radius and Depth Predicted by MELCOR for LCHP-PS-R-N Sequence

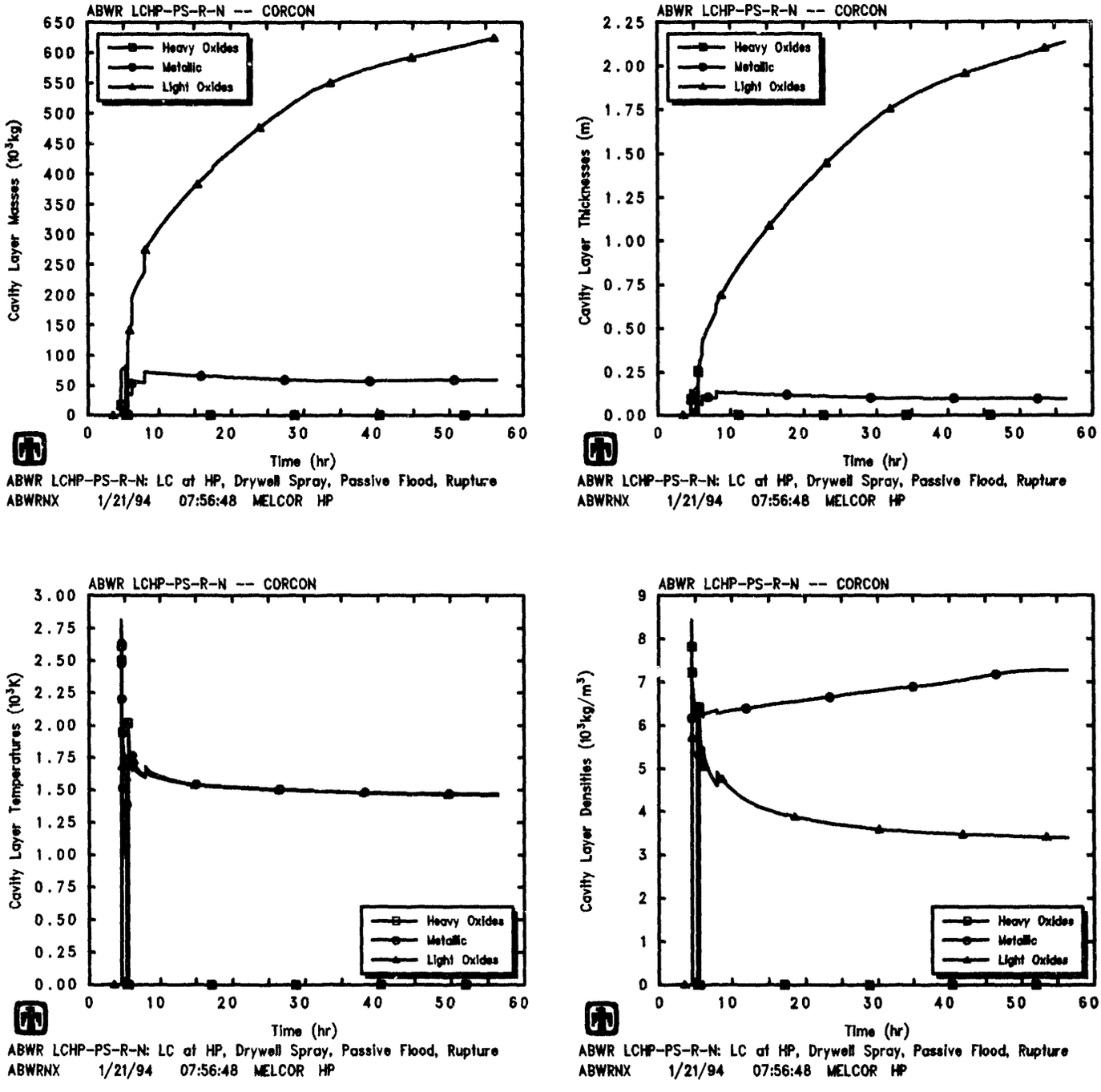

Figure 5.5.12. Cavity Layer Masses (upper left), Thicknesses (upper right), Temperatures (lower left) and Densities (lower right) Predicted by MELCOR for LCHP-PS-R-N Sequence

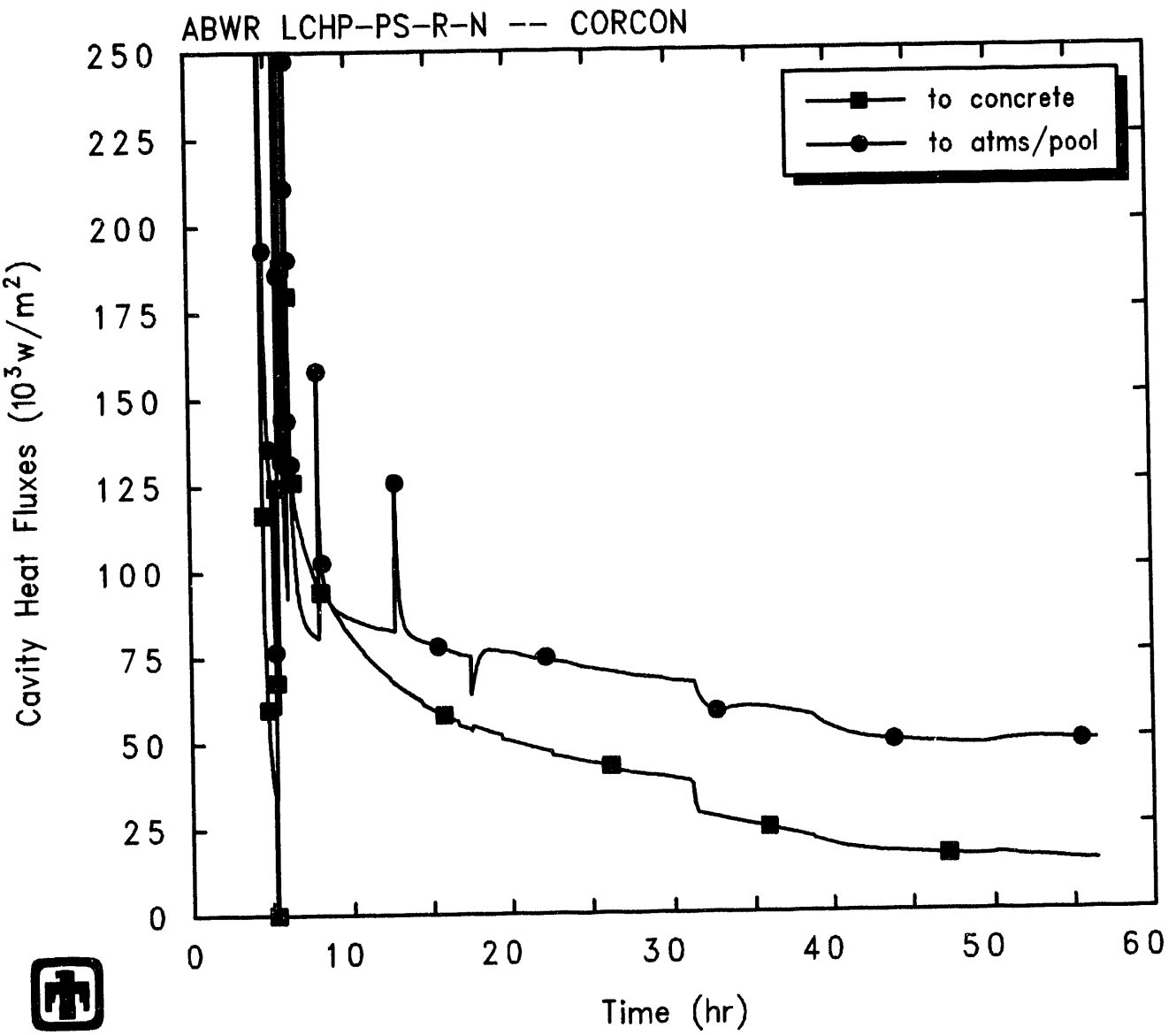

Figure 5.5.13. Cavity Heat Flows Predicted by MELCOR for LCHP-PS-R-N Sequence

Table 5.5.2. Radionuclide Distribution Predicted at 56hr for LCHP-PS-R-N Sequence

Class	Fission Product Distribution (% Initial Inventory)					
	Remaining in Fuel		Released from Fuel			
	Core	Cavity	Primary System	Drywell	Wetwell	Environment
Noble Gases (Xe)	1.18×10^{-8}	0	0.0284	2.36	0.0437	97.6
Alkali Metals (CsOH)	1.26×10^{-8}	$\simeq0$	20.3	14.6	63.8	1.31
Alkaline Earths (Ba)	1.29	10.9	54.6	4.99	29.6	5.23×10^{-4}
Halogens (I)	$\simeq0$	$\simeq0$	$\simeq0$	$\simeq0$	$\simeq0$	$\simeq0$
Chalcogens (Te)	8.34×10^{-9}	0.0206	48.7	8.08	42.9	0.292
Platinoids (Ru)	0.0463	98.5	0.956	0.0777	0.458	5.58×10^{-6}
Transition Metals (Mo)	0.0466	97.1	0.0128	0.655	2.12	0.0274
Tetravalents (Ce)	0.0464	98.7	0.819	0.0678	0.400	1.57×10^{-5}
Trivalents (La)	0.0466	96.2	8.74×10^{-4}	0.543	3.23	4.78×10^{-4}
Uranium (U)	0.0834	99.9	0.0211	2.98×10^{-3}	0.0174	1.19×10^{-5}
More Volatile Main Group Elements (Cd)	0.0466	99.8	5.91×10^{-5}	0.0182	0.109	4.84×10^{-5}
Less Volatile Main Group Elements (Sn)	4.20×10^{-3}	6.89	56.4	5.30	31.4	1.55×10^{-4}
CsI	$\simeq0$	2.61×10^{-4}	12.4	15.9	70.0	1.59

Table 5.5.3. Radionuclide Release and Released Distribution Predicted at 56hr for LCHP-PS-R-N Sequence

Class	Released from Fuel (% Initial Inventory)			Distribution (% Released Mass)			
	Core	Cavity	Total	Primary System	Drywell	Wetwell	Environment
Noble Gases (Xe)	99.97	0.02	99.99	0.0284	2.36	0.0437	97.57
Alkali Metals (CsOH)	99.95	0.02	99.97	20.33	14.55	63.80	1.31
Alkaline Earths (Ba)	81.42	0.32	81.74	60.80	5.60	33.16	5.87×10^{-4}
Halogens (I)	$\simeq$0	$\simeq$0	$\simeq$0	0.012	1.85	0.034	98.10
Chalcogens (Te)	99.95	1.17×10^{-3}	99.95	48.59	8.08	42.86	0.0292
Platinoids (Ru)	0.87	4.08×10^{-4}	0.87	64.08	5.21	30.71	3.74×10^{-4}
Transition Metals (Mo)	0	1.63	1.63	0.455	23.29	75.28	0.975
Tetravalents (Ce)	0.72	8.67×10^{-4}	0.72	63.66	5.27	31.07	1.22×10^{-3}
Trivalents (La)	0	2.19	2.19	0.0232	14.39	85.58	0.0127
Uranium (U)	0.018	0.005	0.024	50.88	6.96	41.89	0.0288
More Volatile Main Group Elements (Cd)	0	0.074	0.074	0.0466	14.37	85.54	0.038
Less Volatile Main Group Elements (Sn)	89.00	0.006	89.02	60.57	5.69	33.74	1.66×10^{-4}
CsI	99.95	0.021	99.98	12.42	15.95	70.04	1.59

Class 1 (noble gases), Class 2 (CsOH), Class 5 (Te) and Class 16 (CsI) radionuclide species are released, primarily in-vessel, as are most (~80-90%) of the Class 3 (Ba) and Class 12 (Sn) inventories. The next major release fractions are of Ru and Mo, Ce and La, all between ~1% and ~2%. Finally, a total $\leq$0.1% of the initial inventory of uranium and Class 11 (Cd) are predicted to be released. (Note that the CORSOR-M fission product release model option used in all these analyses has identically zero release in-vessel of Class 7, Class 9 and Class 11.)

Most of the released radionuclides remain in the primary system and/or the containment; only the noble gases show a significant release to the environment. Of the volatiles, about 1-2% of the CsOH and CsI are released to the environment, together with about 0.3% of the Te. Of the other radionuclides, >0.1% of the initial inventories are released to the environment. Of the species with significant (>80%) release from fuel, the wetwell retains most (60-70%) of the released CsOH and CsI volatiles, the Te is retained about equally in the primary system and in the wetwell, while the Ba and Sn aerosols are held up both in the primary system (60%) and in the wetwell (33%).

The predicted release to the environment of each radionuclide species is much lower for the LCHP-PS-R-N sequence than calculated for the LCHP-PF-P-M sequence (for the same reasons as already discussed in Section 5.4), but slightly higher for the LCHP-PS-R-N scenario than calculated for the LCHP-FS-R-N scenario, possibly reflecting differences in response to a recirculating spray in LCHP-PS-R-N *vs* an injection spray in LCHP-FS-R-N. The spray flow rate used was significantly higher in the LCHP-PS-R-N sequence (228.54l/s) than in the LCHP-FS-R-N sequence (83.33l/s), but had much less condensation potential because it was not subcooled to 305K (as in LCHP-FS-R-N).

Figures 5.5.14 and 5.5.15 give the retention factors for the various radionuclides calculated by MELCOR, for the primary system and for the overall containment, respectively. The retention factors are defined as the fraction of material released in, or transported into, a region which remains in that region. The vessel retention factors fall into the same four sets as found for the LCHP-FS-R-N sequence (in Figure 5.4.14):

- essentially no retention for the noble gases and for the negligible amount of I_2 present,
- a retention of 20-30% for the cesium radionuclide species (*i.e.*, CsOH and CsI),
- a retention of 50% for the other radionuclide species with non-zero vapor pressure (*i.e.*, Te), and
- a $\geq$60% retention of those classes which form aerosols only.

The containment retention factors fall into several distinct categories also, and are very similar to the values for the LCHP-FS-R-N sequence shown in Figure 5.4.15, with less retention of the noble gases:

- <1-2% retention for the noble gases and for I_2 after COPS rupture,

- a retention of about 80% for the cesium radionuclide species (*i.e.*, CsOH and CsI),
- a retention of ~[illegible] for Te, which also has both aerosol and vapor forms, and for uranium, and
- for the other classes which form aerosols only, there is a 30-40% retention for those which had some in-vessel release (Ba, Ru, Ce and Sn) and a ~100% retention of those with only ex-vessel release (Mo, La and Cd).

Figures 5.5.16 and 5.5.17 give the decontamination factors (DFs) for the various radionuclides calculated by MELCOR, for the suppression pool and for the overall containment, respectively. The period of interest in these plots is after ~22hr when the containment is calculated to vent and depressurize through the rupture disk opening. After containment depressurization, the suppression pool and overall containment DFs are simply DF=1.0 for the noble gases and for I_2 (of which there is very little), not shown explicitly in these figures.

The suppression pool DFs after containment depressurization for this LCHP-PS-R-N scenario vary over a much wider range of magnitudes than found in the LCHP-FS-R-N sequence (Figure 5.4.16):

- $DF_{SP} \leq 100$ for the volatile classes (CsOH, Te and CsI) and for Mo,
- $DF_{SP} \sim 1000\text{-}5000$ for La, Cd and for uranium,
- $DF_{SP} \sim 10{,}000\text{-}30{,}000$ for Class 3 (Ba), Class 6 (Ru) and Class 8 (Ce), and
- $DF_{SP} \leq 100{,}000$ for Class 12 (Sn).

The magnitude of the various DFs calculated by MELCOR for the LCHP-PS-R-N sequence are generally higher than those calculated by MELCOR for the LCHP-FS-R-N sequence; the classes predicted to have relatively higher wetwell decontamination factors are also different in the two analyses, reflecting differences in release and distribution.

The overall containment DFs sequence predicted for the LCHP-PS-R-N scenario are somewhat different than those calculated by MELCOR for the LCHP-FS-R-N sequence, presented in Figure 5.4.17:

- $DF_{Cont} < 100$ for the cesium radionuclide classes (CsOH and CsI),
- $DF_{Cont} \sim 100\text{-}200$ for the other volatile class (Te) and for Mo,
- DF_{Cont} between ~1,000 and ~10,000 for several classes (La, U and Cd),
- $DF_{Cont} \leq 100{,}000$ for Class 3 (Ba), Class 6 (Ru) and Class 8 (Ce), and
- $DF_{Cont} \geq 200{,}000$ for Class 12 (Sn).

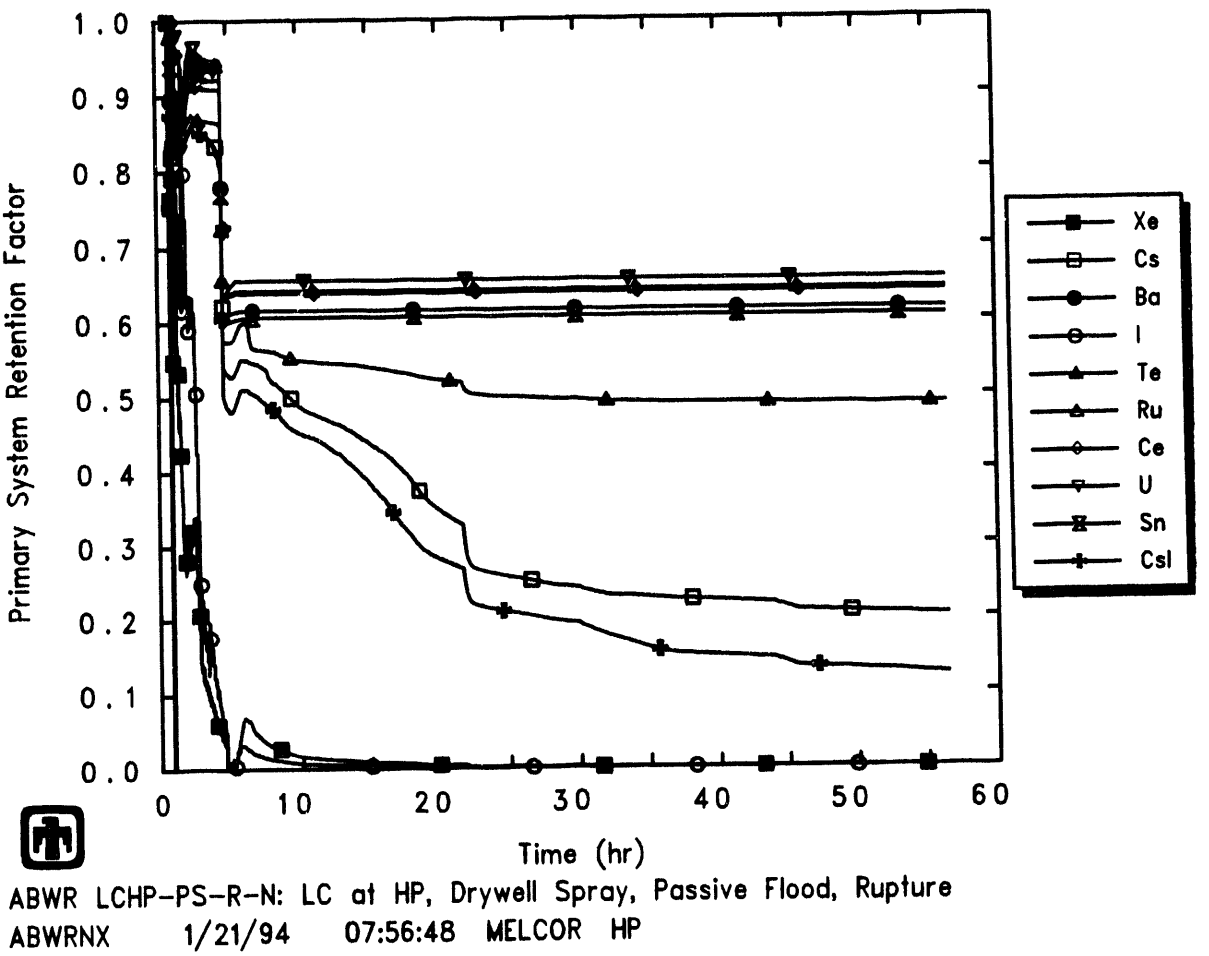

Figure 5.5.14. Primary System Retention Factors Predicted by MELCOR for LCHP-PS-R-N Sequence

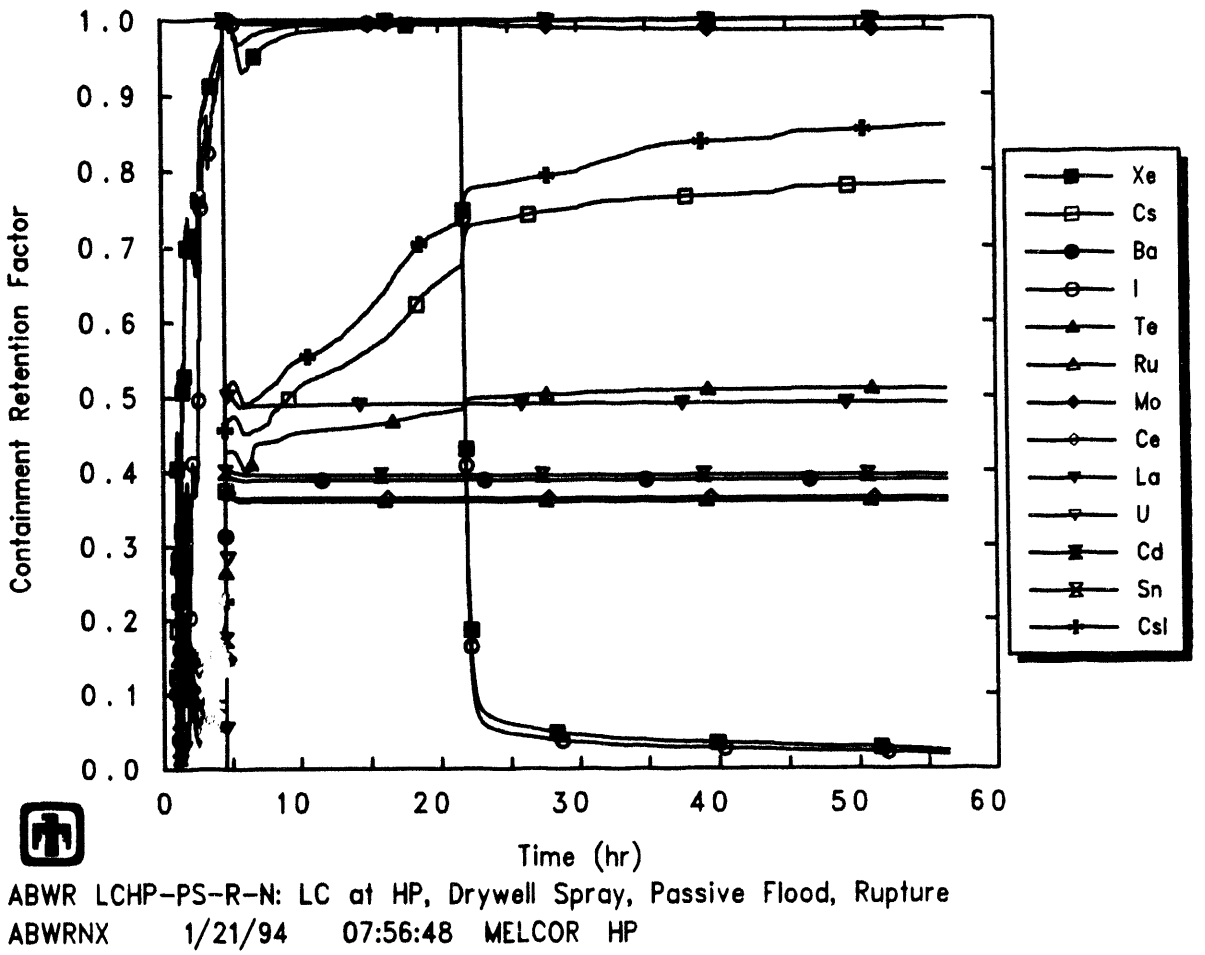

Figure 5.5.15. Containment Retention Factors Predicted by MELCOR for LCHP-PS-R-N Sequence

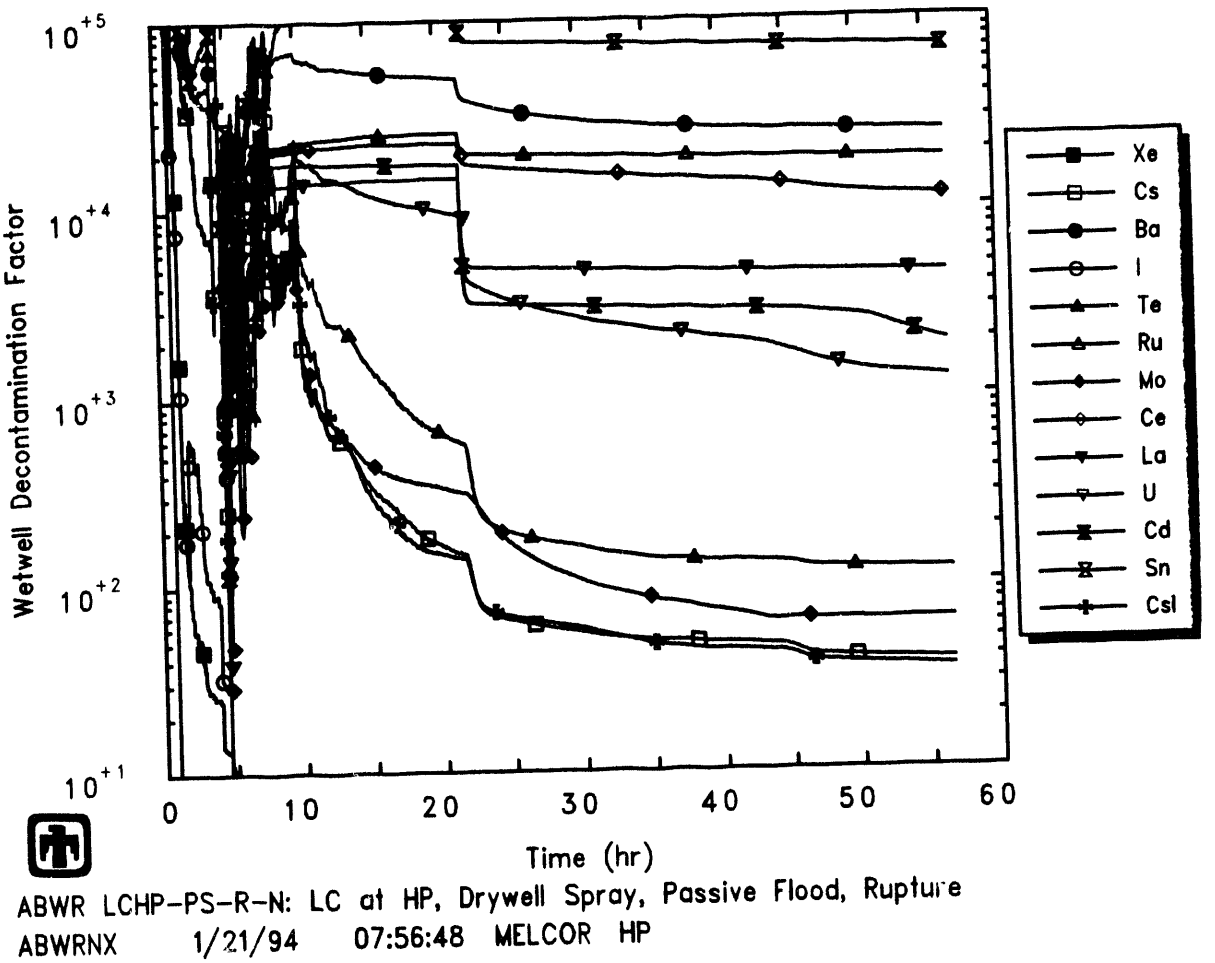

Figure 5.5.16. Suppression Pool Decontamination Factors Predicted by MELCOR for LCHP-PS-R-N Sequence

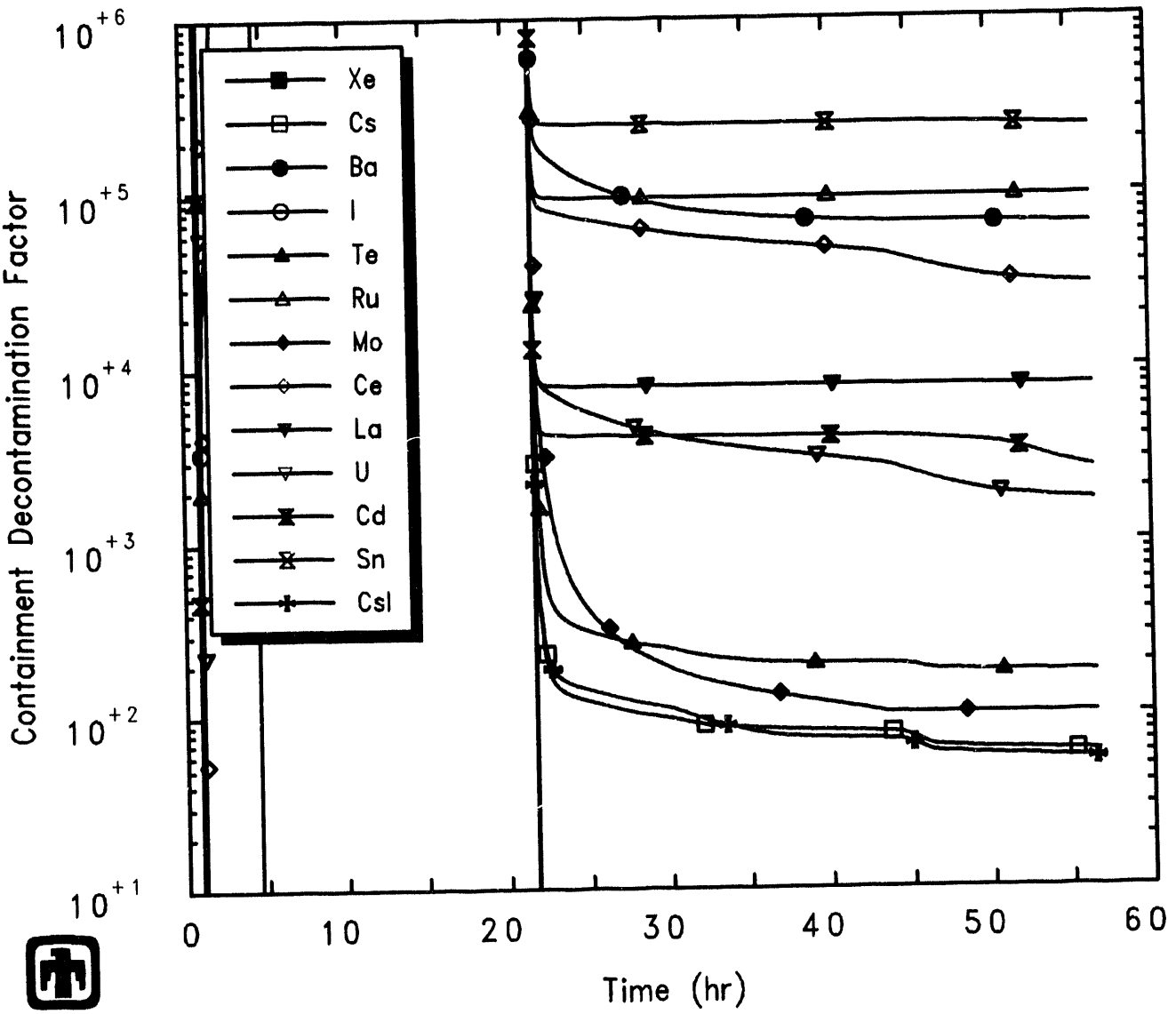

Figure 5.5.17. Overall Containment Decontamination Factors Predicted by MELCOR for LCHP-PS-R-N Sequence

While the overall containment decontamination factors predicted by MELCOR for the LCHP-PS-R-N are slightly lower in magnitude than for the LCHP-FS-R-N sequence, the relative differences between DFs for various radionuclide classes are generally similar in the two calculations.

Note that both the suppression pool and overall containment decontamination factors remain nearly constant or drop very slowly for most classes after containment rupture disk opening, but drop steadily for several radionuclide species (*i.e.*, CsOH, Te, Mo and CsI). These are the classes for which a continuing release to the environment is predicted, while for the other classes there is only a single step-like release at COPS rupture, as illustrated in Figure 5.5.18. That continuing release comes from two different causes. The non-zero vapor pressure of CsOH, Te and CsI causes continuous vaporization from the suppression pool and replenishment of these fission product vapors in the wetwell atmosphere as those fission product vapors in the wetwell atmosphere are lost out the COPS rupture. Class 7 (Mo) has no non-zero vapor pressure and therefore remains an aerosol throughout the problem. However, this class is the only one with substantial and continuing radionuclide release in the cavity, and a small fraction of that continuing release (while mostly remaining in the cavity and/or suppression pools) does survive pool scrubbing and get released to the wetwell atmosphere and then out the COPS rupture disk to the environment.

Figure 5.5.18 does not include the release of the noble gases, to allow expansion of the scale for the environmental release of the other radionuclide classes. In the MAAP analysis, the release of noble gases is nearly complete 8hr after the rupture disk opens; the release of most of the noble gases in the MELCOR calculation also occurs soon after containment rupture disk actuation. The release of the volatile species, CsI and CsOH, continues for about 25hr in the MAAP analysis after the rupture disk opens at about 25hr; the release fraction of CsI at 72hr is less than 10^{-7}. The MELCOR calculation shows environment release fractions by the end of the calculation (56hr) of about 10^{-2} for CsOH and CsI. The release fractions calculated by MELCOR are significantly higher than the values predicted by MAAP. This difference is a result of a number of modelling differences in MELCOR and MAAP, including the continuing steaming of cavity water by non-quenched debris in MELCOR and the lack of a model for hygroscopic effects on aerosol behavior in MELCOR. However, the MELCOR release fractions are still small fractions of the fission product inventories initially present, released but retained within containment even after COPS rupture and containment depressurization.

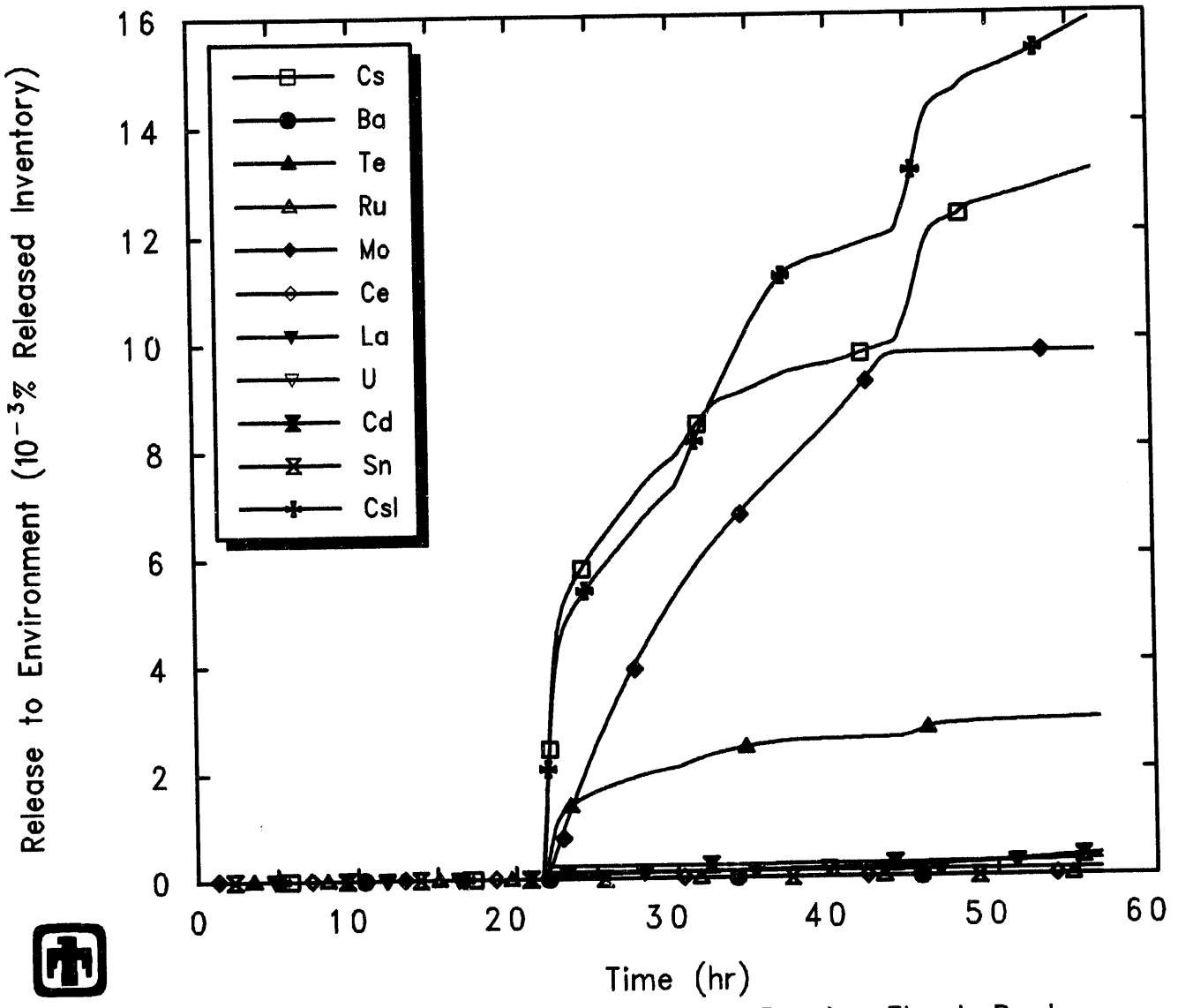

Figure 5.5.18. Radionuclide Environmental Releases Predicted by MELCOR for LCHP-PS-R-N Sequence

6 Sensitivity and Variational Studies

6.1 LCLP-PF-R-N Sequence with Limestone Concrete

This accident scenario is the same as discussed in Section 5.1, but with limestone concrete in the cavity rather than basaltic concrete. The sequence of events predicted by MELCOR for this accident is given in Table 6.1.1, with the timings of the various events as calculated by MELCOR and by MAAP with basaltic concrete included for comparison. The MELCOR calculations with basaltic and with limestone concrete should be the same up to the time of vessel failure and debris ejection into the cavity; the small differences seen in timing between the two MELCOR calculations in Table 6.1.1 are due to using different code versions for these two analyses.

Much of the containment behavior calculated for the LCLP-PF-R-N sequence assuming limestone concrete is very similar to the response predicted in the reference calculation with basaltic concrete for this scenario (described in Section 5.1), albeit shifted somewhat in time due to differences in parameters such as time to rupture disk opening. For example, Figure 6.1.1 give the lower drywell and wetwell pool masses for the MELCOR analyses both with limestone concrete and with basaltic concrete, compared to the pool masses calculated by MAAP for basaltic concrete. In both MELCOR calculations, there appears to be a small difference in the suppression pool initial mass (and/or level) in the two calculations, and MELCOR predicts a bigger short-term drop in suppression pool level and corresponding rise in cavity pool level upon opening the passive flooder. However, the results are generally similar, with an initial rise in suppression pool level (due to condensation of steam from the vessel), a drop and then recovery to a slightly lower level after the passive flooder opens, then maintenance of that level until the containment rupture disk opens, followed by a gradual but continual drop in suppression pool level. During the first 42hr, the MELCOR calculations with basaltic and with limestone concrete show generally very similar results for the drywell and wetwell pool masses; after cavity rupture and calculation end for the basaltic concrete case, the calculation assuming limestone concrete obviously continues the same overall response.

The pressures calculated by MELCOR in the various containment control volumes assuming either limestone or basaltic concrete are depicted in Figure 6.1.2, together with the containment pressure for MAAP (with basaltic concrete). Although the MELCOR calculation with limestone concrete was run for 100hr, only the first 45hr are shown in the figure to highlight the containment behavior around the time of rupture disk opening. The results are all generally similar qualitatively, but with a number of quantitative differences and shifts in timing. For this MELCOR calculation with limestone concrete, the containment rupture disk opening setpoint of 0.72MPa (90psig) is reached at 12.1hr, compared to rupture disk opening times of 14.7hr and 20.2hr with basaltic concrete in MELCOR and MAAP, respectively. The overall containment pressurization rate for basaltic concrete is slower in MAAP than in MELCOR, probably because the core debris in the cavity is quenched in the MAAP calculation but not in the MELCOR calculation; the overall pressurization is faster in MELCOR for limestone concrete than for basaltic

Table 6.1.1. Sequence of Events Predicted by MELCOR for LCLP-PF-R-N Sequence with Limestone Concrete and with Basaltic Concrete, Compared to MAAP with Basaltic Concrete

Event	Time		
	MAAP basaltic	MELCOR basaltic	MELCOR limestone
Accident initiation (MSIV Closure)	0.0	0.0	0.0
Reactor scrammed	4.2s		
Core uncovery begins		1,626.1s (0.45hr)	1,627.3s (0.45hr)
Water level at 2/3 core height; ADS	0.4hr	2,350.7s (0.65hr)	2,355.3s (0.65hr)
Clad failure/Gap release			
(Ring 1)		2,980.7s (0.83hr)	3,133.1s (0.87hr)
(Ring 2)		3,825.1s (1.06hr)	3,992.1s (1.11hr)
(Ring 3)		4,548.9s (1.26hr)	4,713.5s (1.31hr)
(Ring 4)		6,731.0s (1.87hr)	6,934.5s (1.93hr)
Core plate failed			
(Ring 1)		11,818.0s (3.28hr)	11,306.5s (3.14hr)
(Ring 2)		14,838.4s (4.12hr)	14,069.4s (3.91hr)
(Ring 3)		15,303.8s (4.25hr)	17,912.2s (4.98hr)
(Ring 4)		21,586.3s (6.00hr)	23,814.8s (6.62hr)
Vessel lower head failed	1.8hr		
Vessel LH penetration failed			
(Ring 1)		11,933.5s (3.31hr)	11,433.8s (3.18hr)
(Ring 2)		11,938.0s (3.32hr)	11,433.8s (3.18hr)
(Ring 3)		11,939.5s (3.32hr)	11,439.0s (3.18hr)
(Ring 4)		11,948.2s (3.32hr)	11,450.1s (3.18hr)
Commence debris ejection		11,933.5s (3.31hr)	11,433.8s (3.18hr)
Water in lower drywell boiled off	2.7hr	~22,470s (6.2hr)	~16,140s (4.48hr)
Passive flooder opens	5.4hr	22,473.7s (6.24hr)	16,144.4s (4.48hr)
Rupture disk opens	20.2hr	52,931.5s (14.70hr)	43,506.7s (12.10hr)
Concrete ablation $\geq$2m		150,967s (41.94hr)	360,000s (100hr)
End of calculation	100hr	150,967s (41.94hr)	360,000s (100hr)

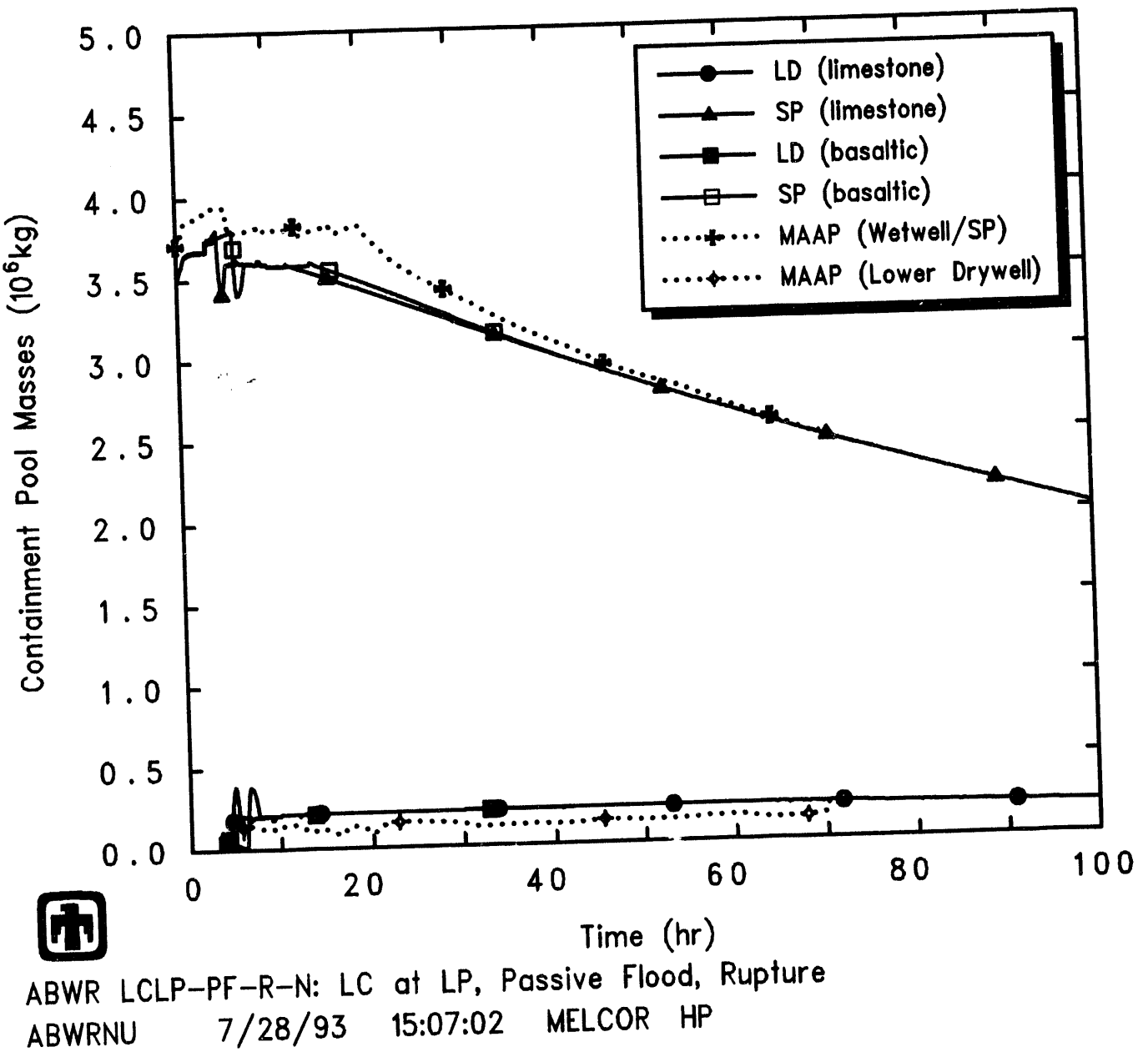

Figure 6.1.1. Lower Drywell and Suppression Pool Masses Predicted by MELCOR for LCLP-PF-R-N Sequence with Limestone Concrete and with Basaltic Concrete, Compared to MAAP with Basaltic Concrete

concrete due to the much greater generation of carbon monoxide (as discussed a little later in this section).

The MELCOR calculations with basaltic and with limestone concrete also show generally similar results for the containment temperatures during the first 42hr, shifted somewhat in time due to differences in containment response, such as time to rupture disk opening. The behavior of the total and partial pressures, and the mole fractions, in the atmospheres of the containment control volumes in the calculation with limestone concrete is very similar to that illustrated in Figures 5.1.19 and 5.1.20 for the LCLP-PF-R-N calculation with basaltic concrete, just shifted in time. The lower drywell and DW/WW vent atmospheres consist of almost all steam from vessel failure through calculation end; in the upper drywell, most of the atmosphere consists of steam after vessel failure; in the suppression pool, steam does not predominate until after containment rupture disk opening, while about half of the wetwell atmosphere between vessel failure and containment venting is hydrogen.

The total mass of debris in the cavity, the mass of ejected core debris and the mass of ablated concrete in the cavity calculated by MELCOR are illustrated in Figure 6.1.3; results are included both for this calculation with limestone concrete in the cavity and for the reference calculation with basaltic concrete specified. The debris ejection can be seen to occur in discrete steps or stages, while the mass of concrete ablated increases continuously with time. The total amounts of core debris and of ablated concrete are very similar in the two MELCOR calculations with limestone and with basaltic concrete, as seen in Figure 6.1.3. The total amounts of core debris are very similar because the in-vessel core degradation process is unaffected by the concrete composition. The total amounts of concrete ablated are very similar because both calculations were run until stopped "cavity rupture", *i.e.*, ablation of the initial cavity 2m depth at some point, which required ablating about the same amount of material. Note that the concrete ablation was much slower in the calculation with limestone concrete than with basaltic concrete, taking more than twice as long to ablate that amount.

There is much more noncondensable gas production in the cavity predicted with limestone concrete than with basaltic concrete. As soon as the core debris was predicted to enter the cavity, core-concrete interaction began, resulting in the production of carbon dioxide and hydrogen; reduction of these gases by the molten metal also gave rise to carbon monoxide and hydrogen. Figure 6.1.4 presents the production of various noncondensable gases in the cavity due to core-concrete interaction, calculated by MELCOR for a limestone concrete cavity. Almost all of the cavity gas production in this case is in the form of carbon monoxide, with much smaller amounts of the other gases predicted; with a basaltic cavity almost all of the cavity gas production was in the form of hydrogen, with a small and growing amount of CO produced after 32-33hr. The hydrogen gas generation from basaltic concrete compares well in order of magnitude with the hydrogen gas generation from limestone concrete, but the CO production is increased by an order of magnitude with a limestone concrete cavity. In all cases, CO is produced only after all the zironium in the cavity is oxidized to ZrO_2, because before that time Zr is assumed to reduce any CO_2 generated to pure carbon ("coking"); with basaltic concrete,

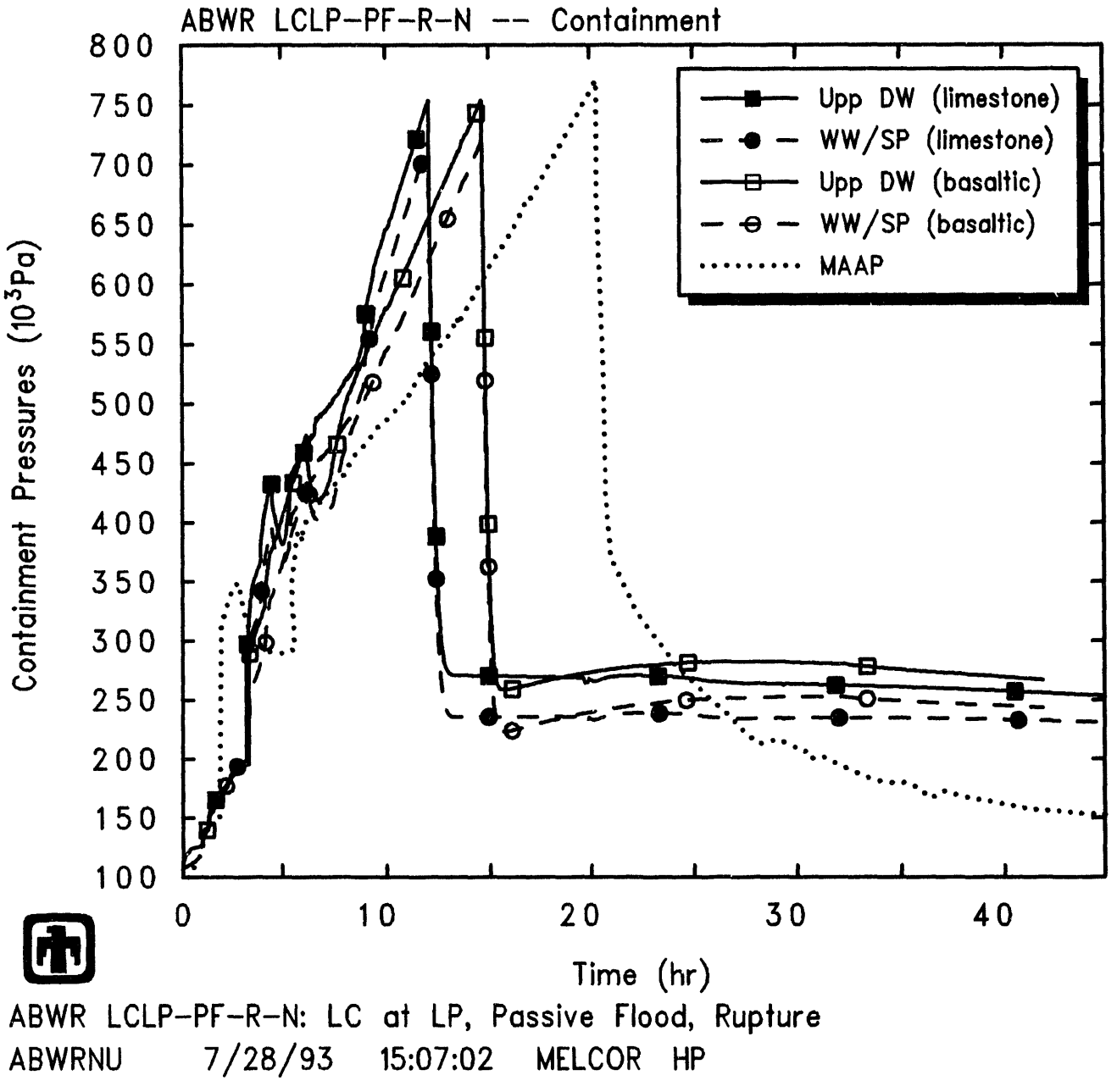

Figure 6.1.2. Containment Pressures Predicted by MELCOR for LCLP-PF-R-N Sequence with Limestone Concrete and with Basaltic Concrete, Compared to MAAP with Basaltic Concrete

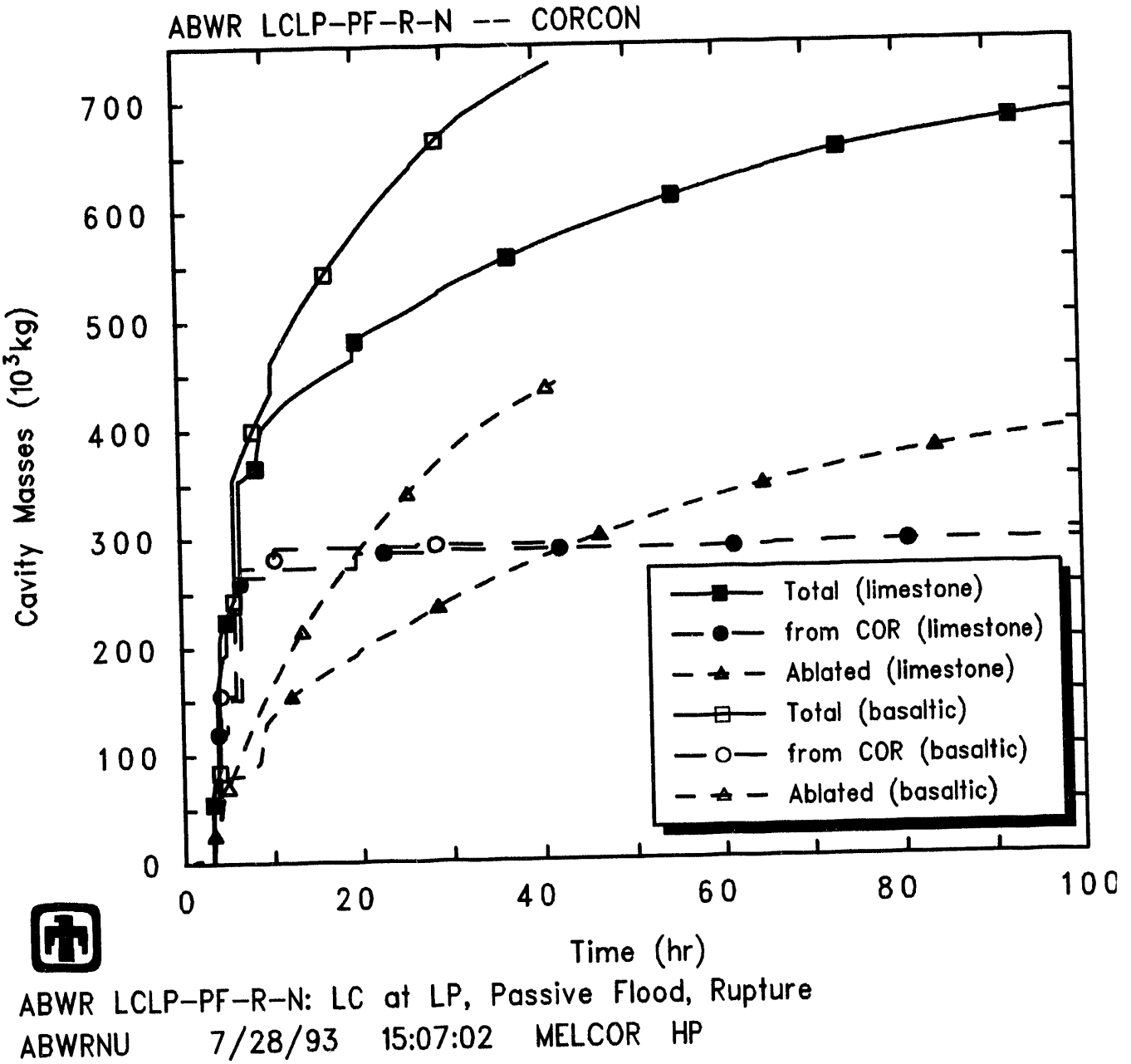

Figure 6.1.3. Cavity Material Masses Predicted by MELCOR for LCLP-PF-R-N Sequence with Limestone Concrete and with Basaltic Concrete

the zirconium was all oxidized by about 30hr, while with the increased gas generation rates in limestone concrete, the zirconium was all oxidized by about 10hr.

Figure 6.1.5 gives the calculated maximum cavity depths and radii predicted by MELCOR in this sensitivity study assuming a limestone concrete cavity and in the reference calculation with a basaltic concrete cavity specified. (Note that these represent maximum, not average, ablation distances.) Immediately after core debris is first ejected from the vessel to the cavity upon vessel breach, there is a brief period of rapid radial ablation lasting a few hr, which stops after <20cm of concrete loss, in both cases. The bulk of the concrete ablation calculated is axially downward, with the MELCOR calculation stopping when the axial ablation equals and tries to exceed the specified available concrete thickness of 2m; this is predicted at just over 100hr in the MELCOR calculation with a limestone concrete cavity compared to occurring at 42hr in the MELCOR reference calculation with a basaltic concrete cavity.

A heavy oxide layer is calculated to exist in the cavity for a short time after debris ejection from the vessel; subsequently, MELCOR calculates a stable configuration of a light oxide layer above a metallic debris layer throughout most of the transient period calculated. The metallic layer mass and thickness decrease significantly within 100hr due to oxidation reactions in the limestone concrete cavity; for a basaltic concrete cavity, the metallic layer mass and thickness remained nearly constant (Figure 5.1.25), but that calculation ran only to <45hr. The light oxide layer mass and thickness increase continuously (and the density decreases) as ablating concrete (with its resultant low-density silicate oxides) continues to dilute the high-density zirc oxide and steel oxide debris to an average density value less than the metallic debris density. After some initial oscillations, the temperatures of both layers remain nearly equal, at $\simeq$1500K, throughout the transient period calculated, quite similar to the behavior found with basaltic concrete.

The heat transfer from the cavity debris pool in the MELCOR analysis, both downward and outward to the concrete surface and upward to the cavity volume atmosphere, is shown in Figure 6.1.6. Results are included for both the MELCOR sensitivity study calculation with a limestone concrete cavity and for the MELCOR reference calculation with a basaltic concrete cavity. In both cases, the energy transfer from the debris in the cavity upward through the debris bed surface to the lower drywell atmosphere and/or overlying water pool is 2-5 times greater than the energy transferred downward (and sideways) to the concrete. The heat fluxes calculated by MELCOR for a limestone concrete cavity are generally lower than those calculated by MELCOR for a basaltic concrete cavity.

Tables 6.1.2 and 6.1.3 give the distribution of the released radionuclides at the end of the calculation (*i.e.*, at 100hr). The release behavior predicted by MELCOR for the LCLP-PF-R-N sequence assuming a limestone cavity is very similar to the release behavior predicted by MELCOR for the LCLP-PF-R-N sequence reference analysis with a basaltic cavity (presented in Tables 5.1.4 and 5.1.5). Almost all ($\simeq$100%) of the volatile Class 1 (noble gases), Class 2 (CsOH), Class 5 (Te) and Class 16 (CsI) radionuclide species are released, primarily in-vessel, as are most (80-90%) of the Class 3 (Ba) and Class 12 (Sn) inventories. The next major release fractions are of Ru and Mo, Ce and La, all

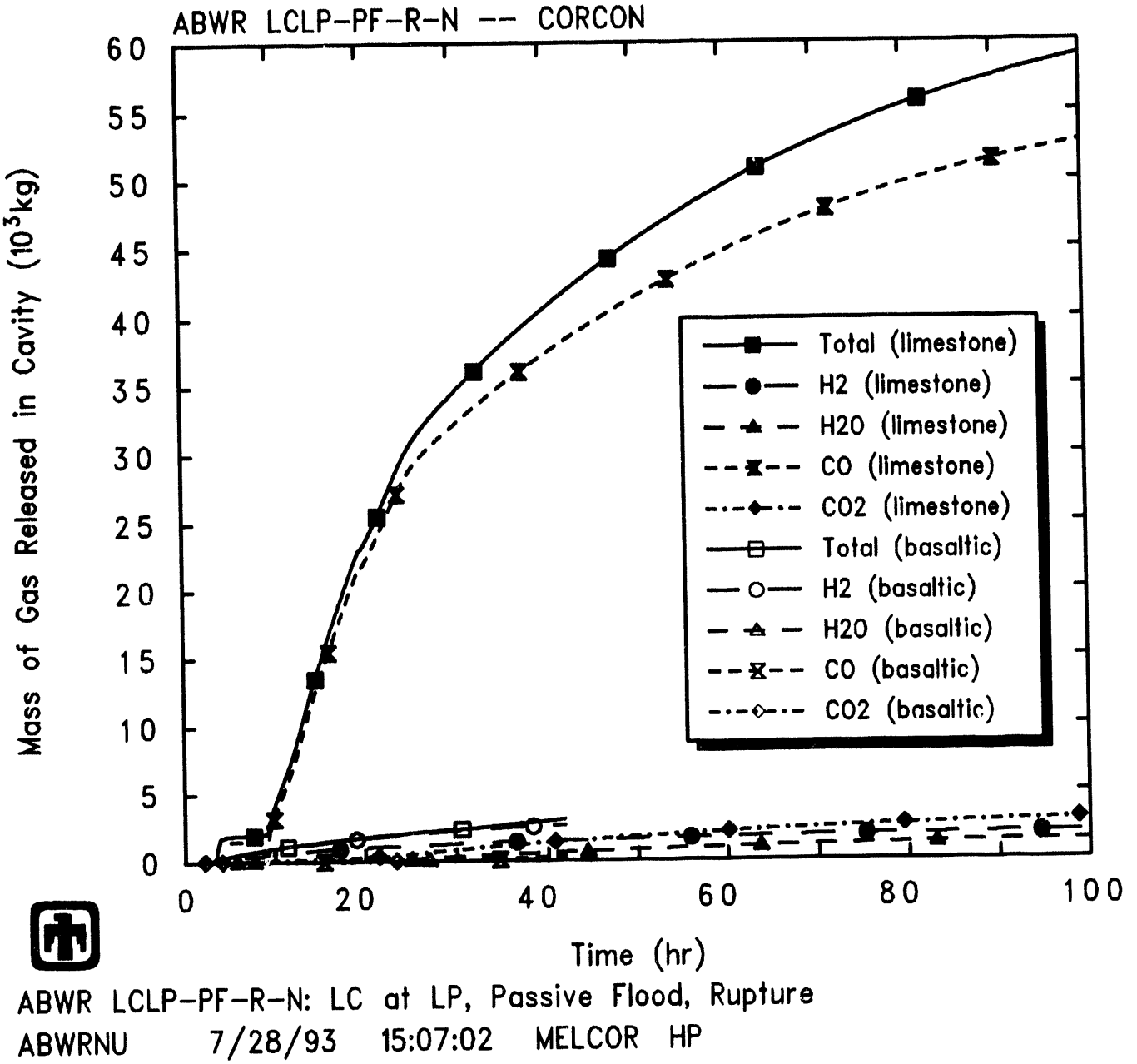

Figure 6.1.4. Cavity Gas Production Predicted by MELCOR for LCLP-PF-R-N Sequence with Limestone Concrete and with Basaltic Concrete

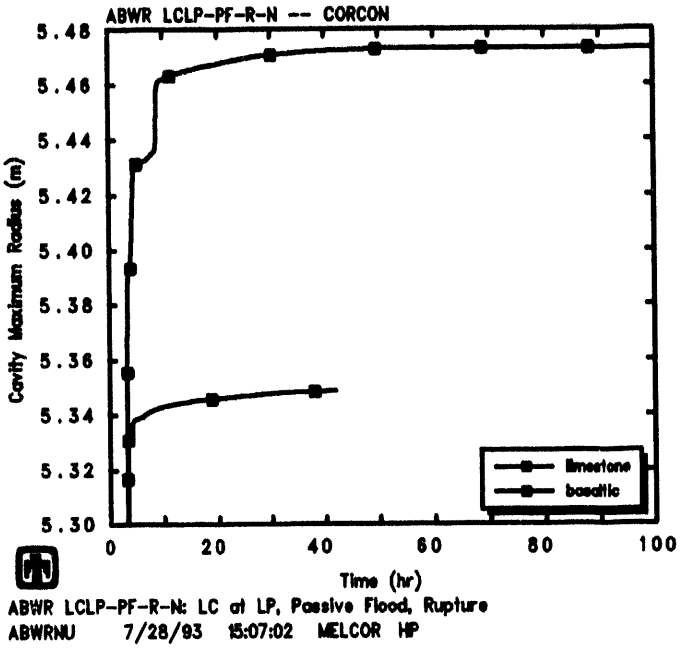

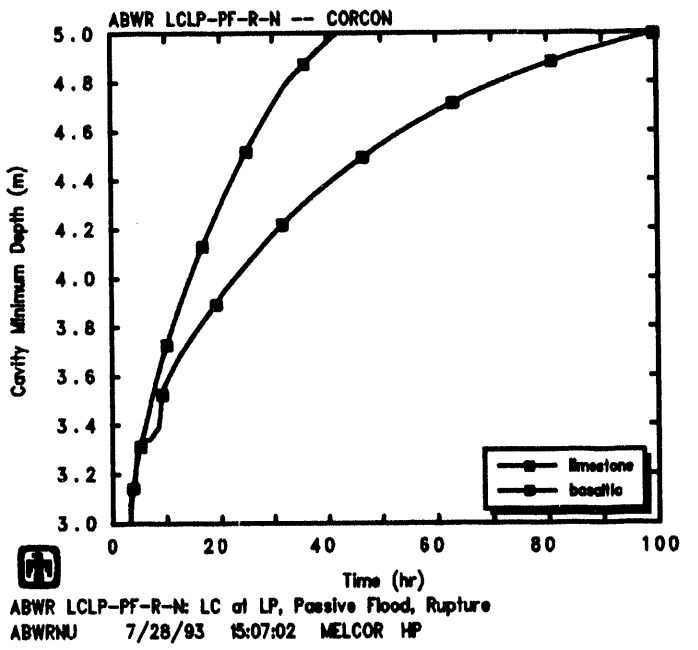

Figure 6.1.5. Cavity Maximum Radius (top) and Depth (bottom) Predicted by MELCOR for LCLP-PF-R-N Sequence with Limestone Concrete and with Basaltic Concrete

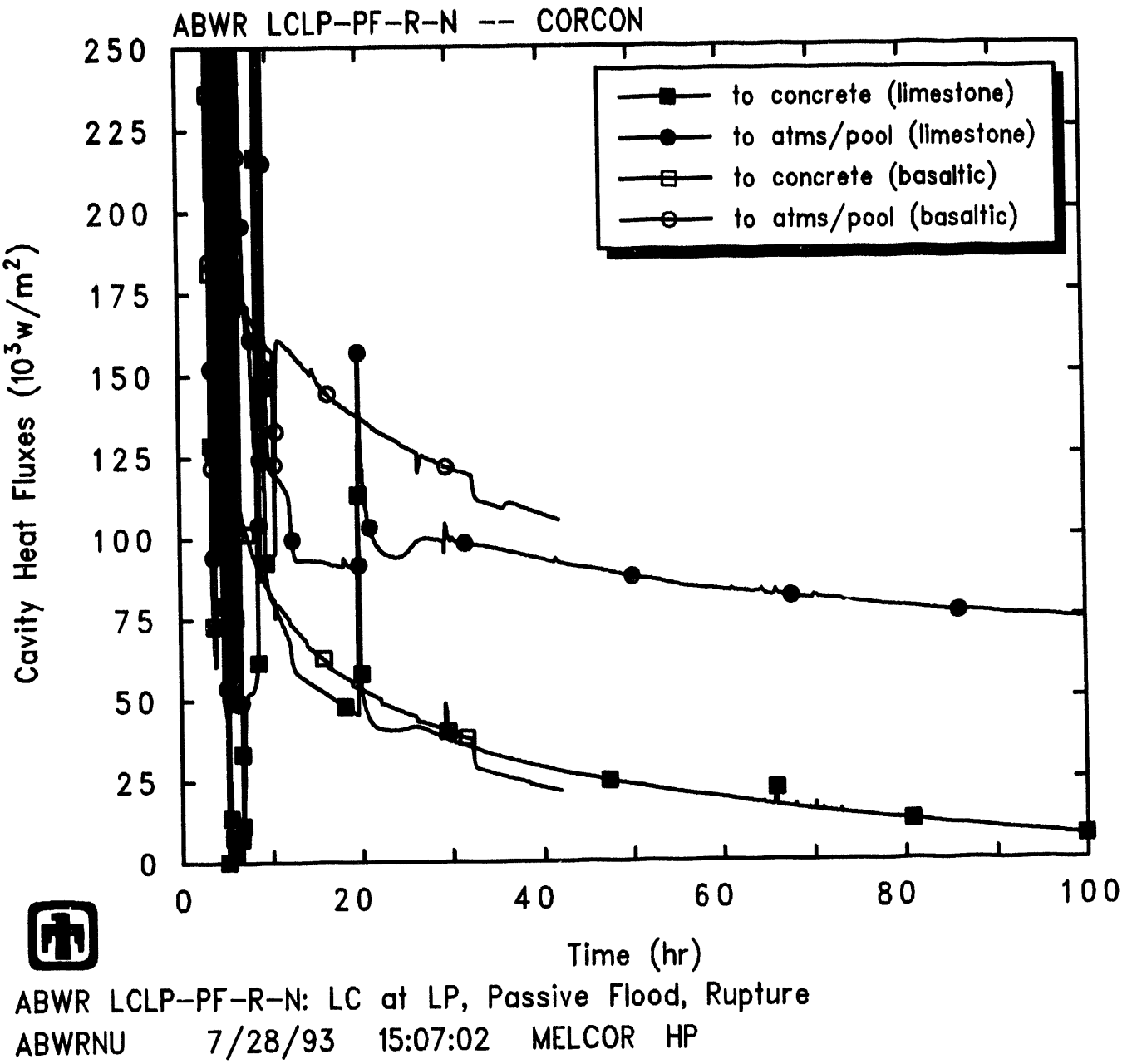

Figure 6.1.6. Cavity Heat Flows Predicted by MELCOR for LCLP-PF-R-N Sequence with Limestone Concrete

between 2% and 4%. Finally, a total $\leq$0.1% of the initial inventory of uranium and Class 11 (Cd) are predicted to be released. (Note that the CORSOR-M fission product release model option used in these analyses has identically zero release in-vessel of Class 7, Class 9 and Class 11.)

Most of the released radionuclides remain in the primary system and/or the containment; only the noble gases show a significant release (>90%) to the environment. Of the other radionuclides, 0.2-0.6% of the total volatile masses (CsOH, Te and CsI) are released to the environment in the MELCOR LCLP-PF-R-N sensitivity study calculation with limestone concrete, slightly higher than the 0.15-0.25% release predicted in the MELCOR reference calculation with basaltic concrete. The higher releases calculated for limestone concrete are probably a direct result of the longer time that calculation ran after rupture disk opening, extending the release period (over 80hr, compared to less than 30hr in the corresponding reference calculation with basaltic concrete. In both cases, $\ll$0.1% of the other radionuclides' initial inventory is released to the environment. Also, of the species with significant (>80%) release from fuel, the wetwell is predicted to retain most (50-70%) of the released CsOH, Te and CsI volatiles, while the Ba and Sn aerosols are held up both in the primary system ($\geq$40%) and in the wetwell ($\leq$40%) with both concrete types.

The retention factors for the various radionuclides in the primary system and in the overall containment are slightly lower and higher, respectively, in the MELCOR LCLP-PF-R-N sensitivity study calculation with a limestone concrete cavity than in the MELCOR reference calculation with a basaltic concrete cavity. The decontamination factors for the various radionuclides for the suppression pool and for the overall containment are very similar in the MELCOR LCLP-PF-R-N sensitivity study calculation with limestone concrete and in the MELCOR reference calculation with basaltic concrete.

In this LCLP-PF-R-N analysis assuming limestone concrete, which ran much longer than the reference LCLP-PF-R-N analysis with basaltic concrete, the suppression pool and overall containment decontamination factors continue to drop steadily for several radionuclide species (*i.e.*, CsOH, Te, Mo, Cd, U and CsI). These are the classes for which a continuing release to the environment is predicted, while for the other classes there is only a single step-like release at COPS rupture, as illustrated in Figure 6.1.7. These results resemble those given in Figure 5.1.31 for the reference analysis with basaltic concrete, given the longer period of release between containment rupture disk opening and transient end at cavity rupture in the calculation with limestone concrete.

6.2 LCLP-FS-R-N Sequence with Limestone Concrete

The first part of this sequence, through core uncovery, heatup and degradation, and vessel lower head failure, is identical to the LCLP-FS-R-N sequence with basaltic concrete discussed in Section 5.2 and to the LCLP-PF-R-N sequence with limestone concrete discussed in Section 6.1. The difference is that the firewater system is used in spray mode to add external water to the containment. The sequence of events for this accident is given

Table 6.1.2. Radionuclide Distribution Predicted at 100hr for LCLP-PF-R-N Sequence with Limestone Concrete

Class	Fission Product Distribution (% Initial Inventory)					
	Remaining in Fuel		Released from Fuel			
	Core	Cavity	Primary System	Drywell	Wetwell	Environment
Noble Gases (Xe)	8.86×10^{-6}	0	0.0343	1.47	2.02×10^{-3}	98.5
Alkali Metals (CsOH)	9.46×10^{-6}	$\simeq$0	22.8	17.8	59.2	0.244
Alkaline Earths (Ba)	1.50×10^{-4}	15.3	37.4	20.9	26.4	0.0205
Halogens (I)	$\simeq$0	$\simeq$0	$\simeq$0	$\simeq$0	$\simeq$0	$\simeq$0
Chalcogens (Te)	1.42×10^{-5}	0.0237	26.6	18.0	55.4	0.333
Platinoids (Ru)	1.50×10^{-4}	97.8	0.587	1.25	0.341	1.58×10^{-4}
Transition Metals (Mo)	1.50×10^{-4}	96.8	8.02×10^{-3}	1.22	1.92	0.0344
Tetravalents (Ce)	1.50×10^{-4}	97.4	0.655	1.60	0.396	2.92×10^{-4}
Trivalents (La)	1.50×10^{-4}	97.8	3.52×10^{-3}	1.23	0.984	4.41×10^{-3}
Uranium (U)	5.07×10^{-4}	$\simeq$100	0.0121	0.0239	0.0105	1.24×10^{-4}
More Volatile Main Group Elements (Cd)	1.50×10^{-4}	99.9	9.82×10^{-5}	0.0288	0.0276	1.32×10^{-3}
Less Volatile Main Group Elements (Sn)	1.48×10^{-4}	8.88	37.6	19.2	34.3	0.0155
CsI	$\simeq$0	1.78×10^{-5}	18.8	18.4	62.1	0.617

Table 6.1.3. Radionuclide Release and Released Distribution Predicted at 100hr for LCLP-PF-R-N Sequence with Limestone Concrete

Class	Released from Fuel (% Initial Inventory)			Distribution (% Released Mass)			
	Core	Cavity	Total	Primary System	Drywell	Wetwell	Environment
Noble Gases (Xe)	99.98	0.02	≃100	0.0343	1.47	2.02×10^{-3}	98.5
Alkali Metals (CsOH)	99.98	0.02	≃100	22.85	17.8	59.24	0.244
Alkaline Earths (Ba)	81.05	3.64	84.69	44.15	24.7	31.12	0.0242
Halogens (I)	≃0	≃0	≃0	3.71×1^{-3}	1.83	2.45×10^{-3}	97.88
Chalcogens (Te)	99.96	7.50×10^{-3}	99.97	30.75	22.43	69.15	0.0328
Platinoids (Ru)	2.18	2.01×10^{-4}	2.18	26.97	57.34	15.57	7.24×10^{-3}
Transition Metals (Mo)	0	3.56	3.56	0.25	38.30	60.36	1.085
Tetravalents (Ce)	2.65	2.03×10^{-3}	2.65	24.73	60.30	14.96	0.011
Trivalents (La)	0	2.22	2.22	0.0158	55.29	44.36	0.199
Uranium (U)	0.038	0.0096	0.048	25.89	51.29	22.55	0.267
More Volatile Main Group Elements (Cd)	0	0.058	0.058	0.17	49.81	47.73	2.29
Less Volatile Main Group Elements (Sn)	91.06	0.063	91.12	41.27	21.12	37.59	0.017
CsI	99.97	0.024	≃100	18.8	18.4	62.1	0.617

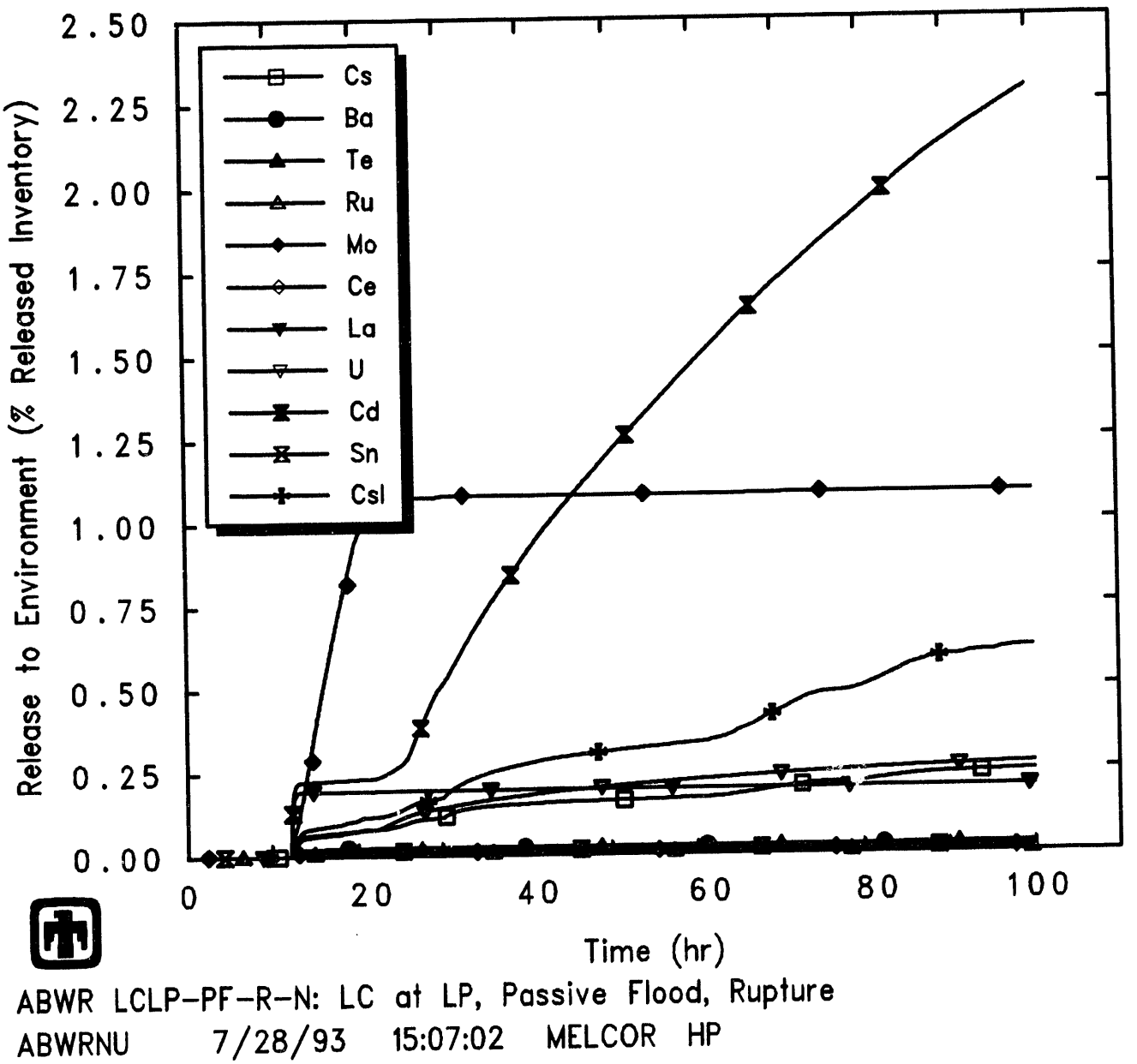

Figure 6.1.7. Radionuclide Environmental Releases Predicted by MELCOR for LCLP-PF-R-N Sequence with Limestone Concrete

in Table 6.2.1, with the timings of the various events as calculated by MELCOR and by MAAP with basaltic concrete included for comparison. The MELCOR calculations with basaltic and with limestone concrete should be the same up to the time of vessel failure and debris ejection into the cavity; the small differences seen in timing in Table 6.2.1 and the small differences in timing between Tables 6.1.1 and 6.2.1 are due to using different code versions for these two analyses.

One major difference between the MAAP results and both MELCOR calculations, with limestone and basaltic concrete, for this sequence can be seen in Table 6.2.1. In the MELCOR calculations, as soon as the cavity goes dry, the lower drywell atmosphere temperature rises rapidly due to heat transfer from the unquenched debris and very quickly reaches the 500K spray initiation setpoint at 5-6hr and the 533K passive-flooder setpoint very soon afterwards; the spray later turns off, after 10-12hr of injection, followed by containment rupture disk actuation still later. In the MAAP analysis, the sprays begin at 4hr but the passive flooder does not open until 61.1hr, after the firewater spray has stopped (23.6hr), the containment rupture disk has opened (31.6hr), and the cavity has dried out (56.6hr). Thus, not only are the timings of various events different, the relative ordering of events is different.

Much of the containment behavior calculated for the LCLP-FS-R-N sequence assuming limestone concrete is very similar to the response predicted in the reference calculation with basaltic concrete for this scenario (described in Section 5.2), albeit shifted somewhat in time due to differences in parameters such as time to rupture disk opening. The effect of varying the concrete type in the LCLP-FS-R-N scenario is similar to the effects found for the LCLP-PF-R-N sequence, discussed in Section 6.1.

Figure 6.2.1 give the drywell and wetwell pool masses for both MELCOR analyses, with limestone concrete and with basaltic concrete, compared to the pool masses calculated by MAAP (with basaltic concrete). There appears to be a small difference in the suppression pool initial mass (and/or level) in the two calculations, and MELCOR predicts a bigger short-term drop in suppression pool level and corresponding rise in cavity pool level upon opening the passive flooder. However, the results are generally in good qualitative agreement, with both codes showing a long-term rise in suppression pool level due to firewater spray injection, followed by a gradual drop in suppression pool level. The lower drywell pool masses predicted by MELCOR in both cases are also in good overall qualitative agreement, although some timing shifts are visible. The lower drywell pool mass remains similar as water continues to be transferred from the suppression pool to the lower drywell where it is boiled away by the core debris in the cavity; the lower drywell mass predicted then drops after the spray is stopped, at 12.1hr in the MELCOR calculation assuming limestone concrete, and at 18.5hr in the MELCOR reference analysis using basaltic concrete.

The pressures calculated by MELCOR in the various containment control volumes are depicted in Figure 6.2.2, for the sensitivity study calculation with limestone concrete and including results for the reference analysis with basaltic concrete, together with the containment pressure from the MAAP analysis. The results are all generally similar qualitatively, but with a number of quantitative differences and shifts in timing. Both

Table 6.2.1. Sequence of Events Predicted by MELCOR for LCLP-FS-R-N Sequence with Limestone Concrete and with Basaltic Concrete, Compared to MAAP with Basaltic Concrete

Event	Time		
	MAAP basaltic	MELCOR basaltic	MELCOR limestone
Accident initiation (MSIV Closure)	0.0	0.0	0.0
Reactor scrammed	4.2s		
Core uncovery begins		1,629.1s (0.45hr)	1,627.3s (0.45hr)
Water level at 2/3 core height; ADS	0.4hr	2,355.9s (0.65hr)	2,350.7s (0.65hr)
Clad failure/Gap release			
(Ring 1)		2,985.9s (0.83hr)	2,986.8s (0.83hr)
(Ring 2)		3,825.9s (1.06hr)	3,826.7s (1.06hr)
(Ring 3)		4,513.3s (1.25hr)	4,524.3s (1.26hr)
(Ring 4)		6,688.4s (1.86hr)	6,724.7s (1.87hr)
Core plate failed			
(Ring 1)		12,257.1s (3.40hr)	11,921.2s (3.31hr)
(Ring 2)		13,580.5s (3.77hr)	16,678.0s (4.63hr)
(Ring 3)		16,928.4s (4.70hr)	22,668.2s (6.30hr)
(Ring 4)		20,436.4s (5.86hr)	32,020.1s (8.89hr)
Vessel bottom head failed	1.8hr		
Vessel LH penetration failed			
(Ring 1)		12,351.5s (3.43hr)	12,044.8s (3.35hr)
(Ring 1)		12,351.5s (3.43hr)	12,044.8s (3.35hr)
(Ring 1)		12,348.5s (3.43hr)	12,045.7s (3.35hr)
(Ring 1)		12,348.5s (3.43hr)	12,065.5s (3.35hr)
Commence debris ejection		12,348.5s (3.43hr)	12,044.8s (3.35hr)
Water in lower drywell boiled off	2.7hr	~22,000s (6.1hr)	~18,570s (5.16hr)
Firewater spray started	4.hr	21,942.4s (6.10hr)	18,577.2s (5.16hr)
Suppression pool overflows to lower drywell	7.0hr		
Firewater spray stopped	23.6hr	66,584.7s (18.50hr)	53,864.5s (14.96hr)
Rupture disk opens	31.6hr	89,922.6s (24.98hr)	60,324.5s (16.76hr)
Water in lower drywell boiled off	56.6hr		
Passive flooder opens	61.hr	21,976.4s (6.10hr)	18,585.2s (5.16hr)
Firewater spray started			237,282s (65.91hr)
Firewater spray stopped			238,192s (66.16hr)
Firewater spray started			261,649s (72.68hr)
Firewater spray stopped			262,554s (72.93hr)
Firewater spray started			282,293s (78.41hr)
Firewater spray stopped			283,197s (78.67hr)
Firewater spray started			300,468s (83.46hr)
Firewater spray stopped			301,375s (83.72hr)
Concrete ablation≥2m		156,454s (43.46hr)	313,126s (86.98hr)
End of calculation	100hr	156,454s (43.46hr)	313,126s (86.98hr)

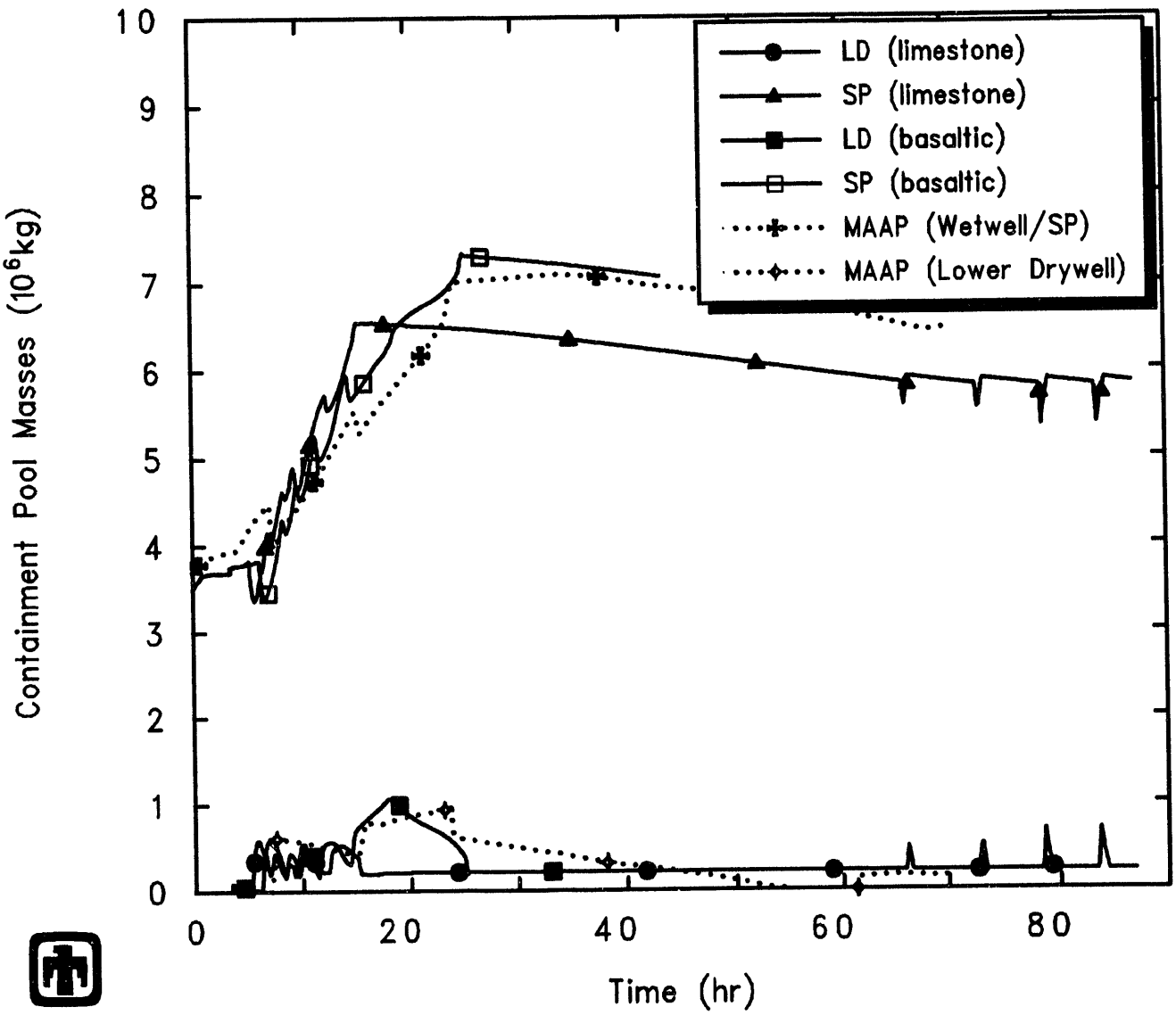

Figure 6.2.1. Lower Drywell and Suppression Pool Masses Predicted by MELCOR for LCLP-FS-R-N Sequence with Limestone Concrete and with Basaltic Concrete, Compared to MAAP with Basaltic Concrete

MELCOR cases predict a rapid pressure increase in containment immediately after vessel failure, due to steam generation from hot debris and water falling into the cavity from the lower plenum. In the MAAP containment pressure history, after the water in the lower drywell boils off, the drywell pressure decreases because steam is condensed on the containment heat sinks but there is no additional steam generated; in the MELCOR calculation, the containment pressure continues to rise as hot, unquenched core debris continues to boil off the cavity water pool. For the MELCOR calculation with a limestone concrete cavity, the containment rupture disk opening setpoint of 0.72MPa (90psig) is reached at 16.8hr, compared to rupture disk opening times of 25hr and 31.6hr with basaltic concrete in MELCOR and MAAP, respectively. The overall containment pressurization rate for basaltic concrete is slower in MAAP than in MELCOR, because the core debris in the cavity is quenched in the MAAP calculation but not in the MELCOR calculation; the overall pressurization is faster in MELCOR for limestone concrete than for basaltic concrete due to the much greater generation of carbon monoxide (as discussed a little later in this section). No penetration leakage is predicted by MAAP or by either MELCOR calculation, since the temperature in the upper drywell remains below 533K (500°F) until well after the rupture disk opens.

The MELCOR calculations with basaltic and with limestone concrete also show generally similar results for the containment temperatures during the first 43hr, shifted somewhat in time due to differences in containment response, such as time to rupture disk opening. The behavior of the total and partial pressures, and the mole fractions, in the atmospheres of the containment control volumes is the same as illustrated in Figures 5.2.6 and 5.2.7 for the LCLP-FS-R-N calculation with basaltic concrete, just shifted in time. The lower drywell and DW/WW vent atmospheres consist of almost all steam from vessel failure through calculation end; in the upper drywell, most of the atmosphere consists of steam after vessel failure; in the suppression pool, steam does not predominate until after containment rupture disk opening, while about half of the wetwell atmosphere between vessel failure and containment venting is hydrogen.

The total mass of debris in the cavity, the mass of ejected core debris and the mass of ablated concrete in the cavity calculated by MELCOR are illustrated in Figure 6.2.3; results are included both for this calculation with limestone concrete in the cavity and for the reference calculation with basaltic concrete specified. The debris ejection can be seen to occur in discrete steps or stages, while the mass of concrete ablated increases continuously with time. The total amounts of core debris and of ablated concrete are very similar in the two MELCOR calculations with limestone and with basaltic concrete. The total amounts of core debris are very similar because the in-vessel core degradation process is unaffected by the concrete composition. The total amounts of concrete ablated are very similar because both calculations were run until stopped "cavity rupture" (*i.e.*, ablation of the initial cavity 2m depth at some point), which required ablating about the same amount of material. Note that the concrete ablation was much slower in the calculation with limestone concrete than with basaltic concrete, taking about twice as long to ablate that amount.

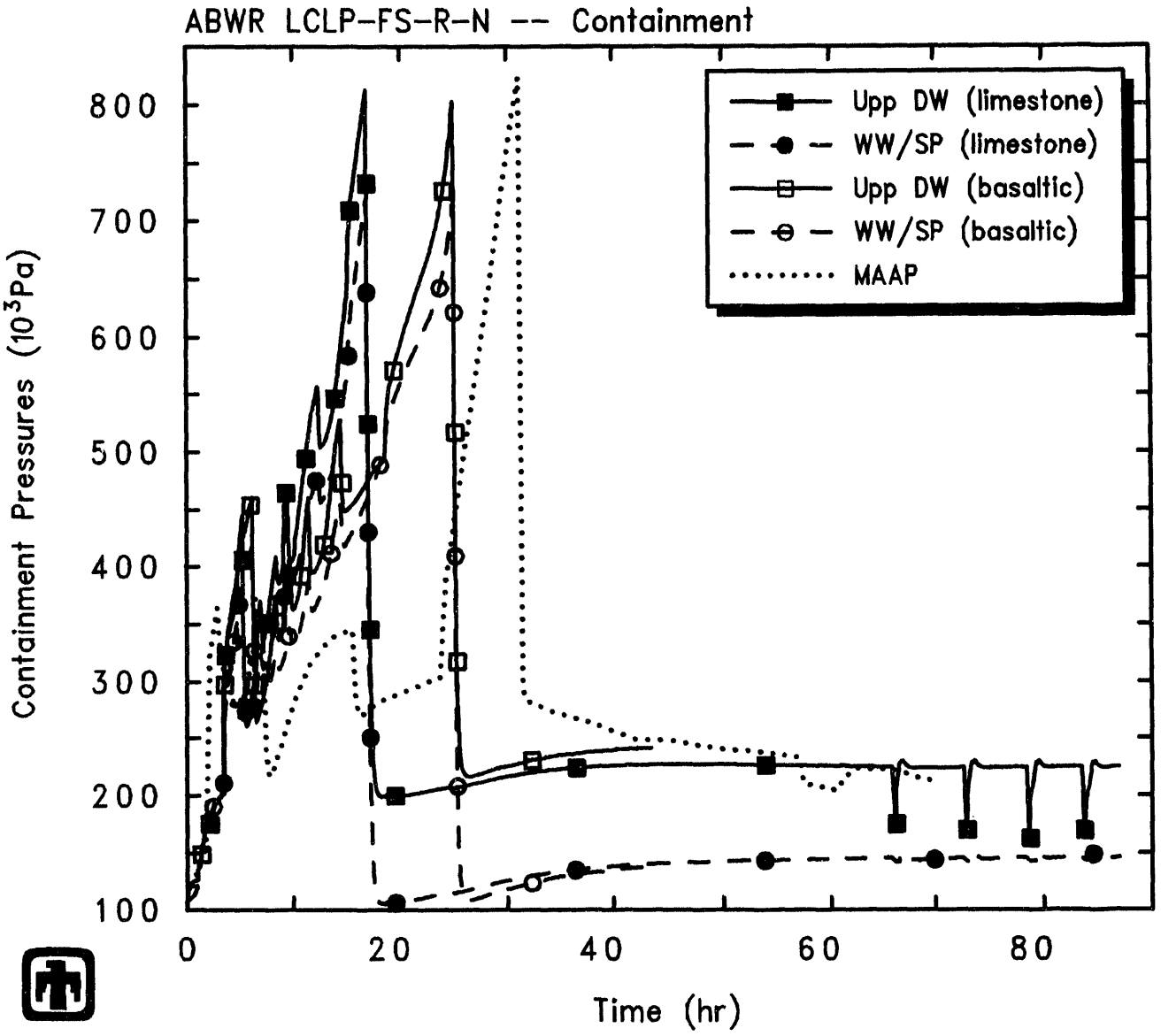

Figure 6.2.2. Containment Pressures Predicted by MELCOR for LCLP-FS-R-N Sequence with Limestone Concrete, Compared to MAAP with basaltic concrete

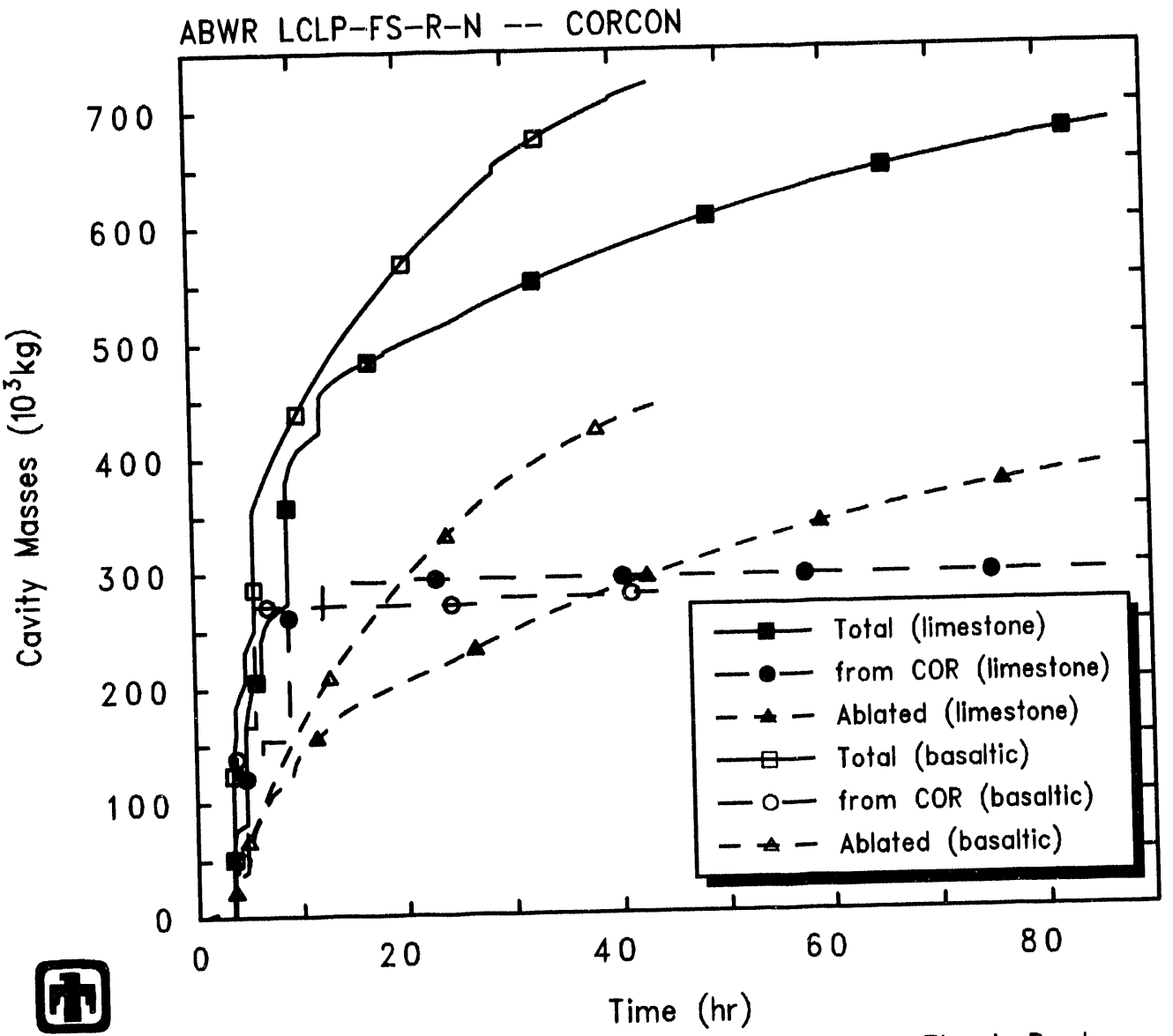

Figure 6.2.3. Cavity Material Masses Predicted by MELCOR for LCLP-FS-R-N Sequence with Limestone Concrete and with Basaltic Concrete

As found for the LCLP-PF-R-N sequence with limestone *vs* basaltic concrete (shown in Figure 6.1.4), there is much more noncondensable gas production in the cavity predicted with limestone concrete than with basaltic concrete. As soon as the core debris was predicted to enter the cavity, core-concrete interaction began, resulting in the production of carbon dioxide and hydrogen; reduction of these gases by the molten metal also gave rise to carbon monoxide and hydrogen. Figure 6.2.4 presents the production of various noncondensable gases in the cavity due to core-concrete interaction, calculated by MELCOR for a limestone concrete cavity. Almost all of the cavity gas production in this case is in the form of carbon monoxide, with much smaller amounts of the other gases predicted; with a basaltic cavity almost all of the cavity gas production was in the form of hydrogen, with a growing amount of CO produced after 30hr. The hydrogen gas generation from basaltic concrete compares well in order of magnitude with the hydrogen gas generation from limestone concrete, but the CO production is increased by an order of magnitude with a limestone concrete cavity, even though there is a rapid increase in CO production after 30hr with the basaltic concrete cavity. In all cases, CO is produced only after all the zironium in the cavity is oxidized to ZrO_2, because before that time Zr is assumed to reduce any CO_2 generated to pure carbon ("coking") with basaltic concrete, the zirconium was all oxidized by about 30hr, while with the increased gas generation rates in limestone concrete, the zirconium was all oxidized by about 10hr.

Figure 6.2.5 gives the calculated maximum cavity depths and radii predicted by MELCOR in this sensitivity study assuming a limestone concrete cavity and in the reference calculation with a basaltic concrete cavity specified. (Note that these represent maximum, not average, ablation distances.) Immediately after core debris is first ejected from the vessel to the cavity upon vessel breach, there is a brief period of rapid radial ablation lasting a few hr, which stops after <15cm of concrete loss, in both cases. The bulk of the concrete ablation calculated is axially downward, with the MELCOR calculation stopping when the axial ablation equals and tries to exceed the specified available concrete thickness of 2m; this is predicted at 87hr in the MELCOR calculation with a limestone concrete cavity compared to occurring at 44hr in the MELCOR reference calculation with a basaltic concrete cavity.

The heat transfer from the cavity debris pool in the two MELCOR analyses with limestone and with basaltic concrete, both downward and outward to the concrete surface and upward to the cavity volume atmosphere, is shown in Figure 6.2.6. The energy transfer from the debris in the cavity upward through the debris bed surface to the lower drywell atmosphere and/or overlying water pool is 2-4 times greater than the energy transferred downward (and sideways) to the concrete. The heat fluxes calculated by MELCOR for a limestone concrete cavity are generally lower than those calculated by MELCOR for a basaltic concrete cavity.

Tables 6.2.2 and 6.2.3 give the distribution of the released radionuclides at the end of the calculation (*i.e.*, at 87hr). The release behavior predicted by MELCOR fall into the same subgroups as for all these ABWR analyses. Almost all ($\simeq$100%) of the volatile Class 1 (noble gases), Class 2 (CsOH), Class 5 (Te) and Class 16 (CsI) radionuclide species are released, primarily in-vessel, as are most (80-90%) of the Class 3 (Ba) and

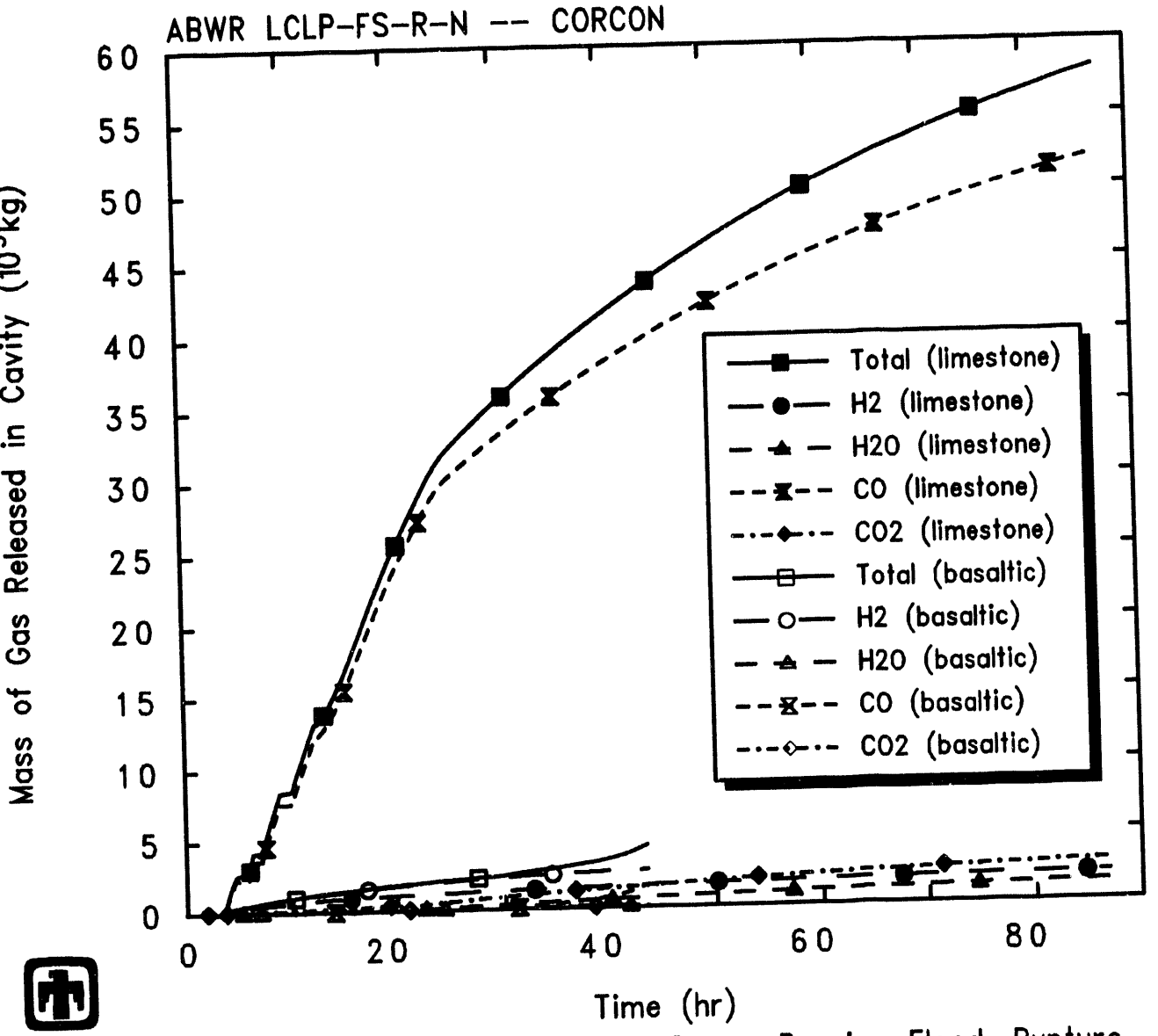

Figure 6.2.4. Cavity Gas Production Predicted by MELCOR for LCLP-FS-R-N Sequence with Limestone Concrete and with Basaltic Concrete

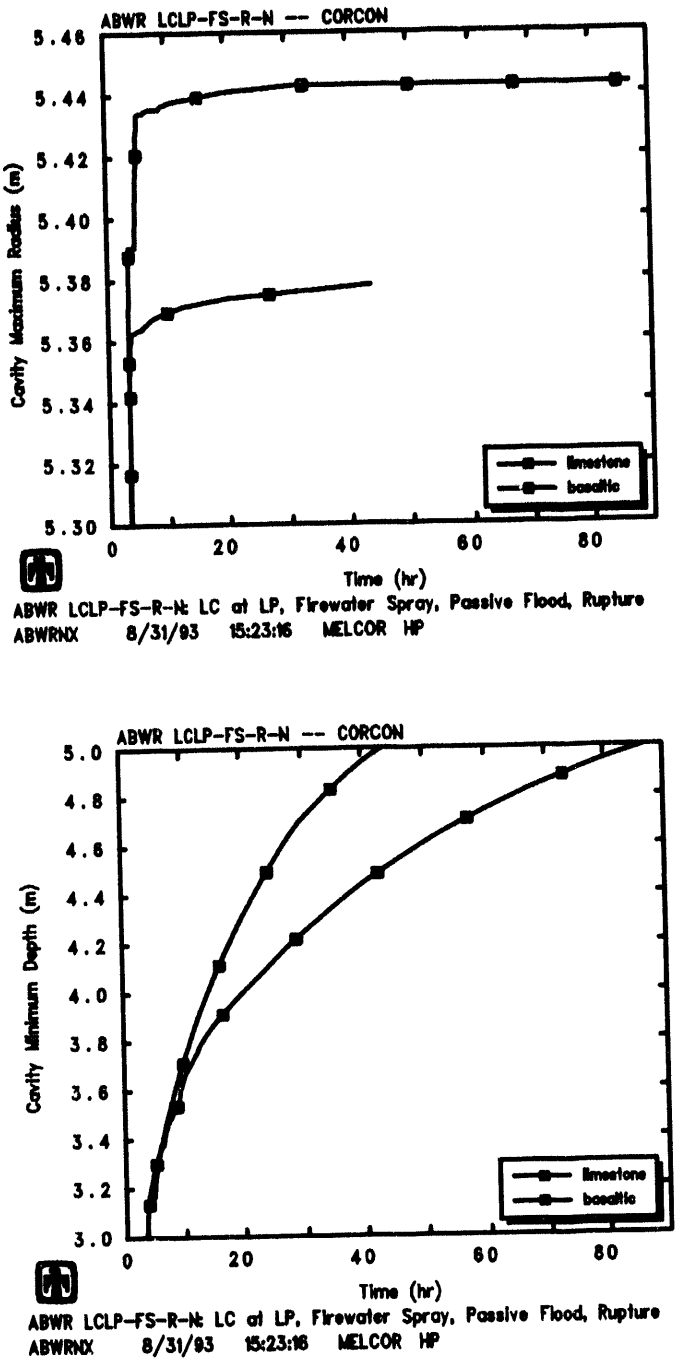

Figure 6.2.5. Cavity Maximum Radius (top) and Depth (bottom) Predicted by MELCOR for LCLP-FS-R-N Sequence with Limestone Concrete and with Basaltic Concrete

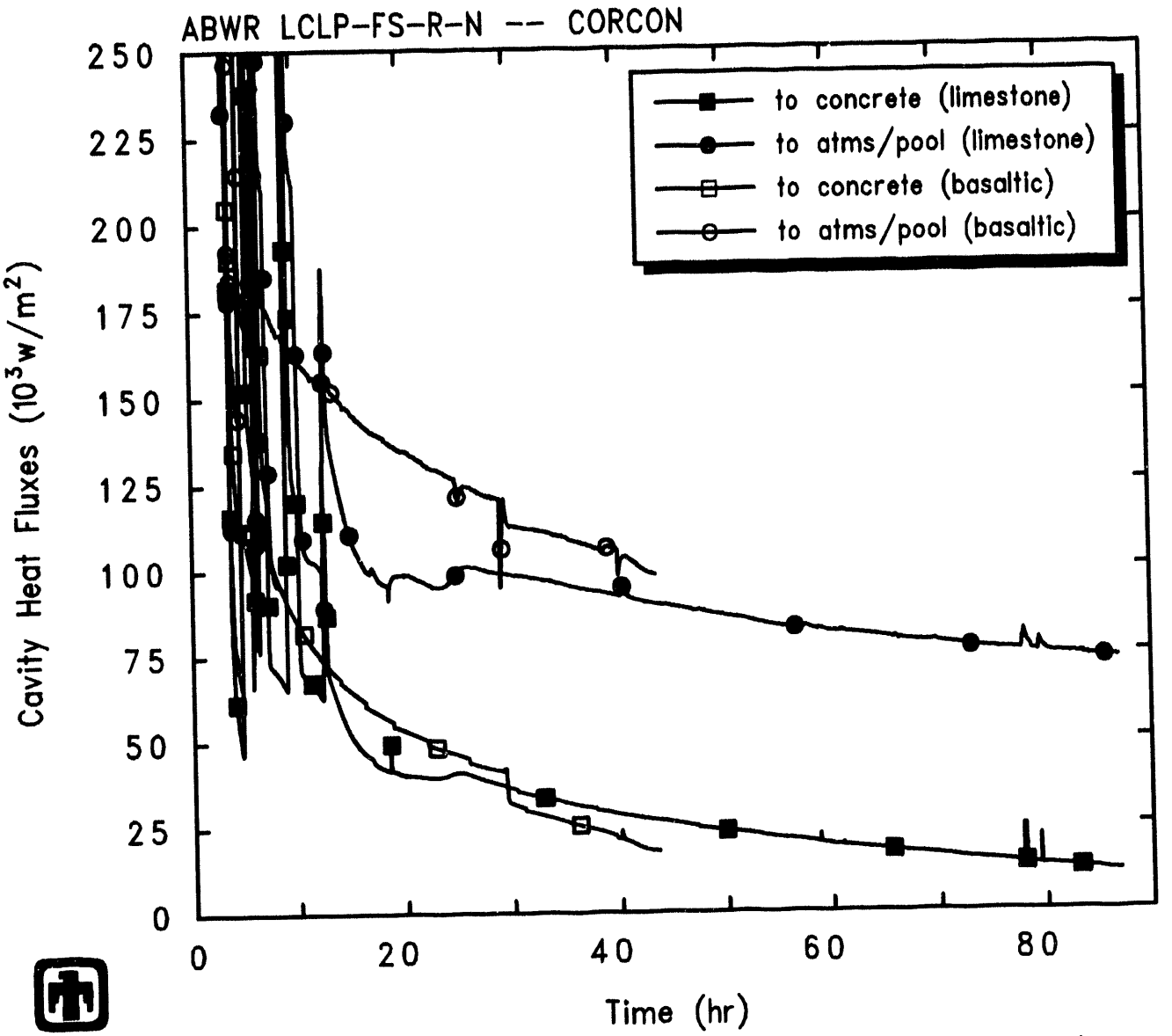

Figure 6.2.6. Cavity Heat Flows Predicted by MELCOR for LCLP-FS-R-N Sequence with Limestone Concrete and with Basaltic Concrete

Class 12 (Sn) inventories. The next major release fractions are of Ru and Mo, Ce and La, all between 2% and 4%. Finally, a total $\leq$0.1% of the initial inventory of uranium and Class 11 (Cd) are predicted to be released. This is very similar to the fission product release behavior predicted by MELCOR for the LCLP-PF-R-N sequence. (Note that the CORSOR-M fission product release model option used in these analyses has identically zero release in-vessel of Class 7, Class 9 and Class 11.)

Most of the released radionuclides remain in the primary system and/or the containment; only the noble gases show a significant release to the environment. Of the other radionuclides, <1% of the Cd and <0.1% of the initial inventories are released to the environment. Of the species with significant (>80%) release from fuel, the wetwell retains most of the released CsOH, Te and CsI volatiles, while the Ba and Sn aerosols are held up both in the primary system and in the wetwell.

The predicted release to the environment of each radionuclide species is lower for the LCLP-FS-R-N sequence than calculated for the LCLP-PF-R-N sequence, either with limestone concrete or with basaltic concrete; the fractions retained in the wetwell are higher, and the fractions in the drywell generally lower, for the LCLP-FS-R-N sequence analysis than calculated for the LCLP-PF-R-N sequence, reflecting the sprays removing fission products from the containment atmosphere and/or structures (*via* draining condensate films) into the suppression pool.

The retention factors for the various radionuclides in the primary system and in the overall containment are quite similar in the MELCOR LCLP-PF-R-N sensitivity study calculation with a limestone concrete cavity and in the MELCOR reference calculation with a basaltic concrete cavity. The decontamination factors for the various radionuclides for the suppression pool and for the overall containment are also very similar in the MELCOR LCLP-PF-R-N sensitivity study calculation with limestone concrete and in the MELCOR reference calculation with basaltic concrete. The retention factors predicted by MELCOR for the LCLP-FS-R-N scenario with either concrete are about the same as for the LCLP-PF-R-N scenario with either concrete; the magnitude of the various DFs calculated by MELCOR for the LCLP-FS-R-N sequence are generally higher than those calculated by MELCOR for the LCLP-PF-R-N sequence, with either type of concrete, reflecting the sprays removing fission products from the containment atmosphere and/or structures (*via* draining condensate films) into the suppression pool. While the overall containment decontamination factors predicted by MELCOR for the LCLP-FS-R-N are greater in magnitude than for the LCLP-PF-R-N sequence, the relative differences between DFs for various radionuclide classes are generally similar in the two sequences.

Both the suppression pool and overall containment decontamination factors remain nearly constant or drop very slowly for most classes after containment rupture disk actuation, but drop steadily for several radionuclide species. These are the classes for which a continuing release to the environment is predicted, while for the other classes there is only a single step-like release at containment depressurization, as illustrated in Figure 6.2.7. These results resemble those given in Figure 5.2.18 for the reference analysis with basaltic concrete, given the longer period of release between containment rupture disk opening and transient end at cavity rupture in the calculation with limestone concrete.

Table 6.2.2. Radionuclide Distribution Predicted at 87hr for LCLP-FS-R-N Sequence with Limestone Concrete

Class	Fission Product Distribution (% Initial Inventory)					
	Remaining in Fuel		Released from Fuel			
	Core	Cavity	Primary System	Drywell	Wetwell	Environment
Noble Gases (Xe)	4.40×10^{-9}	0	0.0188	4.06	7.76×10^{-3}	95.9
Alkali Metals (CsOH)	2.76×10^{-9}	$\simeq$0	14.3	5.63	79.9	0.172
Alkaline Earths (Ba)	2.30×10^{-6}	10.8	52.3	6.29	30.6	7.87×10^{-3}
Halogens (I)	$\simeq$0	$\simeq$0	$\simeq$0	$\simeq$0	$\simeq$0	$\simeq$0
Chalcogens (Te)	2.09×10^{-9}	0.0456	22.5	5.05	72.2	0.176
Platinoids (Ru)	1.51×10^{-5}	96.8	2.09	0.593	0.551	8.98×10^{-5}
Transition Metals (Mo)	1.52×10^{-5}	96.4	0.0118	0.810	2.73	2.74×10^{-3}
Tetravalents (Ce)	1.51×10^{-5}	96.0	2.54	0.793	0.667	1.28×10^{-4}
Trivalents (La)	1.52×10^{-5}	98.1	1.36×10^{-3}	0.796	1.14	2.04×10^{-3}
Uranium (U)	2.65×10^{-5}	99.9	0.0412	0.0124	0.0150	3.58×10^{-5}
More Volatile Main Group Elements (Cd)	1.52×10^{-5}	$\simeq$100	4.80×10^{-5}	0.0186	0.0306	3.33×10^{-4}
Less Volatile Main Group Elements (Sn)	9.09×10^{-7}	4.23	51.2	4.82	39.8	6.78×10^{-3}
CsI	$\simeq$0	5.47×10^{-5}	15.4	5.24	79.2	0.0999

Table 6.2.3. Radionuclide Release and Released Distribution Predicted at 87hr for LCLP-FS-R-N Sequence with Limestone Concrete

Class	Released from Fuel (% Initial Inventory)			Distribution (% Released Mass)			
	Core	Cavity	Total	Primary System	Drywell	Wetwell	Environment
Noble Gases (Xe)	99.94	0.05	99.99	0.0188	4.06	7.76×10^{-3}	95.9
Alkali Metals (CsOH)	99.94	0.05	99.99	14.35	5.63	79.94	0.172
Alkaline Earths (Ba)	86.52	2.68	89.21	58.63	7.05	34.31	8.83×10^{-3}
Halogens (I)	$\simeq0$	$\simeq0$	$\simeq0$	0.032	3.72	7.14×10^{-3}	96.24
Chalcogens (Te)	99.95	0.012	99.96	22.5	5.05	72.2	0.176
Platinoids (Ru)	3.24	1.75×10^{-4}	3.24	64.63	18.33	17.04	2.78×10^{-3}
Transition Metals (Mo)	0	3.56	3.56	0.33	22.76	76.83	0.077
Tetravalents (Ce)	3.99	1.93×10^{-3}	4.00	63.45	19.84	16.71	3.19×10^{-3}
Trivalents (La)	0	1.94	1.94	0.0696	41.06	58.77	0.105
Uranium (U)	0.061	0.009	0.070	60.08	18.01	21.86	0.052
More Volatile Main Group Elements (Cd)	0	0.050	0.050	0.097	37.55	61.68	0.67
Less Volatile Main Group Elements (Sn)	95.75	0.031	95.78	53.44	5.04	41.52	7.08×10^{-3}
CsI	99.94	0.049	99.99	15.4	5.24	79.2	0.0999

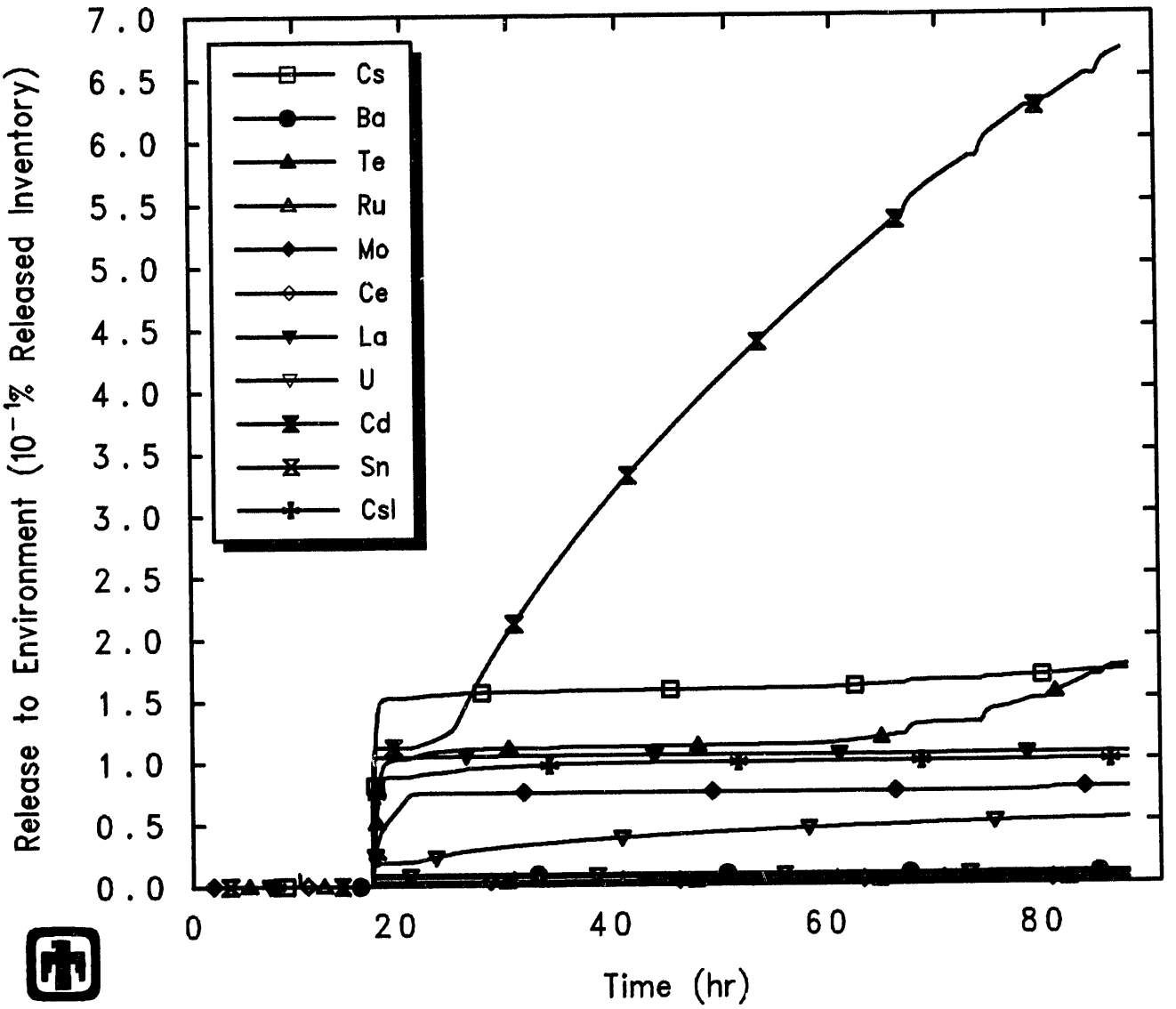

Figure 6.2.7. Radionuclide Environmental Releases Predicted by MELCOR for LCLP-FS-R-N Sequence with Limestone Concrete

6.3 LCLP-PF-R-N Sequence with "Quenched" Debris

This accident scenario is the same as discussed in Section 5.1, but with "quenched" debris in the cavity rather than unquenched, hot debris. Here, quenched debris is debris that is not hot enough to undergo significant core-concrete interaction; such debris is probably cooled enough to have formed a substantial solidified crust. The core debris is quenched in the MAAP calculation, since the average corium temperature in the lower drywell was less than 500K throughout most of the transient (as indicated in Figure 19E.2-2D in [1]), while there is no ex-vessel debris quenching model in MELCOR; the MELCOR calculation therefore predicts that the debris in the cavity remains hot ($\geq$1500K), irregardless of potential cooling and quenching by the lower drywell water pool.

However, MELCOR calculations have been done for some sequences in the ABWR with "quenched" debris. The debris was not quenched due to modelling the physical quench process, but due to numerical problems and coding errors in MELCOR. In these calculations, CORCON-calculated "layer flips" have been observed to occur every few cycles, with the cavity debris configuration oscillating between a state with metal on the bottom and one with oxide on the bottom. This behavior is physically unrealistic but, by repeatedly bringing hot debris to the top surface, increases the rate of heat loss from the debris to the overlying pool or atmosphere in the associated control volume.

The "flipping" results from small changes in the calculated densities of the metallic and oxidic phases of the debris. In reality, these phases would be mixed by the stirring action of concrete-decomposition gases unless there is a significant density gradient. CORCON-Mod2 [11], currently used in the CAV package in MELCOR, assumes complete separation of the phases regardless of how small the density difference may be. A new mixing model in CORCON-Mod3 [12] should eliminate such unphysical behavior by allowing the combination of the metallic and oxidic debris into a single heterogeneous mixture layer. In the meantime, the "layer flipping" problem can be reduced or eliminated by disabling the treatment of chemical reactions involving concrete oxides. When this reaction is omitted, ablated oxides are always added directly to the oxide layer and thus tend to reduce its density, which drives the debris bed toward a stable oxide-over-metal configuration. (When the reaction is included, reduction of concrete oxides results in addition of low-density aluminum and silicon to the metal layer whenever it is on the bottom; this tends to reduce the density of the metal layer and briefly restore the metal-over-oxide configuration.)

We emphasize that this numerical "quenching" is not physical, *i.e.*, these calculations should not be considered as predicting that debris quench would occur. However, using these "uncorrected", "quenched" calculations allows us to study how much of the differences found between MELCOR and MAAP calculations of the same sequence are a consequence of the continued core-concrete interaction in MELCOR, due to the unquenched *vs* quenched cavity debris.

The sequence of events predicted for the LCLP-PF-R-N accident is given in Table 6.3.1, with the timings of the various events as calculated by MAAP and by MELCOR

with "quenched" debris and with unquenched, hot debris (*i.e.*, the reference calculation results from Section 5.1) included for comparison. The MELCOR calculations with unquenched, hot debris and with "quenched" debris are the same up to the time of vessel failure and debris ejection into the cavity, as would be expected.

Much of the containment behavior calculated for the LCLP-PF-R-N sequence assuming "quenched" debris is very similar to the response predicted in the reference calculation with unquenched, hot debris for this scenario (described in Section 5.1), albeit shifted somewhat in time due to differences in parameters such as time to rupture disk opening. Figure 6.3.1 gives the lower drywell and wetwell pool masses for the MELCOR analyses both with "quenched" debris and with unquenched, hot debris, compared to the pocl masses calculated by MAAP (for quenched debris). During the first 42hr while results from both analyses are available, the MELCOR calculations with unquenched, hot debris and with "quenched" debris show generally very similar results for the drywell and wetwell pool masses; after cavity rupture and calculation end for the unquenched, hot debris case, the calculation assuming "quenched" debris obviously continues the same overall response.

The pressures calculated by MELCOR in the various containment control volumes assuming either "quenched" or unquenched, hot debris are presented in Figure 6.3.2, together with the containment pressure for MAAP (with quenched debris). Although the MELCOR calculation with "quenched" debris was run for 100hr, only the first 45hr are shown in the figure to highlight the containment behavior around the time of rupture disk opening. The results are all generally similar qualitatively, but with a number of quantitative differences and shifts in timing.

The differences before about 5hr are due to differences in predicted vessel failure timing and debris ejection history. The overall containment pressurization rate with "quenched" debris is very similar in MELCOR and in MAAP, confirming that the difference in pressurization rate between the MELCOR reference calculation described in Section 5.1 and the MAAP analysis is due to the core debris in the cavity being quenched in the MAAP calculation but not in the MELCOR calculation. The overall pressurization is faster in MELCOR for unquenched, hot debris than for "quenched" debris due both to the continued boiling of the overlying cavity pool water and to greater generation of noncondensable gases due to core-concrete interaction. For the MELCOR calculation with unquenched, hot debris, the containment rupture disk opening setpoint of 0.72MPa (90psig) is reached at 14.7hr, compared to rupture disk opening times of 20.7hr and 20.2hr with "quenched" debris in MELCOR and in MAAP, respectively. The higher pressures in both these MELCOR calculations at later times suggest that the loss coefficient for the rupture disk flow path is too high in the MELCOR input model.

The MELCOR calculations with unquenched, hot debris and with "quenched" debris also show generally similar results for the containment temperatures during the first 42hr, shifted somewhat in time due to differences in containment response, such as time to rupture disk opening. The behavior of the total and partial pressures, and the mole fractions, in the atmospheres of the containment control volumes is the same as illustrated in Figures 5.1.19 and 5.1.20 for the LCLP-PF-R-N calculation with unquenched, hot

Table 6.3.1. Sequence of Events Predicted by MELCOR for LCLP-PF-R-N Sequence with "Quenched" Debris and with Hot Debris, Compared to MAAP

Event	Time		
	MAAP quenched	MELCOR unquenched	MELCOR "quenched"
Accident initiation (MSIV Closure)	0.0	0.0	0.0
Reactor scrammed	4.2s		
Core uncovery begins		1,626.1s (0.45hr)	1,626.1s (0.45hr)
Water level at 2/3 core height; ADS	0.4hr	2,350.7s (0.65hr)	2,350.7s (0.65hr)
Clad failure/Gap release			
(Ring 1)		2,980.7s (0.83hr)	2,980.7s (0.83hr)
(Ring 2)		3,825.1s (1.06hr)	3,825.1s (1.06hr)
(Ring 3)		4,548.9s (1.26hr)	4,548.9s (1.26hr)
(Ring 4)		6,731.0s (1.87hr)	6,731.0s (1.87hr)
Core plate failed			
(Ring 1)		11,818.0s (3.28hr)	11,818.0s (3.28hr)
(Ring 2)		14,838.4s (4.12hr)	15,084.1s (4.19hr)
(Ring 3)		15,303.8s (4.25hr)	15,813.8s (4.39hr)
(Ring 4)		21,586.3s (6.00hr)	20,671.2s (5.74hr)
Vessel lower head failed	1.8hr		
Vessel LH penetration failed			
(Ring 1)		11,933.5s (3.31hr)	11,929.0s (3.31hr)
(Ring 2)		11,938.0s (3.32hr)	11,938.0s (3.32hr)
(Ring 3)		11,939.5s (3.32hr)	11,939.5s (3.32hr)
(Ring 4)		11,948.2s (3.32hr)	11,948.2s (3.32hr)
Commence debris ejection		11,933.5s (3.31hr)	11,933.5s (3.31hr)
Water in lower drywell boiled off	2.7hr	~22,470s (6.2hr)	~20,730s (5.76hr)
Passive flooder opens	5.4hr	22,473.7s (6.24hr)	20,734.3s (5.76hr)
Rupture disk opens	20.2hr	52,931.5s (14.70hr)	74,657.7s (20.74hr)
Concrete ablation $\geq$2m		150,967s (41.94hr)	
End of calculation	100hr	150,967s (41.94hr)	360,000s (100hr)

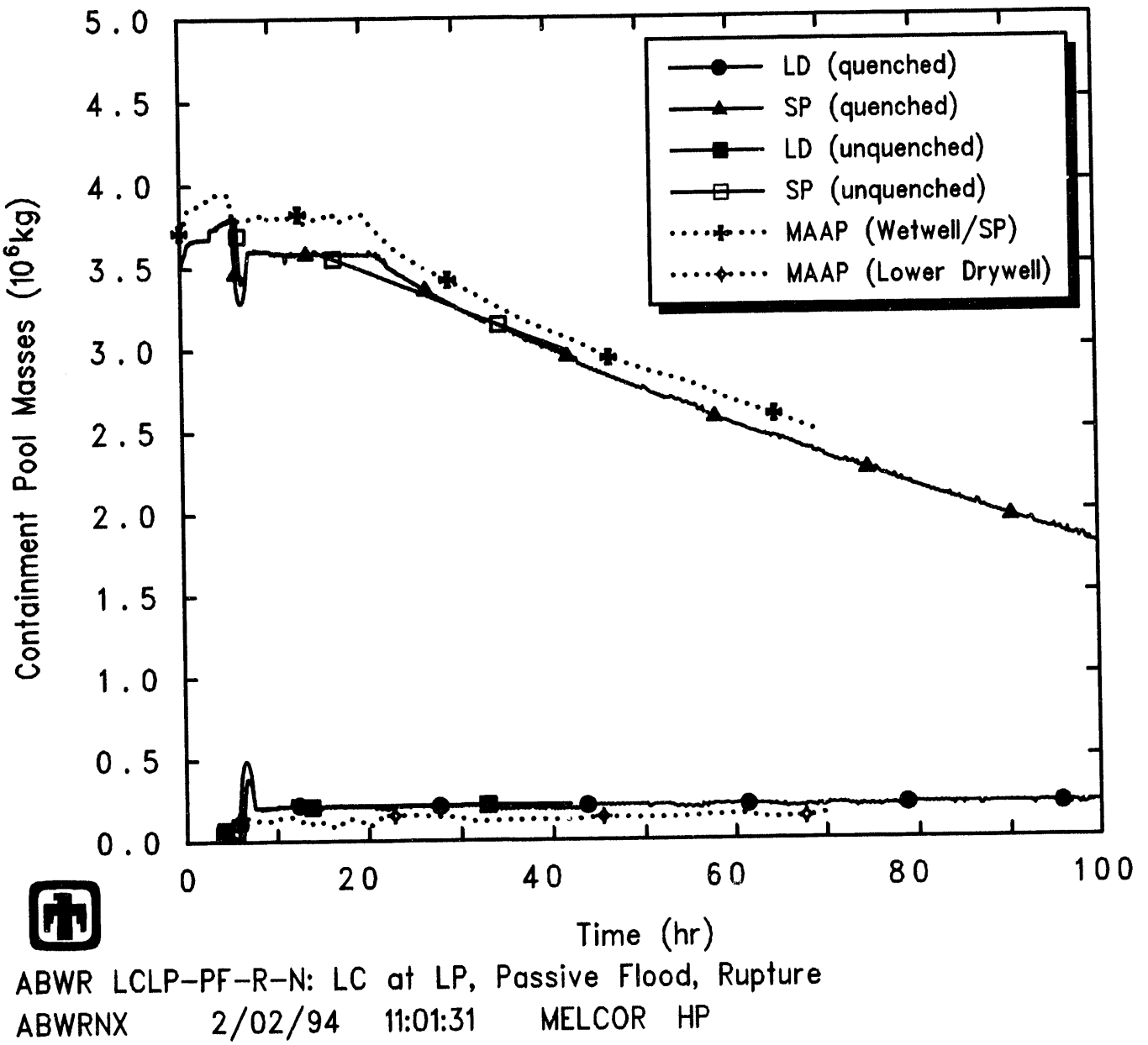

Figure 6.3.1. Lower Drywell and Suppression Pool Masses Predicted by MELCOR for LCLP-PF-R-N Sequence with "Quenched" Debris and with Hot Debris, Compared to MAAP

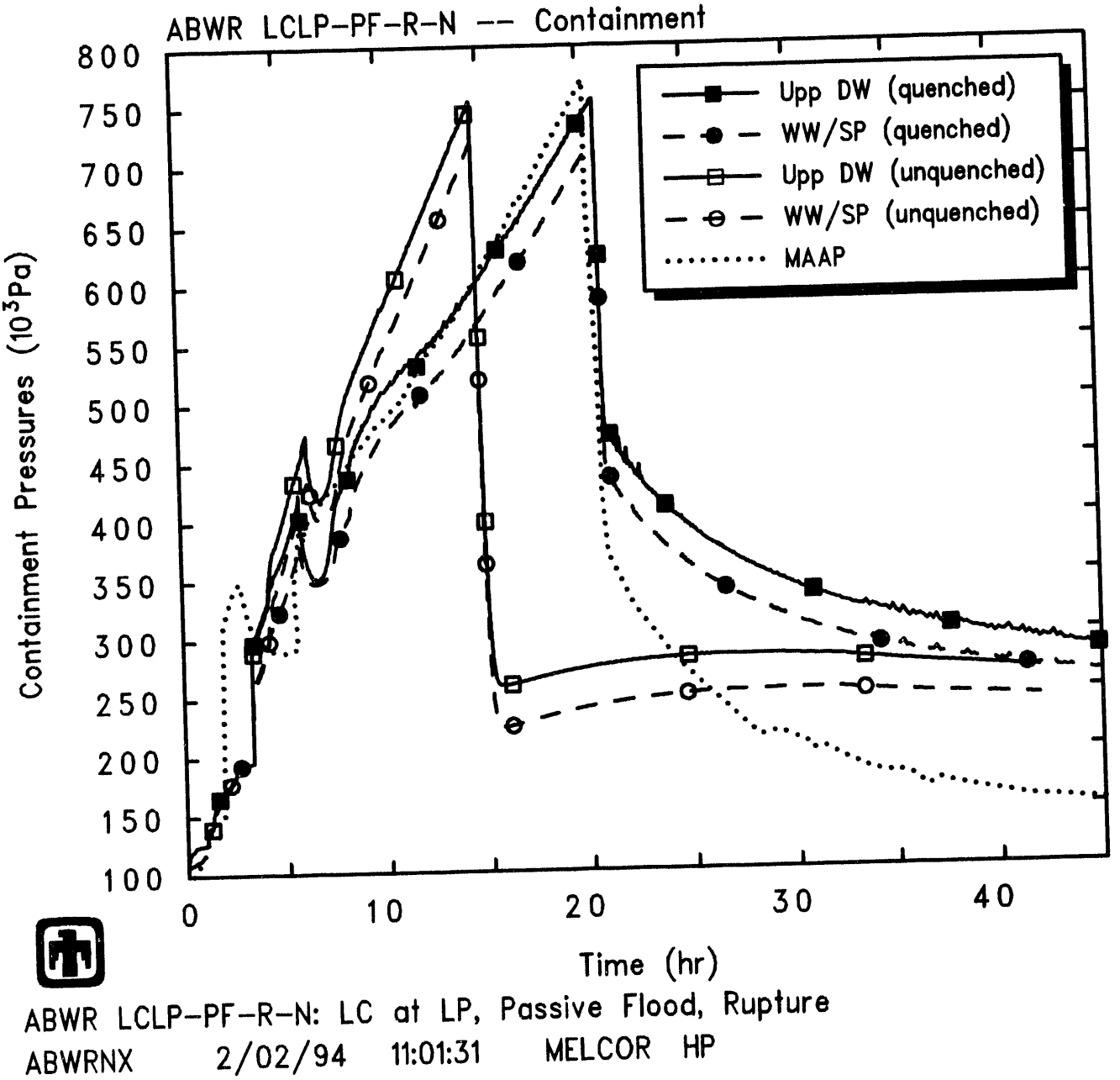

Figure 6.3.2. Containment Pressures Predicted by MELCOR for LCLP-PF-R-N Sequence with "Quenched" Debris and with Hot Debris, Compared to MAAP

debris, just shifted in time. The lower drywell and DW/WW vent atmospheres consist of almost all steam from vessel failure through calculation end; in the upper drywell, most of the atmosphere consists of steam after vessel failure; in the suppression pool, steam does not predominate until after containment rupture disk opening, while about half of the wetwell atmosphere between vessel failure and containment venting is hydrogen.

The total mass of debris in the cavity, the mass of ejected core debris and the mass of ablated concrete in the cavity calculated by MELCOR are illustrated in Figure 6.3.3; results are included both for this calculation with "quenched" debris in the cavity and for the reference calculation with unquenched, hot debris specified. The debris ejection can be seen to occur in discrete steps or stages, and is very similar for both these MELCOR calculations (as would be expected), because the in-vessel core degradation process is unaffected by the state of any debris in the cavity. The mass of concrete ablated increases continuously with time in the MELCOR reference calculation with unquenched, hot debris, but remains nearly constant after some initial ablation in the MELCOR analysis with "quenched" debris. The reference calculation with unquenched, hot debris ran until stopped by "cavity rupture", *i.e.*, ablation of the initial cavity 2m depth at some point, at 42hr; the calculation with "quenched" debris was simply stopped at 100hr.

Figure 6.3.4 presents the production of various noncondensable gases in the cavity due to core-concrete interaction, calculated by MELCOR for "quenched" debris and for the unquenched, hot debris in the reference calculation. Much lower amounts of noncondensable gases are produced in a cavity with "quenched" debris than for unquenched, hot debris. Almost all of the cavity gas production in both these calculations is in the form of hydrogen, with much smaller amounts of the other gases predicted, and with a small but growing amount of CO produced after 30-40hr in the reference analysis with unquenched, hot debris and continuing core-concrete interaction.

Figure 6.3.5 gives the calculated maximum cavity depths and radii predicted by MELCOR in this sensitivity study assuming "quenched" debris and in the reference calculation with unquenched, hot debris. (Note that these represent maximum, not average, ablation distances.) Immediately after core debris is first ejected from the vessel to the cavity upon vessel breach, there is a brief period of rapid radial ablation lasting a few hr, which stops after only 5cm of concrete loss in the reference calculation with unquenched debris but continues gradually to about 10cm of concrete loss in the sensitivity study calculation with "quenched" debris. The bulk of the concrete ablation calculated in the calculation with hot, unquenched debris is axially downward in both cases. The reference calculation stops when the axial ablation equals and tries to exceed the specified available concrete thickness of 2m at about 42hr; the calculation with "quenched" debris has ablated less than 40cm of concrete vertically by 100hr when the run was stopped.

A heavy oxide layer is calculated to exist in the cavity only for a short time after debris ejection from the vessel. In this sensitivity study calculation, MELCOR calculates a rapidly alternating configuration of a light oxide layer above a metallic debris layer reversing to a metallic debris layer above a heavy oxide layer throughout most of the transient period calculated. The metallic layer mass and thickness drop very slowly until 100hr; the mass and thickness of whichever oxide layer (light and/or heavy) is present

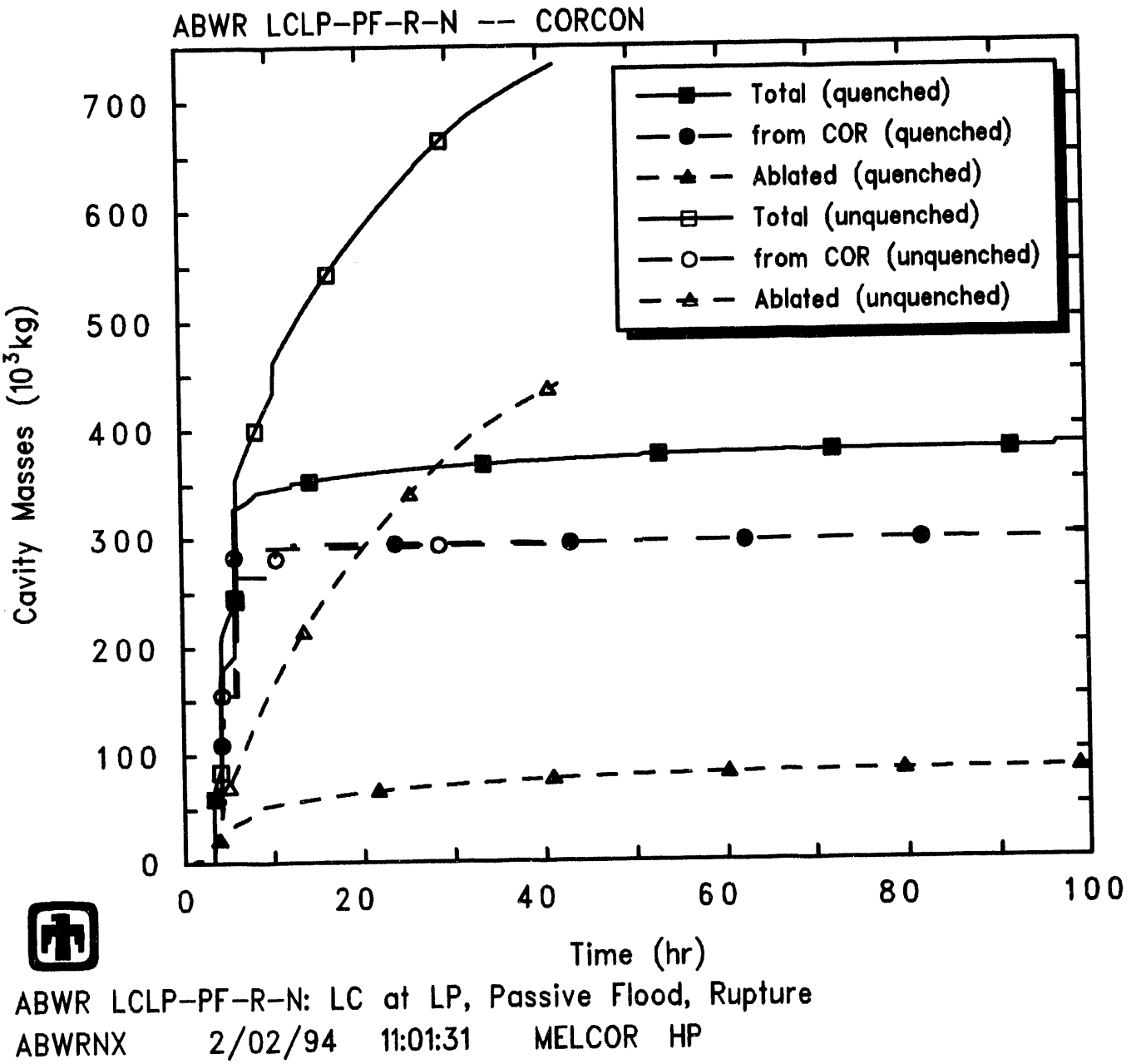

Figure 6.3.3. Cavity Material Masses Predicted by MELCOR for LCLP-PF-R-N Sequence with "Quenched" Debris and with Hot Debris

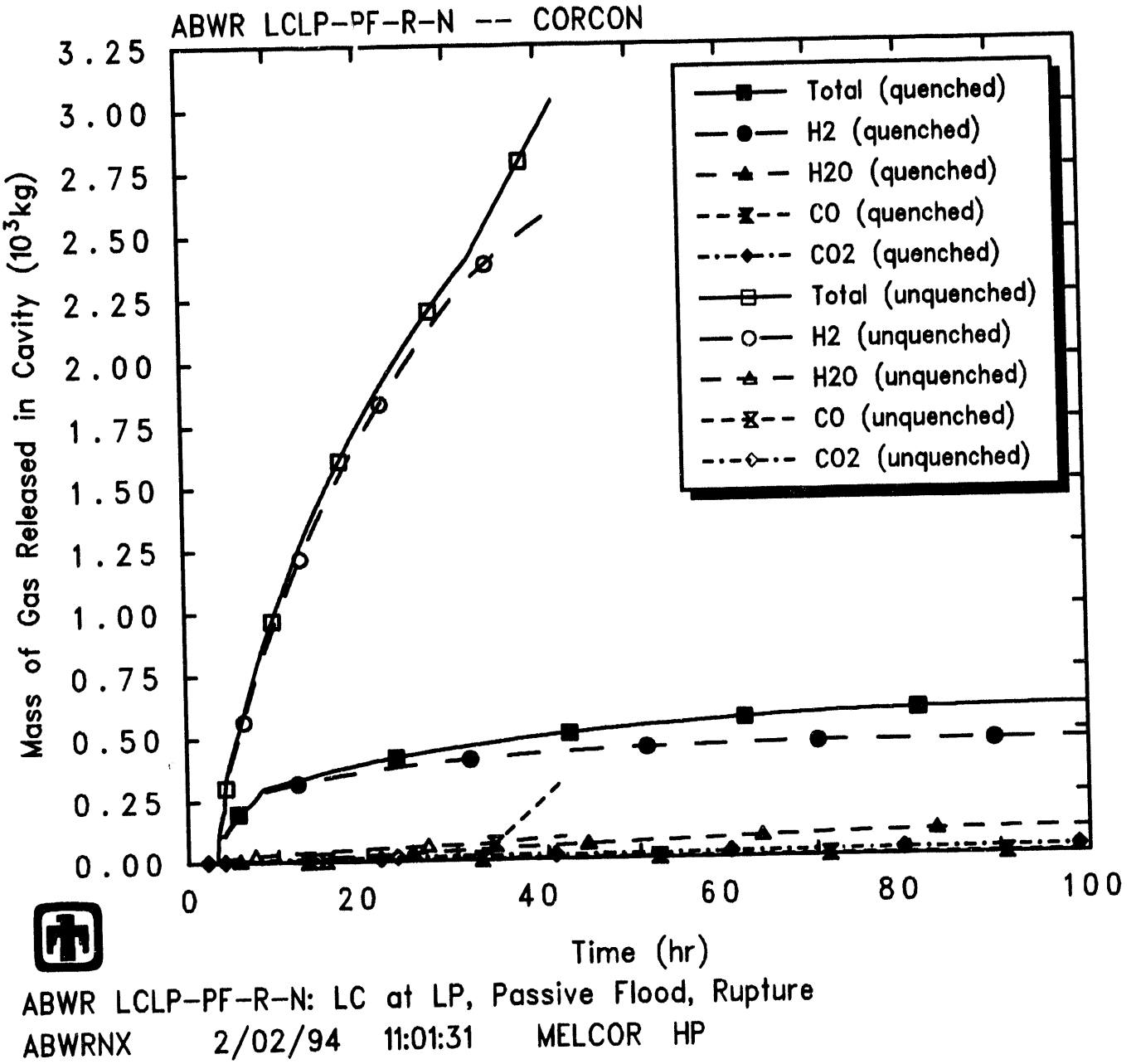

Figure 6.3.4. Cavity Gas Production Predicted by MELCOR for LCLP-PF-R-N Sequence with "Quenched" Debris and with Hot Debris

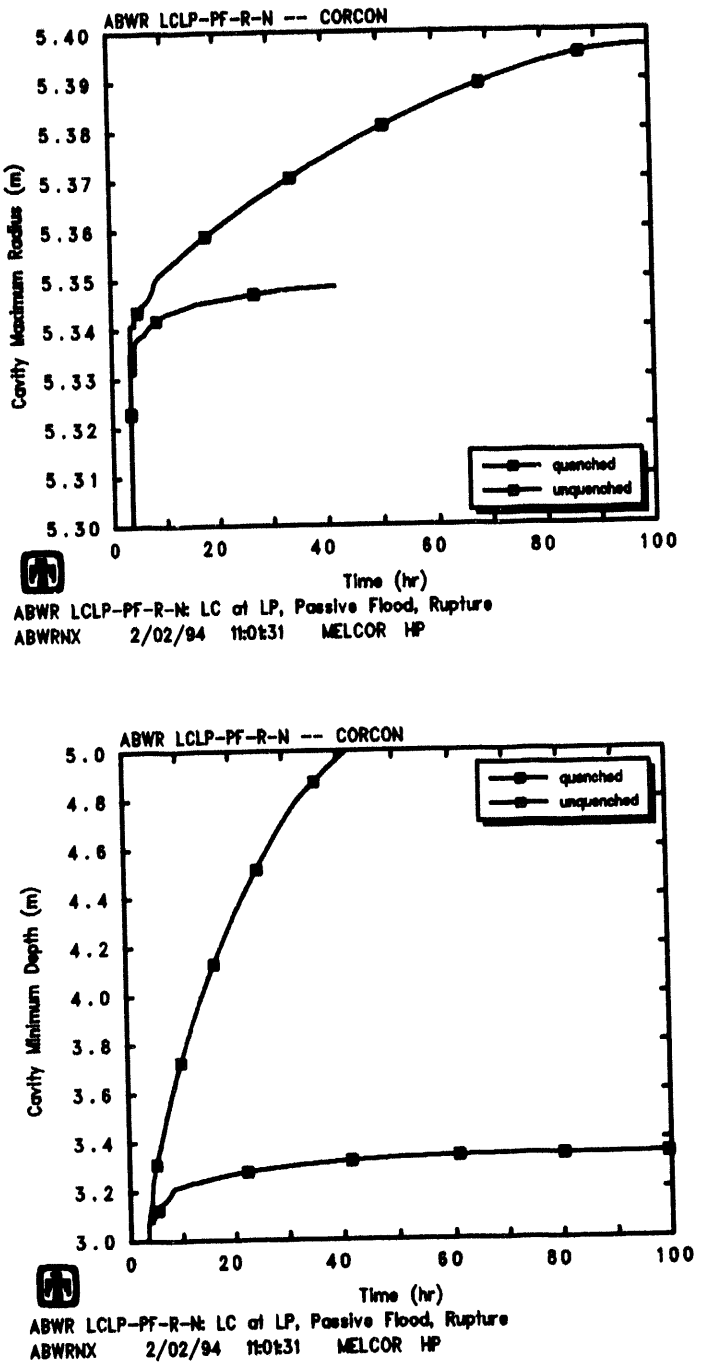

Figure 6.3.5. Cavity Maximum Radius (top) and Depth (bottom) Predicted by MELCOR for LCLP-PF-R-N Sequence with "Quenched" Debris and with Hot Debris

increase very slowly until 100hr, with the mass and thickness of the other, temporarily-vanished oxide layer going to zero. In the reference calculation with hot, unquenched debris and continuing core-concrete interaction, the metallic layer mass and thickness remain nearly constant while the light oxide layer mass and thickness increase rapidly (and the density decreases) as ablating concrete (with its resultant low-density silicate oxides) continues to dilute the high-density zirc oxide and steel oxide debris to an average density value less than the metallic debris density.

The heat transfer from the cavity debris pool in the MELCOR analysis, both downward and outward to the concrete surface and upward to the cavity volume atmosphere, is shown in Figure 6.3.6. Results are included for both the MELCOR sensitivity study calculation with "quenched" debris and for the MELCOR reference calculation with unquenched, hot debris. The "layer flipping" oscillations, which intermittently bring hot debris to the surface into contact with the overlying water pool, are clearly visible as increases in the heat flux at the debris pool surface. In both calculations, the energy transfer from the debris in the cavity upward through the debris bed surface to the lower drywell atmosphere and/or overlying water pool is 2-5 times greater than the energy transferred downward (and sideways) to the concrete. The heat fluxes calculated by MELCOR for "quenched" debris appear to be generally much lower than those calculated by MELCOR for a unquenched, hot debris cavity.

Tables 6.3.2 and 6.3.3 give the distribution of the released radionuclides at the end of the calculation (*i.e.*, at 100hr). The release behavior predicted by MELCOR for the LCLP-PF-R-N sequence assuming "quenched" debris is very similar to the release behavior predicted by MELCOR for the LCLP-PF-R-N sequence reference analysis with hot, unquenched debris (presented in Tables 5.1.4 and 5.1.5); the fission product release predicted has been quite similar for all the sequences and variations analyzed. Almost all ($\simeq$100%) of the volatile Class 1 (noble gases), Class 2 (CsOH), Class 5 (Te) and Class 16 (CsI) radionuclide species are released, primarily in-vessel, as are most (80-90%) of the Class 3 (Ba) and Class 12 (Sn) inventories. The next major release fractions are of Ru and Mo, Ce and La, all between 2% and 4%. Finally, a total $\leq$0.1% of the initial inventory of uranium and Class 11 (Cd) are predicted to be released. (Note that the CORSOR-M fission product release model option used in these analyses has identically zero release in-vessel of Class 7, Class 9 and Class 11.)

Most of the released radionuclides remain in the primary system and/or the containment; only the noble gases show a significant release (>90%) to the environment. Of the other radionuclides, 0.2-0.3% of the total volatile masses (CsOH and CsI) are released to the environment in the MELCOR LCLP-PF-R-N sensitivity study calculation with "quenched" debris, about the same as the 0.15-0.25% release predicted in the MELCOR reference calculation with unquenched, hot debris. The slightly higher releases calculated for "quenched" debris are probably a direct result of the longer time that calculation ran after rupture disk opening, extending the release period (about 80hr, compared to about <30hr in the corresponding reference calculation with unquenched, hot debris). In both cases, $\ll$0.1% of the other radionuclides' initial inventory is released to the environment.

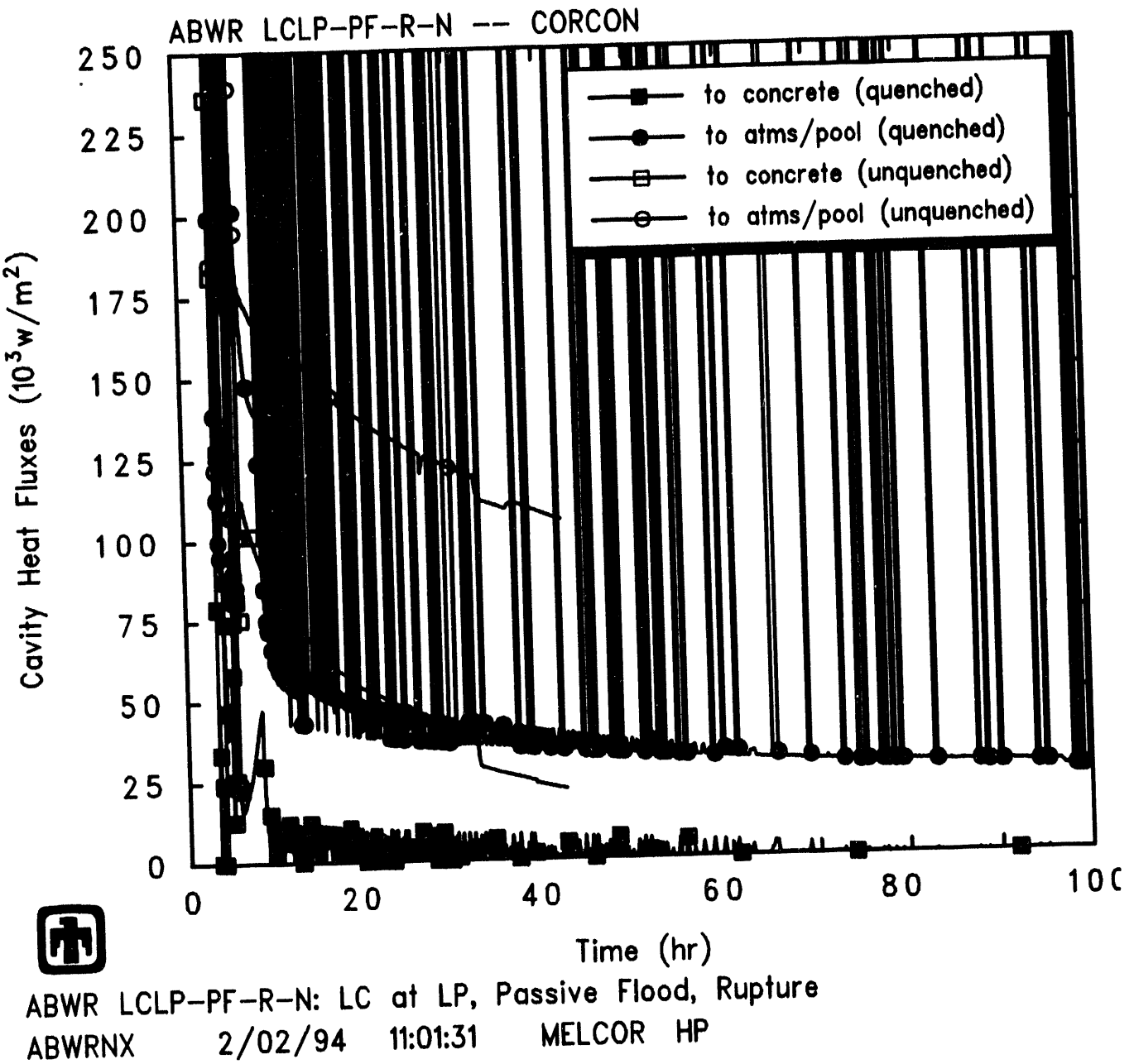

Figure 6.3.6. Cavity Heat Flows Predicted by MELCOR for LCLP-PF-R-N Sequence with "Quenched" Debris

Table 6.3.2. Radionuclide Distribution Predicted at 100hr for LCLP-PF-R-N Sequence with "Quenched" Debris

Class	Fission Product Distribution (% Initial Inventory)					
	Remaining in Fuel		Released from Fuel			
	Core	Cavity	Primary System	Drywell	Wetwell	Environment
Noble Gases (Xe)	2.35×10^{-7}	0	5.12×10^{-9}	8.77×10^{-8}	1.37×10^{-8}	$\simeq$100
Alkali Metals (CsOH)	3.04×10^{-7}	$\simeq$0	11.1	12.1	76.6	0.218
Alkaline Earths (Ba)	3.53×10^{-7}	14.7	43.8	10.6	30.9	5.84×10^{-3}
Halogens (I)	$\simeq$0	$\simeq$0	$\simeq$0	$\simeq$0	$\simeq$0	$\simeq$0
Chalcogens (Te)	3.30×10^{-7}	0.0389	27.2	9.60	63.0	0.154
Platinoids (Ru)	3.50×10^{-7}	97.0	1.61	0.919	0.517	4.71×10^{-5}
Transition Metals (Mo)	3.51×10^{-7}	99.0	2.89×10^{-3}	0.412	0.573	9.30×10^{-4}
Tetravalents (Ce)	3.50×10^{-7}	96.1	1.99	1.24	0.625	5.22×10^{-5}
Trivalents (La)	3.50×10^{-7}	97.5	1.73×10^{-3}	1.15	1.33	1.87×10^{-3}
Uranium (U)	1.42×10^{-7}	99.9	0.0284	0.0186	0.0140	1.05×10^{-5}
More Volatile Main Group Elements (Cd)	3.50×10^{-7}	$\simeq$100	3.97×10^{-5}	0.0223	0.0273	4.27×10^{-5}
Less Volatile Main Group Elements (Sn)	3.49×10^{-7}	8.30	43.7	9.22	38.7	3.99×10^{-3}
CsI	$\simeq$0	0.0123	10.7	11.8	77.2	0.257

Table 6.3.3. Radionuclide Release and Released Distribution Predicted at 100hr for LCLP-PF-R-N Sequence with "Quenched" Debris

Class	Released from Fuel (% Initial Inventory)			Distribution (% Released Mass)			
	Core	Cavity	Total	Primary System	Drywell	Wetwell	Environment
Noble Gases (Xe)	99.96	0.04	≃100	∼0	∼0	∼0	≃100
Alkali Metals (CsOH)	99.96	0.04	≃100	11.1	12.1	76.64	0.281
Alkaline Earths (Ba)	81.91	3.45	85.37	51.30	12.44	36.25	6.85×10^{-3}
Halogens (I)	≃0	≃0	≃0	∼0	∼0	∼0	≃100
Chalcogens (Te)	99.96	1.43×10^{-3}	99.96	27.20	9.60	63.04	0.154
Platinoids (Ru)	3.05	2.15×10^{-4}	3.05	52.93	30.12	16.95	1.55×10^{-3}
Transition Metals (Mo)	0	0.989	0.989	0.292	40.53	57.93	0.094
Tetravalents (Ce)	3.86	1.35×10^{-3}	3.86	51.63	32.17	16.20	1.35×10^{-3}
Trivalents (La)	0	2.49	2.49	0.0695	46.25	53.60	0.0754
Uranium (U)	0.053	0.0096	0.062	46.57	30.48	22.93	0.0171
More Volatile Main Group Elements (Cd)	0	0.050	0.050	0.0798	44.91	54.92	0.0858
Less Volatile Main Group Elements (Sn)	91.67	0.037	91.71	47.70	10.05	42.24	4.36×10^{-3}
CsI	99.97	0.025	≃100	10.7	11.8	77.2	0.257

The retention factors for CsOH and CsI in the primary system and in the overall containment are slightly (about 10%) lower and higher, respectively, in the MELCOR LCLP-PF-R-N sensitivity study calculation with "quenched" debris than in the MELCOR reference calculation with unquenched, hot debris; the retention factors for the other radionuclides in the primary system and in the overall containment are quite similar in these two calculations. The decontamination factors for the suppression pool are generally similar for a few radionuclide species (Mo, La and Cd) in the MELCOR LCLP-PF-R-N sensitivity study calculation with "quenched" debris and in the MELCOR reference calculation with hot, unquenched debris, but quite different for most of the other radionuclide species:

- $DF_{SP} \leq 100$ for classes with no in-vessel release (*i.e.*, Mo, La and Cd), and for the cesium classes (CsOH and CsI),
- $DF_{SP} \sim 200$ for Class 12 (Sn), and for Class 5 (Te) by 100hr,
- $DF_{SP} \sim 700$ for several other classes (Ba, Ru and U), and
- $DF_{SP} \geq 2000$ for Class 8 (Ce).

The overall containment DFs seem to fall into subdivisions in the MELCOR LCLP-PF-R-N sensitivity study calculation with "quenched" debris similar to those found in the MELCOR reference calculation with unquenched, hot debris, but larger in magnitude:

- $DF_{Cont} \geq 300$ for the cesium volatiles (CsOH and CsI),
- $DF_{Cont} \sim 500$ for the other volatile species (Te) by 100hr,
- $DF_{Cont} \sim 1000$ for classes with no in-vessel release (*i.e.*, Mo, La and Cd),
- $DF_{Cont} \sim 3000$ for classes with $\ll 1\%$ in-vessel release (U),
- $DF_{Cont} \sim 10{,}000$ for Class 3 (Ba) and Class 12 (Sn), and
- $DF_{Cont} \geq 30{,}000$ for Class 6 (Ru) and Class 8 (Ce).

In this LCLP-PF-R-N analysis assuming "quenched" debris, which ran much longer than the reference LCLP-PF-R-N analysis with unquenched, hot debris, the suppression pool and overall containment decontamination factors continue to drop steadily for several radionuclide species (most noticeably for Te, less noticeably for Mo). These are the classes for which a continuing release to the environment is predicted, while for the other classes there is only a single step-like release at COPS rupture, as illustrated in Figure 6.3.7.

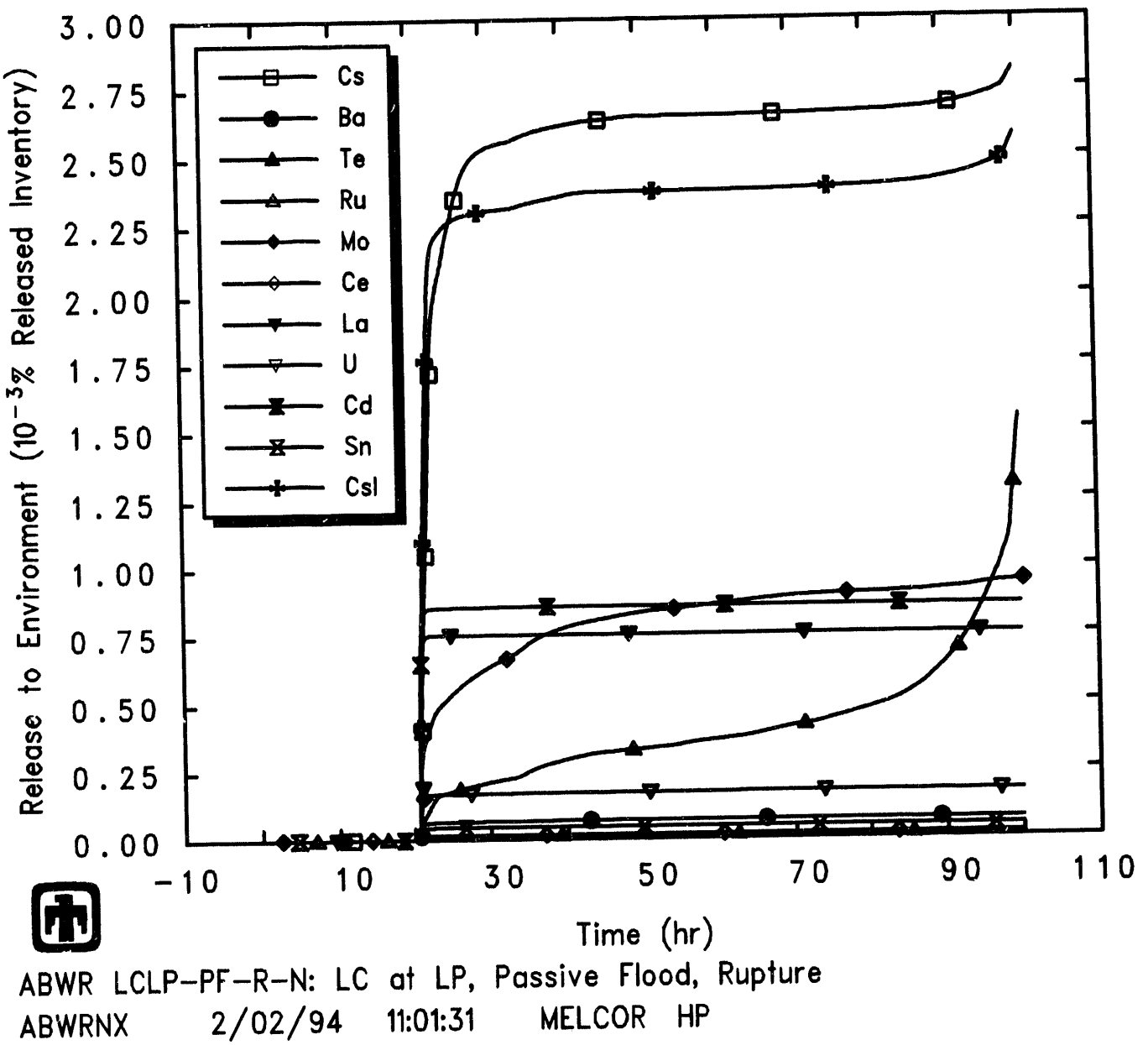

Figure 6.3.7. Radionuclide Environmental Releases Predicted by MELCOR for LCLP-PF-R-N Sequence with "Quenched" Debris

7 Summary

This report summarizes the results from MELCOR calculations of severe accident sequences in the ABWR and presents comparisons with MAAP calculations for the same sequences. MELCOR was run for two low-pressure and three high-pressure sequences to identify the materials which enter containment and are available for release to the environment (source terms), to study the potential effects of core-concrete interaction, and to obtain event timings during each sequence; the source terms include fission products and other materials such as those generated by core-concrete interactions.

All calculations, with both MELCOR and MAAP, analyzed loss-of-cooling accidents in the ABWR plant. The LCLP-PF-R-N and LCLP-FS-R-N sequences are accidents starting with a loss of all core cooling and with vessel failure occurring at low pressure; the LCHP-PF-P-M, LCHP-FS-R-N and LCHP-PS-R-N sequences also are accidents starting with a loss of all core cooling but with vessel failure occurring at high pressure. In all these sequences, the passive flooder automatically floods the lower drywell. The containment depressurizes as planned through a relief rupture disk, except in the LCHP-PF-P-M sequence where containment leakage occurs through movable penetrations. In the LCLP-FS-R-N and LCHP-FS-R-N sequences, the firewater spray provides additional containment cooling; in the LCHP-PS-R-N sequence, the drywell spray provides additional containment cooling.

MELCOR generally reproduced the event sequences predicted by MAAP, albeit usually with timing shifts. The major differences found were in core degradation and vessel failure time, and in core-concrete interaction and containment depressurization time.

In all cases, the core was predicted to uncover slightly later by MELCOR than by MAAP, at 27min for MELCOR compared to 18min for MAAP. The core degradation process also was slower in the MELCOR analyses than for MAAP - MELCOR calculated vessel failure to occur later than in the MAAP analyses, at 3.3hr *vs* 1.8hr for the LCLP sequences and at 4.5hr *vs* 2.0hr for the LCHP sequences. However, both MELCOR and MAAP predict vessel failure to occur earlier in sequences with ADS depressurizing the primary system than in scenarios where the vessel fails at pressure.

The core debris in the cavity is quenched by the passive flooder in the MAAP analyses, so little or no core-concrete interaction occurs. MELCOR does not have an ex-vessel debris quench model, so the core debris in the cavity remains unquenched and hot in the MELCOR calculations, resulting in significant and continued core-concrete interaction predicted. This in turn results in faster containment pressurization and earlier rupture disk opening predicted by MELCOR, due both to more generation of noncondensables in core-concrete interactions and to continued boiling of the cavity water pool by contact with the hot, unquenched debris.

Both MELCOR and MAAP predict release of almost all the noble gas initial inventory and small releases of all other fission products in the sequences depressurizing containment through the rupture disk, although the releases calculated by MELCOR are slightly higher than those predicted by MAAP for the volatiles CsOH and CsI (although

<1% in all cases). Some portion of the higher releases predicted by MELCOR is due to continued release from the unquenched, hot core debris in the cavity; another contributor to higher releases in MELCOR is the lack of hygroscopic effects in the MELCOR aerosol modelling.

Both MAAP and MELCOR predict much greater releases for most fission products (but lower for the noble gases) if the containment leaks through movable penetration seals than if the containment depressurizes as intended through the rupture disk in the wetwell vapor space, verifying the benefit of suppression pool scrubbing on reducing the source term to the environment. The releases to the environment calculated by MELCOR for the volatiles CsOH and CsI in this case (10-15%) are in good agreement with the values predicted by MAAP (8-10%), as are the releases of the noble gases (about 50% with both codes).

Sensitivity studies were done on the impact of assuming limestone rather than basaltic concrete, and on the effect of quenching core debris in the cavity compared to having hot, unquenched debris present. Assuming limestone concrete in the cavity resulted in faster containment pressurization and earlier rupture disk opening due to more generation of noncondensables in core-concrete interactions. Having "quenched" debris in the cavity in the MELCOR calculations resulted in slower containment pressurization and later rupture disk opening, in better agreement with the MAAP results. Varying the concrete type or the debris temperature (*i.e.*, "quenched" *vs* unquenched) had no major effect on the fission product release calculated by MELCOR.

Bibliography

[1] Sections from the ABWR SSAR, private communication from J. Monninger, NRC, to L. N. Kmetyk, SNL, April 21, 1993.

[2] R. M. Summers *et al.*,"MELCOR 1.8.0: A Computer Code for Severe Nuclear Reactor Accident Source Term and Risk Assessment Analyses", NUREG/CR-5531, SAND90-0364, Sandia National Laboratories, January 1991.

[3] Letter from M. K. Carmel, SNL, to Jae Jo. BNL, dated November 12, 1990.

[4] J. A. Gieseke *et al.*, "Source Term Code Package: A User's Guide (Mod 1)", NUREG/CR-4587, BMI-2138, Battelle Memorial Institute, 1986.

[5] B. Wolfe, D. R. Wilkins, "Improvements in Boiling Water Reactor Designs and Safety", in Proceedings of the International Topical Meeting on Safety of Next Generation Power Reactors, Seattle, Washington, May 1-5, 1988.

[6] S. A. Hucik, "Modern Technology Applied in the Advanced BWR (ABWR)", in Proceedings of the International Topical Meeting on Safety of Next Generation Power Reactors, Seattle, Washington, May 1-5, 1988.

[7] M. R. Kuhlman, D. J. Lehmicke, R. O. Meyer, "CORSOR User's Manual", NUREG/CR-4173, BMI-2122, Battelle Memorial Institute, March 1985.

[8] L. N. Kmetyk, L. N. Smith, "Summary of MELCOR 1.8.2 Calculations for Three LOCA Sequences (AG, S2D, and S3D) at the Surry Plant", NUREG/CR-6107, SAND93-2042, Sandia National Laboratories, to be published.

[9] L. N. Kmetyk, "MELCOR 1.8.2 Assessment: Surry PWR TMLB' (with a DCH Study)", SAND93-1899, Sandia National Laboratories, to be published.

[10] J. J. Carbajo, "Severe Accident Source Term Characteristics for Selected Peach Bottom Sequences Predicted by the MELCOR Code", NUREG/CR-5942, ORNL/TM-12229, Oak Ridge National Laboratory, September 1993.

[11] R. K. Cole, D. P. Kelly, M. A. Ellis, "CORCON-Mod2: A Computer Program for Analysis of Molten-Core Concrete Interactions", NUREG/CR-3920, SAND84-1246, Sandia National Laboratories, 1984.

[12] D. R. Bradley, D. R. Gardner, J. E. Brockmann, R. O. Griffith, "CORCON-MOD3: An Integrated Computer Model for Analysis of Molten Core-Concrete Interactions", NUREG/CR-5843, SAND92-0167, Sandia National Laboratories, October 1993.

External Distribution:

U. S. Nuclear Regulatory Commission (19)
Attn: S. Acharya, TWF-9F31
Y. S. Chen, TWF-10K8
M. A. Cunningham, TWF-9F31
F. Eltawila, TWF-10K8
R. B. Foulds, TWF-10K8
S. Basu, TWF-10K8
C. Gingrich, TWF-10K8
C. G. Tinkler, TWF-10K8
R. O. Meyer, TWF-10G6
A. Mitchell, TWF-17G21
C. P. Ryder, TWF-9F31
L. Soffer, TWF-10F13
J. A. Murphy, TWF-10E50
L. M. Shotkin, TWF-10G6
N. Lauben, TWF-10G6
R. Landry, OWFN 11D23
A. Drozd, OWFN 8E1
J. D. Monninger, OWFN 8E1
R. Palla, OWFN 8E1
Washington, DC 20555

S. Y. Chen
Argonne National Laboratory
9700 South Cass Avenue
Argonne, IL 60439

Battelle Columbus Laboratories (3)
Attn: P. Cybulskis
M. Carmel
R. S. Denning
505 King Avenue
Columbus, OH 43201

Brookhaven National Laboratory (2)
Attn: I. K. Madni
T. Pratt
Bldg. 130
32 Lewis
Upton, NY 11973

Idaho National Engineering Laboratory (5)
Attn: A. Brown
R. J. Dallman
D. W. Golden
S. E. Reed
G. W. Johnsen
EG&G Idaho
P. O. Box 1625
Idaho Falls, ID 83404

D. Jones
EI International
P. O. Box 50736
Idaho Falls, ID 83405

Electric Power Research Institute (3)
Attn: E. Fuller
R. N. Oehlberg
P. O. Box 10412
Palo Alto, CA 94303

Los Alamos National Laboratory (2)
Attn: B. E. Boyack, K-551
D. R. Liles, K-553
P. O. Box 1663
Los Alamos, NM 87545

Oak Ridge National Laboratory (11)
P. O. Box 2009
Oak Ridge, TN 37831-8057
Attn: S. R. Greene, MS-8057
R. H. Morris, MS-8057
S. E. Fisher, MS-8057
R. Sanders, MS-8057
T. L. Heatherly, MS-8057
S. A. Hodge, MS-8057
C. R. Hyman, MS-8057
B. W. Patton, MS-8057
D. B. Simpson, MS-8057
R. P. Taleyarkhan, MS-8057
M. L. Tobias, MS-8088

W. P. Barthold
Barthold & Associates
132 Seven Oaks Drive
Knoxville, TN 37922

K. C Wagner
Science Applications Intl. Corp.
2109 Air Park Rd. SE
Albuquerque, NM 87106

Savannah River Laboratory (2)
Attn: B. DeWald
D. Allison
Westinghouse Savannah River Co.
Bldg. 773-41A
Aiken, SC 29808-0001

Westinghouse Hanford Co. (2)
Attn: D. Ogden
O. Wang
P. O. Box 1970
Richland, WA 99352

General Electric Company (3)
Knolls Atomic Pwer Laboratory
Attn: D. F. McMullan
G. H. Epstein
E. Mennard
Bldg. F3, Room 8
P. O. Box 1072
Schenectady, NY 12301-1072

Bettis Atomic Power Laboratory (3)
Attn: Mark Riley
Jow Semanchik
Vincent Baiamonte
P. O. Box 79
West Mifflin, PA 15122

Mohsen Khatib-Rahbar
Energy Research Inc.
P. O. Box 2034
Rockville, MD 20852

V. K. Dhir
2445 22nd Street
Santa Monica, CA 90403

R. Viskanta
Purdue University
Heat Transfer Laboratory
School of Mechanical Engineering
West Lafayette, IN 47907

Dr. Jim Gieseke
Battelle Memorial Institute
505 King Ave.
Columbus, Ohio 43201

M. A. Kenton
Gabor, Kenton & Associates
770 Pasquinelli Drive
Suite 426
Westmont, IL 60559

University of California
Attn: T. Theofanous
ERC-CRSS
Santa Barbara, CA 93106

Professor K. B. Cady
Nuclear Science and Engineering
Cornell Universioty
Ward Laboratory
Ithaca, NY 14853-7701

F. E. Haskin
University of New Mexico
Department of Chemical and Nuclear Engineering
Albuquerque, NM 87131

J. C. Lee
University of Michigan
Lept. of Nuclear Engineering
Cooley Building, North Campus
College of Engineering
Ann Arbor, MI 48109-2104

University of Wisconsin (2)
Dept. of Nuclear Engineering
Attn: M. L. Corradini
G. A. Moses
Engineering Research Building
1500 Johnson Drive
Madison, WI 53706

Ramu K. Sundaram
Manager, LOCA Analysis Group
Nuclear Engineering
Yankee Atomic Electric Company
580 Main Street
Bolton, MA 01740

John Bolin
CEGA
P. O. Box 85608
San Diego, CA 92186-9784

M. Plys
Fauske & Associates
16W070 West 83rd Street
Burr Ridge, IL 60521

Nick Trikouros
GPU Nuclear Corporation
One Upper Pond Road
Parsippany, NJ 07054

B. Raychaudhuri
Nebraska Public Power District
PRA & Engineering Review Group
P. O. Box 499
Columbus, NE 68601

Frank Elia
Stone & Webster Engineering Corp.
245 Summer Street
Boston, MA 02210

Prof. Dr. Johann Korkisch
Institute of Analytical Chemistry
University of Vienna
A-1090 Vienna, Währingerstrasse 38
AUSTRIA

Samir S. Girgis
Atomic Energy of Canada Limited
CANDU Operations
Sheridan Park Research Community
Mississagua, Ontario
CANADA L5K1B2

Paul J. Fehrenbach
Chalk River Nuclear Laboratories
Fuel Engineering Branch, RSR Division
Chalk River, Ontario
CANADA KOJ1J0

Dr. Bohumír Kujal
Department of Reactor Technology
Nuclear Research Institute Řež plc
250 68 Řež
CZECH REPUBLIC

Andrej Mitro
Institute of Radioecology and Applied Nuclear Techniques
Garbiarska 2
P. O. Box A-41
040 61 Košice
CHECHOSLOVAKIA

Shih-Kuei Cheng
Institute of Nuclear Energy Research
P. O. Box 3-3
Lung-Tan. Taiwan
REPUBLIC OF CHINA

Mr. Yi-Bin Chen
Department of Nuclear Technology
Atomic Energy Council
67, Lane 144
Keelung Road, Section 4
Taipei, Taiwan 106
REPUBLIC OF CHINA

Technical Research Centre of Finland (3)
Nuclear Engineering Laboratory
Attn: Lasse Mattila
Ilona Lindholm
Esko Pekkarinen
P. O. Box 208 (Tekniikantie 4)
SF-002151 Espoo
FINLAND

Jorma V. Sandberg
Finnish Center Radiation & Nucl. Safety,
Dept. of Nuclear Safety
P. O. Box 268
SF-00101 Helsinki
FINLAND

Akihide Hidaka
Safety Research Department
Reactor Accident Studies and Modelling Branch
DRS/SEMAR
Cadarache Nuclear Center
13108 Saint-Paul-Lez-Durance Cedex
FRANCE

Dr. Lothar Wolf
Battelle Institute EV
AM Romerhof 35
D-6000
Frankfurt/Main90
GERMANY

Gesellschaft fur Anlagen- und Reaktorsicherheit (3)
Attn: Ulrich Erven
Walter Erdmann
Manfred Firnhaber
Schwertnergasse 1
D-5000 Koln 1
GERMANY

Kernforschungzentrum, Karlsruhe (3)
Attn: P. Hofmann
Werner Scholtyssek
Philipp Schmuck
P. O. Box 3640
D-7500 Karlsruhe 1
GERMANY

Udo Brockmeier
University of Bochum
Energietechnik
IB-4-128
D-4630 Bochum
GERMANY

György Gyenes
Central Research Institute for Physics
Institute for Atomic Energy Research
H-1525 Budapest, P. O. Box 49
HUNGARY

Joint Research Center
Commission of the European Communities
Attn: Alan Jones
Iain Shepherd
Safety Technology Institute
21020 Ispra (Va)
ITALY

Giovanni Saponaro
ENEA
Natl. Comm. for R&D of Nuclear Energy
Via Vitaliano Brancati, 48
00144 Rome
ITALY

Japan Atomic Energy Research Institute (3)
Attn: Kunihisa Soda
Jun Sugimoto
Norihiro Yamano
Tokai-mura, Naka-gun, Ibaraki-ken
319-11, JAPAN

Dr. Masayoshi Shiba, Director General
Institute of Nuclear Safety
Nuclear Power Engineering Corporation
Fujita Kankou Toranoman Bldg. 7F
3-17-1, Toranoman
Minato-Ku, Tokyo, 105
JAPAN

Masao Ogino
Mitsubishi Atomic Power Industries
4-1 Shibakoen 2-Chome
Minatoku Tokyo
JAPAN

Hidetoshi Okada
Nuclear Power Engineering Corporation
3-17-1, Toranomon Bldg. 5F
Minato-ku, Tokyo 105
JAPAN

Hirohide Oikawa
Toshiba Corporation
8, Shin-Sugita, Isogo-ku
Yokohama
JAPAN

Korea Atomic Energy Research Inst. (3)
Attn: Kun-Joong Yoo
Song-Won Cho
Dong-Ha Kim
P. O. Box 7, Daeduk Danji
Taejon
SOUTH KOREA 305-353

Jae Hong Park
Safety Assessment Department
Korea Atomic Energy Research Institute
P. O. Box 16, Daeduk-Danji
Taejon
SOUTH KOREA 305-353

Netherlands Energy Research Foundation (2)
Attn: Karel J. Brinkmann
E. J. Velema
P. O. Box 1
1755 ZG Petten
THE NETHERLANDS

Dr. Valery F. Strizhov
Russian Academy of Science
Institute of Nuclear Safety
Moscow, G. Tulsky, 52
113191, RUSSIA

Dr. B. Mavko
Institut Josef Stepan
Odsek za Reaktorsko Tehniko
61111 Ljubljana
Jamova 39
P. O. Box 100
SLOVENIA

Universidad Politecnica de Madrid (2)
Attn: Augustin Alonzo Santos
Francisco Martin
E.T.S. Ingenieros Industriales
Jose Gutierrez Abascal, 2
28006 Madrid
SPAIN

Juan Bagues
Consejo de Seguridad Nuclear
Justo Dorado, 11
28040, Madrid
SPAIN

Oddbjörn Sandervåg
Statens Kärnkraftinspektion
Swedish Nuclear Power Inspectorate
Box 27106 102 52 Stockholm
SWEDEN

L. Hammar, Director
Division of Research
Swedish Nuclear Power Inspectorate
Statens Karnkraftinspektion
Sehlstedtsgatan 11
Box 27106
S-102-50 Stockholm
SWEDEN

B. Raj Sehgal
Department of Nuclear Power Safety
Royal Institute of Technology
Brinellvagen 60
S-100 44 Stockholm
SWEDEN

Swiss Federal Nuclear Safety Inspectorate (4)
Attn: S. Chakraborty
Sang Lung Chan
U. Schmocker
H. P. Isaak
CH-5232 Villigen-HSK
SWITZERLAND

United Kingdom Atomic Energy Agency (3)
Winfrith Technology Center
Attn: T. Haste
S. R. Kinnersley
D. W. Sweet
Winfrith, Dorchester, Dorset
UNITED KINGDOM, DTS 8DH

C. Wheatley
United Kingdom Atomic Energy Authority
Safety & Reliability Directorate
Wigshaw Lane, Culcheth, Warrington
Cheshire, WA3 4NE
UNITED KINGDOM

Geoffrey Brown
AEA Technology
Consultancy Services
Thomson House
Risley, Warrington WA3 6AT
UNITED KINGDOM

Internal Distribution:

MS1328 R. S. Longenbaugh, 6342
MS0736 N. R. Ortiz, 6400
MS0744 W. A. von Riesemann, 6403
MS0744 D. A. Powers, 6404
MS0747 A. L. Camp, 6412
MS0747 S. E. Dingman, 6412
MS0748 F. T. Harper, 6413
MS0742 J. E. Kelly, 6414
MS0745 S. L. Thompson, 6418 (10 copies)
MS0745 R. K. Cole, 6418
MS0745 A. A. Elsbernd, 6418
MS0745 L. N. Kmetyk, 6418 (10 copies)
MS0745 R. C. Smith, 6418
MS0745 D. S. Stuart, 6418
MS0745 R. M. Summers, 6418
MS0899 Technical Library, 7141 (5 copies)
MS0619 Technical Publications, 7151
MS0100 Document Processing for DOE/OSTI, 7613-2 (10 copies)
MS9018 Central Technical Files, 8523-2

*U.S. GOVERNMENT PRINTING OFFICE 1994-0-573-026/00011

DATE
FILMED
10/31/94

END